Experimental Study of Photonic Band Gap Accelerator Structures

by

Roark A. Marsh

B.S. (Physics), UC Santa Cruz (2003)
B.A. (Mathematics and Classical Studies), UC Santa Cruz (2003)

Submitted to the Department of Physics
in partial fulfillment of the requirements for the degree of

Doctor of Philosophy in Physics

at the

MASSACHUSETTS INSTITUTE OF TECHNOLOGY

June 2009

Author .....
Department of Physics
April 27, 2009

Certified by .....
Richard J. Temkin
Senior Scientist, Department of Physics
Thesis Supervisor

Accepted by .....
Thomas J. Greytak
Associate Department Head for Education

Experimental Study of Photonic Band Gap Accelerator Structures

by

Roark A. Marsh

Submitted to the Department of Physics
on April 27, 2009, in partial fulfillment of the
requirements for the degree of
Doctor of Philosophy in Physics

Abstract

This thesis reports theoretical and experimental research on a novel accelerator concept using a photonic bandgap (PBG) structure. Major advances in higher order mode (HOM) damping are required for the next generation of TeV linear colliders. In this work, PBG HOMs are studied theoretically and experimentally for the first time. PBG HOMs are shown in simulation to be low Q lattice modes, removed from the cavity defect and beam position. Direct wakefield measurements were made in hot test using the bunch train produced by the MIT HRC 17 GHz linear accelerator. Measurements are compared with beam-loading theory, and wakefield simulations using *ANALYST*. Excellent agreement is observed between theory predictions and power measured in the 17 GHz fundamental operating mode; reasonable agreement is also seen with the 34 GHz wakefield HOM. In order to understand the performance of PBG structures under realistic high gradient operation, an X-band (11.424 GHz) PBG structure was designed for high power testing in a standing wave breakdown experiment at SLAC. The PBG structure was hot tested to gather breakdown statistics, and achieved an accelerating gradient of 65 MV/m at a breakdown rate of two breakdowns per hour at 60 Hz, and accelerating gradients above 110 MV/m at higher breakdown rates. High pulsed heating occurred in the PBG structure, with many shots above 270 K, and an average of 170 K for 35×10^6 shots. Damage was observed in both borescope and scanning electron microscope imaging. No breakdown damage was observed on the iris surface, the location of peak electric field, but pulsed heating damage was observed on the inner rods, the location of magnetic fields as high as 1 MA/m. Breakdown in accelerator structures is generally understood in terms of electric field effects. PBG structure results highlight the unexpected role of magnetic fields on breakdown. The hypothesis is presented that the low level electric field on the inner rods is enhanced by pulsed heating surface damage, and causes breakdown. A new PBG structure was designed with improved pulsed heating, and will be tested. These results greatly further the understanding of advanced structures with wakefield suppression that are necessary for future colliders.

Thesis Supervisor: Richard J. Temkin
Title: Senior Scientist, Department of Physics

Acknowledgments

I would like to thank Rick for being an amazing adviser, and for his wisdom. Rick's curt reply to most complaints regarding the weather or other trivialities is that they "build character". The experiences I have had here at MIT: in courses, in the office or lab, during IAP or PE classes, or exploring the multitude of other experiences offered in the larger world of Cambridge and Boston have certainly built character, and allowed me to grow a great deal during my time here at MIT. I would like to thank those who have provided feedback on my thesis: Emilio Nanni, Michael Shapiro, and especially, the members of my thesis committee: Richard Temkin, Miklos Porkolab, and Jan Egedal.

I would not have made it here if it weren't for the many teachers and professors I have had over the years. Mr. Ko singled out academics as a goal worth pursuing, and constructed my experience into something that has launched me henceforth. Ms. Strub provided balance and support when I desperately needed both. Mr. Alison introduced me to Physics, and his enthusiasm has remained with me for years.

This point in my life has been made possible thanks to the financial support of a great number of people who have contributed to my education. Valley Scholars and Gordon Moore provided more than college counseling and scholarship money, but through Judith Schweikert, another supportive parent. The UC Regents, much despised for cutting down trees and raising tuition, supported my undergraduate degrees. The US Department of Energy, Office of Science, High Energy Physics program has funded the grants that have made my graduate research possible. PAC, AAC, and EPAC have all generously supported my attendance to conferences which have been vital learning experiences. The USPAS and ILC have both sponsored my attendance at summer schools, which have single-handedly provided my formal education in accelerator physics.

The Waves and Beams division has been, and continues to be a wonderful place to work. For that I wish to thank the group as it has been constituted over my time here: Michael Shapiro, Chiping Chen, Paul Woskov, Mark Hess, Steve Korbly,

Jenya Smirnova, Ronak Bhatt, Jing Zhou, Ksusha Samokhvalova, Seong-Tae Han, Yoshi Hidaka, Hae Jin Kim, Melissa Hornstein, Jim Anderson, Eunmi Choi, Colin Joye, Antoine Cerfon, Antonio Torrezan, Nick Comfoltey, David Tax, Emilio Nanni, Elizabeth Kowalski. I would especially like to thank Bill Mulligan, without whom no interlock would function; Ivan Mastovsky who gets everything built more quickly and simply than you originally planned; Jags Sirigiri, who juggles both foreseeable and unforeseeable problems to keep the experiments running; Amit Kesar, who stuck with me until I really could not only turn everything on in the lab, but could manage running, tuning and rebuilding on my own; and Brian Munroe for rapidly transitioning to picking up the pieces of our lab, and making it his own. I would also like to thank a de facto member of our group, Jake Haimson, who sticks with us till it clicks, even if he did figure out and solve our problems some time in the 1960s. I would like to thank Chad Marchewka, for being the best officemate I ever had at MIT, and making all my Physics knowledge sound more impressive than I thought.

The bulk of my latest thesis project was made possible because of the extensive expertise of a large number of people at the SLAC National Accelerator Laboratory. I would specifically like to thank Sami Tantawi for taking an interest in our ideas; Valery Dolgashev for ushering me through the process of design, testing, and analyzing; Jim Lewandowski for cold testing and bead pulling; Dian Yeremian for high power testing, and operational procedures; and Lisa Laurent for SEM micrographs.

None of this thesis would exist without the support of my family in my life. I'd like to thank my brother Ben for being someone who at least pretends to listen to me ranting about my current workout or interest. I'd like to thank Sofy for endless East coast acclimation help, study breaks, and commiseration on grad student life. I'd like to thank Sharon and David for being who they are; for making me feel like my papers, however dubious in content, find their way onto someone's fridge. I need to thank my wife Katie for so many things that deserve more than thanks. I wouldn't be here without you, I wouldn't have made it through things without you, none of it would mean as much without you, as it does with.

For Katelyn

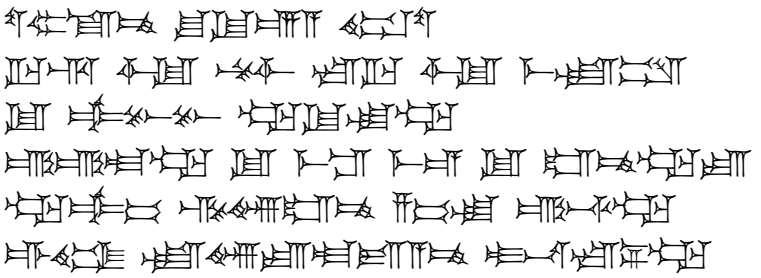

— Gilgamesh, X, III

Contents

List of Figures

List of Tables

Chapter 1

Introduction

1.1 Accelerator Physics

For the last 80 years, High Energy Physics (HEP) has been driven by technological advances in the field of accelerator physics. This evolution can be summarized in the "Livingston" plot shown in Figure 1-1, which plots accelerated particle energy against the year of accelerator commissioning. In turn, accelerator driven HEP has been the biggest motivator for advances in accelerator technology. Advances have made our current understanding of the basic forces and particle constituents of the universe possible. The Standard Model of particle physics is the most precisely vetted physical model Science has brought forth. The Standard Model posits that Quantum Field Theories (QFT) accurately describe the interaction of three generations of Quarks and Leptons with the fundamental Electromagnetic, and Nuclear Strong and Weak forces. Particle interactions within QFT involve massless particles. A quantum theory of gravity has long eluded theorists, though particle mass can be added to QFT. The Standard Model includes a prescription for adding mass to particles using the Higgs mechanism. The additional spontaneously broken symmetry involved in the mechanism predicts an associated spin zero Goldstone boson exists: the Higgs boson. The Higgs boson is the last undiscovered piece of the Standard Model that is predicted and has yet to be observed.

Higgs boson searches have been conducted using previous collider data. No detec-

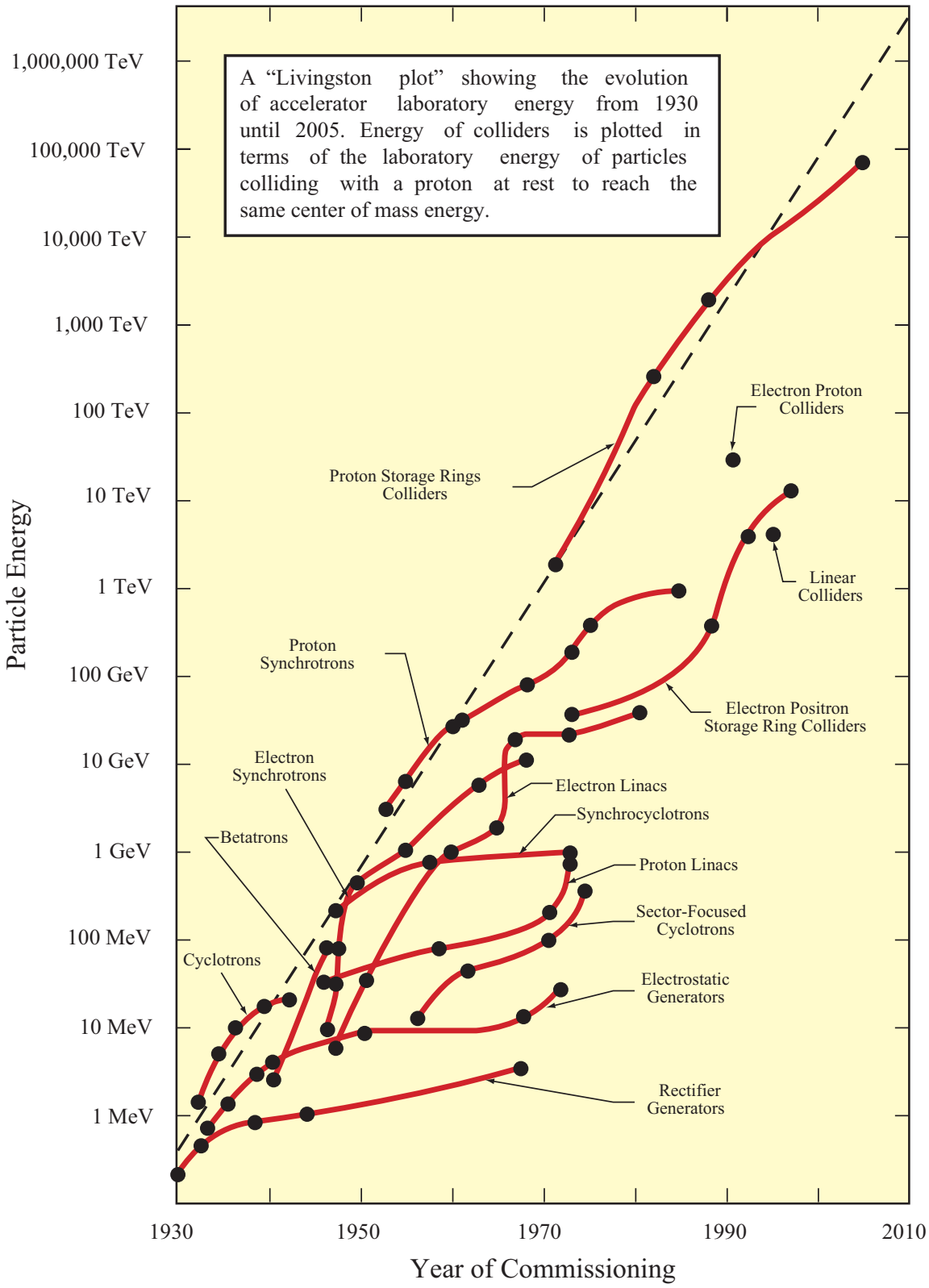

Figure 1-1: "Livingston" plot of accelerated particle energy versus year of accelerator commissioning [1, 2].

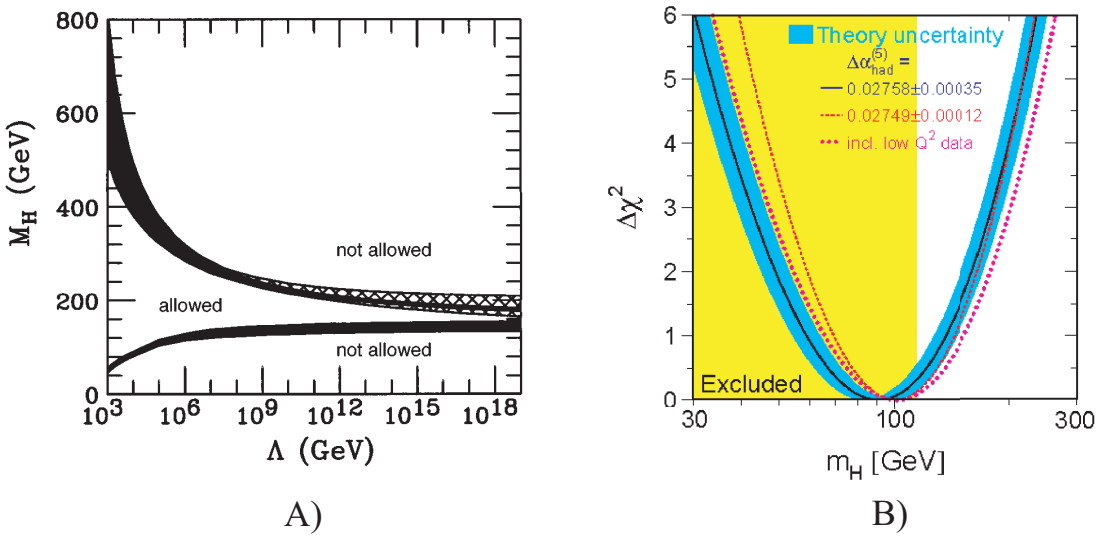

Figure 1-2: Allowable mass range for the Higgs boson. A) is theoretically allowed mass range with the thick lines representing uncertainty in theory parameters [3]. B) is a global fit to all Standard Model data, yielding a fit of 91 + 45 – 32 GeV for the mass of the Higgs boson [4].

tion has been made, which places limits on the acceptable possible Higgs boson mass, as shown in Figure 1-2 [3, 4]. An overall fit to all electroweak parameters predicts a Higgs boson mass of 91 + 45 – 32 GeV. This mass range will be well covered by the upcoming Large Hadron Collider (LHC) operation.

The fundamental issue with LHC coverage of the possible Higgs boson mass range is that LHC events, though capable of detecting Higgs-like particles of the appropriate mass and coupling characteristics, will be hard pressed to carry out precision measurements of the Higgs boson properties, which clearly indicate its identity. Figure 1-3 shows a typical simulated LHC Higgs event, along with the overall Higgs boson detection signal, in Figure 1-4 [5]. Multi-jet events are the golden channel for Higgs detection in the predicted mass range, for proton-proton collisions. Because protons are composite particles, made up of constituent quarks and anti-quarks, the energy in any given collision is not fixed, having some spread, which decreases the number of useable events. In addition, the background processes which also produce multiple hadronic jets (which can appear to be Higgs boson events) are numerous. Though the signal to noise ratio is less than one, the predicted signal is still easily within the

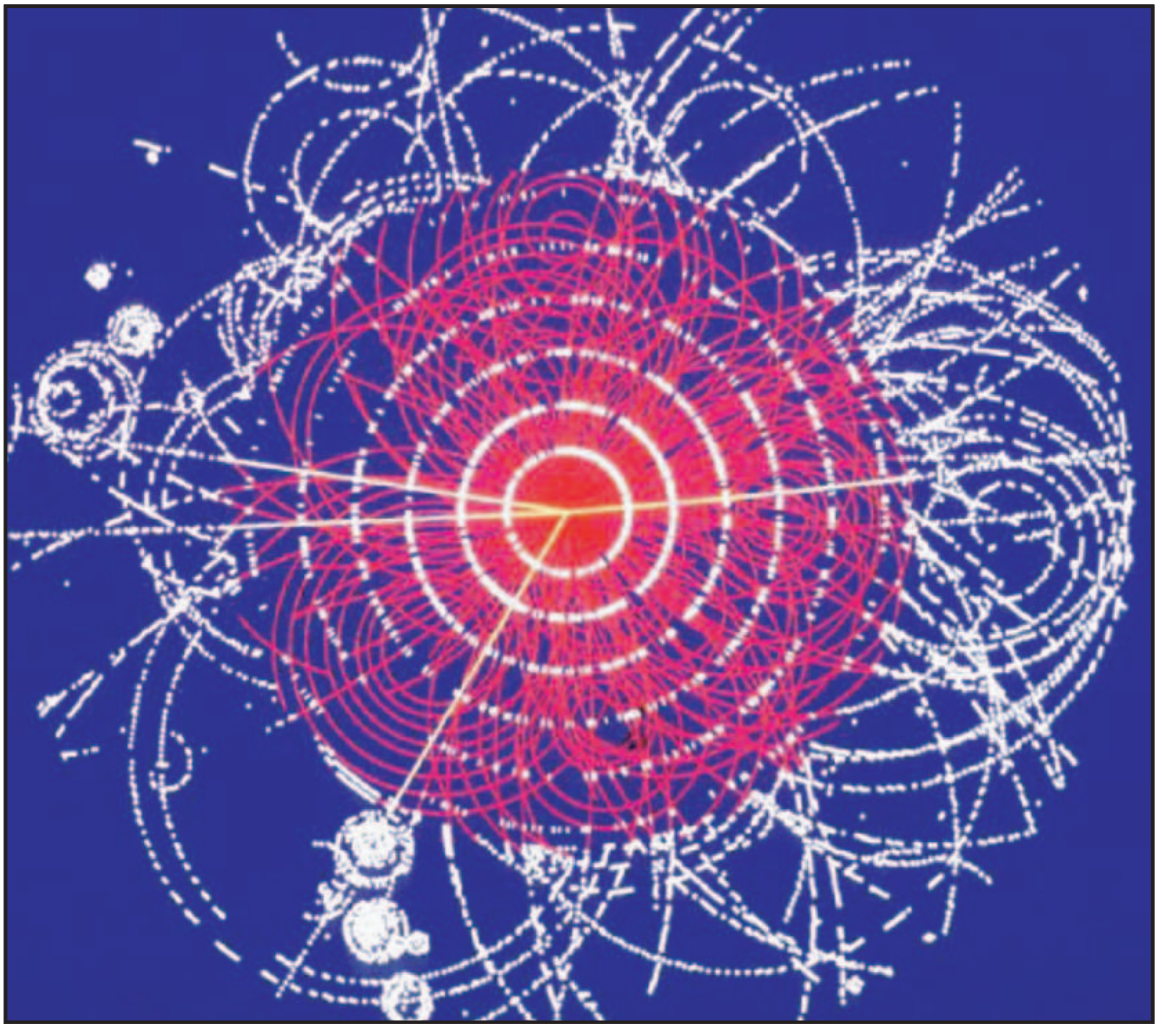

Figure 1-3: Simulated multi-jet event indicative of Higgs boson particle process in LHC detector data [5]. The large number of particles involved is an unavoidable byproduct of colliding composite particles; in this case protons.

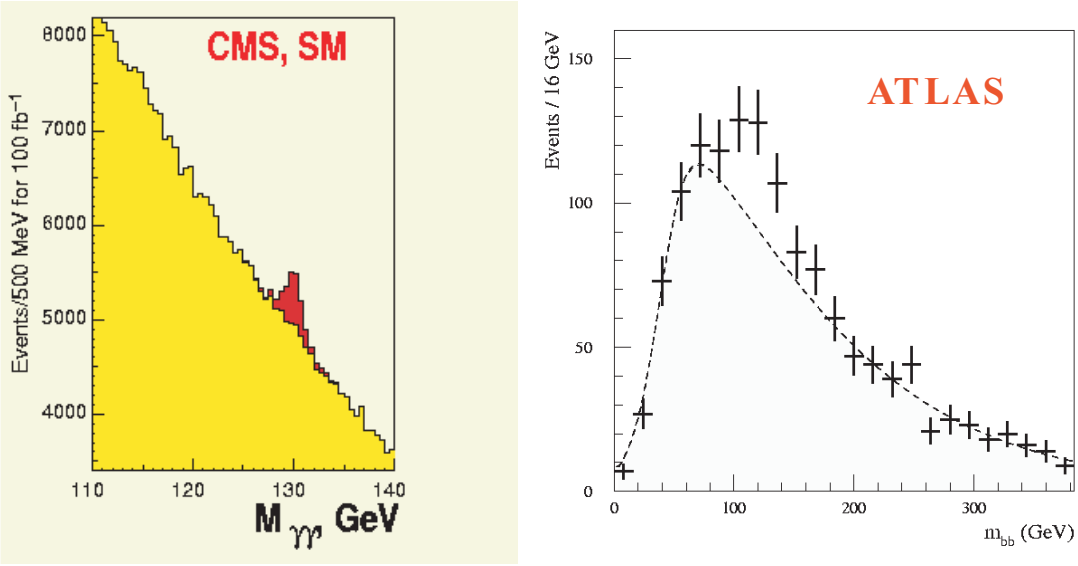

A) B)

Figure 1-4: Low signal to noise ratio inevitable in Higgs boson detection using LHC event data [5]. A) shows simulated Higgs detection on the CMS detector. B) shows simulated Higgs detection on the ATLAS detector.

detector threshold for detection, as is clear from the visible peaks in Figure 1-4.

Precision measurements of the Higgs boson mass and properties are necessary to confirm discovery detection, but the couplings to various channels are also necessary to fully characterize the discovery. In order to carry out precision measurements and measure the Higgs boson couplings to heavy quarks, a high energy electron-positron collider is necessary. The International Linear Collider (ILC) has been proposed by the international accelerator and HEP communities for this purpose. Figure 1-5 shows a typical simulated ILC Higgs boson event, and the overall detection signal is shown in Figure 1-6 [6]. Because the ILC will collide electrons and positrons, each fundamental (non-divisible) leptons, the machine events are much cleaner than LHC events: compare Figure 1-5 to Figure 1-3. The golden channel for Higgs detection at the ILC is quite distinct from possible background events, allowing not only high signal to noise ratios, as seen in Figure 1-6, but additional information to be measured concerning the Higgs boson properties.

The ILC global design effort is underway, and a set of baseline and possible up-

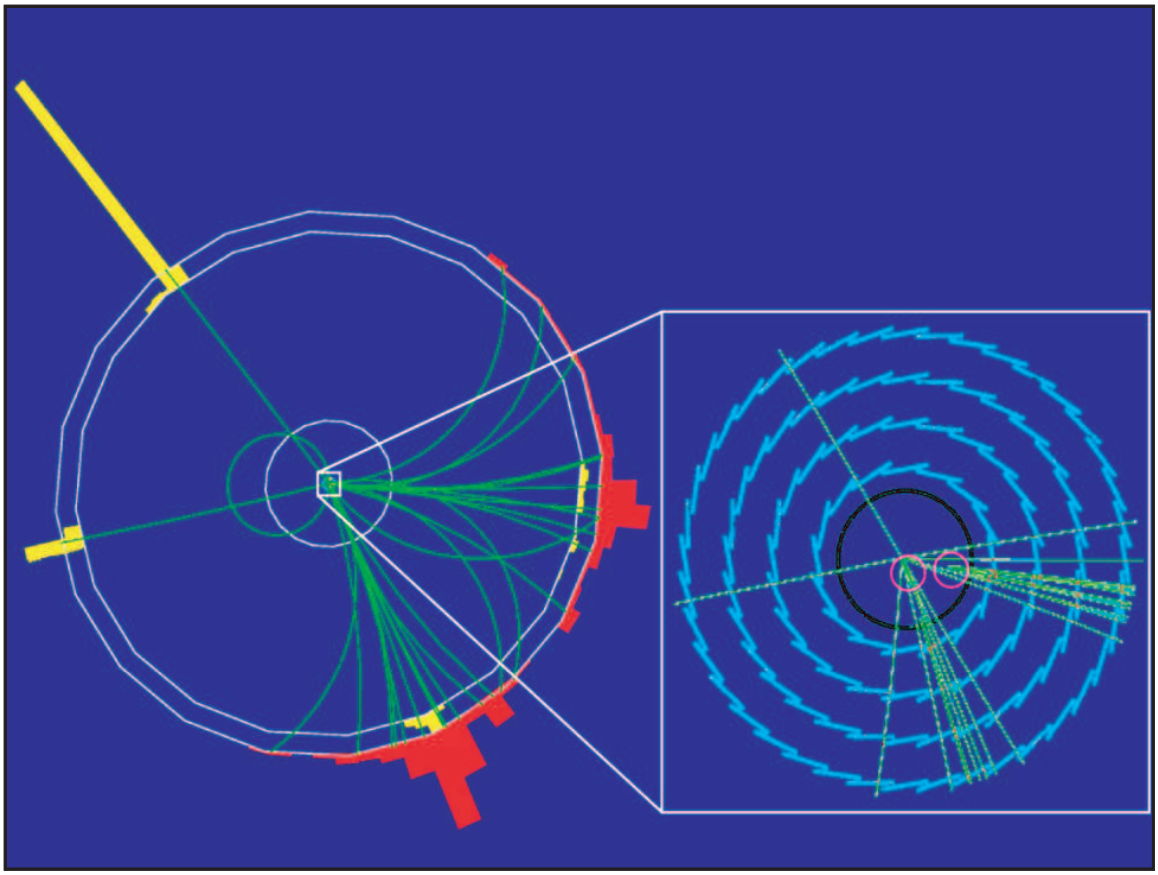

Figure 1-5: Simulated typical Higgs boson event for the proposed ILC [5].

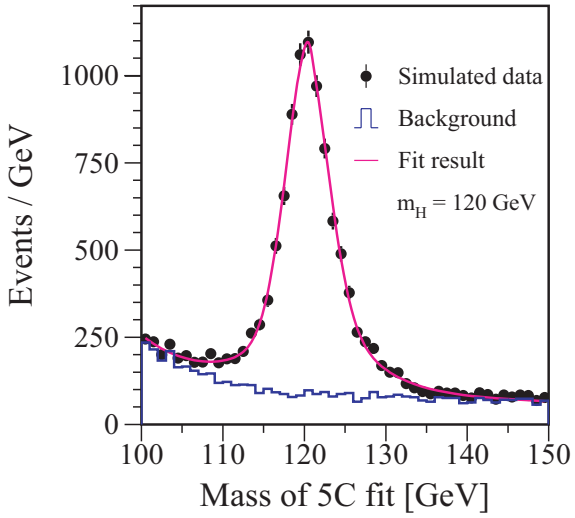

Figure 1-6: High signal to noise ratio possible in Higgs boson detection using simulated ILC event data [6].

grade scenarios have been developed. The baseline design calls for the use of two 15 km superconducting main linear accelerators. Superconducting rf technology was chosen by an international decision panel as the technology for the ILC development. Several significant limitations are intrinsic to, or have since emerged concerning this technology. Superconductors are fundamentally defined to expel all magnetic flux up to a critical field at which they lose their superconductivity. This critical field defines an upper bound on the surface magnetic field allowable in a superconducting accelerating cavity. Geometric optimization and alternate superconducting materials can slightly vary this limit, but an upper bound on accelerating gradient of 50 MV/m is believed to be unavoidable. The gradient actually achieved in single cells, and eventually realistic multi-cell cavities is less than the theoretical fundamental limit of 50 MV/m. Industrialization and standardization in fabrication practices have been claimed as surmountable difficulties, but the current state of progress is still deficient in reaching the specified accelerating gradient for the ILC of 31 MV/m, as shown in Figure 1-7 [7].

Regardless of the current difficulties in ILC cavity construction, the single largest cost driver in the linear collider's construction is associated with the main linac. An improvement in the linac accelerating gradient makes a more economical machine possible. In terms of Physics achievement, a higher gradient makes a more complete discovery possible. An upper achievable energy of 800 GeV–1 TeV was specified for the ILC, or any future electron-positron collider for HEP. Such an energy is necessary to both complement LHC data, as well as to adequately measure the coupling of the Higgs boson with the Standard Model particles. Practical large scale metrology constrains the overall length of any terrestrial accelerator complex to 50 km. In order to reach energies higher than those of the ILC, or to reach the original specification for the ILC performance, in a reasonable length, high gradient acceleration is required.

Because of the fundamental constraint of superconducting structures to operate below a critical field, high gradient acceleration requires conventional normal conducting structures. Standard oxygen free high conductivity (OFHC) copper provides a robust, and well understood material for high gradient accelerator concepts. High

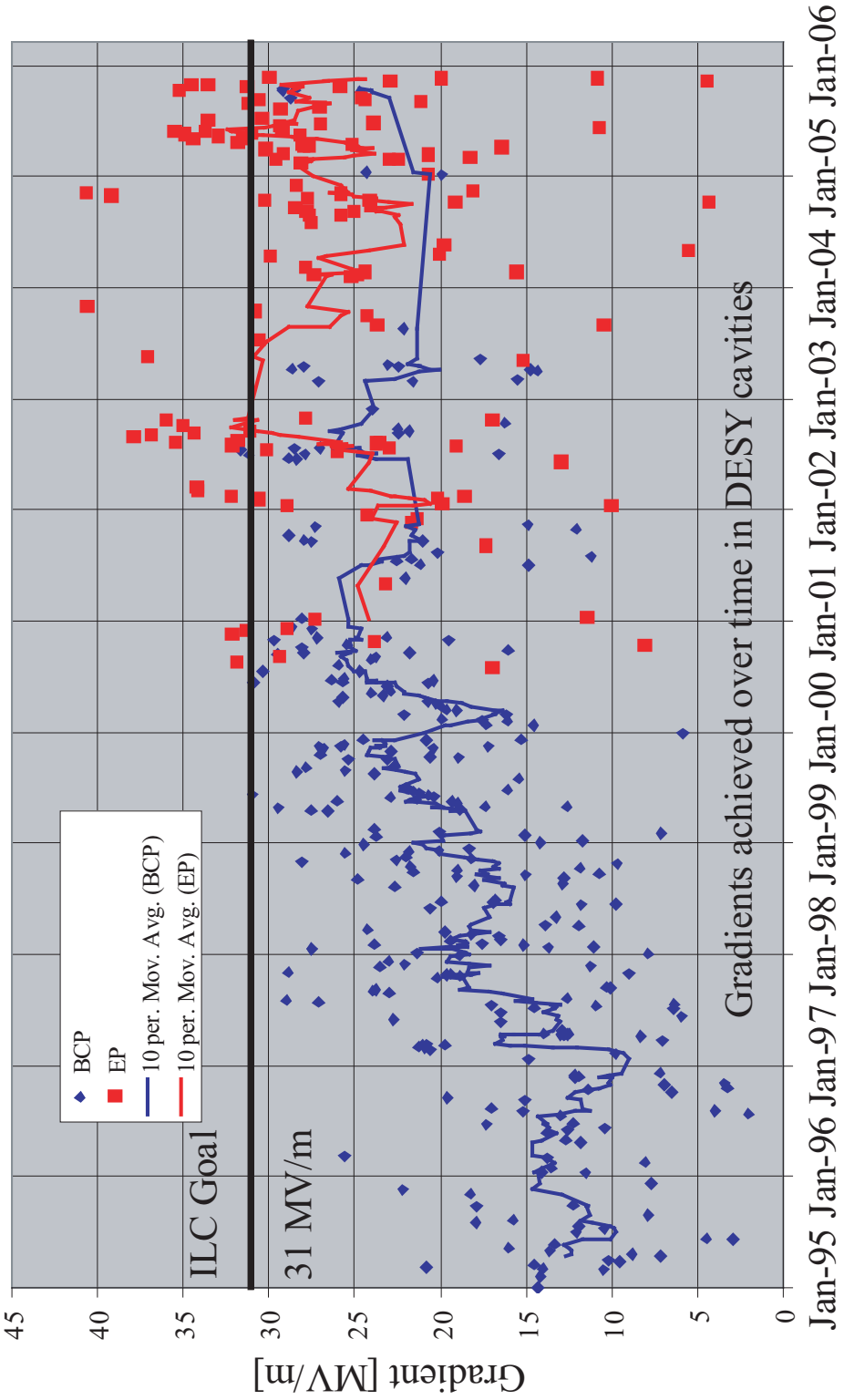

Figure 1-7: Gradient achieved in multi-cell superconducting accelerating cavities as a function of time [7]. The design goal for the ILC gradient of 31 MV/m is shown as a horizontal line. Progress has been steady, but cavities are still produced using all current state-of-the-art procedures demonstrate deficient performance.

accelerating field is the goal in such structures, constrained by material properties, and accelerator performance. Material properties impact the maximum electric surface field a surface can sustain and the repeated cycling of pulsed heating tolerable. Accelerator performance prescribes very high availability of very high quality beams, to maximize the discovery potential of any linear collider concept.

1.2 High Gradient Accelerators

1.2.1 Accelerator Structures

For linear collider operation, charged particles are accelerated to high energy, and then interact. Accelerator cavities are conventional pillbox resonators, operating in a TM_{01} mode, so that an axial electric field is present [8]. Irises must be used to provide a path for the beam from one pillbox cell to another, to impose axial boundary conditions to insure acceleration, and often to allow power to couple from cell to cell.

The axial electric field for the TM_{01} mode of a cylindrical waveguide is given in Equation 1.1 [9]. Equation 1.1 describes a wave propagating in the positive z direction, with magnitude, E_0, wave number, k, and frequency, ω.

$$E_z\left(r,z,t\right) = E_0 J_0\left(k_0 r\right) e^{\imath(kz-\omega t)} \tag{1.1}$$

The wave number, k, is given by Equation 1.2.

$$k^2 = \left(\omega/c\right)^2 - k_0^2 \tag{1.2}$$

For the TM_{01} mode, $k_0 = 2.405/R \equiv \omega_c/c$, where R is the waveguide radius. Equation 1.2 allows the phase velocity, $v_p = \omega/k$, to be calculated for the TM_{01} mode, as shown in Equation 1.3

$$v_p = \frac{\omega}{k} = \frac{c}{\sqrt{1-\left(\frac{\omega_c}{\omega}\right)^2}} > c \tag{1.3}$$

The phase velocity for this mode is greater than the speed of light, which means that particles can not be synchronized with the traveling wave during acceleration. Particles that begin synchronously, and are accelerated, will eventually lose synchronism, and be decelerated. To reduce $v_P \leq c$, iris loading is used to slow the traveling wave down. For electrons, $v \approx c$, and so an accelerator mode is chosen such that $v_p = c$.

1.2.2 Luminosity

The discovery potential of an accelerator is based largely on a figure of merit known as the beam luminosity. The number of events observed per unit time is a function of the rarity of the event in question, or the process cross-section, σ, multiplied by the number of total particle interactions, defined as the beam luminosity, $\mathcal{L}$. For beam-beam colliders, this can be expressed as:

$$\mathcal{L} = \frac{n_b N^2 f_{rep}}{A} H_D \tag{1.4}$$

The luminosity defined in Equation 1.4, $\mathcal{L}$, is written in terms of the number of particle bunches, n_b, the number of particles per bunch, N, the repetition frequency, f_{rep}, the beam cross-sectional area, A, and a beam shape dependent term, H_D. To maximize the luminosity of a collider, a careful balance of the relevant terms in Equation 1.4 must be reached. To maximize the numerator, it is most effective to use the greatest number of particles per bunch; to minimize the denominator the smallest possible bunches should be used to decrease the bunch transverse size. Particle dynamics dilute the beam quality, and so a balance must be reached between particle number and size.

1.2.3 Beam Dynamics

Beam dynamics play a fundamental role in determining the possibility of beam transport and acceleration. As the number of relativistic particles per bunch is increased, the transverse, Lorentz-contracted electric and magnetic fields of the particle bunches become large enough that they can act on subsequent particle bunches. These beam

induced fields, or wakefields, can be separated into two categories, short-range and long-range wakefields. Short-range wakefields are generated by the particles in the head of a bunch and act on the tail of the bunch. Short-range wakefields increase the energy spread of the beam, by decelerating particles in the tail, and deflect the beam, when particles are off-axis. Long-range wakefields are caused by the field of one bunch acting on subsequent bunches, most critically by exciting transversely deflecting modes. The wake potential of a bunch can be written as a sum over cavity eigenmodes.

$$W(z) = \sum_n a_n f_n(\vec{x})\, e^{-\imath\omega_n t} e^{-\omega_n t/2Q_n} \tag{1.5}$$

The wake potential expressed in Equation 1.5, W, is written as a function of the trailing distance behind the bunch, z. This can be written generally as a sum over cavity modes, n, with some coupling strength, a_n, a functional field dependence, $f_n(\vec{x})$, and a time dependence, given as an oscillation at a frequency, ω_n, with damping given as a time constant, $\tau_n = 2Q_n/\omega_n$, where Q_n is the quality factor for mode n. The most dangerous modes are those which have high Q, and field distributions which can excite dangerous motion in the beam, such as transverse deflection. Damping these modes is of paramount concern in order to effectively transport or accelerate bunches of charged particles.

1.2.4 Frequency Scaling

High gradient acceleration is limited by cavity performance in terms of the maximum electric field the surface can tolerate, the maximum magnetic field the surface can tolerate, and particle trapping. Conventional normal conducting structures have been used successfully for accelerator applications for the last 50 years, providing an understanding of the fundamental limits inherent to high gradient acceleration. Figure 1-8 summarizes the frequency scaling of limits to the gradient achievable in linear accelerators: limits are derived for effects associated with electric field breakdown, magnetic field pulsed heating, and particle trapping. These effects are discussed in Sections 1.2.5, 1.2.6, 1.2.7, and more thoroughly described in Section 2.2.

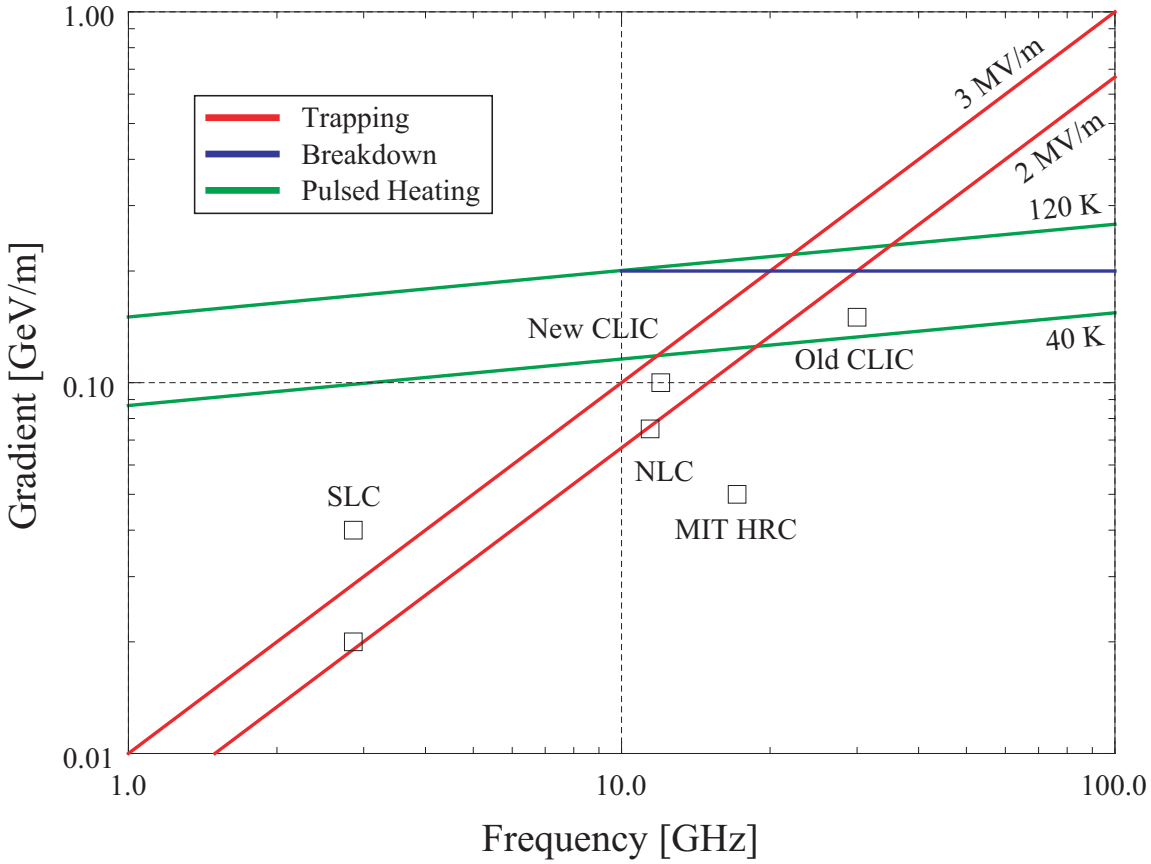

Figure 1-8: Accelerating gradient as a function of frequency. Limits are shown for effects associated with electric field breakdown, magnetic field pulsed heating, and particle trapping. A horizontal electric field line is shown; pulsed heating lines are shown for 40 and 120 K temperature rise; trapping lines are shown for both 2 and 3 MV limits. After [10].

1.2.5 Electric Field

The accelerating gradient, defined as the accelerating field integrated along the beam path, has fundamental physical limits which scale with frequency. At higher frequencies, higher gradients are achievable while avoiding breakdown, pulsed heating, and dark current capture. The maximum surface electric field relates geometrically with the accelerating gradient; structures can be shaped to improve the gradient with respect to the surface field, but generally a ratio of $E_{surface}/E_{gradient} \sim 2.2$ is observed. It was believed that the maximum surface electric field sustainable without breakdown scaled with frequency [11, 12]. This scaling was not observed to hold as hoped at higher frequency, and it is currently believed that breakdown limits high gradient accelerators to surface fields of $\sim$ 450 MV/m [13]. A maximum surface electric field of 450 MV/m and a gradient to surface ratio of 2.25 translates into the breakdown limit line on Figure 1-8.

1.2.6 Magnetic Field

Magnetic field effects have been linked with cyclic fatigue [14, 15]. The surface magnetic field induces surface currents, which ohmically heat the surface. Over the short rf pulse length, this heat is dissipated over a limited surface area, melting it. The temperature rise on high magnetic field areas can be quite high, and bounds for tolerable levels have been experimentally measured [15], and a theory on the pulsed heating lifetime of devices has been developed [14]. The current acceptable thresholds for safe pulsed heating, between 40 and 120 K are shown in Figure 1-8.

1.2.7 Dark Current Trapping

The electric field in high gradient accelerating structures can be high enough that non-energetic background vacuum electrons can be excited to relativistic speeds quickly enough that they can match phase with the accelerating field, and avoid being decelerated when the field changes direction. Dark current both decreases the energy available to accelerate beam particles, and can strongly affect beam dynamics by

forming trapped particle halos. Limits for dark current capture can be derived for specific structures using computer modeling, or can be derived analytically. Calculations from first principles give trapping limits based on what energy trapped electrons are required to gain before they are considered trapped, as discussed further in Section 2.2. These calculations result in the 2 and 3 MV/m trapping limits, as shown in Figure 1-8.

1.2.8 Wakefields

Fundamental to accelerator structure operation is the damping of wakefields, as described briefly in Section 1.2.3. The motivation for high gradient operation at higher frequency can be observed by looking at Figure 1-8, which shows advantageous scaling of gradient limits with increasing frequency. Fabrication and high power source availability restrict development at very high frequencies, but wakefield considerations dominate. Wakefields scale as ω^2 or ω^3, and must be damped [16]. Figure 1-9 shows the simulated electric field of a Gaussian bunch as it traverses a PETRA accelerator cavity. The short-range wakefields can be seen as the electric field lines contacting the iris surface and the long-range wakefields can be seen as the field left in a cavity cell after the bunch has passed [17].

Short-range wakefields affect both the energy spread of the beam and the transverse size of the beam; both effects act to decrease the quality of the beam, and its Physics potential. The longitudinal short-range wakefields, W_L, scale as ω^2, and decrease the energy of tail particles, increasing energy spread. Short-range longitudinal wakefields can be reduced by limiting the bunch charge, increasing the bunch length, or by careful phasing of particles bunches. The transverse short-range wakefields, W_T, act to increase the transverse energy spread, increasing the bunch transverse area. Short-range longitudinal wakefields can be reduced by limiting the bunch charge, increasing the bunch length, or by careful control of transverse particle motion, utilizing tight alignment, strong focusing, and other targeted damping. Clearly, allowing short-range wakefields to go unchecked will decrease collider performance, directly by degrading the luminosity, or indirectly by decreasing the precision attainable due

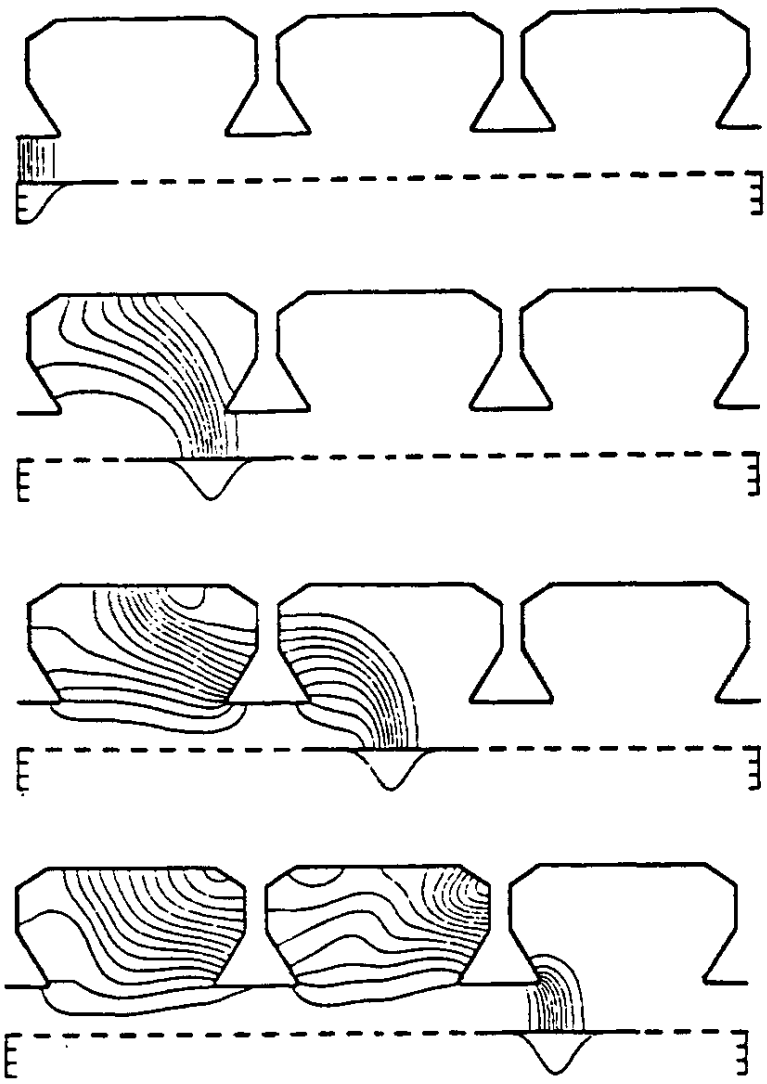

Figure 1-9: Electric field of a Gaussian bunch (Longitudinal bunch length of 2 cm, and bunch charge of 1 μC) traversing a PETRA cavity [17].

to large energy spread. Controlling short-range wakefields by decreasing the bunch charge will also decrease luminosity, and leads to a reliance on the alternate methods mentioned.

Long-range wakefields build up as bunches transit through accelerating structures and excite modes other than the accelerating mode (excitation of the fundamental will occur at such a phasing as to decrease the accelerating field, an effect known as beam-loading). Long-range wakefields degrade the beam quality by increasing the bunch transverse area, and can lead to serious beam instabilities that prohibit the bunch from being safely transported. Long-range wakefields can be reduced by limiting the bunch charge; increasing the bunch length; increasing the bunch spacing; careful control of transverse particle motion, utilizing tight alignment and strong focusing; or targeted damping of the dangerous cavity modes using a variety of damping and detuning techniques. As with controlling short-range wakefields, luminosity preserving countermeasures are preferred. Bunch charge, bunch length, bunch spacing, the strongest practical focusing, and tight transverse tolerances are implemented to control short-range wakefields, and optimize collider luminosity and operational parameters. Detuning is utilized to shift the frequencies of modes over the length of individual accelerator sections so that fields do not coherently act on the beam.

Damping unwanted modes supplements these measures, and can positively impact global parameter optimization by loosening requirements on the other countermeasures. Because mode damping is an important consideration in accelerator structure design, a number of innovative solutions have been suggested in order to provide damping sufficient for the next generation of high energy linear accelerators. These solutions include waveguide damping on the cavity itself [18], on the beam pipe [19], slotted irises [20], higher order mode (HOM) damping couplers [21], choked mode structures [22], and both dielectric [23] and metallic [24] photonic bandgap (PBG) structures. Design of these structures is an active area of research with many innovative and effective ideas.

1.3 Metamaterials and Photonic Bandgaps

Electromagnetic metamaterials can be defined as artificial effectively homogeneous electromagnetic structures with unusual properties not readily available in nature. An effectively homogeneous structure is one whose average cell size is much smaller than the guided wavelength; effectively homogeneous can be defined at the limit where the average cell size is equal to the guided wavelength [25]. Metamaterials can be created with frequency dependent properties, such as negative values of relative permittivity and permeability over a frequency range.

The frequency dependent properties of metamaterials could allow a microwave cavity to be built such that the walls of the cavity reflect the frequency of the fundamental accelerating mode of the structure, but transmit at the frequencies of the dangerous transverse deflecting modes that must be damped. The simplest such cavity can be formed as a two dimensional Photonic bandgap structure. Photonic bandgap materials do not strictly meet the criteria of effective homogeneity, but can be formed to reflect and transmit appropriately to form the damped cavity of interest.

Photonic bandgap materials are formed by a periodic structure of varying dielectric constant [26]. This variation can be in one, two or three dimensions as shown in Figure 1-10. Photonic bandgaps are formed when all electromagnetic radiation in a particular frequency band is entirely reflected. A material that contains a single bandgap can be made to form a resonator at a frequency within the gap, because it acts to completely reflect radiation near that frequency. This cavity can be made by forming a suitable two dimensional photonic crystal, one with an appropriate complete photonic bandgap, and making a defect in the crystal, for example by removing a section of it, to form a cavity.

1.4 Motivated Research

A complete photonic bandgap has been designed for triangular and square lattices of cylindrical metallic rods. This lattice has then been used to form a PBG cavity, by

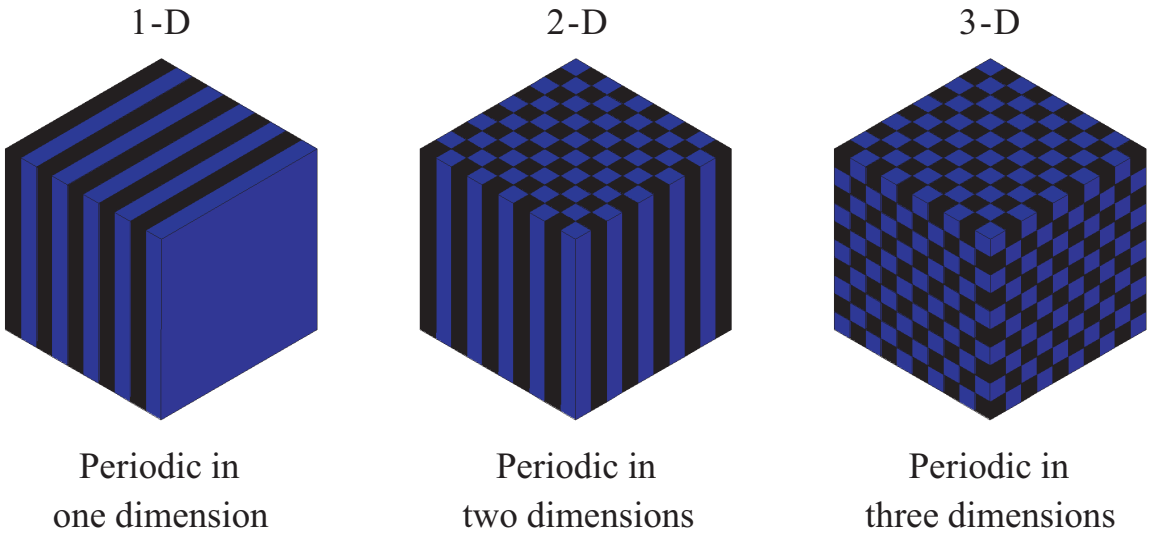

Figure 1-10: Simple examples of one, two, and three dimensional Photonic crystals. The differently colored sections are meant to represent varying dielectric constants. Photonic bandgaps can be designed by changing the size, shape, or dielectric constant of the regions.

removing a single rod. Additional rods have been removed to form adequate coupling into the cavity, id est, in order to form coupling cells. At MIT, a six cell traveling wave accelerator structure has been built, cold tested, tuned, and hot tested, demonstrating a 35 MV/m gradient, as reported in [27, 28, 29]. Following a first demonstration of acceleration using a PBG accelerator structure, there are many important Physics questions remaining.

The previous six cell structure was designed to produce a measurable electron acceleration with low input power; a demonstration that a PBG accelerator is possible. This first proof of principle design is impractical as an actual accelerator design, and these deficiencies must be corrected in order to fully characterize the performance of PBG structures as a high gradient accelerator concept.

The use of a complete photonic bandgap insures an operating mode can be confined to the lattice defect, forming a cavity, but the gap does not guarantee that unwanted modes will not be contained in the cavity; the gap promises complete reflection in a band, it says nothing specific about transmission, except that finite transmission exists. The lattice in any realistic device will be finite, rather than the

infinite lattice required to guarantee gap structure. Finite lattice effects and the propagation of modes outside the gap are open questions. Damping is the motivation for a PBG accelerator structure, but damping in PBG structures has not been observed. A major motivation of this thesis research is to investigate wakefield damping in a PBG structure, both theoretically and experimentally. The performance of more realistic PBG structures is the fundamental major advance of this thesis work.

1.5 Outline of Thesis

This thesis will present the development of PBG accelerator concepts from previous design and first demonstration, to mature and well-understood practical devices. The theory underlying accelerator cavity performance limits, photonic bandgaps, and operating mode wakefields, or beam-loading theory, are presented in Chapter 2. Original research into PBG structure quality factors, and the nature of HOMs in PBG structures, including cold testing and damping are discussed in Chapter 3. Wakefield measurement experiments performed on the MIT Haimson Research Corporation (HRC) accelerator are presented in Chapter 4. The design of X-band PBG breakdown structures, including the design of both a large rod PBG structure, and an improved elliptical rod profile PBG structure is presented in Chapter 5. Chapter 6 details the experimental testing of the large rod PBG structure, including bead pull measurement and cold test, tuning, and high power testing. Conclusions and a discussion of results and future work conclude the thesis in Chapter 7.

Chapter 2

Theory

2.1 Introduction

The experimental work of this thesis is dependent on theoretical models for motivation, relevance in the larger field of accelerator physics, as well as to motivate and aid in structure design, and understand experimental results. These theoretical models are reviewed in more detail than that provided in Chapter 1, where many of the concepts discussed in this Chapter were introduced. Section 1.2.1 reviews the basic concepts behind electromagnetic accelerator structures. Section 2.2 discusses theory used to establish or understand fundamental accelerator performance limits; Section 2.3 develops beam cavity coupling, for the case of the fundamental operating mode (also known as beam-loading), for traveling wave structures, which will be compared with experimental measurements in Chapter 4; Section 2.4 discusses the theory behind photonic bandgaps (PBGs), which will be extended to a discussion of PBG higher order modes (HOMs) in Chapter 3.

2.2 Accelerator Limits

The accelerator structure limits introduced in Chapter 1 have been developed over 50 years of experience with rf linear accelerators. In the following sections they are reviewed in more detail, and the theory underlining the fundamental results is

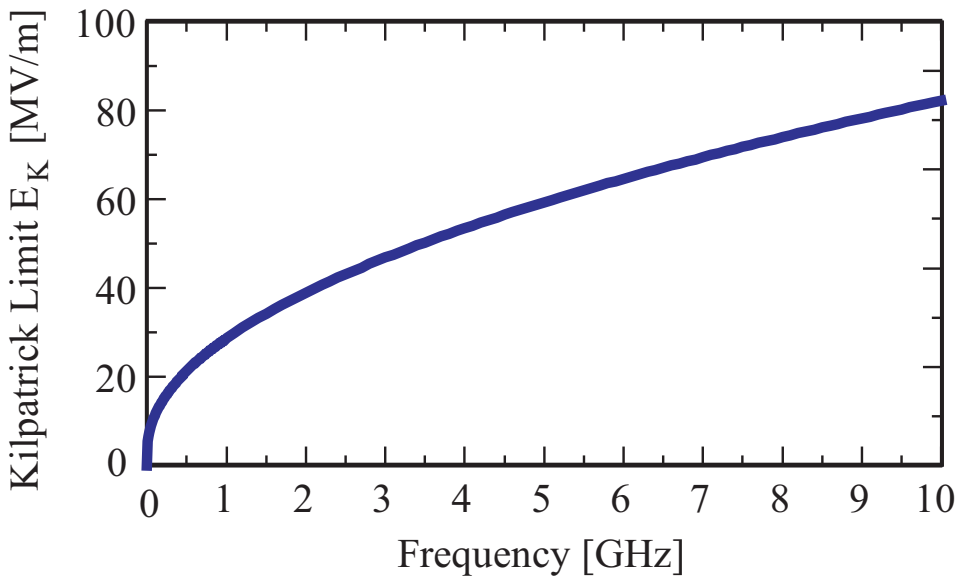

Figure 2-1: Kilpatrick limit electric field strength as a function of frequency. Solution to Equation 2.1 plotted as MV/m versus GHz.

reviewed.

2.2.1 Kilpatrick Limit and Loew-Wang Scaling

At sufficiently high electric field strengths, the surface electric field becomes powerful enough to pull electrons out of the surface material. In practice, breakdown phenomena are observed well below this theoretical limit of $\sim$ 2 GV/m. Empirical scaling laws derived from experiments provide more realistic guidance as to achievable field strengths, avoiding breakdown arcs.

The original analysis of rf and DC breakdown studies was summarized in a formula by W. D. Kilpatrick [11]. This formula can be expressed in the following form [30]:

$$f\,(MHz) = 1.64E_K^2 e^{-8.5/E_K} \tag{2.1}$$

In Equation 2.1 the Kilpatrick limit field, E_K, in MV/m, must be solved for iteratively at a given frequency, f, in MHz. Field strengths below E_K can be sustained without causing surface damage, or instigating breakdown events.

Given the establishment of this limit before high quality vacuum systems were as

Extrapolated Limiting Gradients	11.424 GHz	17.136 GHz
Peak Surface Field [MV/m]	660	807
Accelerating Gradient [MV/m]	264	323

Table 2.1: Predicted gradient limits for high frequency accelerators extrapolated from empirical scaling laws. Accelerating fields assume an $E_s/E_{gradient}$ ratio of 2.5.

developed as they are today, a bravery factor, b, is often used to modify E_K.

$$E_S = bE_K \tag{2.2}$$

Equation 2.2 raises the highest safely applied surface electric field, E_S, by a factor b from the Kilpatrick limit, E_K. Typical values of b range from 1.0 to 2.0, and can be higher for pulsed rf operation [16].

More recent breakdown results concern themselves with pulsed rf, which is what is used in high gradient accelerator operations. G. A. Loew and J. W. Wang sought to extend the Kilpatrick $E_K \propto f^{1/2}$ scaling under pulsed operation in the limit of high frequency [12]. They took data at three frequencies: 2.856, 4.998, and 9.303 GHz; and confirmed Kilpatrick $f^{1/2}$ scaling. They also extended the empirical scaling of breakdown limited electric field to include dependence on the rf pulse length, t, as shown in Equation 2.3 [31, 12].

$$E_S \propto \frac{f^{1/2}}{t^{1/4}} \tag{2.3}$$

These scaling laws predict the peak surface field and corresponding accelerating gradient that can be sustained at high frequency, as summarized in Table 2.1 for both 11.424, and 17 GHz [12]. The possibility of achieving higher than 200 MV/m gradients stimulated research into accelerator structures at these frequencies, including the MIT HRC 17 GHz accelerator laboratory.

More recent results indicate that the optimistic Kilpatrick and Loew-Wang scaling with frequency does not hold above ~ 3 GHz. The Kilpatrick limit was motivated by a theory of breakdown involving ion acceleration and impact, which seems increasingly unlikely at high frequency, given the small amplitude oscillations of ions in high frequency rf fields. Scaling laws motivated by other theoretical models have been

examined, such as the Fowler-Nordheim model used in further testing by J. W. Wang and G. A. Loew [32]. First evidence of an absolute surface field limit of $\sim$ 300 MV/m was clear at 17 GHz, in both experimental and theoretical work on the MIT rf gun [33, 34]. More recent results at 21, 30, and 39 GHz, using precisely scaled cavities, show little change in sustainable field strength with frequency, with an absolute surface field limit between 350 and 400 MV/m [13].

2.2.2 Fowler-Nordheim Field Emission and Breakdown

Field emission of electrons has been examined in depth as a possible source phenomena for rf breakdown. The first quantum-mechanically valid treatment of electron tunneling out of a surface with an applied field was done by R. H. Fowler and L. Nordheim [35]. Fowler and Nordheim used Fermi-Dirac statistics to treat the electrons in a metal surface penetrating the barrier of the surface in the presence of an electric field. They arrived at what is known as the Fowler-Nordheim (FN) relation, which relates the observed current density, J, in Amps per square meter, to the field enhancement factor, β, the surface electric field, E, in Volts per meter, and the surface material work function, ϕ, in electron Volts, as shown in Equation 2.4 [35, 32].

$$J = 1.54 \times 10^{-6} \times 10^{4.52\phi^{-1/2}} \frac{\beta^2 E^2}{\phi} e^{-\frac{6.53\times 10^9 \phi^{3/2}}{\beta E}} \tag{2.4}$$

The main occurrence of the FN model, or its use in breakdown models revolves around the use of β, which can be defined as a local enhancement in field strength, of the form: $E_{local} = \beta E_{average}$. Breakdown phenomena can then be understood as occurring in the regime of $\sim$ GV/m fields in proximity to high β regions. A number of experiments have been done which imply values of β in the range of 10–100. Geometrically, surface defects can be modeled, either analytically or in simulation, to determine β. The theoretical difficulty in applying theory to experiment is in the fact that β is invariant to the actual size of surface defects, depending primarily on the aspect ratio of asperity height to width as shown in Figure 2-2 [32, 36]. This implies that however clean a surface appears, or is prepared to be, small, but high

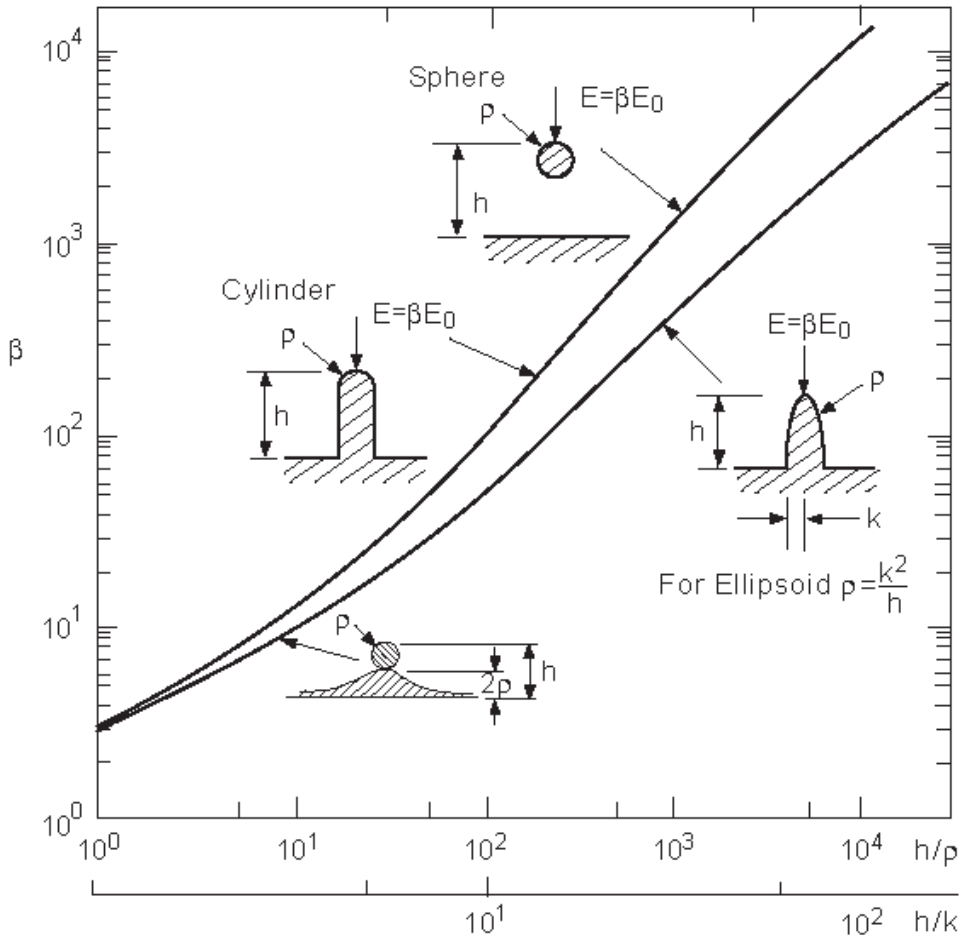

Figure 2-2: Plot of β for differing aspect ratio defects, of varying geometries [32, 36]. Aspect ratio is given as h/ρ or h/k: for a sphere of radius ρ a height h above a plane; a cylinder of height h topped by a hemisphere of radius ρ; an ellipsoid of major radius h and minor radius k, such that $\rho = k^2/h$; and a sphere of radius ρ lying on a smoothed defect of height ρ.

aspect ratio defects will provide high β foci for electric field breakdown events. The effect of stacked perturbations also serves to enhance the effective β as the effect of a perturbation on top of another is geometric, id est, $\beta_{total} = \beta_{lower} \times \beta_{upper}$.

The Fowler-Nordheim model and implied or experimentally measured β (via field emission current measurement; id est, using Equation 2.4 to measure β) are often used to bridge the gap between theoretically motivated limits for electric field breakdown based on fundamental material physics, and experimentally measured limits in breakdown experiments. The effect of high β points, and Fowler-Nordheim field emission is shown in the schematic of breakdown phenomena in Figure 2-3. High β points

exist on the surface, and are the source for breakdown arcs. The arcs themselves form craters that serve to smooth the initial site, but can form secondary sites, which are smoothed by subsequent breakdowns. Damage observed in the high field regions of accelerator structures confirms the topology of breakdown phenomena shown in Figure 2-3.

2.2.3 Dark Current Trapping

Dark current is defined as electrons spontaneously emitted by a microwave cavity when rf power is input, but no beam is injected. This current can be that emitted by a FN-like field emission process, secondary emission or multipactor processes, or can be composed of background gas. Moving under the influence of the rf fields in the cavity, emitted electrons in high gradient cavities can be exposed to field strengths sufficient to accelerate them such that they can match phase with the rf fields and continue to be accelerated, rather than decelerated by the changing phase of the rf fields. The condition for the initiation of electron trapping is given by Equation 2.5 [38].

$$\alpha = \pi\sqrt{\frac{1-\beta}{1+\beta}} = \frac{E_0 e\lambda}{m_0 c^2} \geq \pi \tag{2.5}$$

In Equation 2.5, β is the electron initial velocity divided by the speed of light, c, E_0 is the maximum value of the rf electric field, e and m_0 are respectively, the charge and mass of an electron, and λ is the rf field wavelength. For electrons beginning at rest, Equation 2.5 predicts a trapping threshold scaling with frequency as shown in Equation 2.6.

$$E_0 \geq \frac{\pi m_0 c^2}{e\lambda} = \frac{1.6MV/m}{\lambda} \tag{2.6}$$

The value of 1.6 MV/m in Equation 2.6 is an overly conservative limit for dark current trapping onset. Electrons emitted at the optimal phase will be trapped at this field, but it takes higher field strengths to trap an appreciable phase space of emitted electrons. Lines are plotted for values of 2 and 3 MV/m in Figure 1-8. The

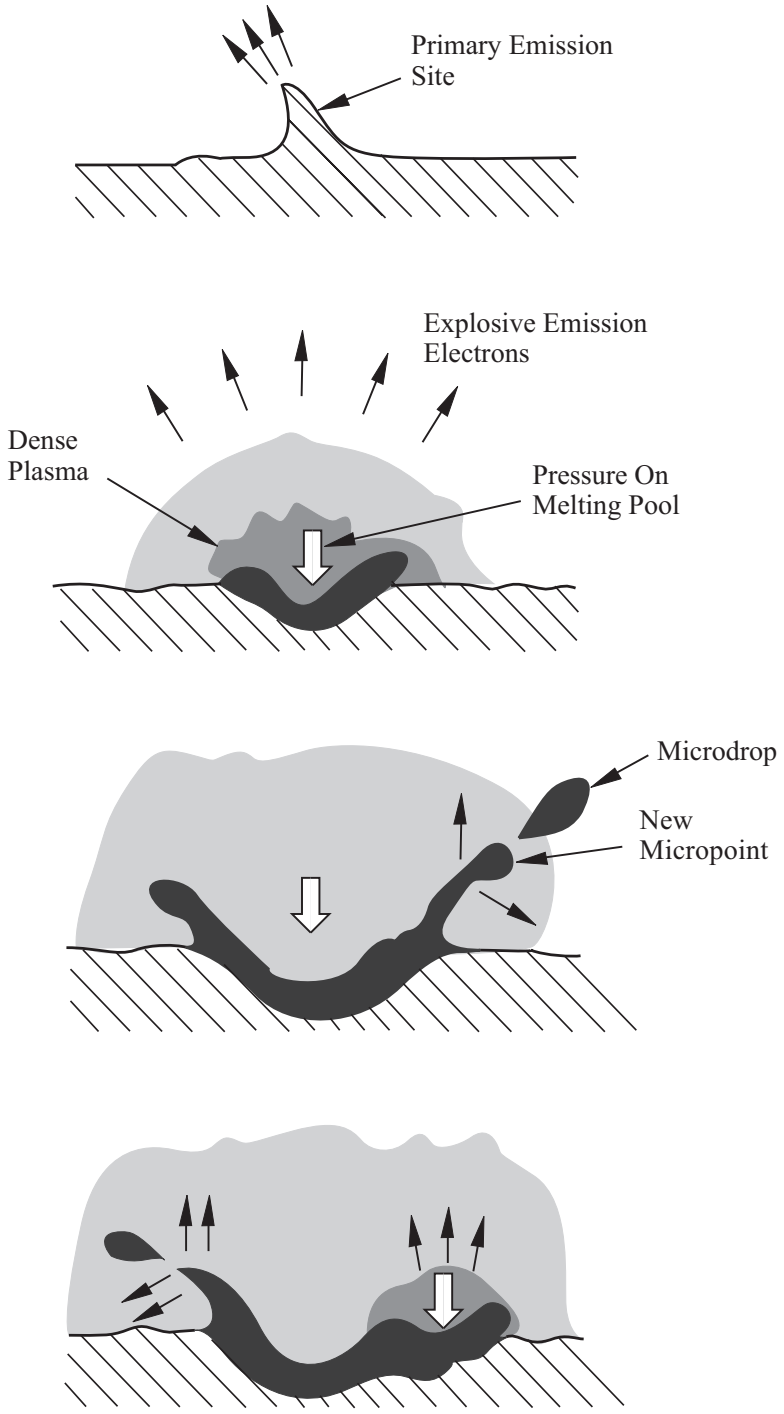

Figure 2-3: Development process of breakdown erosion: primary field emission site; explosive electron emission; pressure on the emission site; plasma; growth of a new micropoint from the liquid metal; microdrops [32, 37].

R_S	Surface resistance	0.034 Ω (at 17 GHz) 0.0279 Ω (at 11.424 GHz)
K	Thermal conductivity	3.95 $W/cm°C$
D	Thermal diffusivity	1.15 cm^2/s

Table 2.2: Material properties of OFHC copper for insertion into Equation 2.7.

effect of dark current is to absorb rf power meant for beam acceleration, but it can also affect the beam path. Dark current measurements in accelerator structures are generally on the milliAmp scale, though simulations have shown much larger electron currents may exist within the structure. In the steady state operation of most linear collider concepts the effect of this dark current on the beam is ignorable [39].

Dark current is also emitted during breakdown events, and in sufficient quantities that the structure breakdown rate can begin to seriously affect beam quality in both energy spread and transverse motion.

2.2.4 Pulsed Heating

The magnetic field strength in accelerating cavities peaks on the walls of conventional pillbox cavities, as well as on input couplers. In advanced concepts, incorporating wakefield damping, the cavity shape is generally modified from a pillbox and as a result, higher peak magnetic fields can be observed on the perturbed surfaces. High surface magnetic fields lead to localized ohmic heating, and can result in very high temperature rise. The peak temperature rise due to pulsed heating, ΔT, can be expressed as a function of the surface material resistance, R_S, conductivity, K, and thermal diffusivity, D, the rf pulse length, t_P, and the maximum surface magnetic field, H_{peak}, as shown in Equation 2.7 [40].

$$\Delta T = \frac{R_S}{K}\sqrt{\frac{Dt_P}{\pi}}|H_{peak}|^2 \tag{2.7}$$

Equation 2.7 can be expressed numerically, using typical values for copper, as shown in Table 2.2.

For realistic pulse shapes, the exact pulsed heating temperature rise can be calcu-

ρ	Density	$8.95 \times 10^3 kg/m^3$
c_ϵ	Specific heat at constant strain	$385 J/kgK$
α_d	Linear thermal expansion coefficient	$1.65 \times 10^{-5} K^{-1}$

Table 2.3: Material properties of OFHC copper for insertion into Equation 2.8.

Temperature Rise	Number of shots
82 ± 3 K	86×10^6
120 ± 10 K	56×10^6
∼ 250 K	56×10^6

Table 2.4: Surface temperature rise and number of shots survived [15]. 250 K temperature rise resulted in enough cracks to cause local melting of the surface

lated for the rf pulse using the general integral formulation shown in Equation 2.8 [15].

$$\Delta T = \frac{1}{\rho c_\epsilon \sqrt{\pi \alpha_d}} \int_0^t \frac{1}{\sqrt{t - t'}} \frac{1}{2} R_S \left| H\left(t'\right) \right|^2 \, dt' \tag{2.8}$$

The values for ρ, c_ϵ, and α_d are given in Table 2.3 [15]. Equation 2.8 simplifies to Equation 2.7 for a square pulse of duration t_P.

Tolerable temperature rise has been a subject of much debate, and has resulted in targeted experimental research. D. P. Pritzkau constructed cavities to apply a specific surface temperature rise on a copper surface. Pritzkau observed that surface temperature rise affected the number of shots the surface would survive, as summarized in Table 2.4. Surface roughness increased, and cracks were observed under scanning electron microscope inspection of the surfaces [15].

The experimental results of Pritzkau have prompted and enabled a two point normalization for the theory of S. V. Kuzikov and M. E. Plotkin [14]. This model develops a thermal-fatigue theory based on the polycrystalline structure of copper. The thermal strains and mechanical loads on copper grains are treated probabilistically, with the ability to either realign or crack under cyclic pulsed heating. Kuzikov uses the two experimental points tested by Pritzkau to normalize a model that predicts the number of shots sustainable by a structure at a given level of pulsed heating. The two points allow an estimation of the two unknown parameters in Equation 2.9, which relates the number of shots to damage a surface, N_f, to the temperature rise,

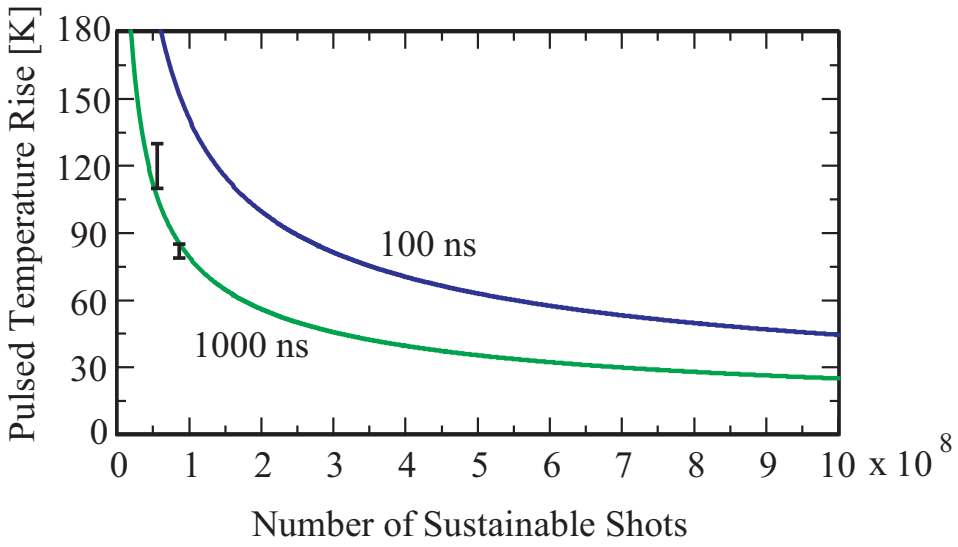

Figure 2-4: Plot of Equation 2.9 from [14] calibrated and with data points from [15]. Temperature rise is plotted as a function of the number of sustainable shots, for pulse lengths of 1000 ns and 100 ns.

ΔT, pulse length, τ, and two surface material dependent parameters, ζ and C [14].

$$N_f = \frac{C}{e^{\zeta\sqrt{\tau}(\Delta T)^2} - 1} \tag{2.9}$$

The two parameters, C and ζ, can be solved for using the first two data points from [15], shown in Table 2.4. The result is shown in Figure 2-4, for pulse lengths of 1 μs and 100 ns, along with the two data points used for calibration. Though only two data points are used to calibrate a two parameter fit, the functional dependence is weak, and the points agree well with the theoretically motivated Equation 2.9, as observed in Figure 2-4. For pulsed heating such that, $\Delta\ T\ \lesssim 50$ K, an accelerating structure should survive a sufficient number of pulses under normal collider operation.

2.3 Beam-Loading in Traveling Wave Accelerators

Accelerating particles in a linear accelerator involves a transfer of energy from the electric field in the structure to the particles. This increase in particle energy necessarily decreases the total accelerating field in the structure: an effect known as beam-loading. In the case of no input power, expressions can be obtained which

predict the power radiated by the beam into the structure. The following treatment of beam-loading makes the following linearity assumptions: linearity with respect to particle motion in time, linearity with respect to the fields in the structure, and power supplied independent of beam-loading effects [41].

The interaction of an electron beam with a traveling wave accelerating structure can be developed starting with the power diffusion equation, as given in Equation 2.10, which relates the change in rf power density, P, with distance, z, as a function of the voltage attenuation per unit length of the structure, I, and the effect of beam-loading, involving a term with the average beam current, i, and the electric field, E.

$$dP/dz = -2IP - iE \tag{2.10}$$

Equation 2.10 can be reëxpressed using the definition of structure shunt impedance, r, given in Equation 2.11.

$$r = \frac{E^2}{dP/dz} = \frac{E^2}{2IP} \tag{2.11}$$

Similar to Equation 2.10, the electric field change with distance, dE/dz, can be written as:

$$dE/dz = -IE - Iir \tag{2.12}$$

Equation 2.10, combined with the definition for shunt impedance in Equation 2.11, and Equation 2.12, can be solved for the electric field as a function of z, $E(z)$, as expressed in Equation 2.13, where E_0 is the initial electric field strength supported by input power.

$$E(z) = E_0 e^{-Iz} - ir\left(1 - e^{-Iz}\right) \tag{2.13}$$

Equation 2.13 can be integrated over the structure length, L, to get the total voltage experienced by the beam. Equation 2.13 can also be used with Equation 2.11 to express the power radiated by the beam, P_b, for no initial power input, id est, for $E_0 = 0$, as shown in Equation 2.14.

$$P_b = \frac{E_b^2}{2Ir} = \left(\frac{i^2 r}{2I}\right)\left(1 - e^{-IL}\right)^2 \tag{2.14}$$

The voltage loss per unit length, I, can be expressed as shown in Equation 2.15, as a function of the structure frequency, ω, group velocity, v_g, and quality factor, Q [38].

$$I = \frac{\omega}{2v_g Q} \tag{2.15}$$

Which allows Equation 2.14 to be rewritten as Equation 2.16.

$$P_b = \left(\frac{i^2 r v_g Q}{\omega}\right)\left(1 - e^{-\frac{\omega L}{2v_g Q}}\right)^2 \tag{2.16}$$

Equation 2.16 can be expanded for small loss, id est, $Q \gg 1$, by Taylor series expansion of the exponential, using $\left(1 - e^{-\frac{\omega L}{2v_g Q}}\right) \approx \left(1 - 1 + \frac{\omega L}{2v_g Q}\right)$. Giving the low loss form of Equation 2.16 as Equation 2.17.

$$P_b = i^2 \frac{\omega L^2}{4v_g}\frac{r}{Q} \tag{2.17}$$

Equation 2.17 contains a dependence on Q only in the combination r/Q, which is a geometric quantity, dependent only on the accelerator structure shape, with the functional dependence on cavity wall losses cancelling out.

2.4 Photonic Band Gaps

Photonic crystals have the ability to form frequency selective walls for accelerator structures, providing simultaneous damping of all wakefields. An axial electric field is required for acceleration, which is generally accomplished using the transverse magnetic (TM) modes of pillbox-like cavities. The TM_{01} mode is the lowest frequency eigenmode of a pillbox cavity, and so the unwanted modes can be identified as higher order modes (HOMs).

Photonic crystals can be formed in one, two or three dimensions, as shown schematically in Figure 1-10, by periodically arranging materials of varying dielectric constants, including metals, or the absence of material in the form of air or vacuum. Much as band gaps are formed in semiconductors representing forbidden energy lev-

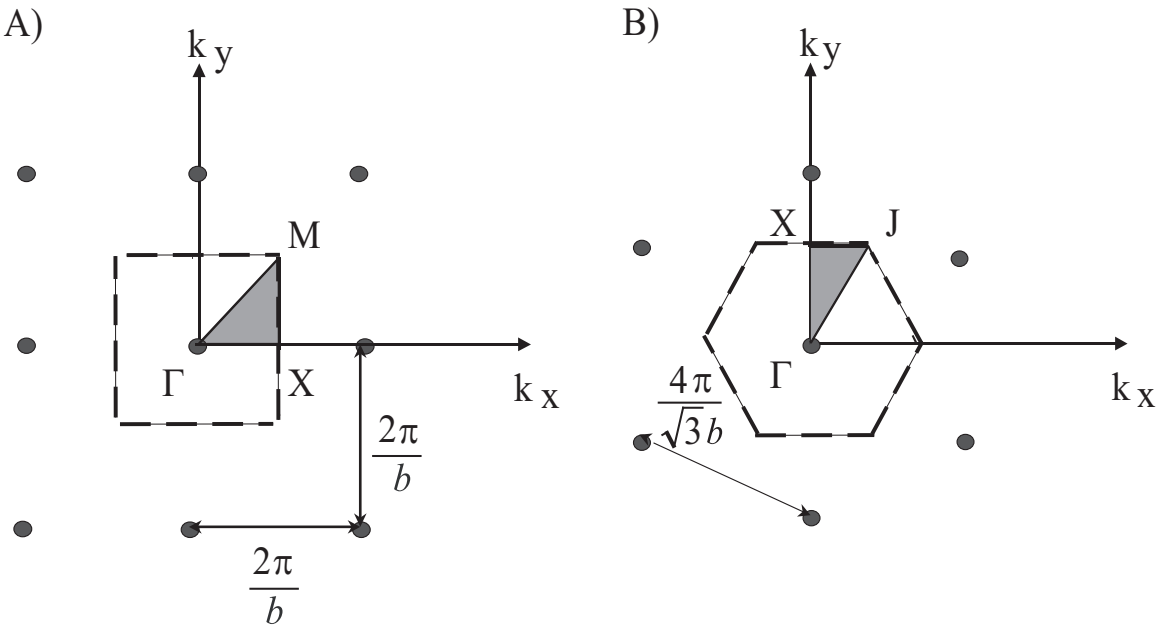

Figure 2-5: Reciprocal lattices and Brillouin zones for A) square lattice, and B) triangular lattice. Irreducible Brillouin zones are shaded [27].

els, bandgaps can be formed in photonic crystals, representing forbidden frequency ranges. Bragg filters are well known examples of photonic crystals in one dimension, reflecting all radiation in a range of frequencies. The dispersion relation can be calculated for a given geometry, which when calculated over an irreducible Brillouin zone, is mathematically complete: videlicet all solutions are recovered. The reciprocal lattices are shown in k-space for two dimensional square and triangular lattices, with their irreducible Brillouin zones in Figure 2-5.

Solving Maxwell's equations in k-space in Bloch form, complete solutions for TM mode dispersion can be represented over the wave vector points in Figure 2-5 for all frequencies, as shown in Figure 2-6. Solutions are shown as lines in Figure 2-6 for the specific geometry shown in Figure 2-7: square and triangular lattices of cylindrical metallic rods, with radii a and lattice spacing b. Gaps can be formed in the dispersion curves, such that for a given frequency, or band of frequencies, no solution exists for any k-vector. Such omni-directional frequency gaps are known as complete or global photonic bandgaps. Reflections from the photonic crystal lattice components add destructively in this band of frequencies to forbid propagation through the lattice.

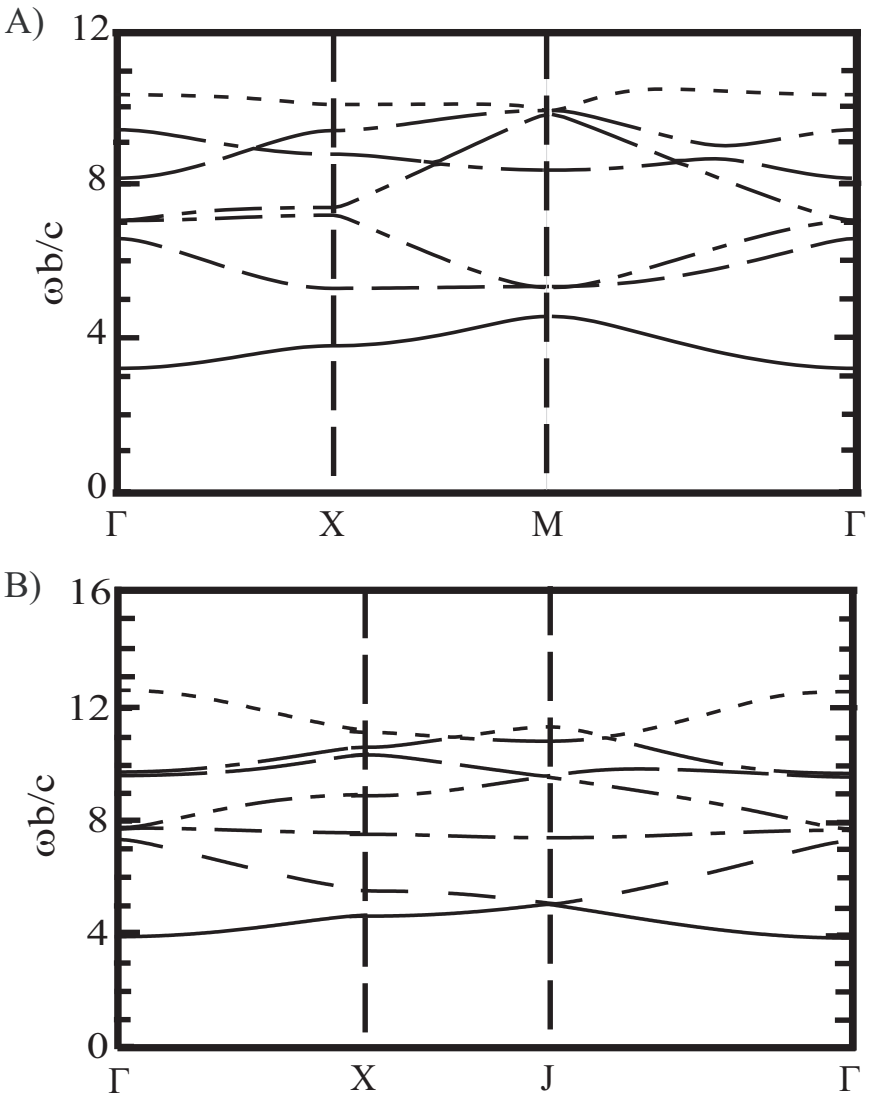

Figure 2-6: Plot of lowest normalized eigenmodes versus the wave vector $\vec{k}_\perp$ for the transverse magnetic field modes as $\vec{k}_\perp$ varies from the center of the Brillouin zone along the points; Γ, X, M or J, and back to Γ as indicated in Figure 2-5. The dispersion curves correspond to an a/b ratio of 0.2 for the geometry indicated in Figure 2-7, for A) square lattice and B) triangular lattice [27].

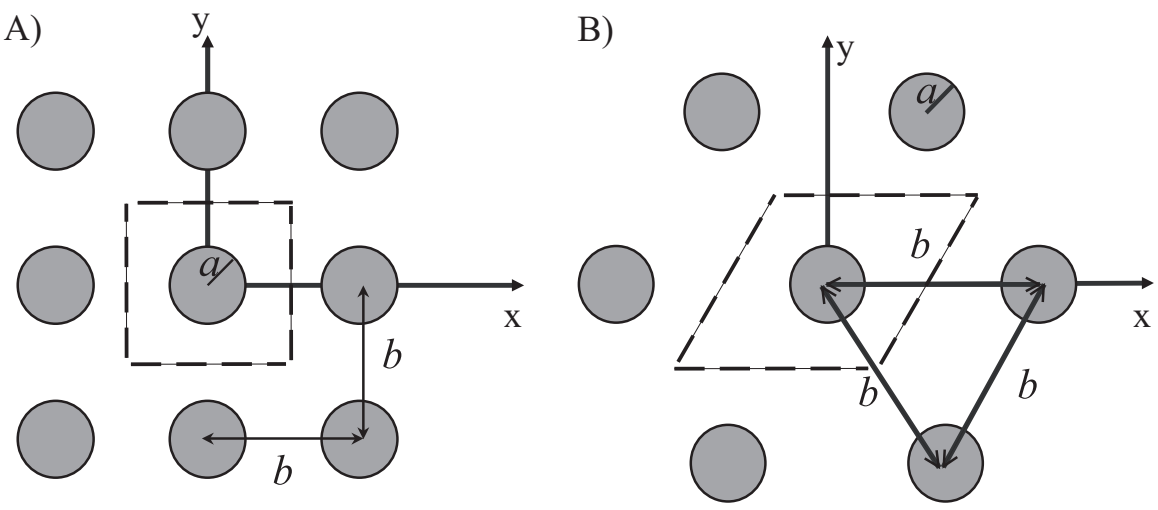

Figure 2-7: Geometry used for dispersion curve and global bandgap calculations. Cylindrical rods of radius a are arranged in A) square, or B) triangular lattice of lattice spacing b. Dashed line box corresponds to irreducible simulation region [27].

These gaps can appear and disappear as the geometry is altered. Figure 2-8 shows a map of the gaps in normalized frequency as the ratio a/b is varied. For metallic lattices of cylindrical rods, a lower gap always exists up to some frequency (an effect also known as an rf cage). Additional gaps open up at higher frequencies as the a/b ratio is increased, until at the extreme right of the plots in Figure 2-8, the entire lattice begins to fill with metal, reflecting at all frequencies.

A photonic crystal lattice with a global bandgap is a starting point for the design of an accelerator structure, but it must be formed into an appropriate cavity. This is accomplished by removing a single rod from the lattices of metallic rods shown in Figure 2-7. This defect in the lattice forms a space in which radiation at a frequency in the bandgap of the surrounding lattice is perfectly reflected, confining the field strength of the mode to the lattice.

A triangular lattice of cylindrical rods was designed by E. I. Smirnova et alia at MIT, and used in the initial PBG accelerator concept and demonstration. Flat metallic plates with a drilled beam hole were used to enforce the design axial mode structure, suitable for accelerating particles. A schematic is shown in Figure 2-9 with design parameters described in Table 2.5, and photographs in Figure 2-10. The

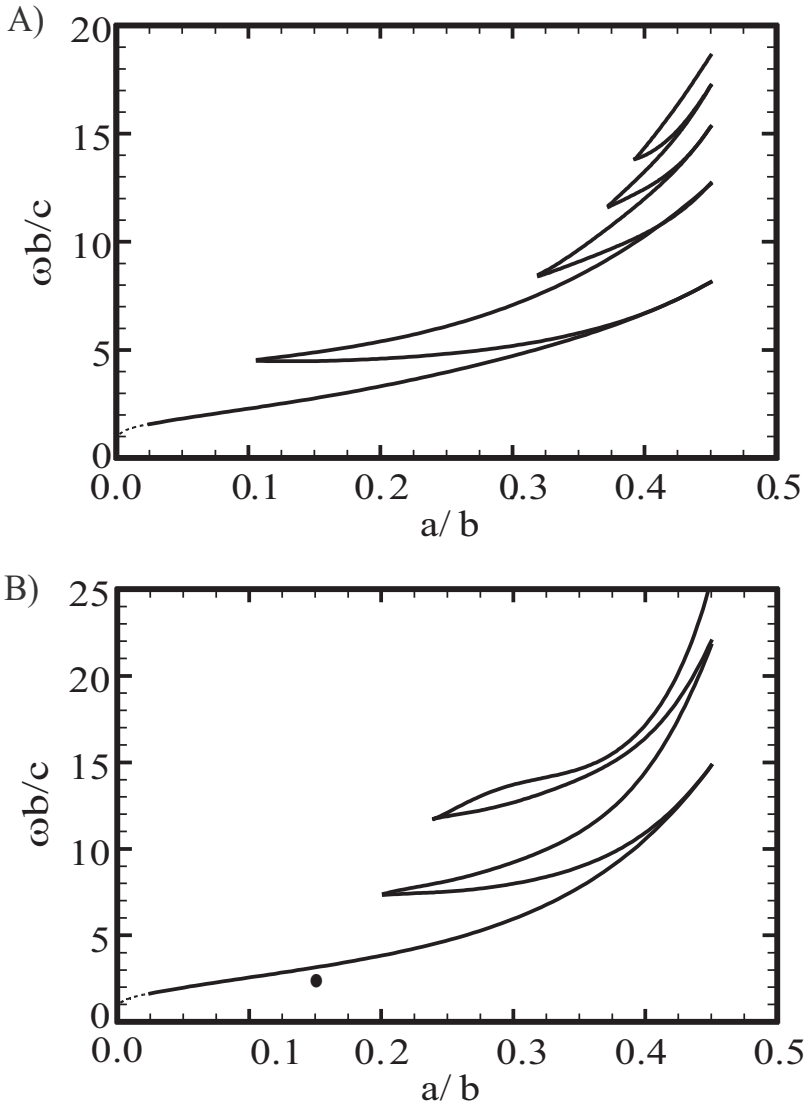

Figure 2-8: Plots of the global bandgaps for transverse magnetic field modes as a function of a/b ratio, as defined in Figure 2-7 for A) square lattice, and B) triangular lattice. The solid dot indicates the design operating point for the MIT 17 GHz six cell PBG structure [27].

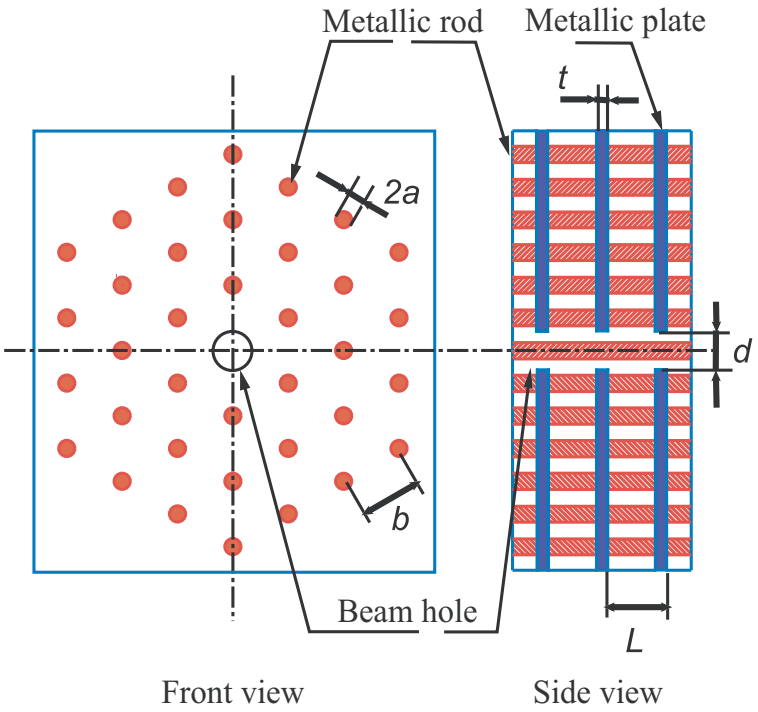

Figure 2-9: Schematic of six cell traveling wave PBG accelerator. Design values for schematic labels are included in Table 2.5.

Rod radius	a	1.04 mm
Rod spacing	b	6.97 mm
Iris thickness	t	1.14 mm
Iris diameter	d	4.32 mm
Cavity length	L	5.83 mm
TM_{01} frequency	f_{rf}	17.14 GHz

Table 2.5: Table of six cell traveling wave PBG accelerator design properties. Lettered abbreviations represent the dimensional labels used in the schematic of Figure 2-9.

structure was tested by measuring the change in energy of an injected electron beam. The electron beam energy increased with the power input into the PBG structure, as shown in Figure 2-11. The acceleration observed corresponds to a maximum gradient of 35 MV/m [27, 28, 29]. This gradient was limited by available power and the fabrication of the structure.

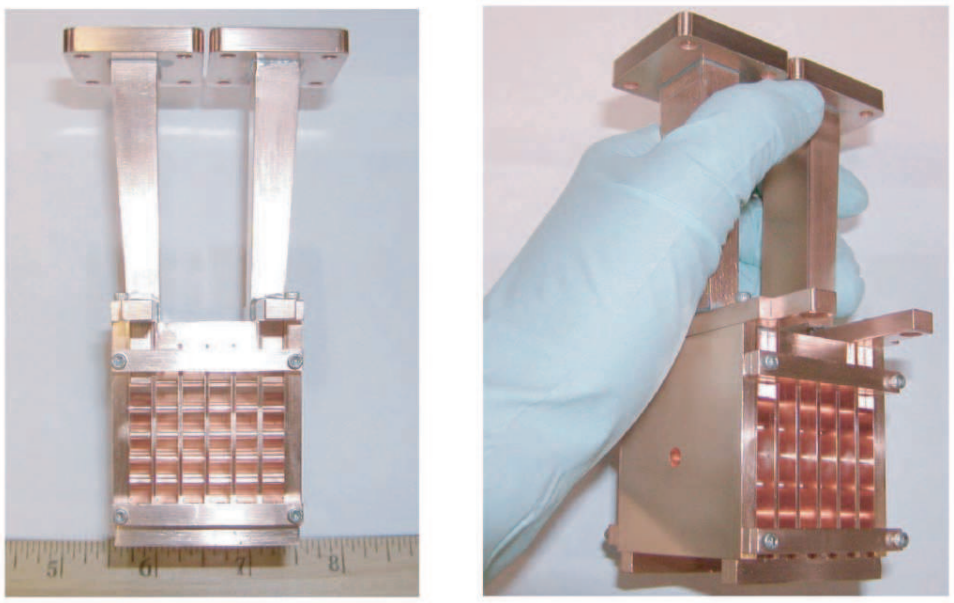

Figure 2-10: Photographs of the six cell traveling wave PBG accelerator.

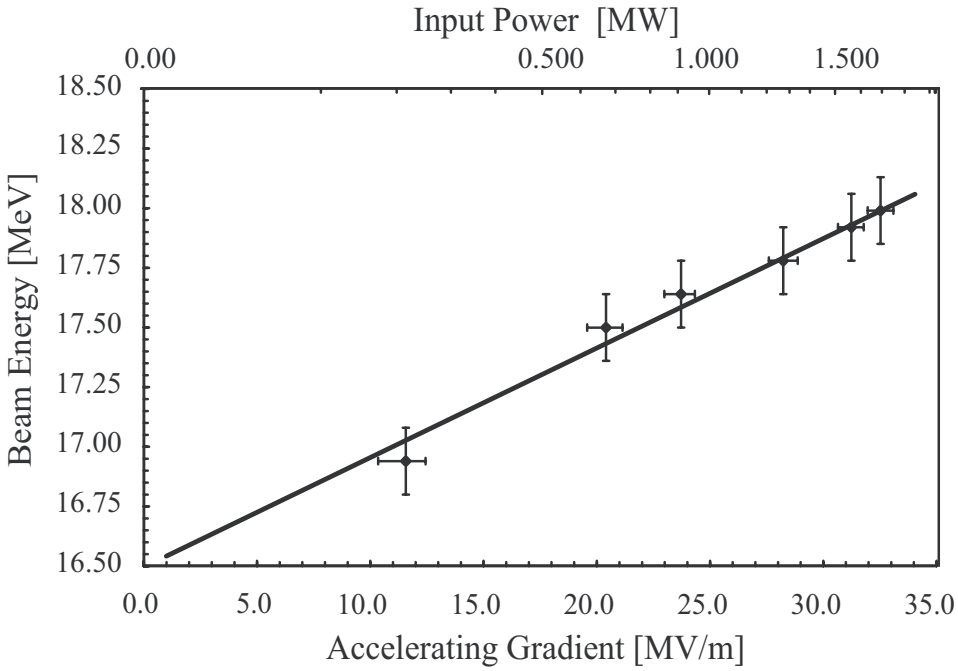

Figure 2-11: Electron beam energy versus PBG input power. A maximum accelerating gradient of 35 MV/m was achieved [27].

Chapter 3

Photonic Bandgap Higher Order Modes

3.1 Introduction

The existence of a photonic bandgap makes the formation of an rf cavity possible, by forming a lattice defect, exempla gratia, removing a single rod from the lattices of Figure 2-7. By forming the defect in the vicinity of the operating point in Figure 2-8, where a single lower frequency gap exists, the lowest frequency TM_{01}-like mode can be used. Any other cavity modes will be of higher frequency, which will have dispersion relation solutions, as shown in Figure 2-6. These solutions guarantee that the modes will escape the cavity, but do not directly contain information regarding their transmission properties. Especially where the dispersion relation solution levels off, id est, $d\omega/dk \approx 0$, modes may escape the PBG lattice very slowly.

PBG structure damping was claimed because no HOMs would be confined to a cavity formed from an appropriate lattice of cylindrical rods, exempla gratia, the operating point in Figure 2-8 chosen for the six cell traveling wave PBG accelerator demonstration. Current accelerator design, especially at high frequency, involves very short bunches of electrons. The Fourier transform of a short electron bunch transiting

a cavity will have a very broad frequency content, as in Equation 3.1.

$$I(\omega) = e^{-\left(\frac{2\pi\sigma}{\lambda}\right)^2} \tag{3.1}$$

Any modes up to Fourier transform limited frequencies will be coherently excited by an electron bunch; for short bunches, modes up to very high frequencies can be excited. As motivated in Equation 1.5, any modes of the structure will make up the bunch wakefields. The only reliable way to quantify damping is in examining the terms involved of Equation 1.5: the beam coupling to the mode can be reduced, as quantified in a_n, but also indirectly by $f_n(\vec{x})$, because the fields of primary importance are those in proximity to the beam; $e^{-\imath\omega_n t}$ is only oscillatory, though high frequency modes will oscillate rapidly enough that any effect on the beam will become incoherent as it is averaged over multiple cycles; $e^{-\omega_n t/2Q_n}$ directly shows that the magnitude of the excited modes damp, so that if low enough Q values are obtained for HOMs they will be damped sufficiently quickly.

All of the HOM terms in Equation 1.5 can be directly tuned and improved in PBG structures over conventional pillbox accelerating structures. HOMs can be extracted from the proximity of the beam, so that their coupling is significantly decreased. HOM loss can also be increased so that they have very low Q. These effects will be described in detail in the following sections: Section 3.2 will detail High Frequency Structure Simulator (*HFSS*) simulations of PBG structures, and Section 3.3 will describe cold testing of the six cell traveling wave PBG structure, including observation of HOMs, and damping improvement with the application of lossy absorbers.

3.2 *HFSS* Simulations

A great deal concerning PBG cavity modes can be learned from *HFSS* simulations. Run as eigenmode simulations, with the capacity for lossy surfaces and radiation boundary conditions, *HFSS* provides full field data which can be used to understand the functional structure of modes as well as their variation with cavity parameters.

PBGs themselves can be probed, using the geometrically irreducible region indicated in Figure 2-7.

Cavity modes are initially discussed in Section 3.2.1. Field data is then used to calculate loss factors, both longitudinal and transverse, which quantify beam coupling to modes, discussed in Sections 3.2.2 and 3.2.3, respectively. Mode quality factors are calculated and examined extensively in Section 3.2.4. Damping solutions are discussed in Section 3.2.5.

3.2.1 Motivation

Initial PBG structure simulations enclosed three rows of PBG lattice rods with a metallic outer wall. As the ratio a/b (schematized in Figure 2-7) was varied, a qualitative difference in mode structure was observed, in expectation with Figure 2-8, as additional bandgaps opened up. This is summarized in Figure 3-1 A–C, showing PBG simulations for an a/b ratio of 0.15 and 0.2 as well as the fields for an equivalent pillbox structure. In Figure 3-1 the fundamental TM_{01} modes are shown on the left, and the first higher order modes, the dipole TM_{11} modes, are shown on the right, as labeled. For comparison, the fundamental and dipole modes for a pillbox structure are shown in Figure 3-1 C.

The dipole mode in Figure 3-1 A was initially believed to be a simulation artifact, while the dipole mode in Figure 3-1 B was real and to be avoided [27]. The two dimensional theory developed by E. I. Smirnova predicts that for an a/b ratio $>$ 0.20 a dipole mode will be confined within the inner row of rods; a process that can be seen as a/b is increased from 0.15 to 0.20 from Figure 3-1 A to Figure 3-1 B. The dipole mode in Figure 3-1 A was assumed to be confined by the metallic outer boundary used in the simulation, and not an actual mode of the structure. The six cell structure that was built contained no outer wall, and so would not confine such HOMs. Investigation into these HOMs reveals that they are in fact insensitive to the outer metallic wall properties: position, conductivity, et cetera. Because they are not strict cavity HOMs, contained in the vicinity of the fundamental mode and the beam, but are restricted to the PBG lattice, they are referred to as lattice HOMs. Lattice

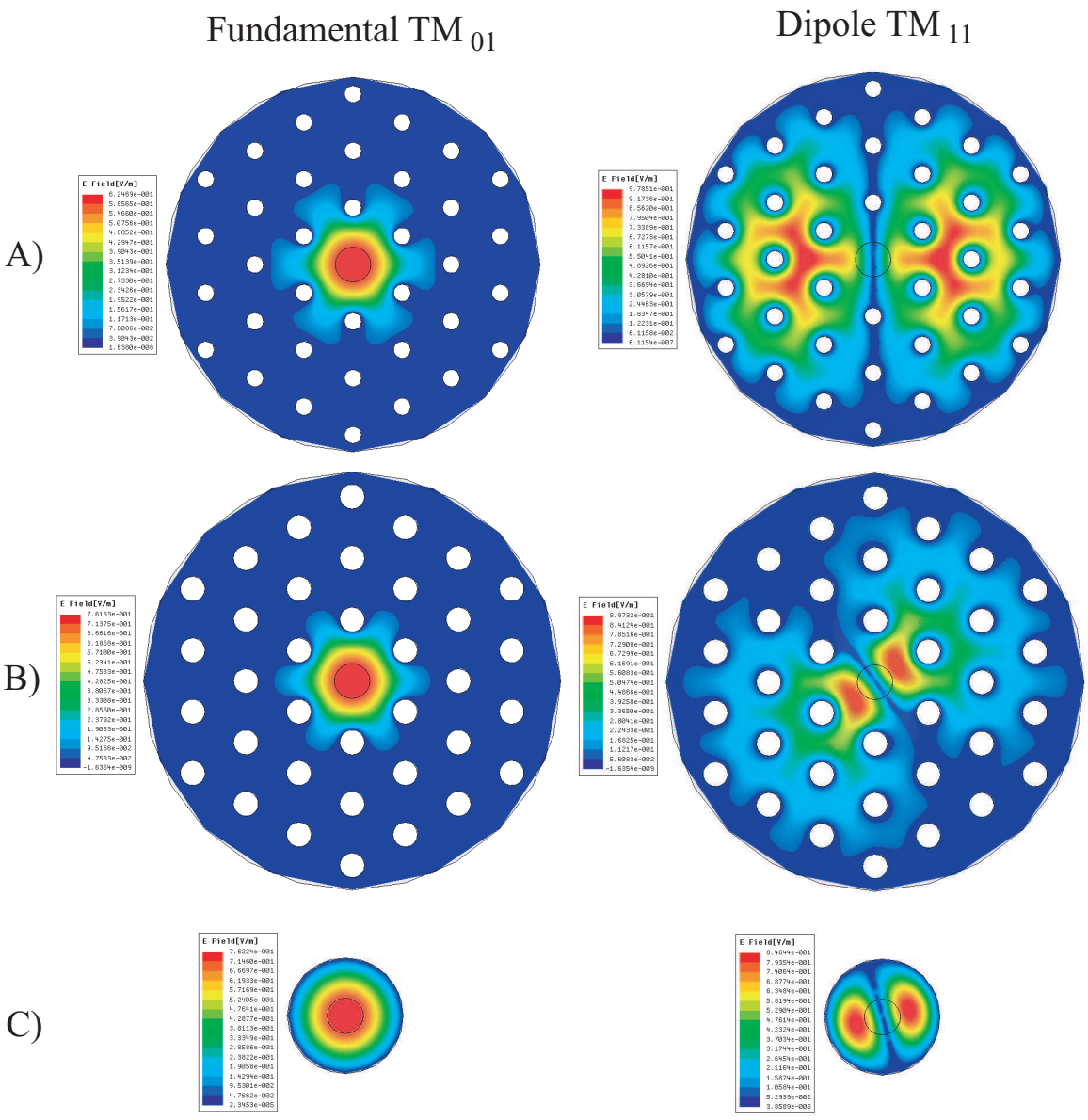

Figure 3-1: *HFSS* simulations of fundamental TM_{01} and dipole TM_{11} modes for PBG structures with A) $a/b = 0.15$ and B) $a/b = 0.2$, and C) an equivalently sized pillbox structure. Electric field strength is shown in contour plots with scales as shown.

HOMs are a large improvement on the conventional pillbox HOMs because they are localized away from the beam, coupling much more weakly, and they are damped, and so decay a great deal before subsequent bunches have the opportunity to interact with them.

3.2.2 Longitudinal Loss Factor Simulations

Longitudinal loss factors, k, with units Volts per Coulomb, are a measure of beam to mode coupling, and can be calculated using Equation 3.2 from [16], and the *HFSS* field data from the simulation of interest.

$$k = \frac{V_b^2}{4U} = \frac{\omega}{4}\frac{R}{Q_0} = \frac{\left|\int E_z(z) e^{i\frac{\omega z}{c}} dz\right|^2}{2\int(\epsilon_0 E^2 + \frac{1}{\mu_0}B^2)dV} \tag{3.2}$$

In Equation 3.2 the longitudinal loss factor is defined as a function of the beam induced voltage, V_b, and the stored energy in the cavity, U, which can be related to the cavity frequency, ω, and cavity R/Q_0 (R/Q_0 differs from r/Q in the specification of R, the total shunt impedance, over r, the shunt impedance per unit length, and Q_0, the unloaded quality factor, over Q, the total quality factor). These cavity parameters can then be calculated as a line integral of E_z, the electric field along the beam path divided by an energy volume integral over the cavity, using the electric and magnetic fields from simulation.

Wakefield theory can be developed as an expansion of cavity eigenmodes with varying coupling to the beam. In an ideal accelerator structure the beam couples very strongly to the operating mode, and very weakly to any HOMs. Using *HFSS* simulations, the frequency, cavity quality factor, and loss factors for various modes can be calculated. These are used with the following relation to arrive at the power lost by a charge q into the n^{th} mode as it passes through a single cell of the unpowered structure [16].

$$\Delta P_n = q^2 \frac{\omega_n k_n}{Q_{0n}} \tag{3.3}$$

The general loss factor formula, Equation 3.2 can then be used to calculate the

charge power loss, ΔP_n, in Watts, using Equation 3.3 for each HOM n. Equation 3.3 is valid for a single bunch, for a train of bunches the total power radiated does not scale linearly, as the bunches can coherently radiate; this is dependent on the group velocity of the mode and the length of the structure. A more complete theoretical treatment of this case, applicable to the traveling wave PBG accelerator structure, was presented in Section 2.3, though it is limited to the case of modes with well-defined and measurable group velocity and shunt impedance.

Loss factors, k_n, relate directly to the wake potential, W, introduced in Section 1.2.3. The longitudinal wakefield, $W_\parallel$ can be written as Equation 3.4 [42].

$$W_\parallel(s) = \sum_n 2k_{\parallel n} e^{-\frac{\omega_n s}{2Q_n c}} \cos\frac{\omega_n s}{c} \tag{3.4}$$

The longitudinal wakefield is written as a function of the path length difference, s, the distance between exciting and witness bunches, and expressed as a sum over modes, indexed with n, with parallel loss factors, $k_{\parallel n}$, frequencies, ω_n, and quality factors, Q_n. This in turn can be expressed in terms of field information, involving the voltage along the path of the exciting bunch, $\vec{x}'$, and witness bunch, $\vec{x}$, $V(\vec{x}')$ and $V(\vec{x})$, respectively, as shown in Equation 3.5 [42, 17].

$$W_\parallel(\vec{x}', \vec{x}, s) = \sum_n \frac{V_n^\star(\vec{x}')\, V_n(\vec{x})}{2U_n} \cos\frac{\omega_n s}{c} \tag{3.5}$$

Here it can be seen that the loss factor, k, takes the place of the beam to mode coupling, and functional dependence implied in Equation 1.2.3.

3.2.3 Transverse Loss Factor Simulations

Much like longitudinal loss factors, transverse loss factors can be defined to quantify the coupling of the beam to transverse deflecting modes, both their excitation and their deflection of subsequent bunches. The transverse wake function, $W_\perp$, can be

written as Equation 3.6 [42].

$$W_{\perp}(s) = \sum_{n} 2k_{\perp n} e^{-\frac{\omega_n s}{2Q_n c}} \sin\frac{\omega_n s}{c} \tag{3.6}$$

As with the longitudinal wake, the transverse wake function can be rewritten in terms of field quantities along the path of the exciting bunch, $\vec{x}'$, and witness bunch, $\vec{x}$. For the transverse wake potential, the Panofsky-Wenzel theorem [43], Equation 3.7, can be exploited to immediately write this down using Equation 3.5.

$$\frac{\partial W_{\perp}}{\partial s} = \nabla_{\perp} W_{\parallel} \tag{3.7}$$

$$W_{\perp}(\vec{x}', \vec{x}, s) = \sum_{n} \frac{c}{\omega_n} \frac{V_n^{\star}(\vec{x}')\,\nabla_{\perp} V_n(\vec{x})}{2U_n} \sin\frac{\omega_{mn} s}{c} \tag{3.8}$$

The transverse wake function is generally expressed in the units Volts per meter, per picoCoulomb of exciting charge, per millimeter of position offset from the axis: $V/m/pC/mm$; generally this is plotted as a function of path length, s. What is necessary for linear collider operation is that the spacing between bunches is sufficient that this wake potential is low enough it will not significantly affect the beam. Exact collider specifications depend on an optimization over a very large set of parameters, which means that the exact level of damping required is not an absolute threshold.

Again it is observed that $k_{\perp}$ is equivalent to the beam to mode coupling, and the functional dependence implied in Equation 1.2.3, and can be calculated using field data, obtained from *HFSS* simulations.

3.2.4 Quality Factor Simulations

In order to study the diffractive Q of the lattice HOMs, *HFSS* simulations were run for an outer boundary that more closely resembles that of the experiment, which is open. This was done using a perfectly matched layer (PML). An *HFSS* PML result is shown in Figure 3-2: the electric field complex magnitude is shown for the 17 GHz TM_{01} fundamental, 23.0 GHz dipole mode, and 34 GHz HOM . The field strength of

the HOMs is localized to the lattice, away from the beam, and very high diffractive loss has been observed for these modes, with diffractive Qs on the order of ~ 100.

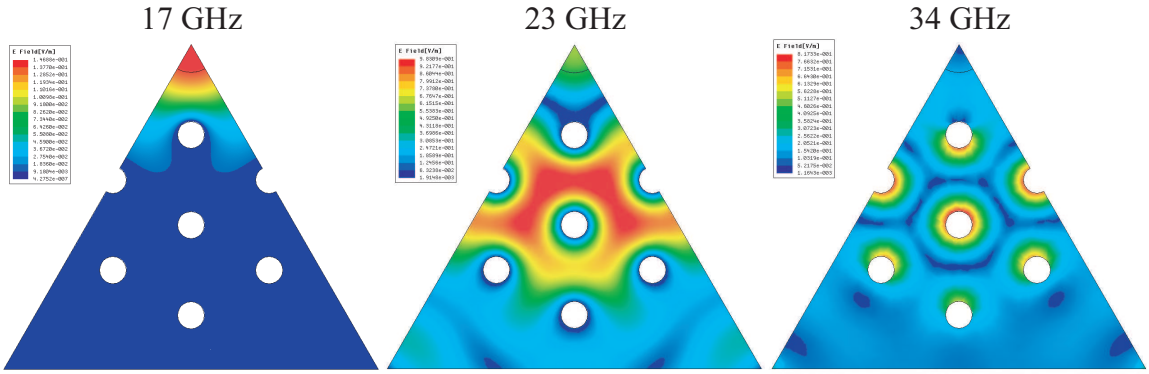

Figure 3-2: *HFSS* simulations of 17, 23, and 34 GHz modes in a one cell 60° slice of a PBG accelerator structure. Irises and the outer boundary are bordered with PMLs, metallic rods and plates are modeled with ohmic losses. The electric field magnitude is shown in color. Simulation results correspond to the $Q_{diffractive}$ runs as shown in Table 3.2.

To directly compare the effect of different structure losses on the cavity Q, *HFSS* simulations were performed with different boundary conditions. The quality factors associated with the different structure losses are: Q_{ohmic}, and $Q_{diffractive}$, which account for losses from ohmic surface heating, and the open nature of the structure, respectively. These quality factors can be combined using Equation 3.9.

$$\frac{1}{Q} = \frac{1}{Q_{total}} = \frac{1}{Q_{ohmic}} + \frac{1}{Q_{diffractive}} \tag{3.9}$$

Using *HFSS* these quality factors can be calculated independently by turning on or off the different loss channels: Q_{ohmic} can be estimated by simulating a single PBG cell with phased boundaries on the irises, a metallic outer boundary, and ohmic losses; $Q_{diffractive}$ can be estimated by simulating a single PBG cell with phased boundaries on the irises, no ohmic losses, and a PML outer boundary; Q_{total} can be estimated by simulating a single PBG cell with phased boundaries on the irises, a PML outer boundary, and ohmic losses. Table 3.1 summarizes the format of these simulations in terms of boundary condition definitions for the calculation of the various independent Q factors. Results can be cross-checked by observing how closely the losses combine

	Q_{total}	Q_{ohmic}	$Q_{diffractive}$
Lossy metal	x	x	
PML outside	x		x

Table 3.1: Table of Q value estimation simulations.

to give a total quality factor in accordance with Equation 3.9.

According to Equation 3.3 the power expected in each channel scales inversely with Q, assuming that the R/Q dependence clear from the loss factor k in Equation 3.2 is a dominantly geometrically determined quantity. This allows the ratio of power radiated into each channel to be predicted based on the following Q values for the 17 GHz fundamental, and the 23 and 34 GHz HOMs, as shown in Table 3.2. The

Mode	Q_{ohmic}	$Q_{diffractive}$	Q_{total}
17 GHz	4500	$2.5 \cdot 10^5$	4400
23 GHz	3500	60	60
34 GHz	3800	130	120

Table 3.2: Table of Q values for power ratio prediction based on Equation 3.3, for 17 GHz fundamental mode, 23 GHz dipole mode and 34 GHz HOM.

17 GHz mode has minimal diffractive loss, whereas the 23 and 34 GHz HOMs are primarily losing power diffractively. The low Q HOMs demonstrate the HOM damping in PBG structures, and predict that most of the power lost in these modes will occur cell by cell, through the open outer boundary of the structure. Some power will couple out of the port, but the modes will not be resonantly built up as they will be for the 17 GHz fundamental mode. The 17 GHz mode requires a more well-developed formalism, which was discussed in Section 2.3.

3.2.5 Damping

Damping can easily be accommodated by either lattice deformation, or the addition of lossy materials. The first inner row of rods predominantly shapes the cavity mode frequency and structure; the second row can be deformed from a single lattice spacing, b, to accomplish a shift in the second row radial position, as shown in Figure 3-3 A. Movement of this second row of rods affects the Q of both the fundamental mode and

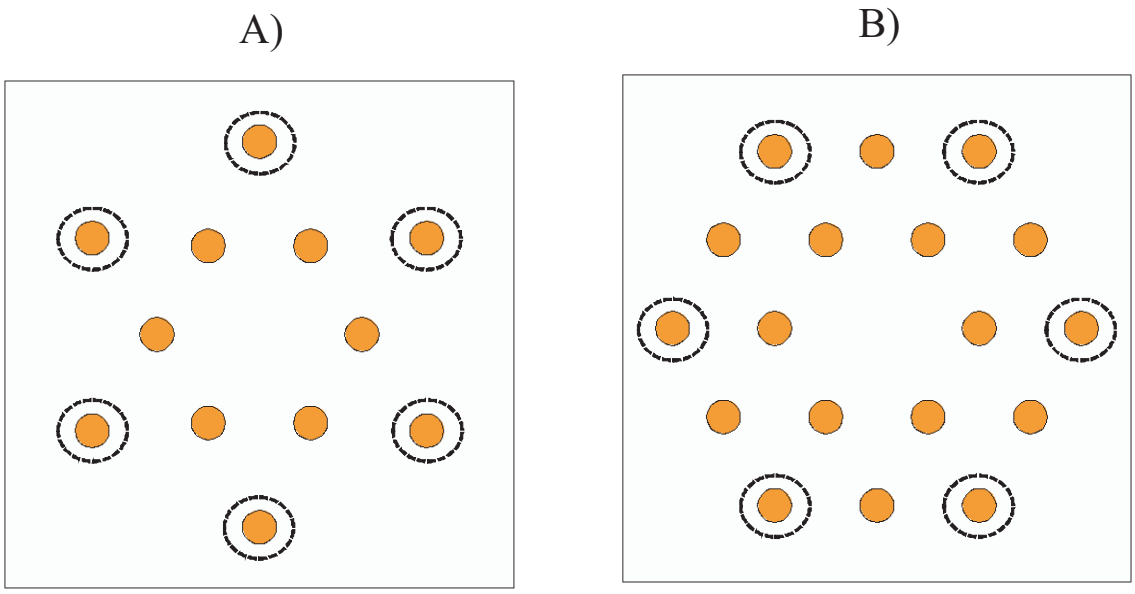

Figure 3-3: Schematic of A) position definition of second row rod placement for deformed lattices, and B) location of damped rods.

the HOMs as shown in Figure 3-4; though the Q of the HOM is certainly much lower than that of the fundamental, it is still not possible to solely decrease the HOM Q without also decreasing the fundamental mode Q. Damping solutions must involve damping material.

The second row of rods, as labeled in Figure 3-3 B can also be made of lossy material, exempla gratia stainless steel or silicon carbide, changing the field pattern as shown in Figure 3-5 and lowering the Q of HOMs significantly. The microwave properties of lossy materials used in simulations come from both the general literature [44] or detailed experimental measurements [45]. Damping can be combined with lattice deformation, especially if heavy damping is needed, but a higher fundamental mode Q is desired.

3.3 17 GHz Structure Cold Test

Cold testing of the six cell PBG structure demonstrates the existence and scale of HOM confinement in the structure. The six cell traveling wave structure was connected to an Agilent E8363B Precision Network Analyzer (PNA). The measured S_{21}

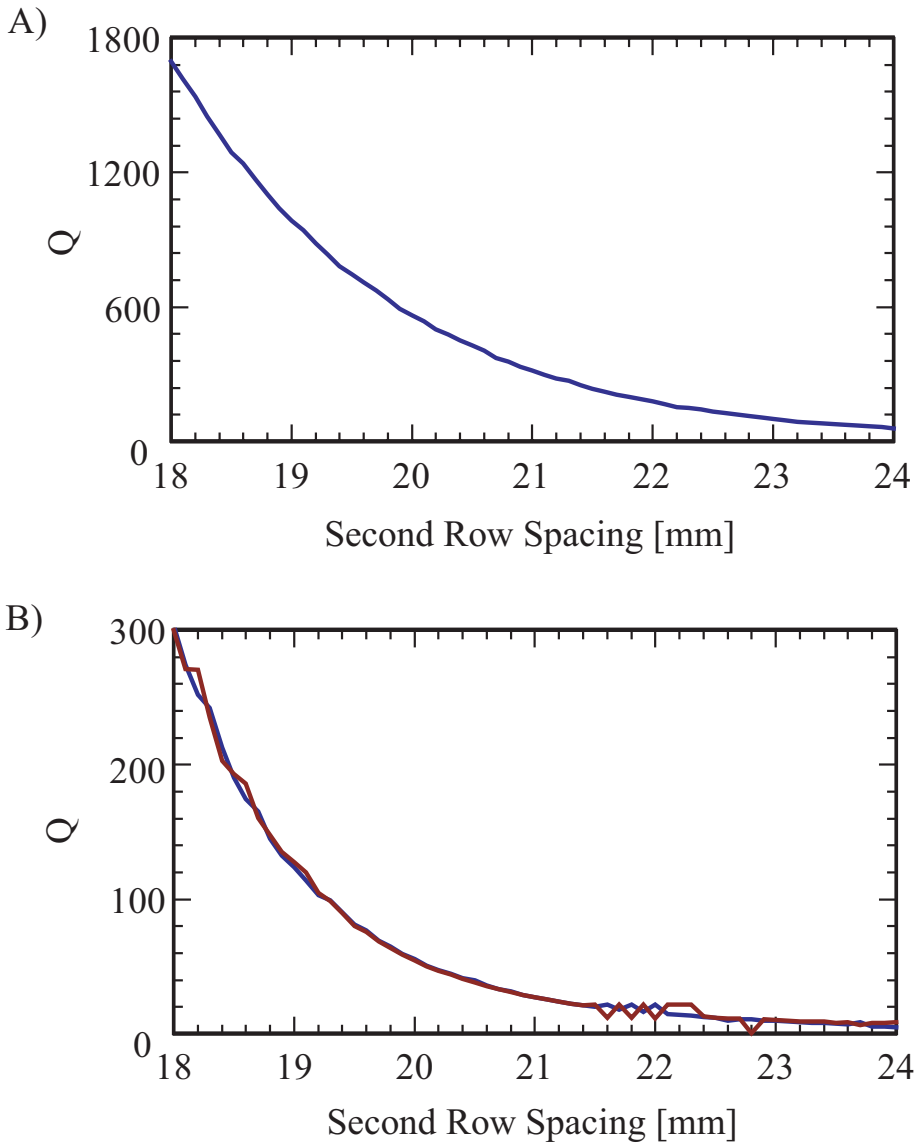

Figure 3-4: *HFSS* simulation results for A) fundamental mode and B) first HOM Q as a function of second row rod placement as schematized in Figure 3-3 A.

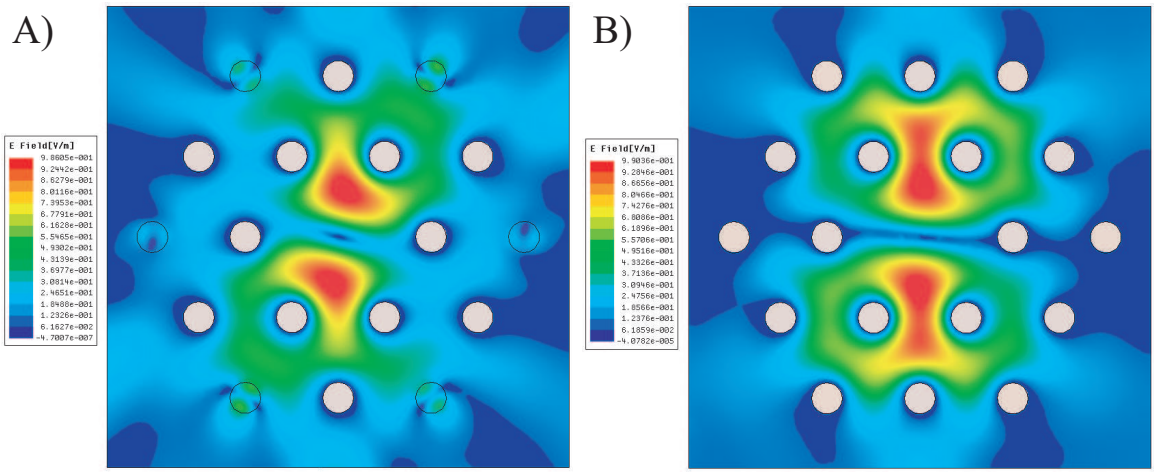

Figure 3-5: *HFSS* simulation results for A) damped and B) undamped rods as labeled in Figure 3-3 B. Damped rods are simulated with the dielectric constant and loss associated with microwaves measurements of Silicon Carbide [45].

parameter is shown in Figure 3-6: for the open structure without damping, in Figure 3-6 A, and with external damping, in Figure 3-6 B. The mode structure is rather complex because there are many modes and because of resonances in the PNA SMA cables. The structure is a six cell traveling wave structure, so that the S-parameters of the observed modes appear very broad, because there are six axial modes.

Modes were distinguishable in both S_{21} and S_{11} measurements at roughly the following frequencies: 17.14 (fundamental operating mode), 23.3, 24.5, 25.7, and 26.7 GHz. The high frequency modes (23–27 GHz) have very low quality factors, and though they have not been fully identified by bead pull measurements, they are near the dipole mode frequency of 23.0 GHz. Antenna excitation measurements have been performed to probe the structure of these modes, which exist off-axis and are most easily excited within the bulk of the PBG lattice, as expected given their field profiles, exempla gratia the 23 GHz mode of Figure 3-2.

Though the HOMs have very high insertion loss, and low quality factors, they are resonantly excited. External damping using a lossy dielectric absorber such as *ECCOSORB* at the outer boundary of the structure can significantly decrease the observed modes, as shown by the blue S_{21} curve in Figure 3-6 B. As observed in simulations, exempla gratia Section 3.2.5, damping in a PBG structure can be quite

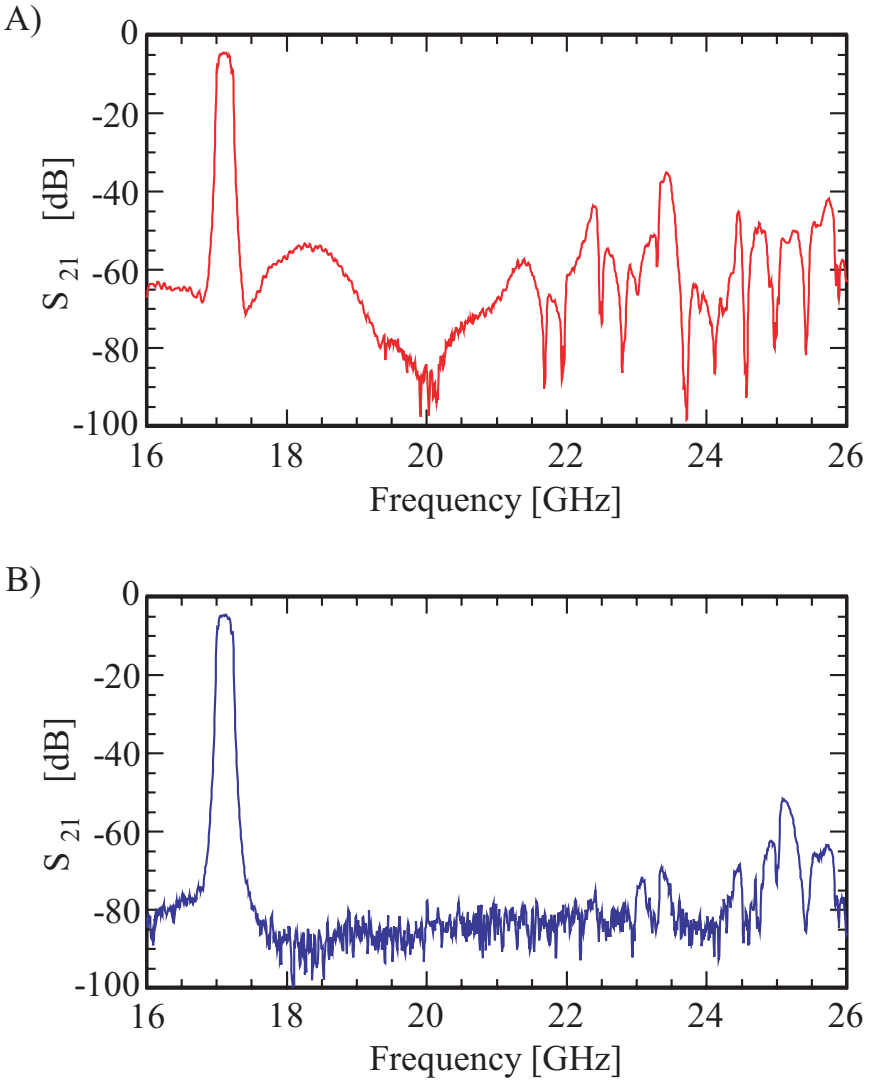

Figure 3-6: Six cell metallic PBG accelerator structure uncalibrated S_{21} measurement. A) is S_{21} in red without damping, B) is S_{21} in blue with external damping. Modes are observed at: 17.14, 23.3, 24.5, 25.7, and 26.7 GHz.

Mode	v_g	I	Q	Parameter source
17.14 GHz	0.0109c	1.04 dB	4000	measurements
17.14 GHz	0.013c	0.8 dB	4200	design

Table 3.3: Cold test parameters for insertion into the equations of Section 2.3.

effective in damping HOMs [46].

These cold test results can be combined with the *HFSS* calculations described in Sections 3.2.2 and 3.2.4, to allow parameters to be input into the traveling wave excitation formalism of Section 2.3, so that power level predictions can be made. A direct measurement of the mode frequency, insertion loss, and group velocity are required. These measurements were carried out for the fundamental 17 GHz TM_{01} mode and the 34 GHz HOM, by measuring the direct S_{21} for the modes in question and the phase as a function of frequency. Results for magnitude and phase are shown in Figure 3-7 and Figure 3-8 for the 17 and 34 GHz modes, respectively. Phase measurements, $d\phi/df$ were then converted into group velocity, $v_g = d\omega/dk$ by changing units. Phase can be converted to wave vector: $d\phi = L\ dk$, where L is the electrical length of the structure. Frequency can be converted to angular frequency: $df = 2\pi\ d\omega$. Table 3.3 presents the measured insertion loss, group velocity, and quality factors, as calculated using Equation 2.15. Power predictions were then derived as further described in Section 2.3 and reported in Chapter 4.

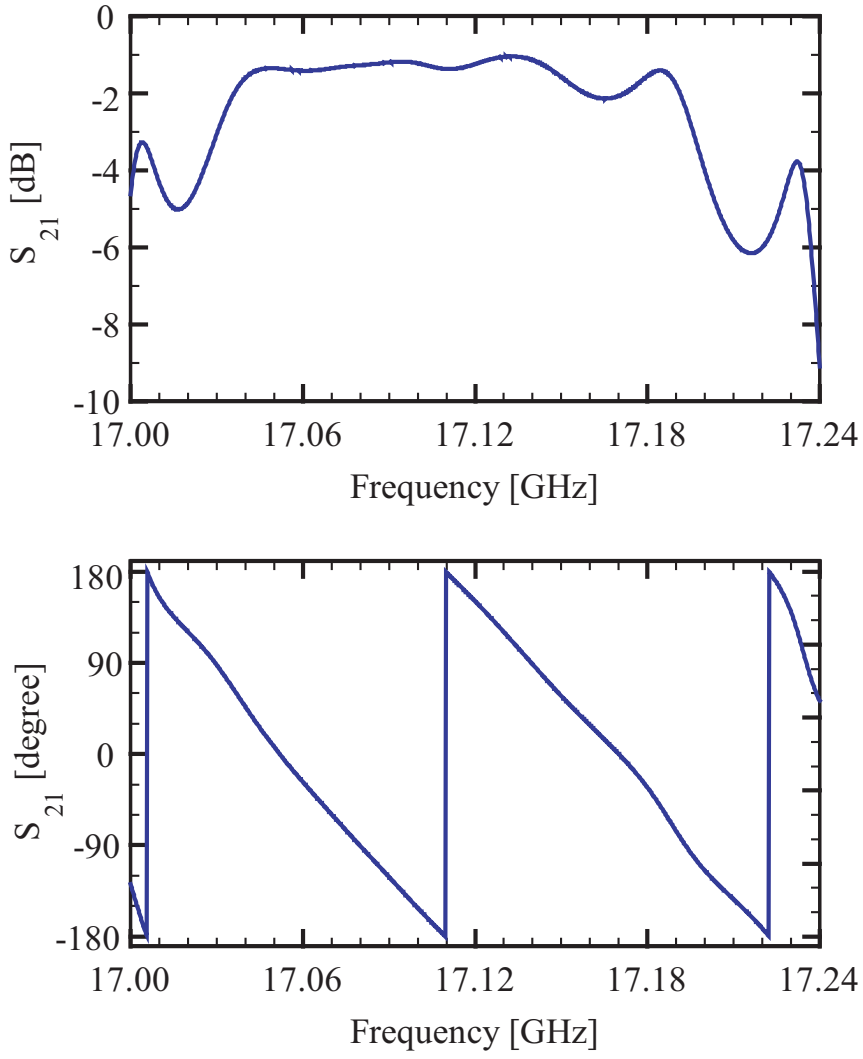

Figure 3-7: S_{21} magnitude and phase measurement for 17 GHz modes.

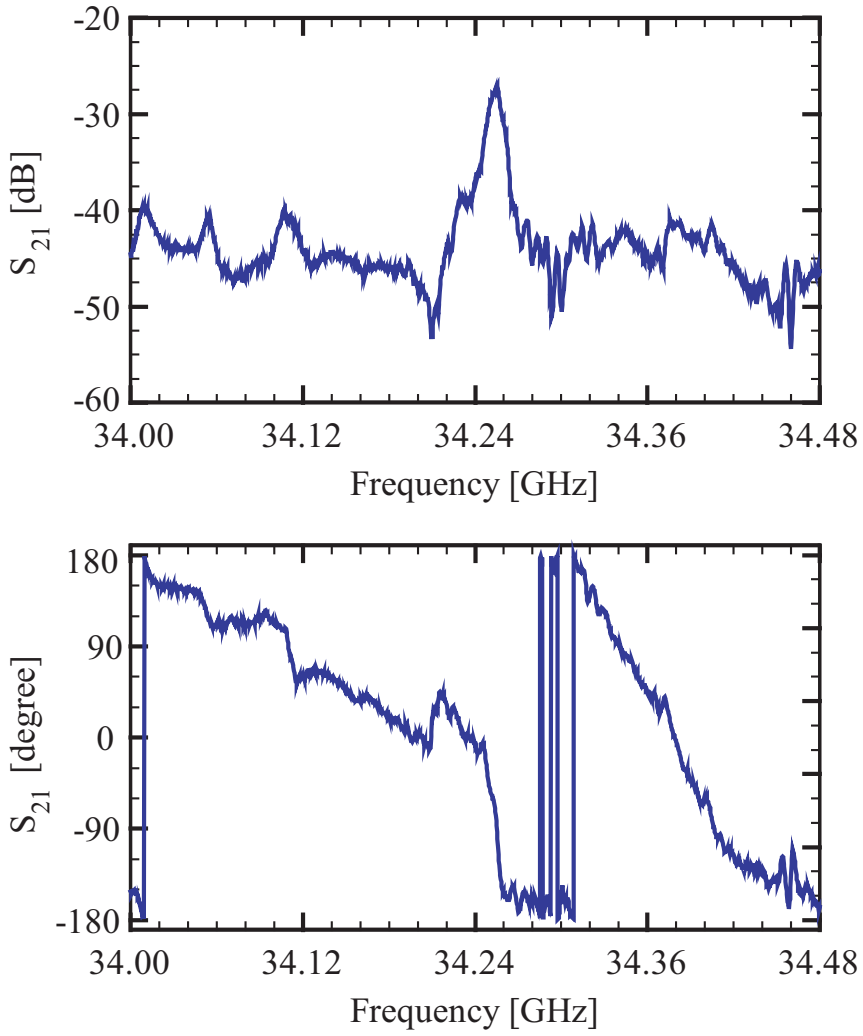

Figure 3-8: S_{21} magnitude and phase measurement for 34 GHz modes.

Chapter 4

17 GHz PBG Structure Wakefield Measurements

4.1 Introduction

The six cell traveling wave accelerator previously fabricated to demonstrate that PBG structures can be used for acceleration, [27, 28, 29], provides an excellent opportunity for direct observation of HOMs in PBGs. Cold test of the structure, reported in Section 3.3, observed HOMs in the structure, though they had very high loss, and low Q. The traveling wave theory of Section 2.3, backed by the simulations of Section 3.2 and the measurements of Section 3.3 provide support for experimental observation of beam induced wakefields in PBG structures.

4.2 MIT HRC 17 GHz Accelerator Laboratory

The MIT HRC 17 GHz accelerator was motivated by the improvement in gradient predicted by the frequency scaling discussed in Section 2.2.1 [11, 12]. Early results with rf photocathode guns showed that the scaling predicted was optimistic, and that surface fields of only $\sim$ 350–400 MV/m were obtainable in experiment. Along with the impetus of establishing frequency scaling, the necessity remains to establish optimal accelerator operating parameters, which includes the selection of an rf frequency.

Source development remains coincident with rf frequency selection; the optimal frequency for beam parameters must be balanced with the availability of microwave sources. Multiples of the original SLAC rf frequency of 2.856 GHz, which itself drove S-band klystron development, remain points of operation; the Next Linear Collider (NLC), exempla gratia, established its operating frequency at 11.424 GHz, four times the SLAC rf frequency. MIT established an accelerator laboratory to take advantage of rf sources available from Haimson Research Corporation at 17.136 GHz, six times the SLAC frequency.

A relativistic beam klystron operates at 500–550 kV, providing up to 25 MW of rf power through a dual arm output [47]. The current generation of the tube has demonstrated 76 dB gain, allowing it to run using solid state pre-amplifiers. Such gain requires isolation to prevent oscillations. Isolation is provided using two very narrow ($\sim$ 50 MHz) drop off low pass filters, which provide $>$ 30 dB attenuation to oscillations reflecting back into the tube. The two output arms are combined in a hybrid coupler, which provides phase matching of the power input from the two output arms, and splits the outgoing power into both the main linac line, and an auxiliary output used for a variety of other experiments.

The klystron and linac high voltage thermionic guns are both powered by 500 kV microsecond flat top pulses from a single high power modulator [48]. The linac gun produces up to 500 mA DC current, which is bunched prior to linac injection using an rf chopper and prebuncher system [49]. Beam current and size is controlled by focusing the beam with solenoidal lenses prior to collimation. For these wakefield measurement experiments, the system was operated in a long pulse mode, in which the DC beam is primarily prebunched, with low chopper power operating only to remove a low energy tail from the bunch; this produced 1 ps bunches, which was verified using a circularly polarized beam deflector bunch length diagnostic [50, 51]. The parameters of the linac are summarized in Table 4.1.

The main linac is a constant gradient traveling wave structure consisting of 94 cells operating in a $2\pi/3$ mode, providing a beam energy of 18 MeV. An rf pulse length of 100 ns corresponds to a bunch train of $\sim$ 40 ns because of the 60 ns fill time of the

rf Frequency, f_{rf}	17.14 GHz
rf Pulse Length	100 ns
Beam Energy	18 MeV
Bunch Length	1 ps
Bunch Spot Size	1 mm
Average Beam Current	20–300 mA

Table 4.1: Operating parameters for MIT HRC 17 GHz accelerator laboratory.

accelerator structure. A toroidal lens follows the linac where the beam is focused to an emittance limited spot size of 1 mm. This size was verified by beam interception measurements. The beam was then passed through the PBG experimental chamber and into a Faraday cup to measure the beam current and serve as a beam dump.

4.3 Experimental Setup

Subsequent to its generation, the bunched, energetic electron beam is transported through the six cell traveling wave PBG accelerator structure shown in Figure 2-10. The six cell PBG structure is housed in a stainless vacuum vessel on the beam line, shown schematically in Figure 4-2 and in the photograph of Figure 4-3. A fused quartz window was installed on the bottom of the vacuum chamber housing the PBG structure, as labeled in Figure 4-2, so that radiation could be observed leaking out of the open PBG structure. The input and output couplers, as labeled in Figure 4-2, were mounted with vacuum windows, shown in Figure 4-3, so that observations could also be made of radiation coupling out of the structure via the input and output coupler ports, with the detectors arranged as shown in Figure 4-2. During these wakefield measurements, no microwave power was injected into the structure.

Two sets of diode detectors were used, at both Ku (12–18 GHz) and Ka (26–40 GHz) bands. They were calibrated using their respective power heads and meters. The horns, waveguide, adapters, attenuators and vacuum windows that were used were calibrated over their respective frequency ranges using an E8363B Agilent PNA. A heterodyne receiver was used to look at the frequencies of the observed radiation. This heterodyne system consisted of an 8–18 GHz YIG local oscillator and a 2–18 GHz

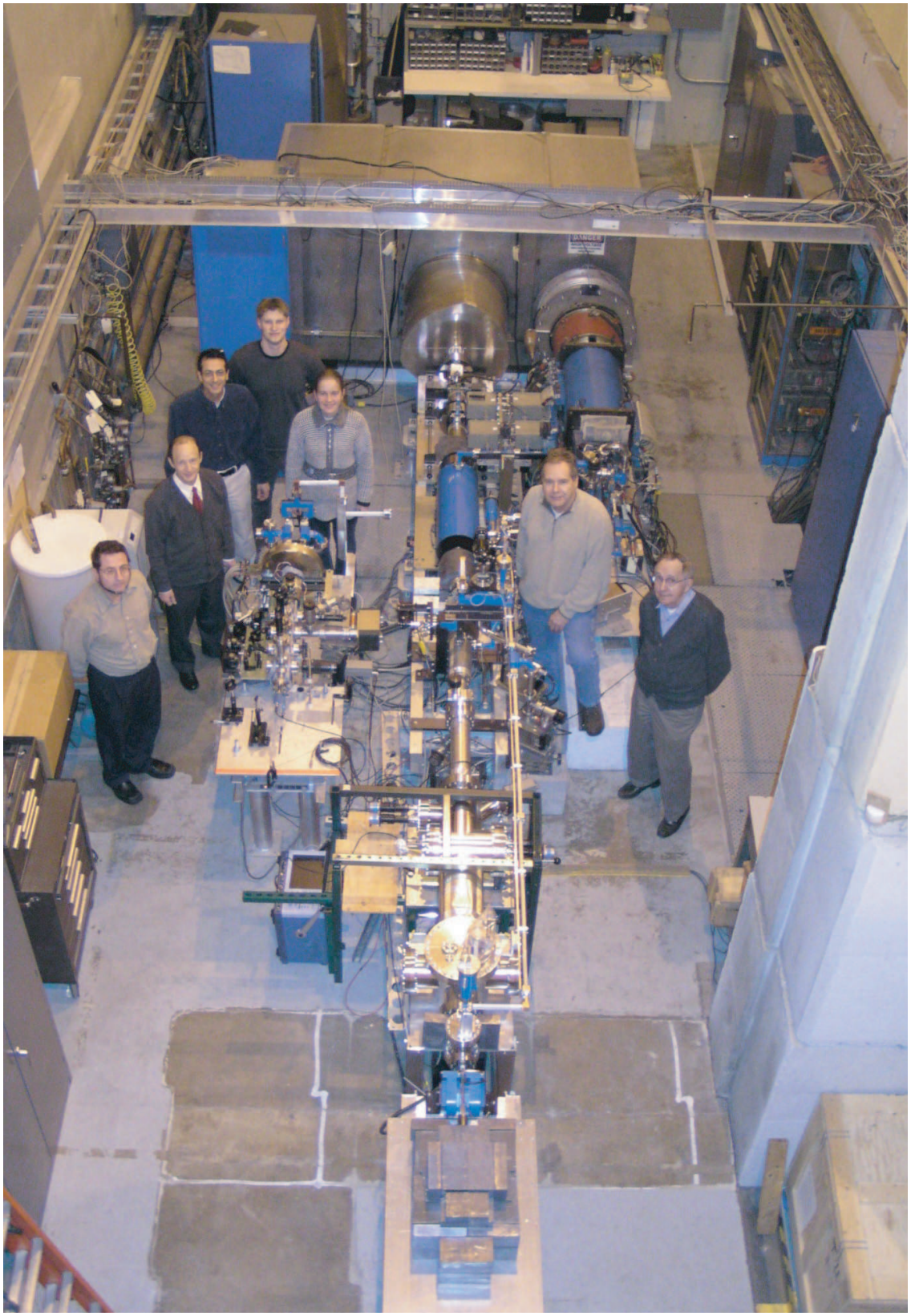

Figure 4-1: Photograph of the MIT HRC 17 GHz accelerator laboratory.

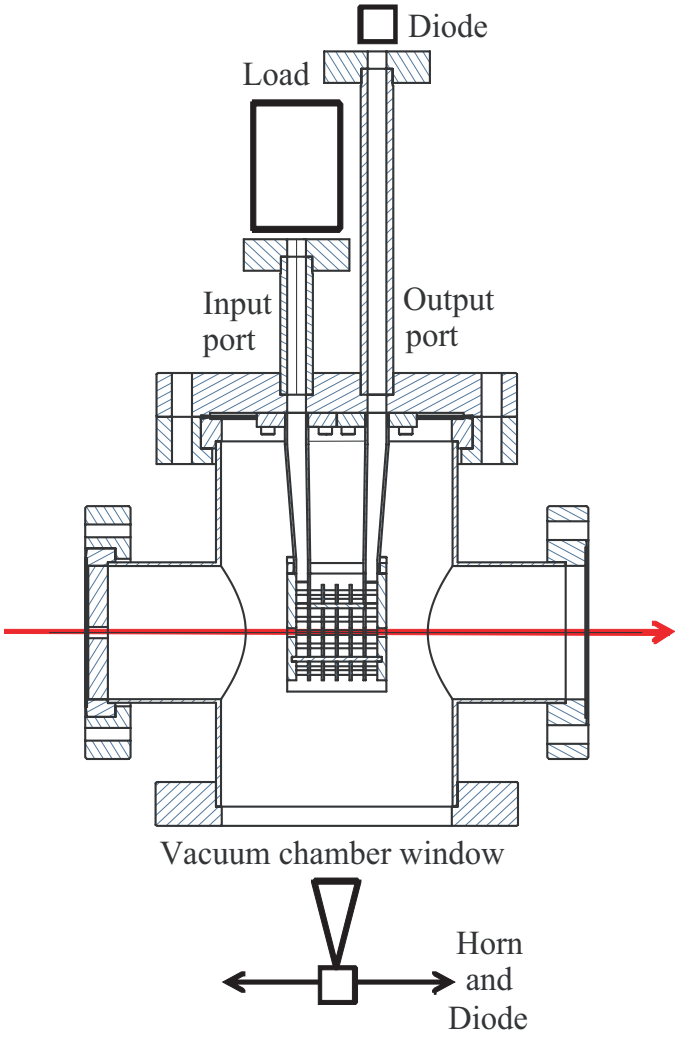

Figure 4-2: PBG accelerator structure vacuum vessel. The waveguide input and output ports, as well as the bottom of the vacuum chamber were mounted with vacuum windows. Location of matched load and diode detectors. Beam direction is indicated with an arrow.

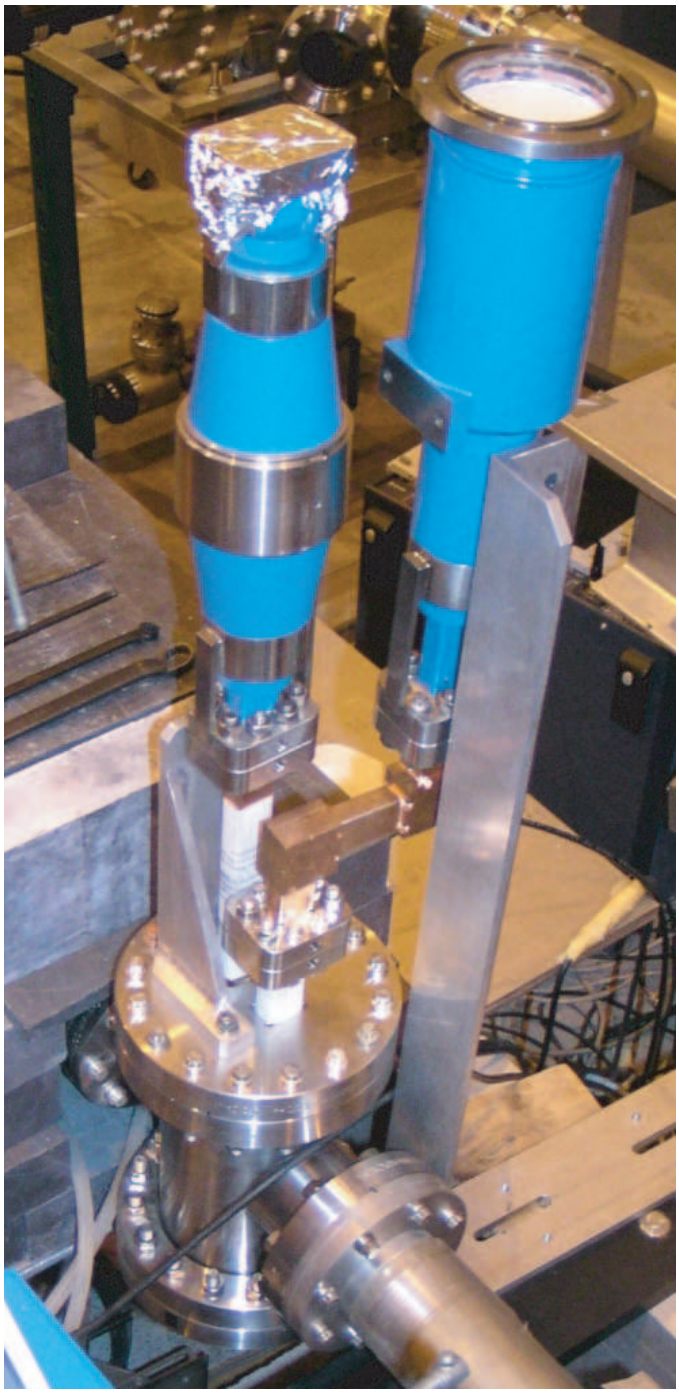

Figure 4-3: Photograph of the PBG accelerator structure vacuum vessel with attached vacuum windows on input and output ports.

double balanced mixer. Wavemeters and waveguide filters were also used to verify the observed frequency content of the wakefields.

4.4 Wakefield Simulations using *ANALYST*

Calculations of wakefields generated by a train of 17.14 GHz bunches transiting the six cell PBG accelerator structure were carried out using the *ANALYST* parallel finite element software package developed by Simulation Technology & Applied Research (STAAR) [52, 53]. For this work the time domain field modeling component of *ANALYST* (called *TD3P*) was used. It uses a high order adaptive finite element method with an implicit time step to accurately compute time domain fields on unstructured tetrahedral meshes of widely varying element size. *TD3P* was used to simulate a train of Gaussian charge bunches traveling at the speed of light along the axis of the PBG structure. The bunch spacing was chosen to be 17.49 mm, giving a 17.14 GHz period corresponding to the spacing used in the experiments. The bunch length was a factor of 10 larger than that used in the experiment in order to minimize meshing requirements and numerical noise in the solution.

The wake calculations were performed with field monitors at both the structure input and output ports, using a length of simulated waveguide to temporally isolate waveguide terminations so that the resulting time domain signals correspond to matched terminations. Fourier transform results are given in Figure 4-4. Power is excited coherently at integer multiples of the bunch repetition frequency, which is equal to f_{rf}, 17.14 GHz; peaks are observed in the spectrum near 17.14, 34.28, 51.42, 68.56, and 85.7 GHz.

The electric field Fourier transform can be used to obtain the ratios of power predicted at different frequencies. The field results are multiplied by the ratio of the Fourier transforms at the specified frequency of the bunch train lengths, in order to extrapolate the results from 10 ps simulations to the experimental Gaussian bunch length of 1 ps. The field numbers are then squared to obtain power figures, and ratios of predicted power are obtained. Observed at the output port, the ratio of 17.14 GHz

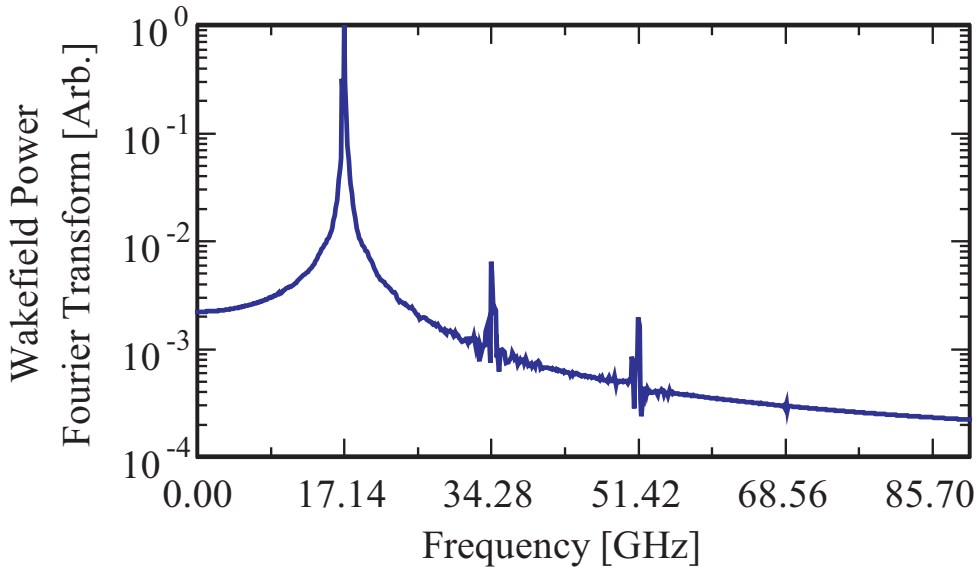

Figure 4-4: Fourier transform of beam induced wakefield electric field versus frequency, as calculated using *ANALYST* for a 10 ps bunch length.

power to 34.28 GHz power is 620. The absolute power level at 17.14 GHz can be obtained by integrating the field data over the waveguide cross-section, predicting 1.5 kW. Combining these figures, 2.4 W of power is expected at 34.28 GHz.

4.5 Experimental Results

Radiation is expected to scale quadratically with bunch charge, as shown in Equation 3.3. Wakefield scaling with current was observed as the average current was varied from 20–300 mA, corresponding to a bunch charge in the range of 1–18 pC. Wakefield measurements were made in a variety of configurations as functions of beam position and current; Table 4.2 shows a sampling of the detector configurations and power measurements, for an average beam current of 100 mA. Table 4.3 presents theory and experiment comparison for both the traveling wave theory of Section 2.3 and the wakefield simulations made using *ANALYST*.

Excellent agreement has been observed between measurements made on the output port with a matched input port, and the corresponding predictions from the traveling wave theory of Section 2.3; Figure 4-5 displays absolute power measurements and the

Frequency	Location	Power Measured
17 GHz	Port	1.46 kW
	Chamber	21 mW
34 GHz	Port	240 mW
	Chamber	240 mW

Table 4.2: Power measurement summary. Frequency of observed wakefields, location of detector, fully calibrated power level detected for 100 mA average beam current.

	Experiment [Watts]	TW Theory [Watts]	*ANALYST* [Watts]
17 GHz	1.46×10^3	1.54×10^3	1.5×10^3
34 GHz	0.24	0.0025	2.4

Table 4.3: Summary of power measurements of output port diode: frequency of observed wakefields, fully calibrated power level detected for 100 mA average beam current, and theory predictions.

theory prediction. Comparable agreement is seen with the wakefield simulations made using *ANALYST*.

Results for the Ka-band diode detector observing on the output coupler port are shown in Figure 4-6. Good agreement is obtained with a quadratic fit, with error arising from both the statistical diode signal variation and shot to shot current fluctuation. The traveling wave theory prediction for the 34 GHz power is two orders of magnitude low, and the *ANALYST* prediction is an order of magnitude high. The traveling wave theory is rather unreliable, given the high insertion loss for the 34 GHz mode. The wakefield simulations demonstrate a large amount of sampling variation over the waveguide cross-section. This numerical noise may be at fault for the large discrepancy between theory and experiment. The experimental systematic error at 34 GHz is also large. Calibration of the detectors is precise, and the overall calibration of the windows and coupler losses is also precise to ~ 1 dB. The coupling of the 34 GHz waveguide mode to the diode detector has the same possible variation as that observed in the simulations; unknown coupling of the waveguide mode to the diode could result in large error.

Wakefield measurements were also made as a function of the beam displacement from the axis. The 1.3 mm beam size, and 3.5 mm input collimator diameter gave

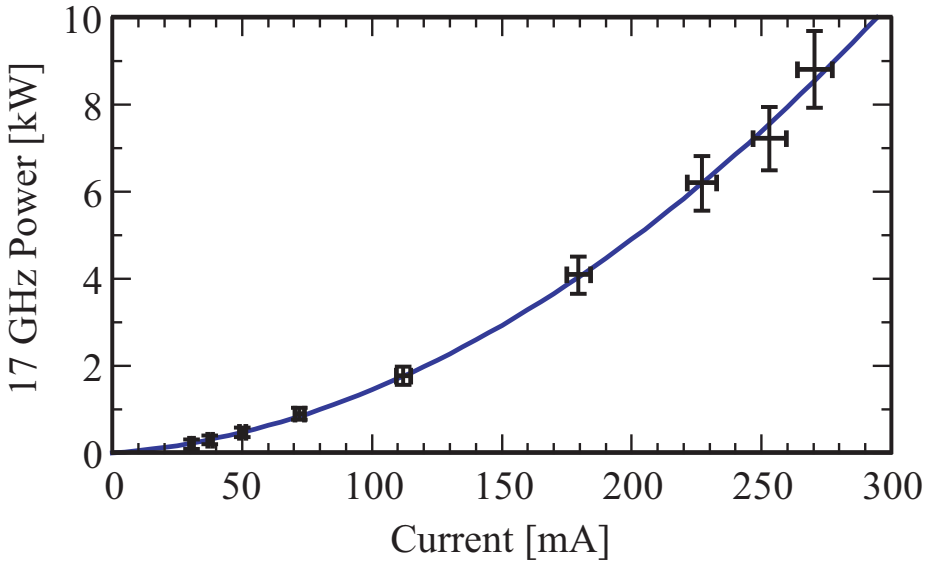

Figure 4-5: Power observed on output port with matched input port, at 17 GHz, versus current. Traveling wave theory expression from Section 2.3 shown in blue with data given as black bars. Current error measured as shot to shot variation; power error calculated as a combination of statistical variation, calibration systematic errors, and beam current error.

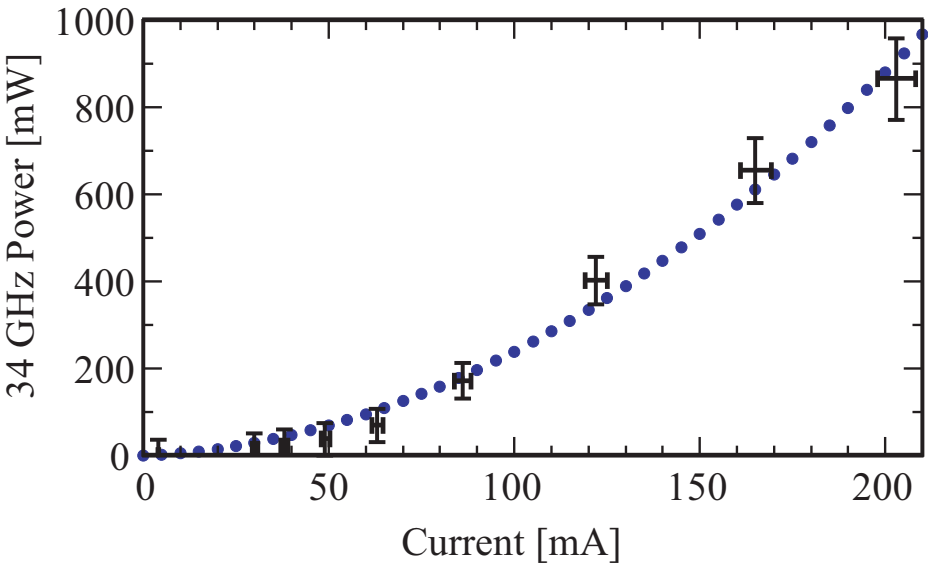

Figure 4-6: Power observed on output port with matched input port, at 34 GHz, versus current. Quadratic fit (motivated by Equation 3.3) to data shown in blue dotted line with data given as black bars.

Frequency	f_{rf} multiple
17.14	1
34.28	2
51.42	3
68.56	4
85.7	5

Table 4.4: Heterodyne receiver observations in GHz, and corresponding integer multiple of f_{rf}, 17.14 GHz.

a reasonable range of position variation. Results proved to be entirely attributable to beam current loss as the beam was intercepted by the input collimator. Current transmitted through the structure varied as would be expected when a 1.3 mm Gaussian profile is passed through a 3.5 mm aperture. After normalizing for beam current variations, the results of observations made with the Ku-band diode were unchanged as a function of beam offset. As expected, the loss factor for the fundamental does not vary with offset position. Observations in the Ka-band similarly show only dependence on the total current through the structure, and little variation with beam offset alone.

Heterodyne frequency measurements were made, and peaks were only observed at integer multiples of the linac rf frequency, 17.14 GHz. A summary of observed frequencies is given in Table 4.4. No clear signal was observed of the dipole HOMs of the PBG structure, such as the 23 GHz mode of Figure 3-2. The heterodyne detector has very high sensitivity to narrow band power, but cannot measure absolute scale power. The power detected at frequencies above 34.28 GHz with the heterodyne system was not observable with diode detectors. HOMs were only observed at multiples of f_{rf}.

Wavemeters were used across K-band to look for signs of other HOMs. Modes were observed in agreement with heterodyne measurements; integer harmonics of f_{rf} were observed, no other HOMs were. Waveguide cutoff frequencies were exploited to filter unwanted 17 GHz wakefields from power measurements in other bands, or near other frequencies, when signals of HOMs were being sought. An adjustable narrow band pass filter was tuned to 34 GHz, with flat transmission within $\sim$ 1 GHz, and

used to verify that all power detected in the 26–40 GHz band was in fact at 34.28 GHz, or twice f_{rf}. No sign of any HOMs not at multiples of f_{rf} was seen. The reduction on Ka-band power seen when using the waveguide filter gives an estimate of out of filter band power of 0.08 ± 0.10 mW at 100 mA average beam current.

4.6 Discussion

Excellent agreement is seen between experimental measurements and theoretical predictions for wakefield power at 17 GHz. This agreement is seen in both the traveling wave theory of Section 2.3 and the wakefield simulations using *ANALYST* of Section 4.4. HOM power predictions using the traveling wave theory are quite low, because the theory is not applicable to modes with as high insertion loss as the PBG structure HOMs. Wakefield simulation calculations using *ANALYST* predict more power in HOMs than is observed in experiments. Minor variations between the experiment and simulations may be at fault, and more precise simulations may show better agreement with experimental measurements. The more likely cause of the discrepancy is the difference between experimental measurement sampling and simulation. The simulations sample the field in the waveguide couplers across the guide cross-section. The experiment uses waveguide tapers and a limited aperture diode; these operate quite well for the fundamental mode, but power may be uncollected in other waveguide modes.

The quality factor ratios calculated in Section 3.2.4, while not directly capable of predicting power levels, provide a great deal of insight as to where the power lost by the beam can be expected. At 17 GHz a traveling wave mode is generated, and very little power is lost due to diffraction out of the PBG lattice. At 34 GHz, diffractive loss dominates, and power is expected to leak out the open outer wall of the structure. Diffractive loss is so dominant that the experimental observation of equal power levels in port and chamber measurements should not be surprising; power measured on the port is only that lost by the beam in the coupling cell directly attached to the port.

The need for well-developed wakefield damping in PBG accelerator structures has

been much demonstrated by these experimental results. Cold test measurements, as in Figure 3-6, showed dramatic HOM damping improvement by adding an external damping material. The beam induced wakefield measurements reported in this Chapter show that measurable power is being radiated into HOMs, and that if these wakes are not damped they escape the structure. Damping these HOMs will prevent the power from escaping the immediate area of the structure only to be reflected back and act incoherently on the beam. The dominance of diffractive loss makes damping HOMs in PBG structures relatively straightforward, and a promising direction for future work, along the lines discussed in the literature [45, 46].

Chapter 5

Experimental Design of an X-Band PBG Structure

5.1 Introduction

Previous work on PBG structures has generated a demonstration of acceleration, a proof of principle experiment [27, 28, 29]. To mature the concept of PBG acceleration, operating under realistic collider parameters is necessary; this includes both realistic design properties and operational levels. The iris aperture, which controls the structure group velocity must be comparable to that considered in collider concepts, such as the NLC operating range of $a/\lambda \sim 0.2$ (a/λ is an iris aperture radius to wavelength ratio) [54]. Breakdown and pulsed heating require contouring of sharp edges, to minimize electric and magnetic field enhancement at discontinuities [55].

High gradient structures are exposed to high power rf, and their performance in this regime is of vital pertinence in determining collider suitability. To accomplish testing on a variety of geometries, components for single cell structure testing have been developed [56]. These components allow single cell standing wave cavities to be tested quickly in order to compare their performance at high rf power, and will be discussed further in Section 5.2. This test stand makes possible the design and testing of a realistic X-band PBG accelerator structure.

The structure design was accomplished using the commercial code *HFSS* [44].

5.1.1 Six Cell PBG Structure

The six cell traveling wave structure was deficient for practical use in that the structure had a very low design group velocity of $v_g = 0.013\,c$, corresponding to an aperture to wavelength ratio of $a/\lambda = 0.123$. In the first demonstration, this low group velocity meant demonstrating acceleration was more easily accomplished, but it makes the experimental achievement inapplicable to a linear collider design. The six cell structure was formed by brazing individually electroformed cells [27]. The structure aperture was formed by drilling a hole through the electroformed cells, resulting in a sharp edged square profile iris aperture [57]. Any rounding will be an improvement over a square aperture; optimized iris profiles have been developed resulting in an elliptic aperture [58, 59].

5.2 SLAC Components

The main components that make single cell testing possible are demountable couplers that allow structures to be manufactured simply, quickly set up for high power testing, and then replaced with subsequent structures [55]. The launcher, or mode converter, couples power from standard WR-90 waveguide into the TM_{01} mode of perpendicular 0.900 inch diameter circular waveguide. The design of this launcher provides very low fields in the launcher, so that breakdown events will occur in the structure, and not upstream in the coupler; for 50 MW input, the peak surface electric field is 35 MV/m, and the peak surface magnetic field is 100 kA/m. The launcher provides a broad match, so that reflections will be minimized and good coupling into structures can be achieved. The mode launcher is shown in Figure 5-1.

The use of a mode converter for all single cell tests requires that the oversized waveguide TM_{01} mode be matched using cells specifically designed for this purpose. The fields in the matching cells need to be balanced so that the field maximum is in the test cell, so that breakdown events occur there, and not in the coupler cells. This will dictate the overall form of the single cell breakdown structures.

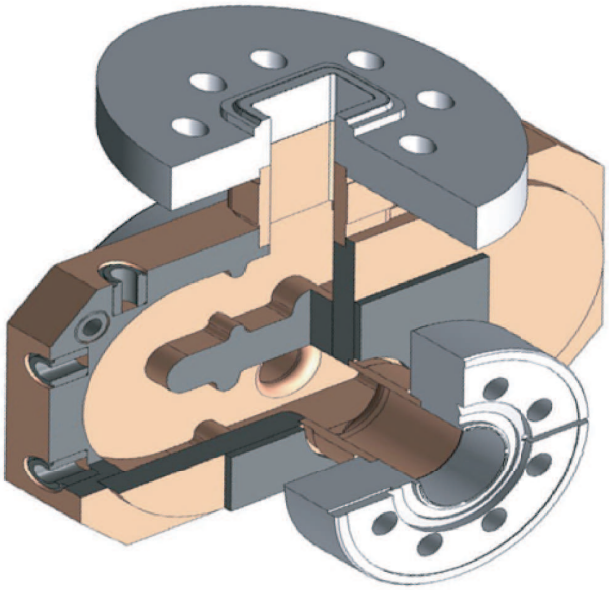

Figure 5-1: TM_{01} mode launcher for coupling into single cell structures.

5.3 X-Band Breakdown Structure Design

To test PBG structures at realistic operating conditions, videlicet high power, high rep rate, reasonable and contoured aperture, a single cell standing wave structure has been designed for testing at SLAC. Indexed as, 1C-SW-A5.65-T4.6-Cu-PBG, this is the first PBG structure to be tested to its limits, as the previous first high power test was limited by available power.

5.3.1 Baseline Pillbox Structure

The general structure form is shown in Figure 5-2. To match into the structure a first pillbox cell is used, with an iris radius optimized to minimize reflection, and maximize coupling into the structure. The central cell is the actual test cell, where the field strength will be maximal; to insure this, a third pillbox cell is used to balance the overall mode structure such that the field in either matching cell is half that of the test cell. The parameters in Table 5.1 detail the design numbers for the SLAC baseline

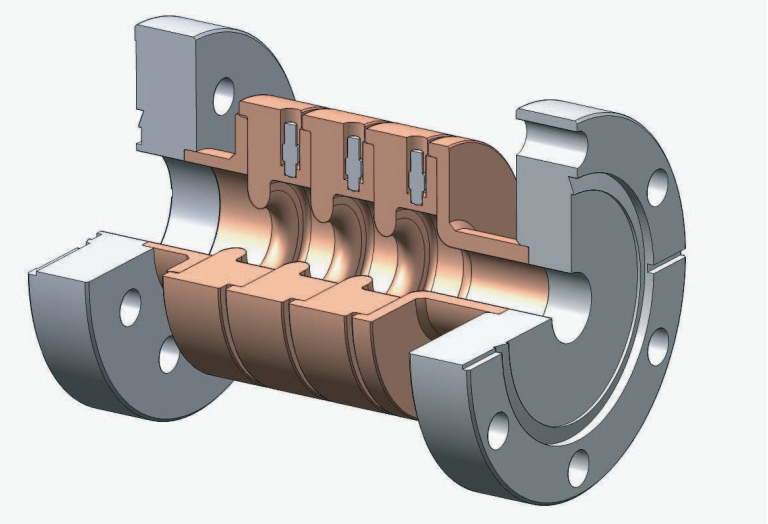

Figure 5-2: Drawing of SLAC baseline pillbox structure, 1C-SW-A5.65-T4.6-Cu.

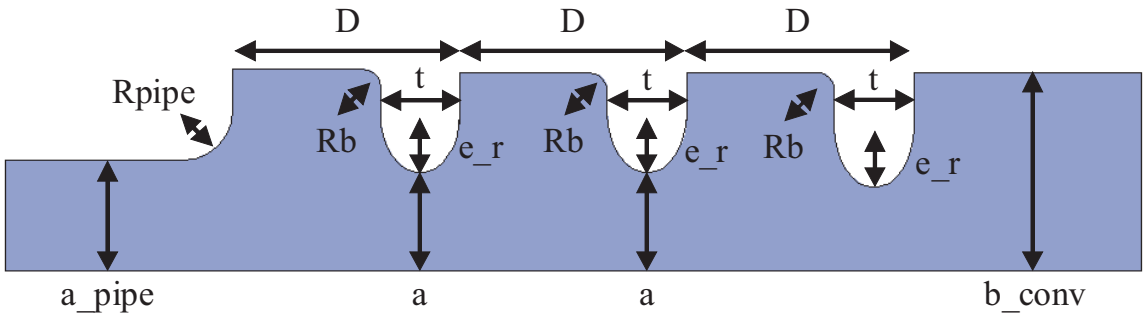

Figure 5-3: Schematic for parameters of SLAC baseline pillbox structure. Parameters shown in Table 5.1.

pillbox structure, 1C-SW-A5.65-T4.6-Cu, shown schematically in Figure 5-3 [58, 59]. Four of this structure have been designed and tested, and provide a sizeable dataset for the comparison of structure geometry modifications, such as the use of a PBG cell as the central test cell.

5.3.2 Assumptions

The PBG breakdown structure will take the general form shown in Figure 5-4: two pillbox matching cells, and a single PBG cell. The pillbox cells will be similar to those of the baseline pillbox structure, with only the coupling aperture radius, and the two cell radii used to tune the coupling, frequency, and field structure. The input

SLAC Parameters	
b_end	11.6206 mm
b_cll	11.4023 mm
b_cpl	11.4428 mm
a_cpl	4.8075 mm
Rpipe	3 mm
Rb	1 mm
t	4.6 mm
e_r	3.4 mm
D	13.116 mm
a	5.6475 mm
a_pipe	6.35 mm
b_conv	11.43 mm

Table 5.1: Parameters for SLAC baseline pillbox structure, values for schematic in Figure 5-3.

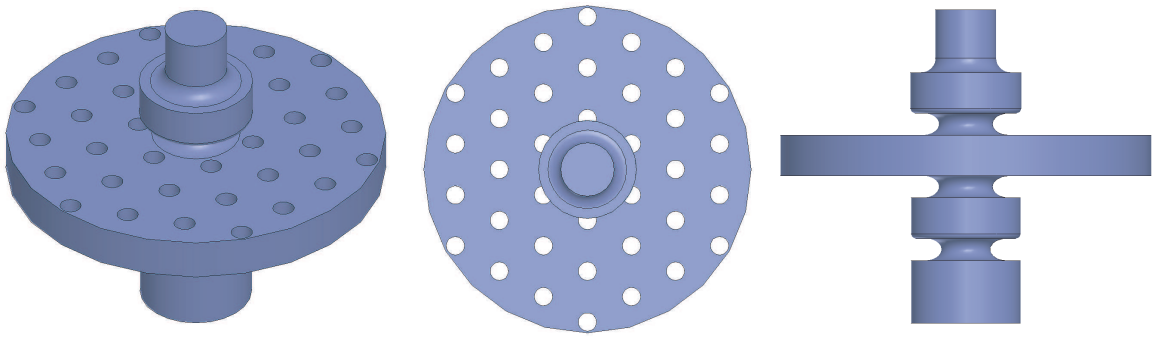

Figure 5-4: General geometry views of the PBG structure.

waveguide will be matched to that of the mode launchers: perpendicular 0.900 inch diameter circular waveguide. The end cell will taper into a cutoff section of perpendicular 0.500 inch diameter circular waveguide, to connect with dark current monitoring or viewing windows. The iris geometry is chosen to be identical to that of the four SLAC pillbox baseline structures, to constrain differences in observed performance as much as possible. The fixed parameters for the structure are shown in Table 5.2 for the schematic of Figure 5-5 B. Tuning parameters are shown in Figure 5-5 A with final design values in Table 5.3.

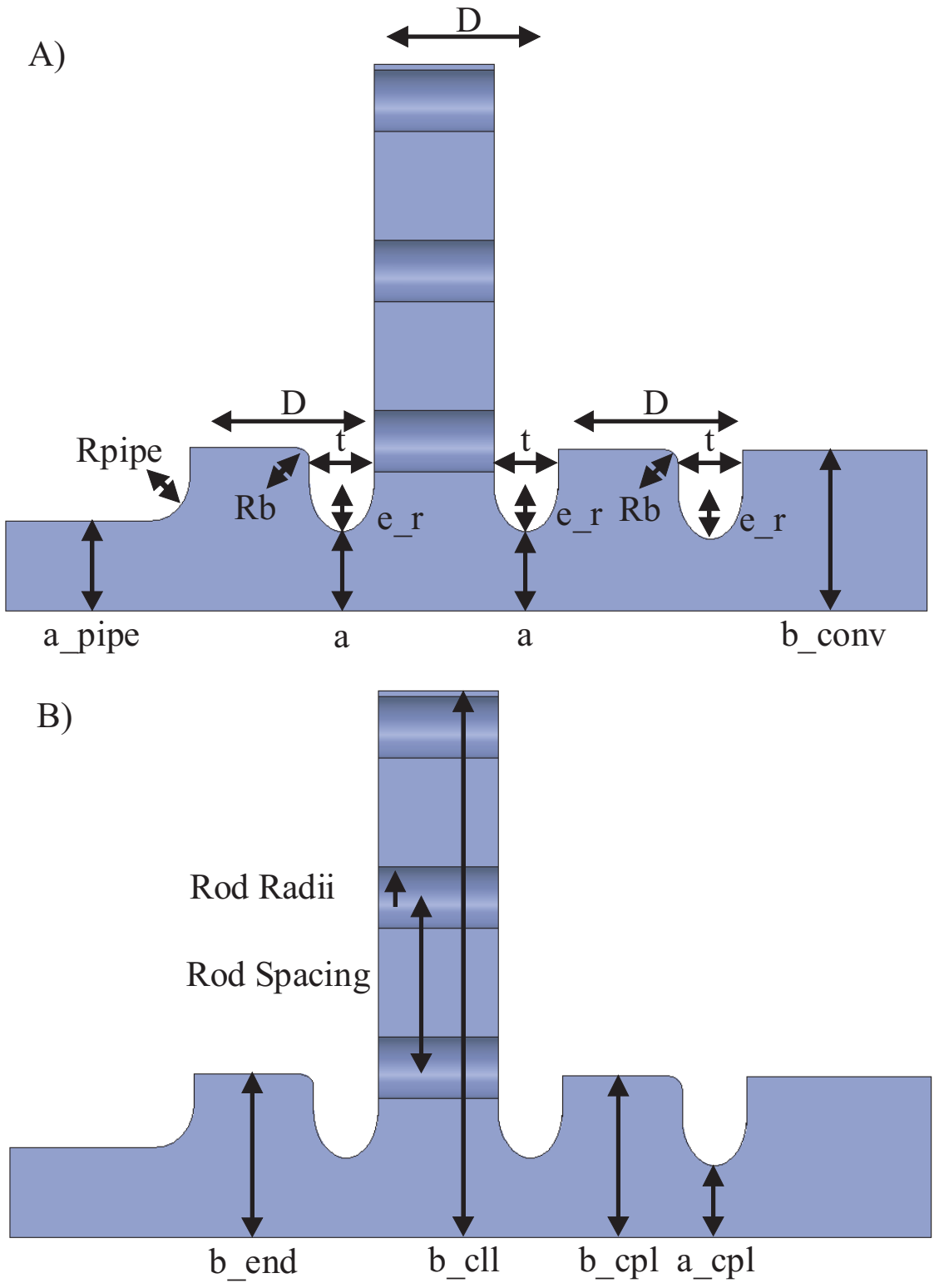

Figure 5-5: Schematics for parameters of PBG structure; A) schematizes fixed parameters for the structure, B) schematizes free tuning parameters, as shown in Table 5.2 and 5.3, respectively.

Fixed Parameters	
Rpipe	3 mm
Rb	1 mm
t	4.6 mm
e_r	3.4 mm
D	13.116 mm
a	5.6475 mm
a_pipe	6.35 mm
b_conv	11.43 mm

Table 5.2: Fixed parameters for PBG structure, values for schematics in Figure 5-5 A.

5.3.3 Requirements

The structure tests are to be performed at X-band, at 11.424 GHz, requiring the design mode to be within$\sim$ 100 MHz of this klystron operating frequency. The mode itself needs to have half the electric field magnitude on axis in the center of each matching cell as in the central test cell. Coupling into the entire structure is accomplished via a TM_{01} mode from the 0.900 inch waveguide, and should be maximized. Slight overcoupling is preferred to precise critical coupling, because the single cell structures that have been fabricated in the past have come out slightly undercoupled [59].

5.3.4 Design Algorithm

The design is accomplished iteratively, by changing the tuning parameters to meet the design requirements, and then assessing the impact the tuning parameter variation has had on the other requirements. This process is shown schematically in Figure 5-6.

The PBG cell is characterized by three parameters: the overall cell radius, b_cll, and the rod radii and spacing. In fact, the cavity properties are insensitive to b_cll, and so a relatively small value is chosen such that the rods are all enclosed. The remaining two parameters determine both the band structure and frequency. The frequency is fixed by the requirement of close comparison to the SLAC baseline pillbox structure. This leaves one free parameter, which determines the specific photonic band gap lattice structure, as in Figure 2-8. Again a triangular lattice is chosen, with a single rod defect. Structure design was done for varying PBG a/b ratios: from

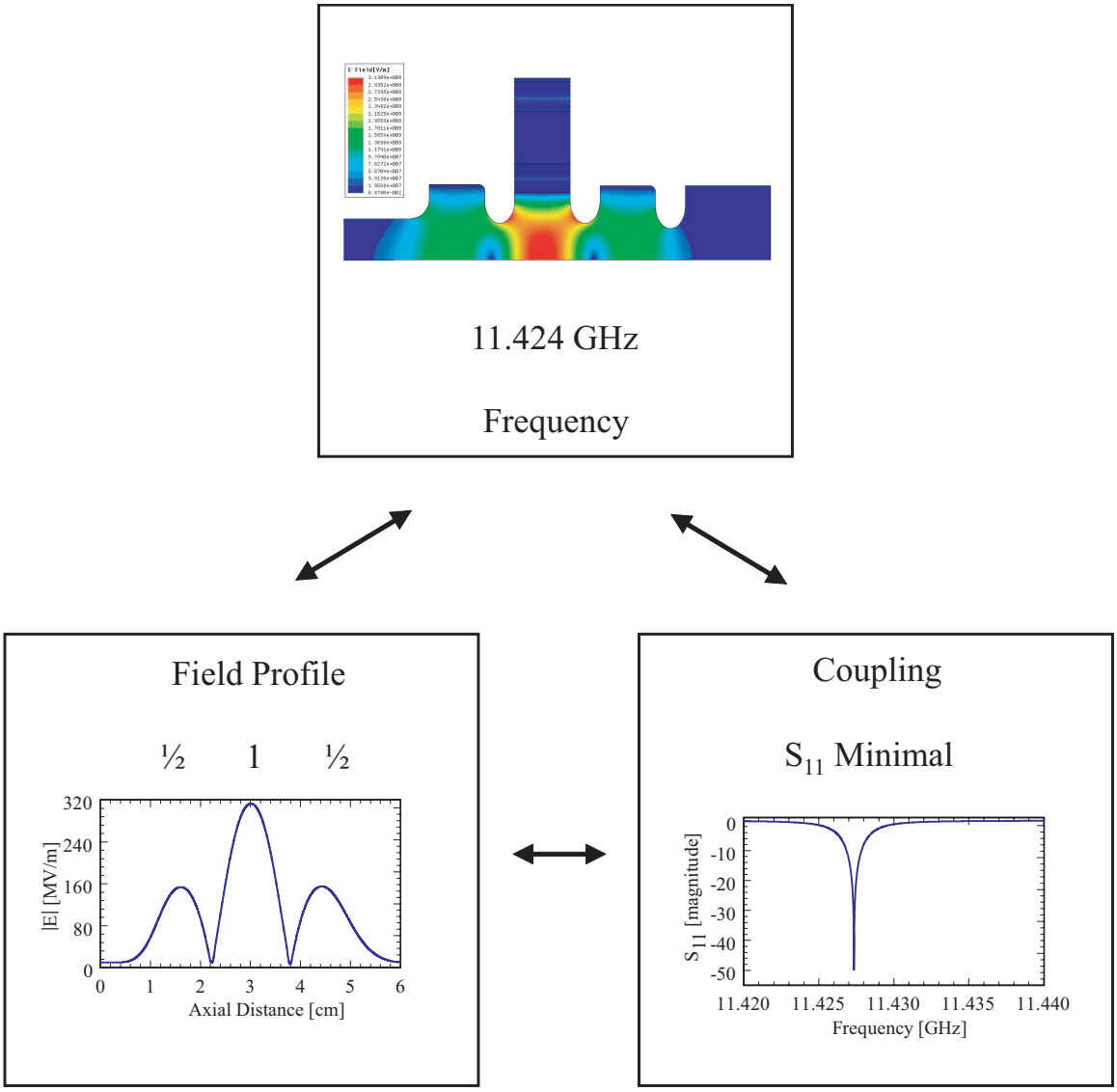

Figure 5-6: Design algorithm schematic.

that used in the six cell structure, $a/b = 0.15$, up to the opening of the next gap, $a/b = 0.20$. Qualitatively the HOM field patterns begin to be localized in the defect as a/b increases. Rods larger than those used in the six cell structure were desirable to reduce fabrication difficulty and provide less intense heating on the rods. An a/b ratio of 0.18 provided an aggressive improvement in rod size without clearly increasing HOM confinement. More detailed analysis of PBG cell design is discussed in Section 5.4, in regard to an improved PBG breakdown structure design.

The four tuning parameters are then the actual unscaled rod spacing or rod radius (only one parameter is free, the other is constrained by radius/spacing = 0.18), the coupling cell radius, the end cell radius, and the coupling iris radius. The coupling iris strongly affects the cavity coupling, and weakly affects the field structure and frequency. The relative cell radii affects the field distribution. The cavity radii can be scaled to alter the frequency. Each step in Figure 5-6 has a dominant set of tuning parameters, but is also weakly coupled to the rest, and so final design is achieved by iteration of individual optimizations.

5.3.5 Design Results

The results of the design process are indicated by the final tuning parameter values shown in Table 5.3. Design properties and field results are from final *HFSS* driven mode solutions for an input power of 10 MW. A 30° section of the actual full structure was used, corresponding to the irreducible geometric section of the triangular PBG lattice, all other components are cylindrically symmetric and insensitive to symmetry boundary conditions.

The normalized axial electric field is shown in Figure 5-7: half field is seen in both matching cells, with peak field on axis in the PBG cell. Some field strength can be seen entering the cavity from the left. Increasing a matching cell radius, holding other parameters constant, results in a small increase in the field strength in that cell.

The structure coupling is shown in Figure 5-8 and Figure 5-9. Fast frequency sweeps were useable in these *HFSS* simulations because the eigenmodes of the structure were well separated, and only a single mode was being excited in the frequency

Tuning Parameters	
b_end	11.627 mm
b_cll	38.87 mm
b_cpl	11.471 mm
a_cpl	5.132 mm
Rod Radii	2.176 mm
Rod Spacing	12.087 mm

Table 5.3: Tuning parameters for PBG structure. Final design values for schematics in Figure 5-5 B.

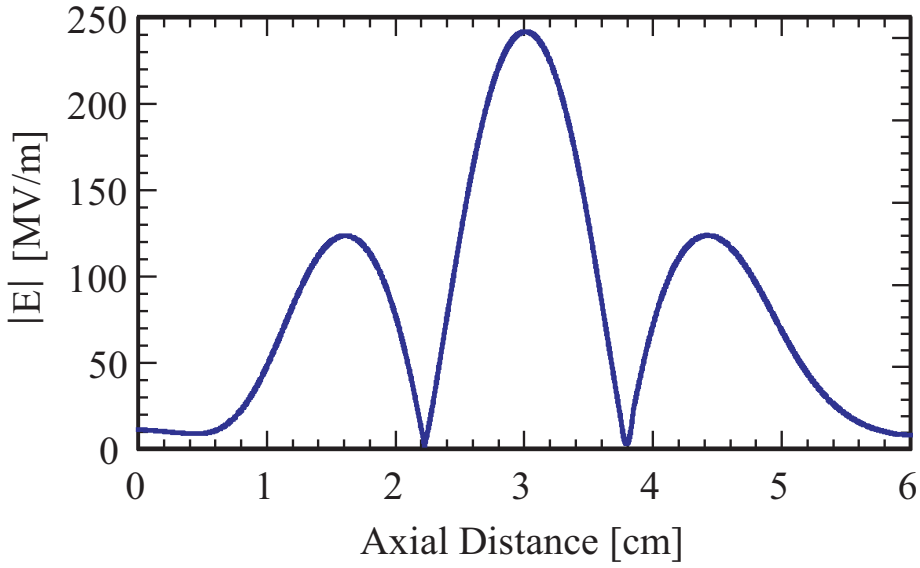

Figure 5-7: Electric field relative magnitude on axis of PBG structure. Power is coupled in from the left; half field is seen in each coupling cell, relative to the central PBG cell.

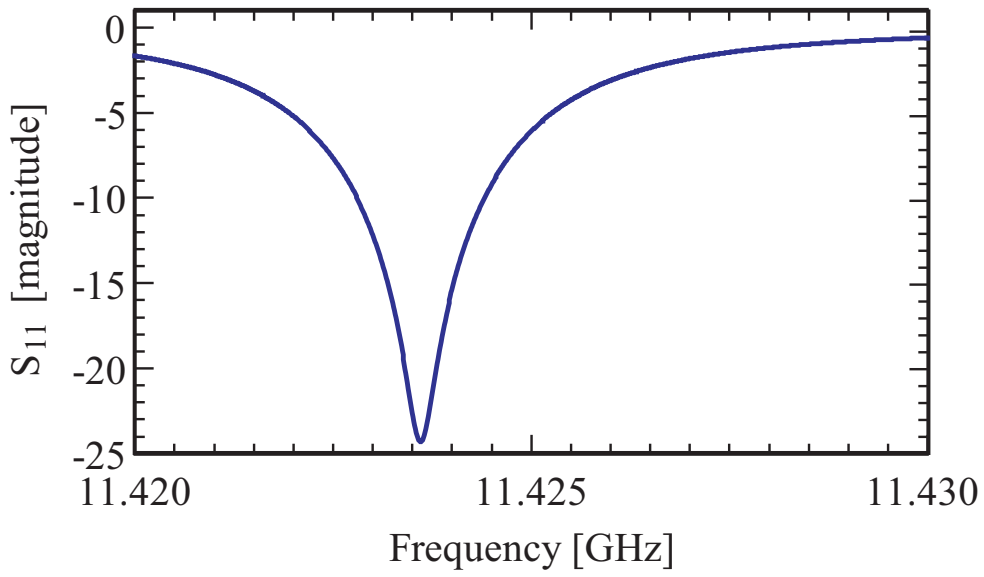

Figure 5-8: S_{11} coupling as a function of frequency for PBG structure.

range of interest. Figure 5-8 shows S_{11} as a function of frequency, showing a good match of -24.3 dB at 11.4236 GHz. The coupling Smith chart is shown in Figure 5-9, demonstrating a Q-circle of slightly larger than unit radius, indicating slight overcoupling, as preferred.

Field plots are shown in Figure 5-10 for the electric and magnetic fields as viewed along a radial cut of the structure through the nearest rod, for 10 MW input power. The electric field is strongest in the central cell, with peaks on axis and on the structure irises. The magnetic field is strongly peaked on the inner edge of the first row of rods. Top views of the electric and magnetic fields are shown in Figure 5-11, for 10 MW input power. For comparison with the PBG structure, the SLAC pillbox structure field plots are shown in Figure 5-12.

Comparison of the fields in the two structures indicates design dictated similarities, along with some important differences. Maximum field values are observed as displayed in Table 5.4. The PBG structure is more inductive than the pillbox structure, so that for the same input power, less electric field strength is seen, and more magnetic field is observed. Decreased electric field strength will not be a problem in breakdown testing because the power requirement is relatively low, and additional power is easily accommodated. Increased magnetic field strength, however, will re-

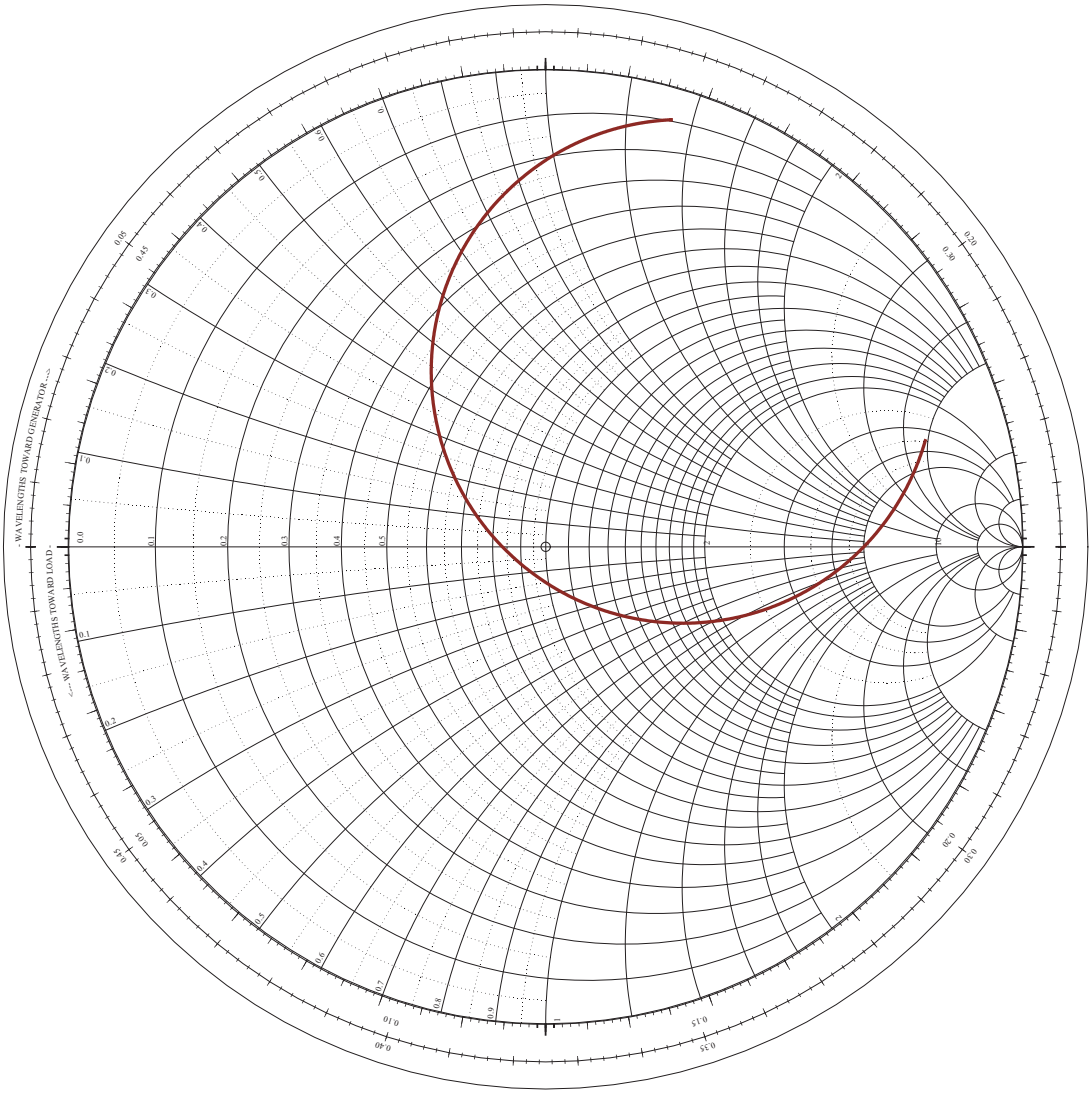

Figure 5-9: Smith chart Q-circle of coupling for PBG structure.

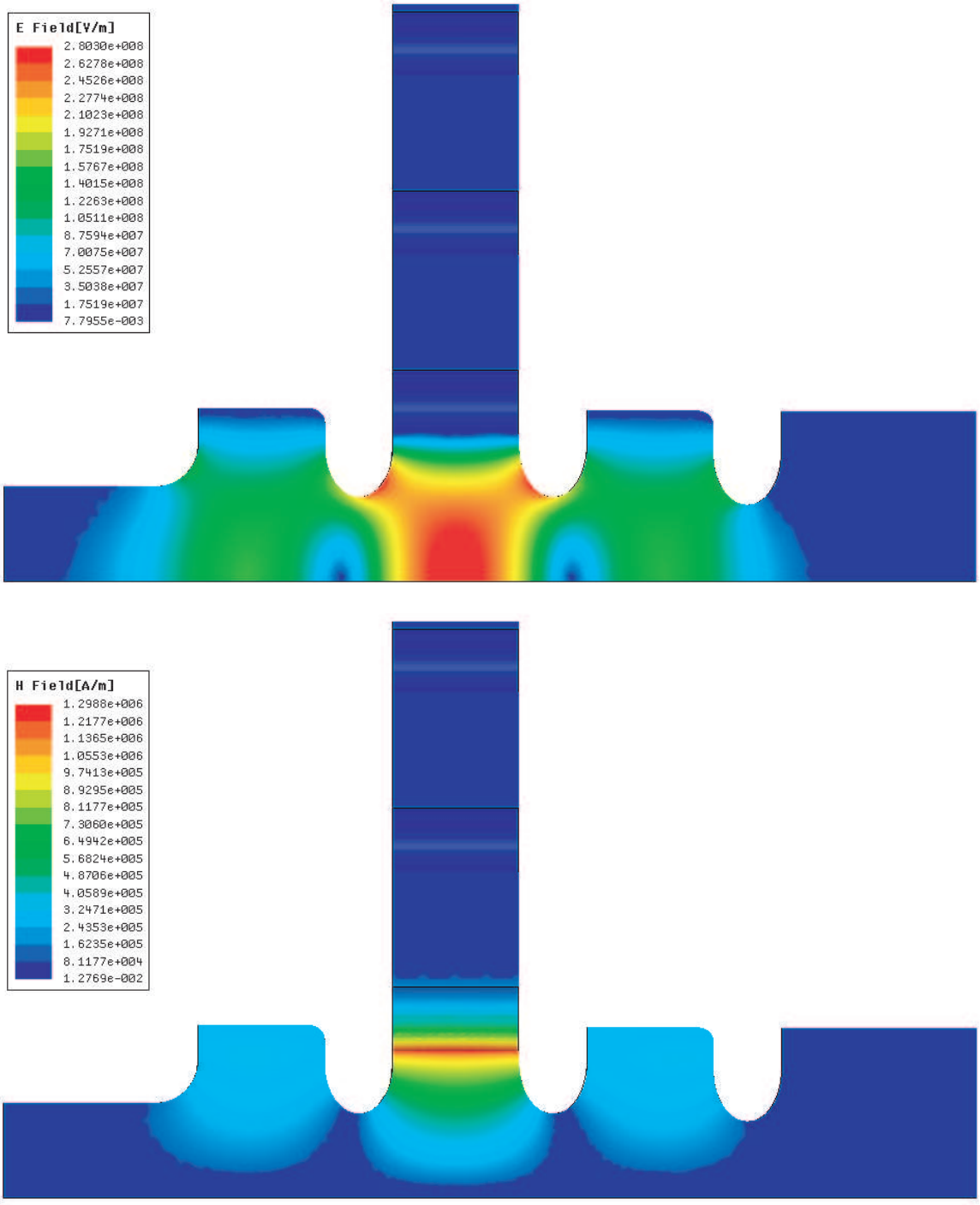

Figure 5-10: Electric and magnetic field for PBG structure. Side views.

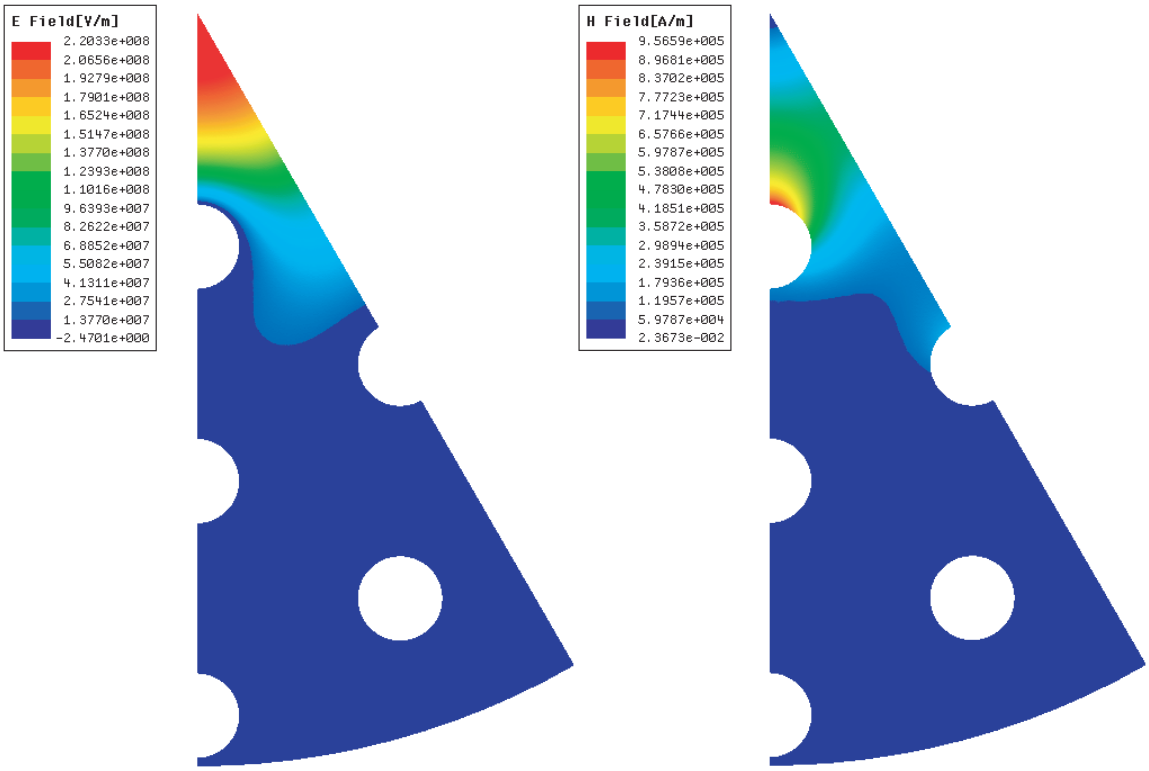

Figure 5-11: Electric and magnetic field for PBG structure. Top views.

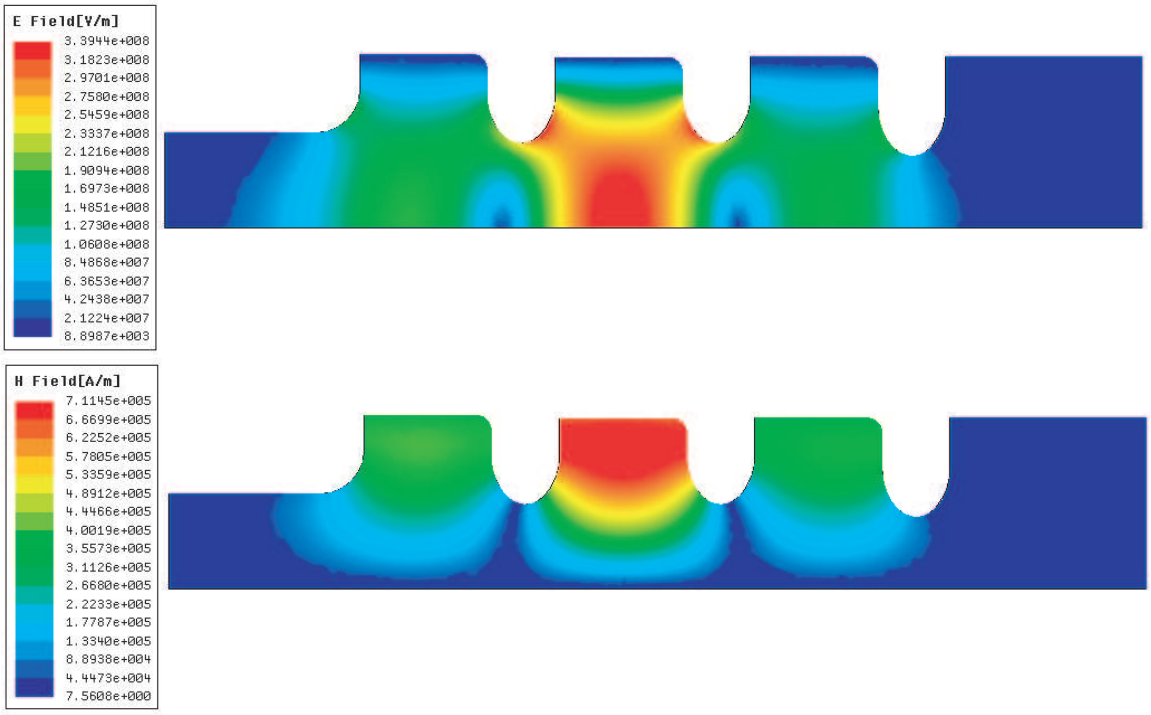

Figure 5-12: Electric and magnetic field for SLAC baseline pillbox structure.

Structure	Electric	Magnetic
PBG	280 MV/m	1300 kA/m
Pillbox	340 MV/m	710 kA/m

Table 5.4: Peak field values observed in the simulations of Figures 5-10 and 5-12.

sult in higher pulsed heating on the structure, as described by Equation 2.7. For 100 MV/m gradient and 100 ns pulse length a temperature rise of 87 K is predicted, limiting the structure to a lifetime of $\gtrsim 250 \times 10^6$ shots, according to Figure 2-4. To improve this number and pulsed heating performance, a new design is required.

5.3.6 *HFSS* Analysis Simulations

PBG Simulations

In the actual experiment, breakdown rates will be calculated and compared with structure input power levels. Breakdown rates are of interest not with regard to power levels, but with respect to the field properties of the accelerator structures. To convert from power level to field properties, *HFSS* simulations are used with an increased focus on field convergence. Driven mode solutions allow power levels to be calibrated with surface fields; a single calibration point suffices as the field scales as the square root of the power. The simulation for this calibration is run with as detailed a mesh as possible. A final mesh with $\sim$ 700,000 tetrahedra was used, and is shown in Figure 5-13.

The primary field quantity of interest is the accelerating gradient. This is calculated for a single cell in an eigenmode *HFSS* simulation with 180° phased iris boundary conditions, in order to model an extended accelerator structure from the simulation results for a single cell. The mesh for this simulation required 300,000 tetrahedra and 1° surface approximation, and is shown in Figure 5-14.

The accelerating gradient is calculated using the *HFSS* field calculator and Equation 5.1. The gradient is the electric field experienced by a particle traveling on axis at the speed of light. Field convergence is a serious concern for such a critical field parameter, and this was insured by steadily finer mesh operations until the result of

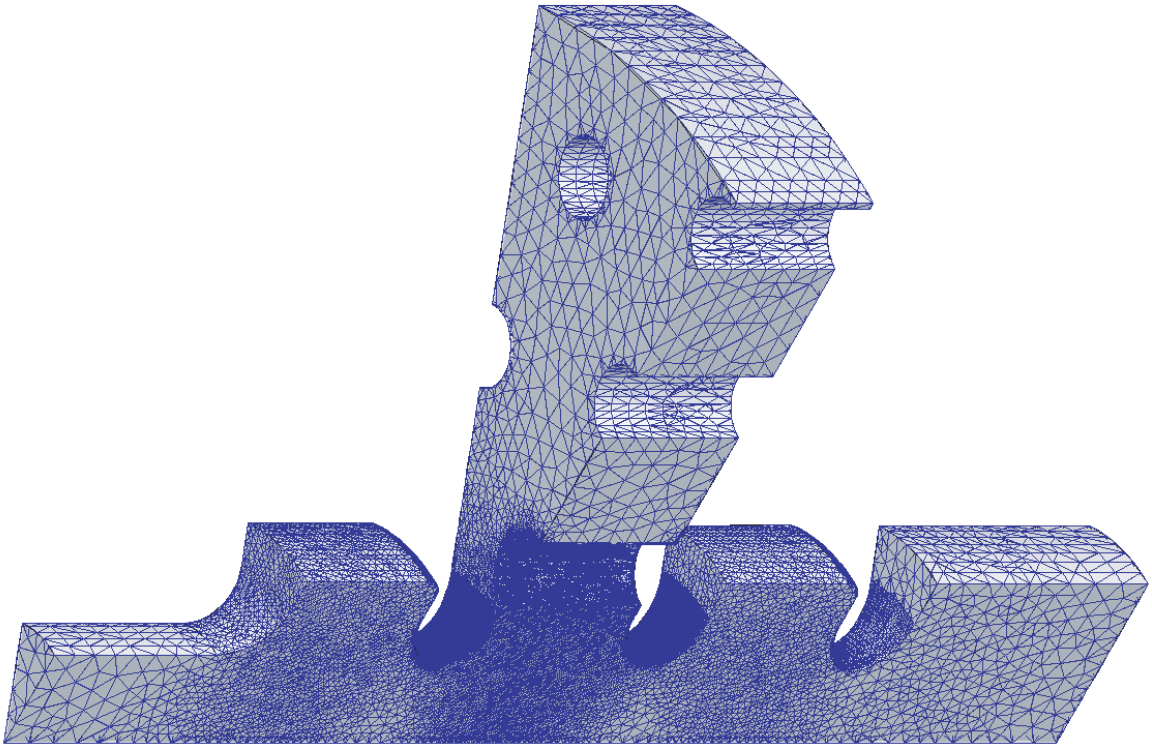

Figure 5-13: 700,000 tetrahedra mesh for power calibration driven mode *HFSS* simulations.

Figure 5-14. The suitability of this mesh was confirmed by calculating the gradient on a large number of slightly off-axis lines. The gradient should be exactly constant; any fluctuations are the result of field sampling.

$$E_{gradient} = \sqrt{\left|\int E_{CM} \sin\frac{2\pi\omega z}{c}\right|^2 + \left|\int E_{CM} \cos\frac{2\pi\omega z}{c}\right|^2} \tag{5.1}$$

The peak surface fields, both electric and magnetic, are also of interest for breakdown statistics. These are calculated using the eigenmode *HFSS* simulations and determining the maximum field value on the surface. Minor variations in the terahedral meshing result in very large fluctuations in the *HFSS* calculated maximum surface fields. The field value along multiple lines must be evaluated, as with the calculation of the gradient. This can be done more efficiently by examining the complex magnitude surface field plots visually. The field plot maximum and minimum are adjusted until the maximum is observed in a continuous fashion on the surface. Final plots for this calculation are shown in Figure 5-15 for the maximum surface electric

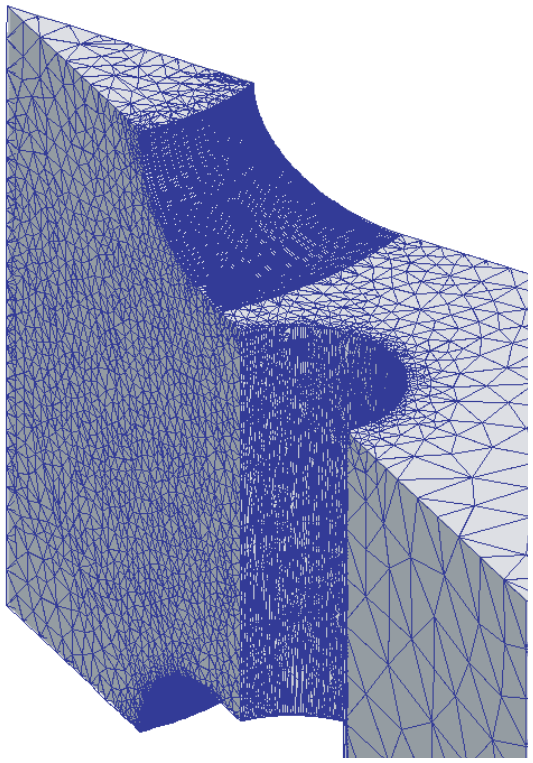

Figure 5-14: 300,000 tetrahedra mesh for field calibration eigenmode *HFSS* simulations.

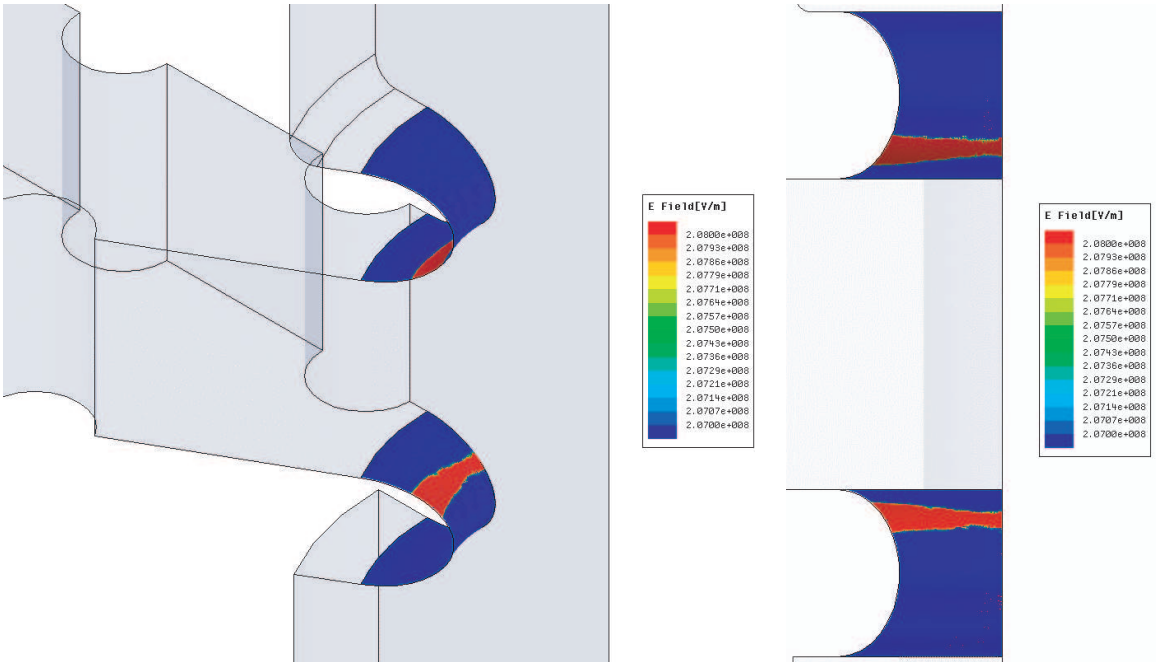

Figure 5-15: Surface electric field maximum from field calibration eigenmode *HFSS* simulations. Contours are plotted on the iris surfaces of a 30° model of the entire structure.

Power	5.9 MW
Gradient	100 MV/m
Surface Electric Field Maximum	208 MV/m
Surface Magnetic Field Maximum	890 kA/m
Rod Surface Electric Field	14 MV/m

Table 5.5: *HFSS* simulation field calibration numbers for PBG structure.

field, which is on the iris, and in Figure 5-16 for the maximum surface magnetic field, which is on the inner rod; field plots are shown for an input power of 5.9 MW, which corresponds to an accelerating gradient of 100 MV/m.

Cross-calibration of driven and eigenmode *HFSS* simulations combine all of these field and power numbers so that the power coupled into the structure can be scaled into accelerating gradient, surface electric field, or surface magnetic field. A summary of the calibration parameters is given in Table 5.5.

The electric field on the inner rod is of interest because that is the location where both magnetic and electric field effects interact. Pulsed heating damage on the rod will provide a source for increased β sharp points, which will enhance any electric

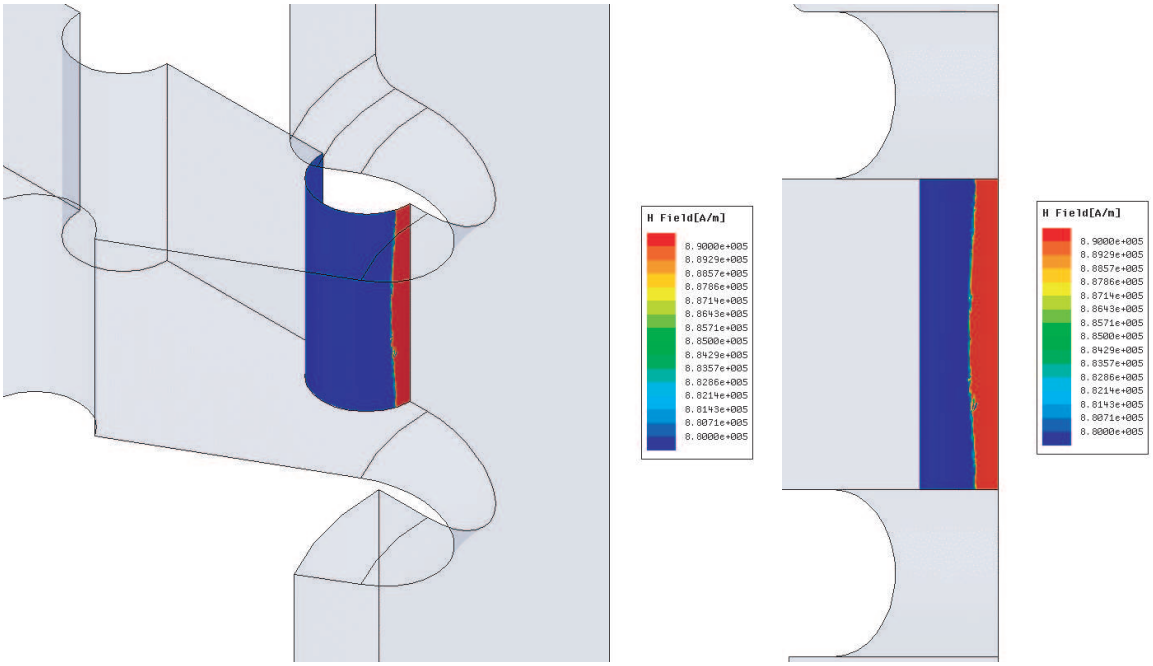

Figure 5-16: Surface magnetic field maximum from field calibration eigenmode *HFSS* simulations. Contours are plotted on the inner rod surface of a 30° model of the entire structure.

field on the rods. The field on the inner rod is shown in Figure 5-17. The field level is much lower than on the structure iris, as can be compared by the field values in Table 5.5: for 100 MV/m gradient, the surface field on the iris is 208 MV/m, and the surface field on the rod is 14 MV/m. The field plot shown in Figure 5-18 shows the same field data as Figure 5-11, but rescaled to the level of the surface field on the rod.

Pillbox Simulations

This simulation process was repeated for the SLAC baseline pillbox structure. These simulations were more straightforward than the PBG simulations because of the cylindrical symmetry of the pillbox structure; very fine meshes were possible with less reliance on meshing operations and sensitivity to field convergence. The calibration results are shown in Table 5.6.

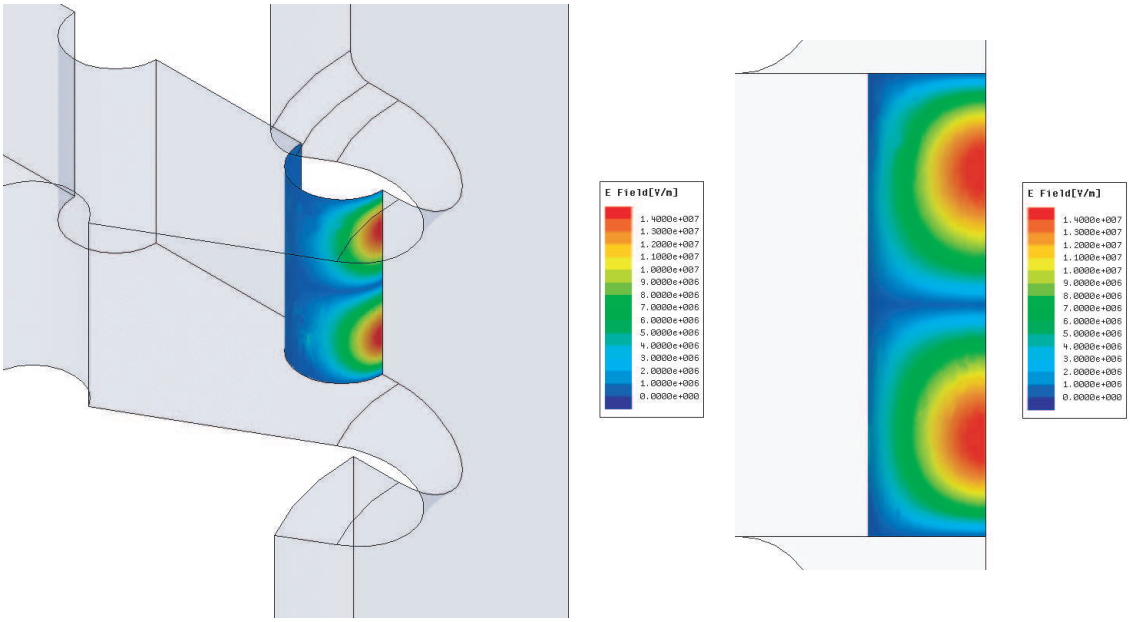

Figure 5-17: Surface electric field on inner rod from field calibration eigenmode *HFSS* simulations.

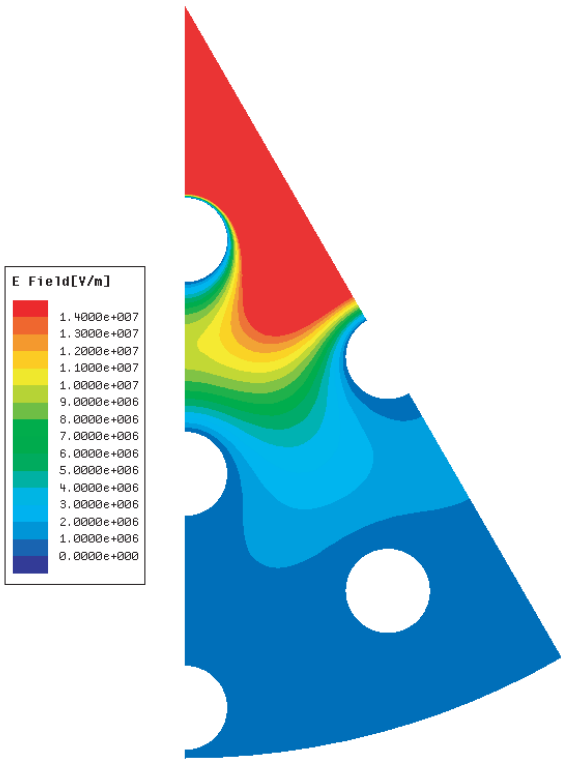

Figure 5-18: Electric field contour plot from field calibration eigenmode *HFSS* simulations. Contours are plotted on the midplane of a 30° model of the entire structure.

Power	4.6 MW
Gradient	100 MV/m
Surface Electric Field Maximum	211 MV/m
Surface Magnetic Field Maximum	418 kA/m

Table 5.6: *HFSS* simulation field calibration numbers for pillbox structure.

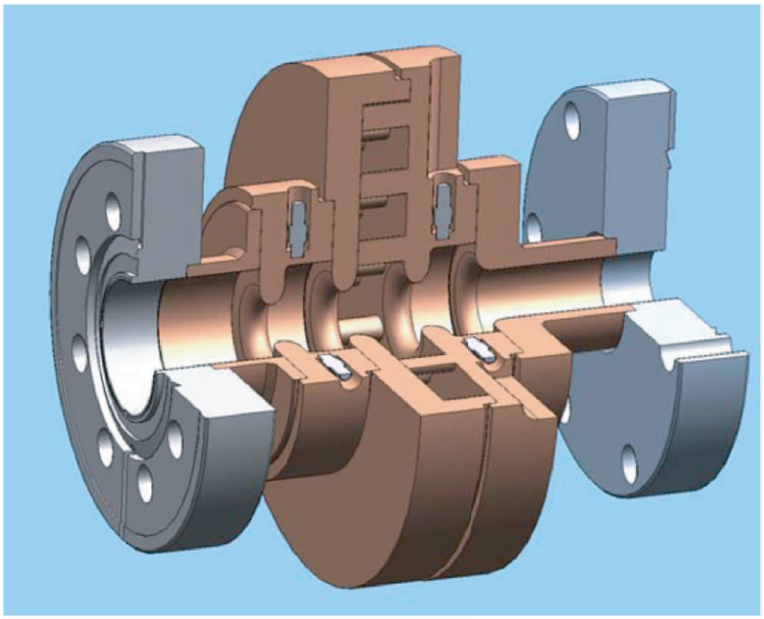

Figure 5-19: Drawing of PBG structure, 1C-SW-A5.65-T4.6-Cu-PBG.

5.3.7 Design Tolerances

For a 1 mil (25 μm) variation in the rod radii or rod spacing, a $\pm$ 25 MHz shift was seen in simulation. The rod radius and spacing sensitivity was found to be approximately 1 MHz/μm. Coupling is maintained into the structure for variations in the coupling aperture. The coupling cells, b_cpl, and b_end are mechanically tunable so that the overall frequency or field pattern observed in cold test can be changed if necessary. The final structure design is shown in Figure 5-19.

5.4 Design Improvements

In order to reduce pulsed heating on the inner row of rods, a new PBG design is required. Variations in PBG lattice geometry, as well as rod deformations are ex-

amined. The goal in changing the PBG structure design is to improve the cavity E/H ratio, as calculated in Ohms, Ω. The immediate side effect of varying cavity parameters to achieve better pulsed heating is that the cavity damping properties are altered. In order to maintain adequate HOM damping, the HOM Q and kick factor $k_\perp$ are tracked as changes are made.

Design iteration simulations rely on convergence of *HFSS* field solutions. *HFSS* itself converges solely on mode frequency, or S-parameters, and so special care must be taken to force sufficient mesh operations to insure field convergence. Limiting the length and maximum aspect ratio to 1–2 mm and 2, respectively, proved adequate. Surface deviation of curved surfaces was a more sensitive issue, requiring less than 5–10° for design sweeps.

HOM damping figures of merit are vital in insuring that improved pulsed heating performance does not result in degraded HOM damping. Longitudinal loss factors, and transverse kick factors were calculated over design variation sweeps. No variation outside the design to design variation attributed to *HFSS* field convergence was observed. HOM mode Q, on the other hand, showed large variation as the PBG design was changed. As discussed in Sections 3.2.2 and 3.2.3, both the beam to mode coupling k, and mode Q affect the strength of the HOM wakefield experienced by trailing bunches. The beam to mode coupling, k, was not observed to vary more than is attributable to *HFSS* field convergence, across all PBG design perturbations. The quantitative figure of merit for redesigned PBG HOM damping is found to be the HOM mode Q.

Both ohmic and diffractive loss combine to affect the HOM Q, so simulations must combine simulating surface losses with PML boundaries to calculate accurate changes to HOM Q as PBG parameters are varied. Two dimensional simulations are adequate for rapid solutions to numerous variations, and were used extensively to provide timely feedback on promising ideas. A large breadth of ideas were attempted, with extensive input on perturbation concepts.

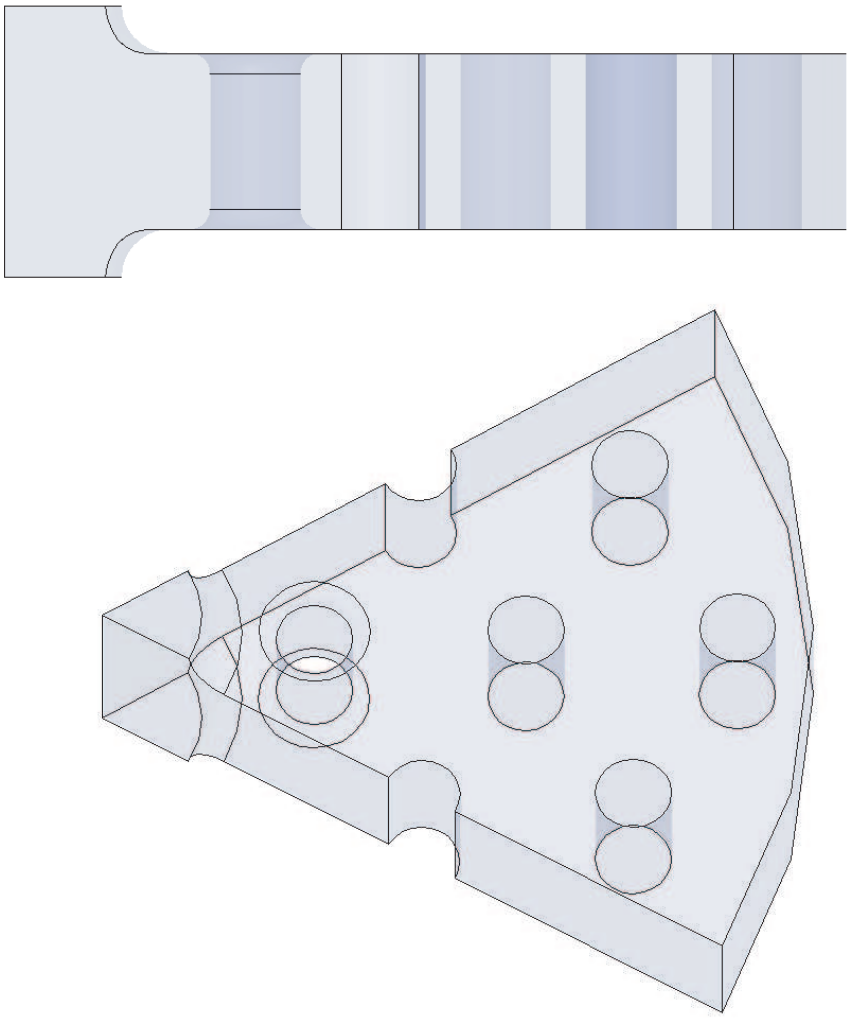

Figure 5-20: Schematic of 1 mm filleted inner rod joint. Side and perspective views.

5.4.1 Fillet

The high peak magnetic field on the inner row of rods is a result of high currents flowing along the rods. In the baseline PBG design, and most PBG structure designs, the rods abut the irised end plates of the structure cells at 90°. A reduction in this sudden change in current flow direction can be accomplished by filleting the rod joint, as shown in Figure 5-20.

Simulations were done with a range of fillet radii, from sub-millimeter to several millimeters. No variation in E/H ratio was accomplished, outside the simulation fluctuation attributed to field convergence, as shown in Figure 5-21.

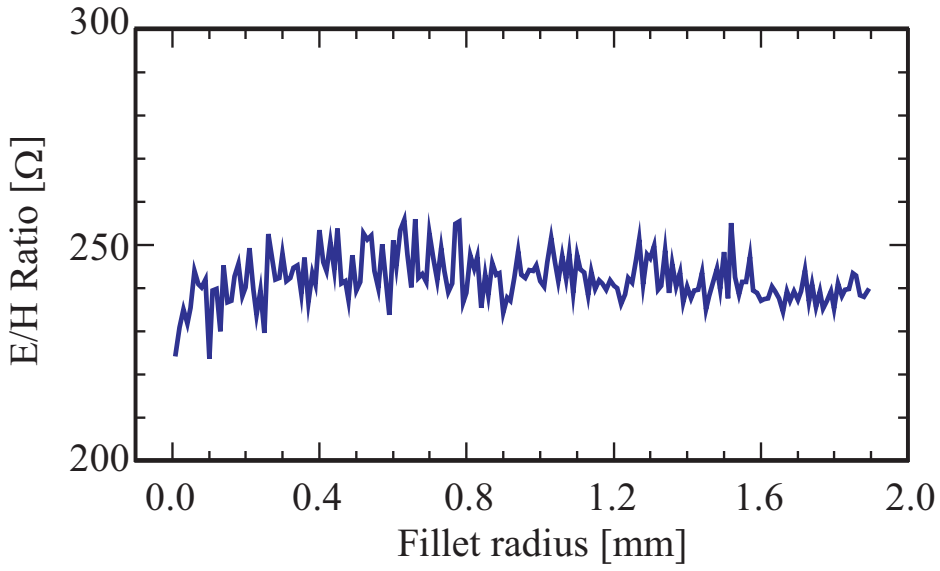

Figure 5-21: E/H ratio versus rod fillet radius.

5.4.2 Ratio

Larger rods, videlicet increasing a/b beyond 0.18 improves the electric to magnetic field ratio; however, HOMs are immediately better confined as well. The positive variation in E/H ratio is shown in Figure 5-22; larger rods mean less magnetic field for a given surface electric field or gradient. Larger rods also confine modes better, including HOMs. Enhanced confinement is seen in the field plots shown in Figure 5-23; both the fundamental and dipole mode are observed to be better confined by larger rods, id est, larger a/b.

The fundamental and dipole mode Qs are shown in Figure 5-24 for the simulations of Figure 5-23. The mode Qs include both ohmic and diffractive losses. The change in mode Q does not track as it is seen to when other structure parameters are changed, such as the outer rod spacing discussed in Section 3.2.5. The ratio of fundamental to dipole mode Q is shown in Figure 5-25. A maxima is observed at an a/b ratio of ~ 0.17. Increasing a/b will mean that while heating will be a smaller concern, the HOM damping attributes desired in a PBG structure will be compromised. An a/b ratio of 0.18 is already aggressive for E/H improvement; a solution to pulsed heating is required beyond larger rods.

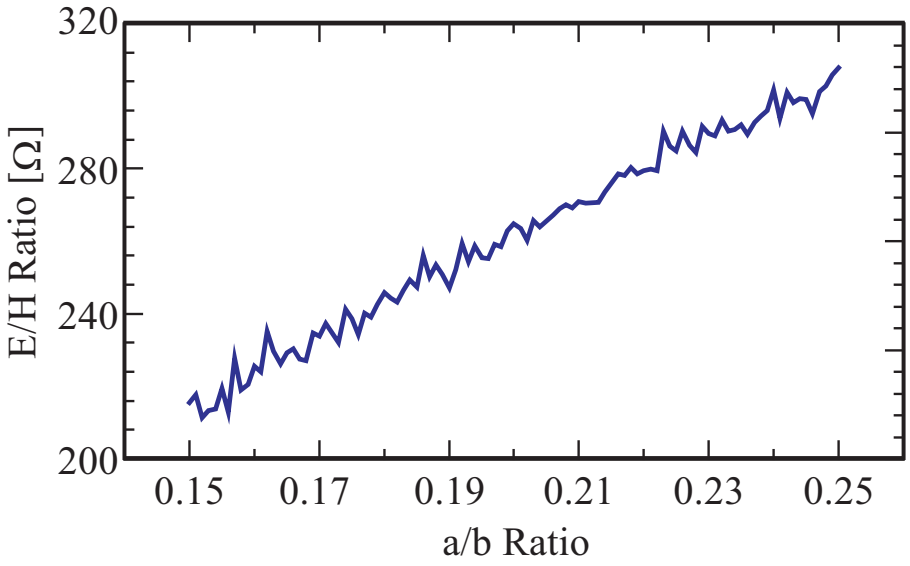

Figure 5-22: E/H ratio versus a/b ratio. A linear increase in E/H is seen as a/b is raised.

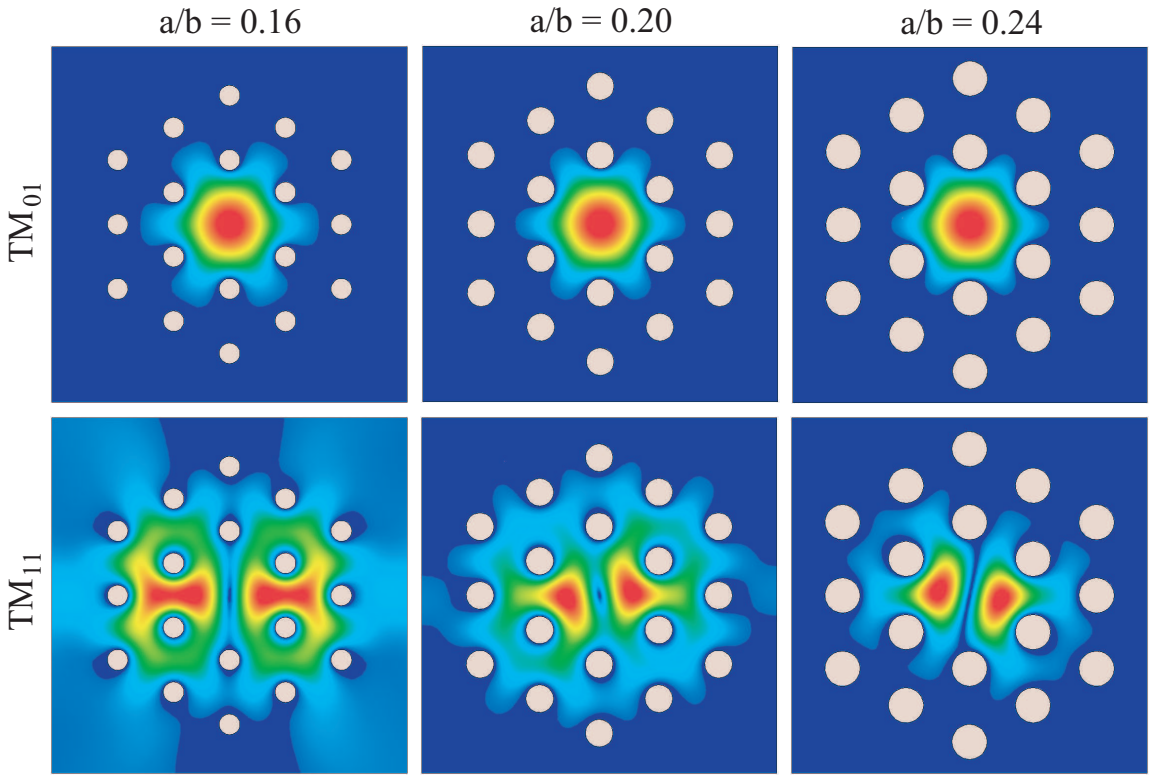

Figure 5-23: Electric field complex magnitude of fundamental and dipole modes for a/b ratios of 0.16, 0.20, and 0.24.

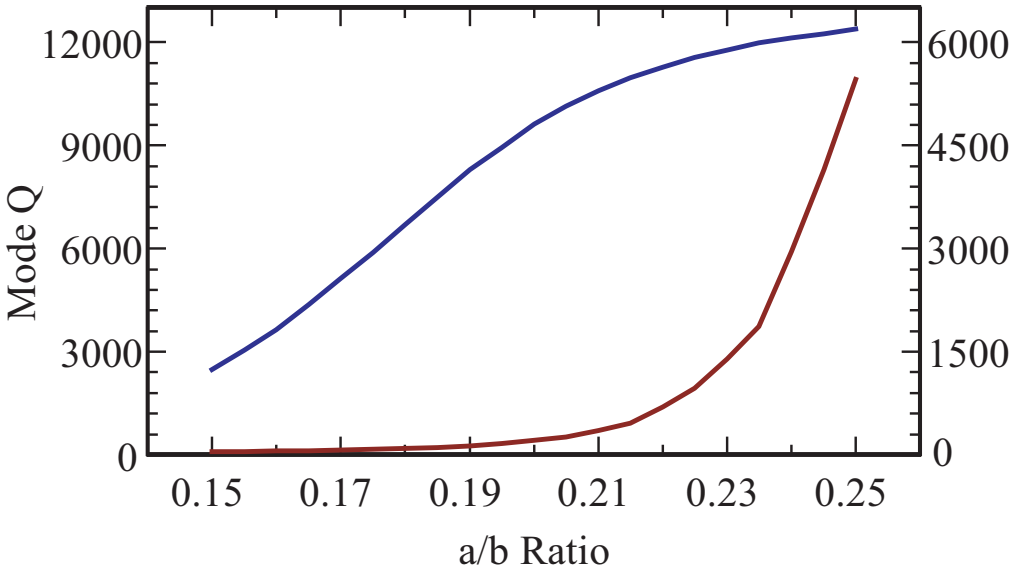

Figure 5-24: Q of fundamental mode (blue, left axis) and dipole mode (red, right axis) as a function of a/b.

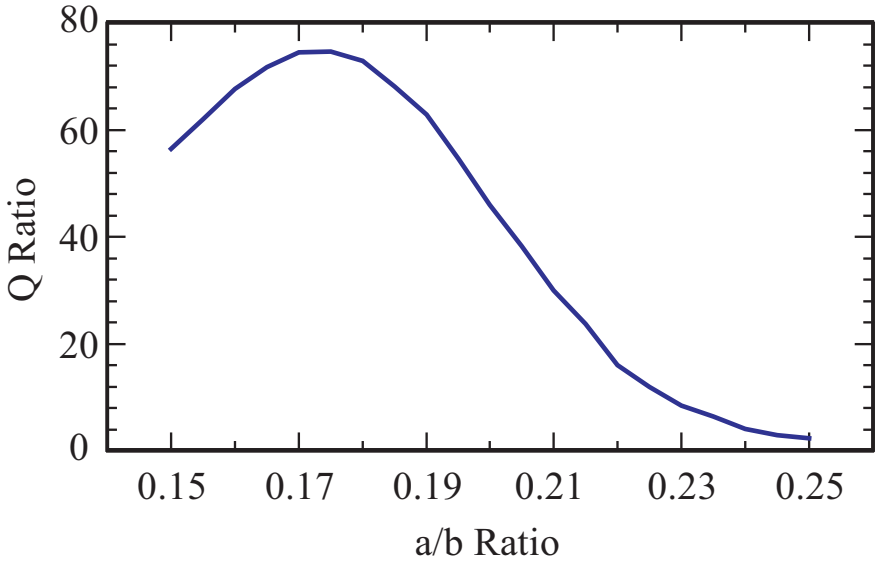

Figure 5-25: Ratio of fundamental to dipole mode Q as a function of a/b.

5.4.3 Movement

Dielectric PBG structures require many rows of rods to confine a high Q fundamental mode for accelerator applications. Recent work has looked at perturbing perfectly symmetric lattices of dielectric rods in order to raise the fundamental mode Q [60]. Similar perturbative algorithms are incorporated into *HFSS* including an implementation of a genetic algorithm. These analyses, and a thorough sweep of parameters have been carried out to examine the effect of moving metallic rods from their ideal PBG lattice positions.

In a metallic PBG, the field is primarily contained and affected by the first row of rods. This makes perturbations in the position of the first row of rods so dramatic, it is more accurate to consider the perturbation the movement of all of the outer rows of rods. Moving an inner rod radially inward or outward merely alters the frequency of the fundamental mode, and all HOMs; similarly the mode Qs are changed as discussed in Section 3.2.5 for outer rod position perturbations.

Changing the position of the inner row of rods from their PBG lattice positions changes the surface E/H ratio. The ratio is insensitive to small changes in rod position, and decreases for large changes. Movement of the rods from their lattice defined positions may be useful for dielectric PBG structures, but is not capable of improving the E/H ratio in metallic PBG structures.

5.4.4 Oblation

Oblation of the inner row of rods can improve the pulsed heating performance of the structure by spreading the magnetic field maximum over a larger area. This oblation can be accomplished by removing material from the ideal circular cross-section rod in either the format indicated in Figure 5-26 A or Figure 5-26 B; the radius of curvature facing the interior of the cavity can be made greater than that of the circular radius of the rod in either a convex or concave fashion.

Sweeps were made over both the center position of the oblation, and the radius of curvature. Both forms of oblation were found to be capable of increasing the E/H

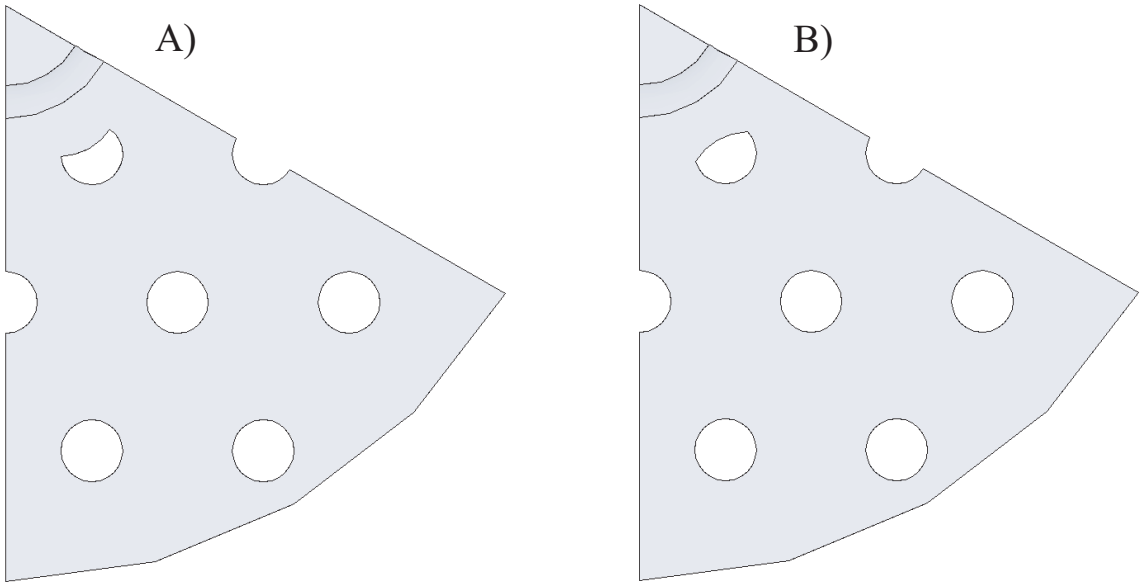

Figure 5-26: Schematic of inner rod oblation; A) concave and B) convex oblation.

ratio. Maximum effect was achieved for large radii of oblation, much larger than that of the rods themselves. The center position offset for the oblation was less critical to affecting E/H, and primarily altered the cavity frequency; removing material from the cavity lowers the mode frequency.

Concave oblation leaves sharp edges of material facing the electric and magnetic field maxima. These edges can be formed such that the E/H ratio is improved, but the maximum surface field is constrained to a small area, so that the surface is more sensitive to damage. Convex oblation increases the effective radius of the inner row of rods, without changing the HOM Q as dramatically as increasing the entire radius of the rods, as discussed in Section 5.4.2. Convex oblation, like increasing the a/b ratio or rod radii increases the area of maximum surface magnetic field.

5.4.5 Elliptical

An additional method to effectively increase the rod radii is to form the rods with an elliptical, rather than circular cross-section. Optimization runs were performed as well as parameter sweeps. As with concave oblation and larger radii rods, the magnetic field maximum is distributed over a larger area. The E/H ratio is also

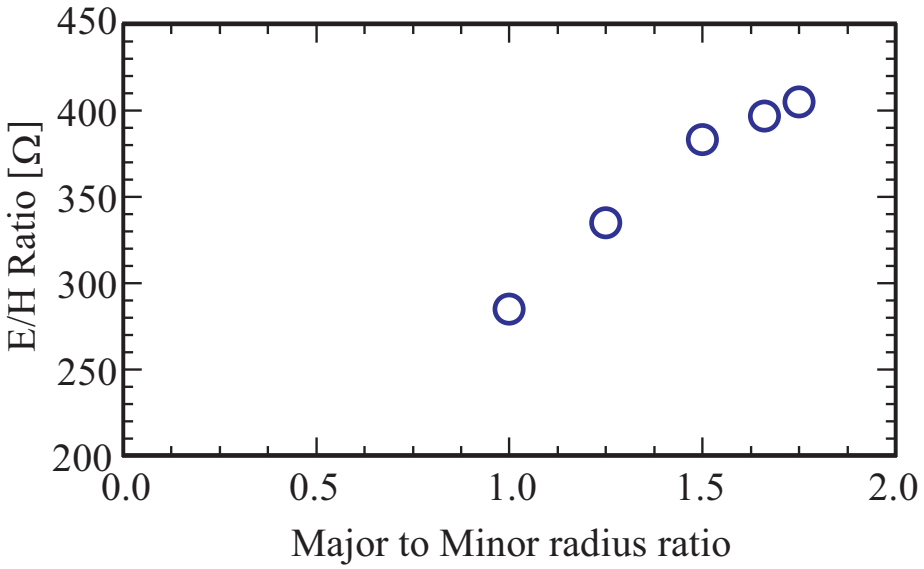

Figure 5-27: E/H ratio as a function of the major to minor radii.

improved for increasing ellipticity. Results are shown for the E/H ratio, as a function of the major to minor radii in Figure 5-27.

The HOM Q is also increased with increasing ellipticity, requiring a global optimization of cavity performance parameters. Such design optimization is beyond the scope of the present work, and so a design goal is set to reduce the cavity pulsed heating by 50%. Pulsed heating, discussed in Section 2.2.4, scales quadratically with the peak magnetic field, so that a 50% reduction in pulsed heating implies an improvement in the E/H ratio of 22%. To accomplish this, and using the same a/b ratio used for the first design, a major to minor radii ratio of 3 to 2 is found adequate in two dimensional simulations. The actual pulsed heating performance requires full design and modeling of a three dimensional structure.

The next step towards a full redesigned structure is a complete three dimensional model. The results of a parametric sweep over a range in major to minor rod radii ratios is shown in Table 5.7. In each of the elliptical rod simulations, the a/b ratio is fixed at 0.18; the radius of the outer rods is equal to the minor radius of the inner rods, $a_{outer} = a_{minor}$; and the rod spacing, b, is tuned so that the TM_{01} mode frequency is $\sim$ 10.1 GHz. A TM_{01} frequency of 10.1 GHz is the same as the pillbox cell, or central PBG cell in the breakdown structures that produces the 11.424 GHz

		TM_{01}		TM_{11}			
Ellipticity a_{major}/a_{minor}	E/H [Ω]	Frequency [GHz]	Q	Frequency [GHz]	Q	Frequency [GHz]	Q
1	285	10.1004	598	15.4631	40	15.4631	40
1.25	335	10.1024	1328	15.6977	94	15.6977	94
1.5	383	10.0673	3125	15.8033	283	15.8034	284
1.66	397	10.1166	5523	15.9519	685	15.9519	676
1.75	405	10.1155	7046	15.9768	1101	15.9768	1110

Table 5.7: Elliptical rod structure simulation results.

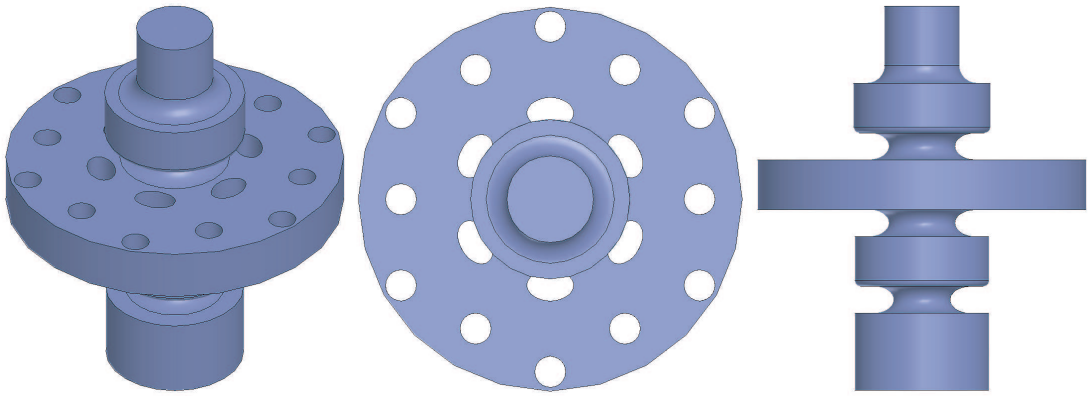

Figure 5-28: General geometry views of the redesigned PBG structure.

mode desired, as in Figure 5-7. For circular rods, an E/H ratio of 285 is achieved. For a major to minor radii ratio of 3 to 2, an E/H ratio of 383 is achieved. The improvement in ratio is sufficient to decrease the pulsed heating by more than 50%. HOM containment, as quantified by HOM Q also improves rapidly with increasing ellipticity. For this first redesign, an improvement in pulsed heating performance is mandated, with as small an increase in HOM Q as possible. Future designs will need to balance performance across multiple domains.

5.5 Final Redesign

A new PBG breakdown structure is designed with an elliptical inner row of rods to improve the pulsed heating performance of the structure with respect to the first PBG breakdown structure design. Fixed parameters remain the same as for the initial PBG structure and its pillbox counterpart, as listed in Table 5.2 and labeled in Figure 5-30.

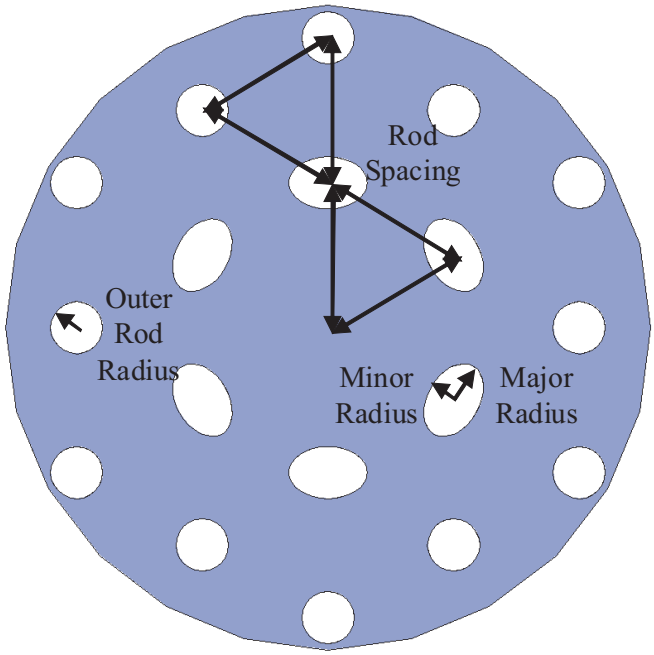

Figure 5-29: Schematic for PBG lattice parameters for redesigned PBG structure.

The redesign process follows the same design algorithm used for the initial design, shown schematically in Figure 5-6.

The tuned axial electric field of the redesigned structure is shown in Figure 5-31. The structure coupling is shown in Figure 5-32 and Figure 5-33. Figure 5-32 shows S_{11} as a function of frequency, demonstrating a match of better than –60.0 dB at 11.4273 GHz. The coupling Smith chart is shown in Figure 5-33, demonstrating a Q-circle of unit radius, indicating critical coupling.

Tuning Parameters	
b_end	11.632 mm
b_cll	28 mm
b_cpl	11.436 mm
a_cpl	4.828 mm
Outer Rod Radii	2.266 mm
Rod Spacing	12.588 mm
Major Radius	3.399 mm
Minor Radius	2.266 mm

Table 5.8: Tuning parameters for PBG structure. Final design values for schematics in Figure 5-30.

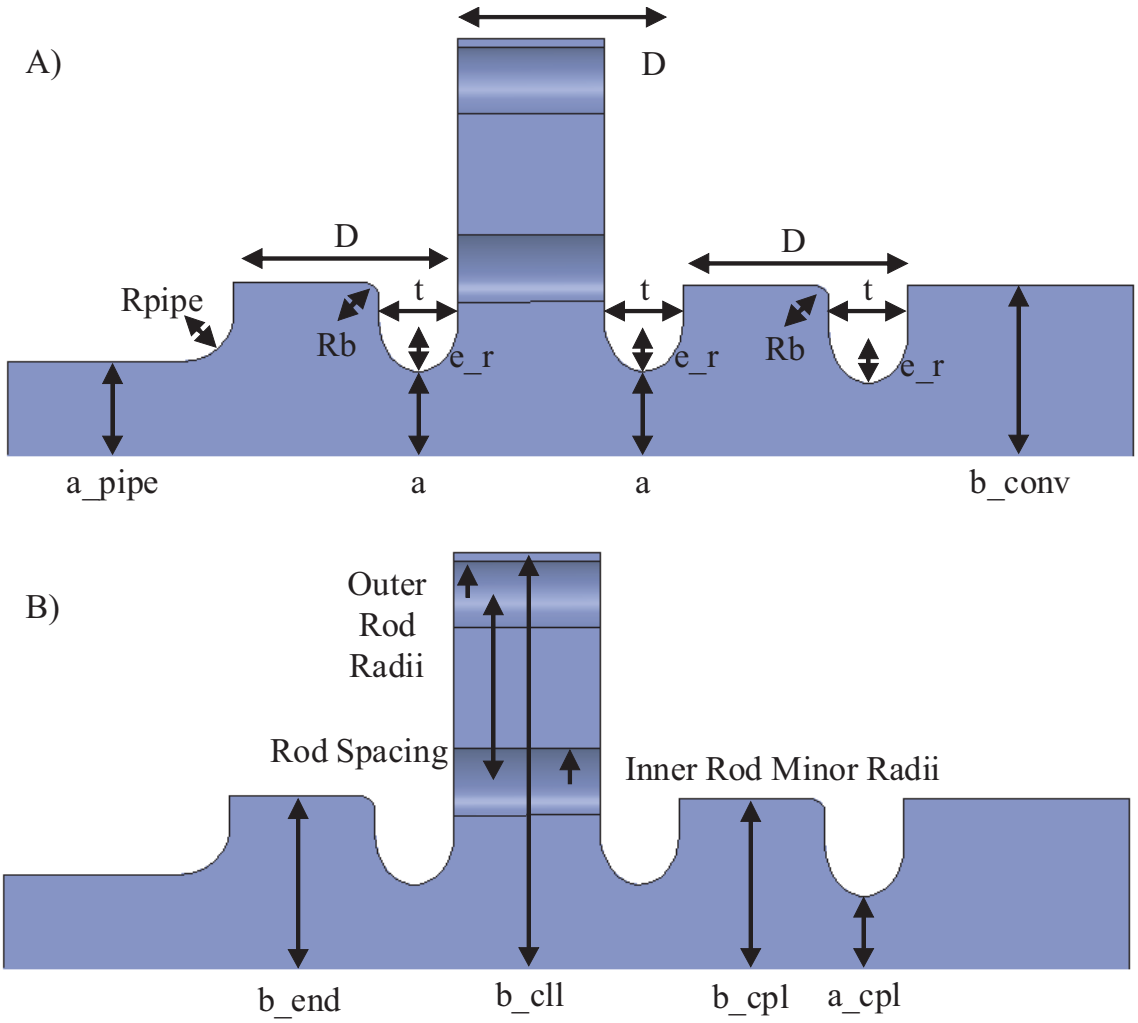

Figure 5-30: Schematics for parameters of redesigned PBG structure; A) schematizes fixed parameters for the structure, B) schematizes tuning parameters, as shown in Table 5.2 and 5.8, respectively.

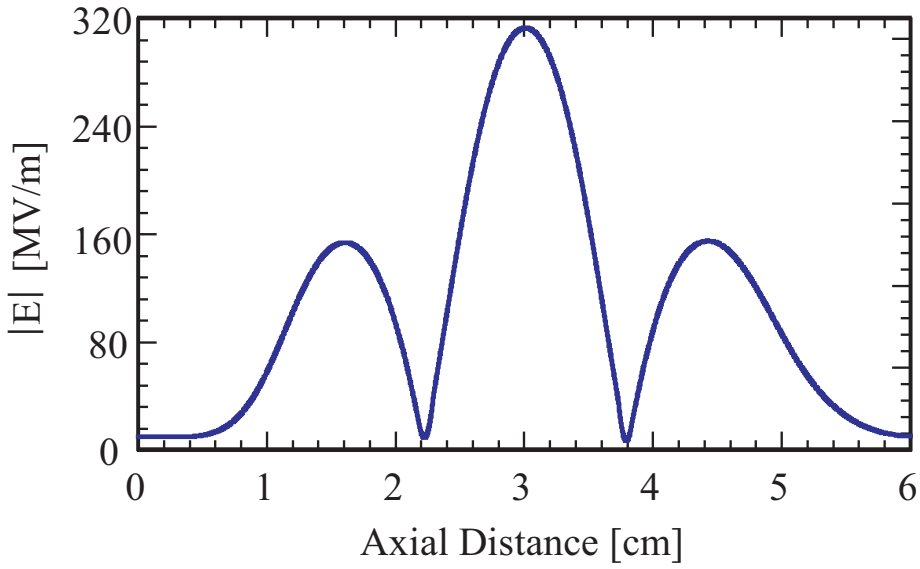

Figure 5-31: Electric field on axis of redesigned PBG structure. Power is coupled in from the left; half field is seen in each coupling cell, relative to the central PBG cell.

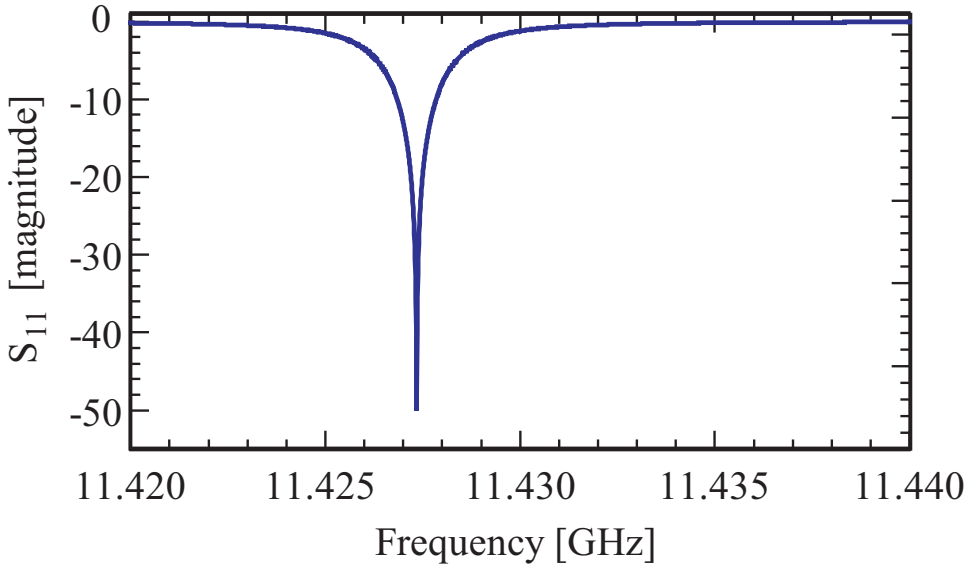

Figure 5-32: S_{11} coupling as a function of frequency for redesigned PBG structure.

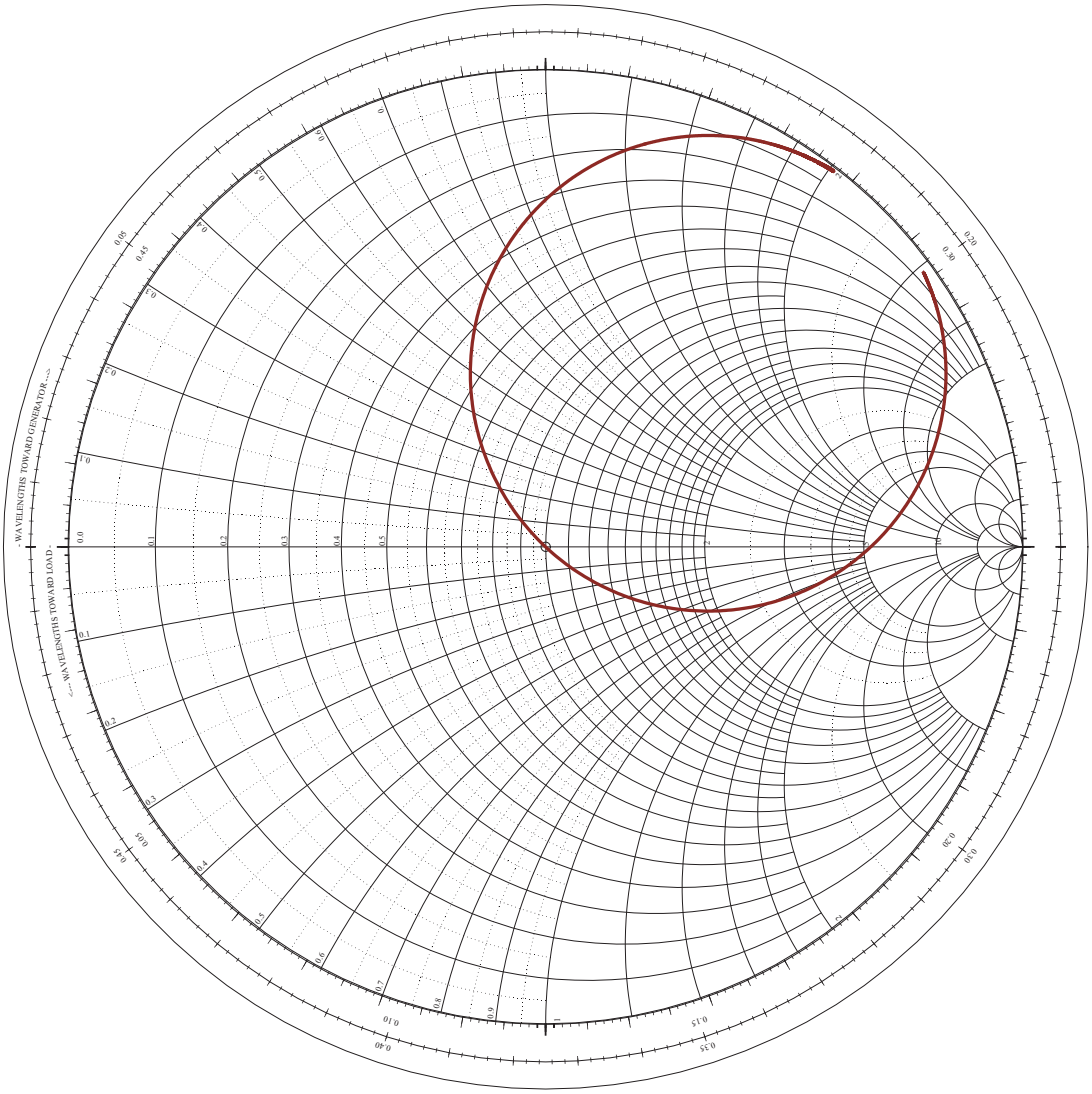

Figure 5-33: Smith chart Q-circle of coupling for redesigned PBG structure.

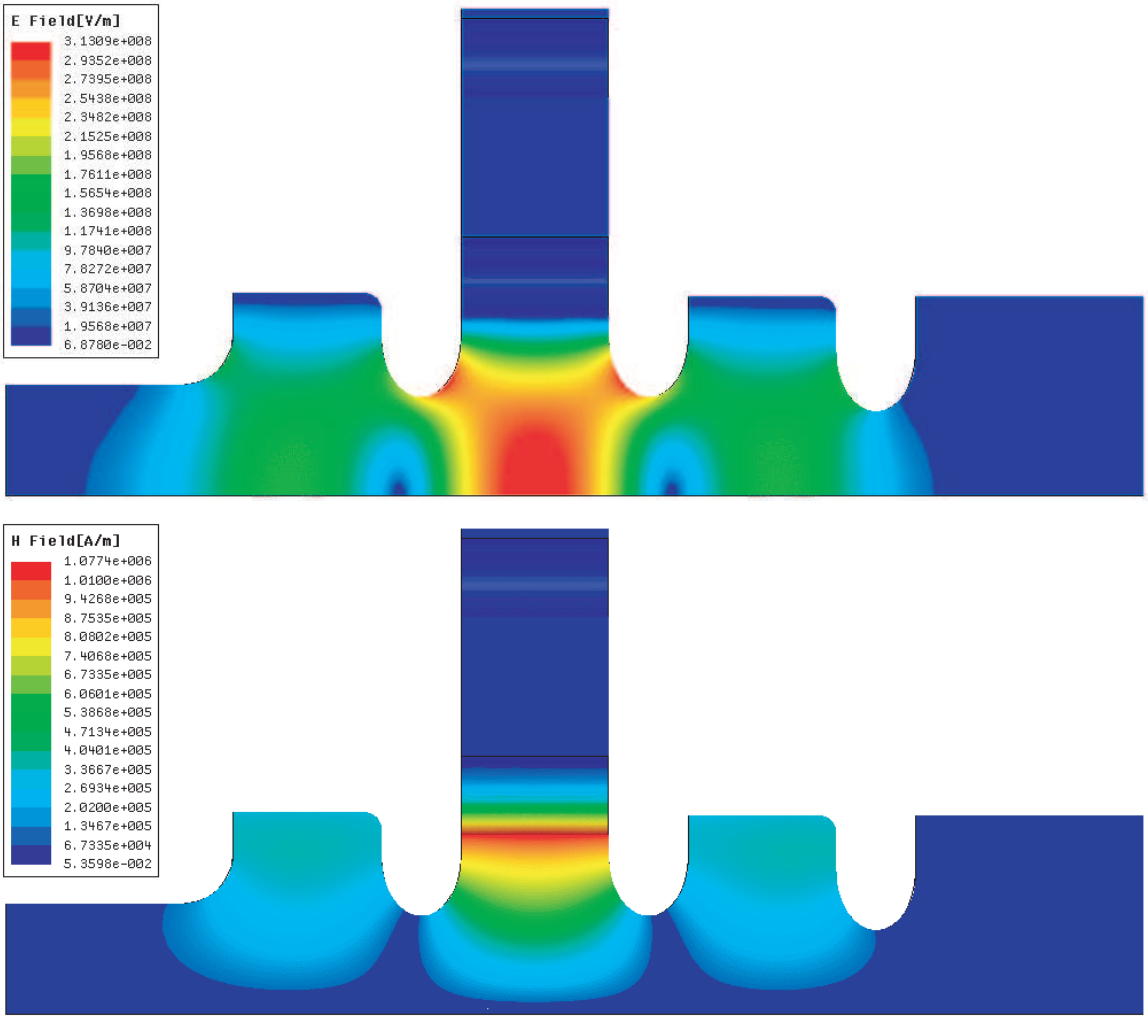

Figure 5-34: Electric and magnetic field for redesigned PBG structure. Side views.

Field plots are shown in Figure 5-34 for the electric and magnetic fields as viewed along a radial cut of the structure through the nearest rod, for 10 MW input power. The electric field is strongest in the central cell, with peaks on axis and on the structure irises. The magnetic field is strongly peaked on the inner edge of the first row of rods. Top views of the electric and magnetic fields are shown in Figure 5-35, for 10 MW input power.

For comparison, the SLAC pillbox structure field plots are shown in Figure 5-12, and the first PBG structure field plots are shown in Figures 5-10 and 5-11; all plots are for 10 MW input power. A summary of field values observed in these simulations is given in Table 5.9. For 100 MV/m gradient and 100 ns pulse length a temperature

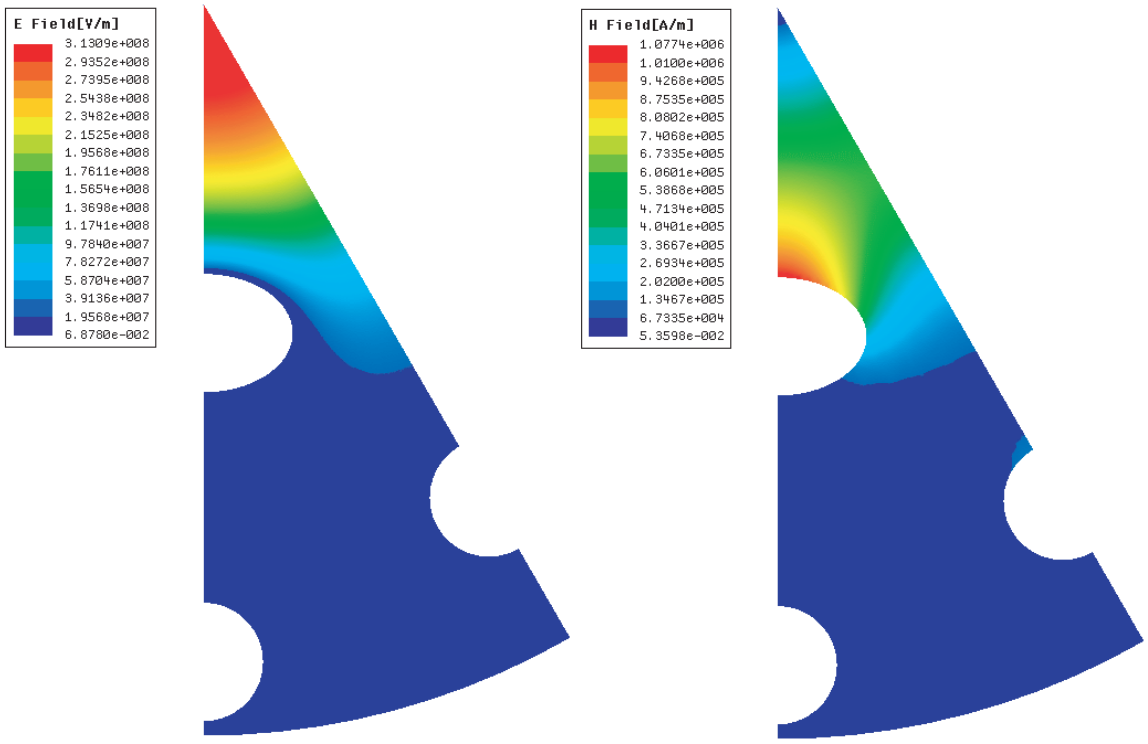

Figure 5-35: Electric and magnetic field for redesigned PBG structure. Top views.

Structure	Gradient	Electric	Magnetic
PBG	130	280 MV/m	1300 kA/m
Elliptical PBG	150	310 MV/m	1070 kA/m
Pillbox	160	340 MV/m	710 kA/m

Table 5.9: Maximum surface field values observed in the simulations of Figures 5-10, 5-12, and 5-34. All simulations are for 10 MW input power.

rise of 48 K is predicted, limiting the structure to a lifetime of $\gtrsim 900 \times 10^6$ shots, according to Figure 2-4. As discussed in Section 2.2.4, a pulsed heating excursion of < 50 K is believed to be acceptable for linear collider accelerator structure operation.

Design tolerances remain consistent with previous specifications for the first PBG breakdown structure. Machining of elliptical rods should be straightforward given the fabrication method used for the first PBG structure, in which the rods were milled from a single block of OFHC copper.

5.6 Future Directions

A deformed PBG lattice quickly loses the necessary symmetry to formally be a photonic crystal, becoming a photonic quasi-crystal. Many of the potentially free parameters defining the positions of the rods of a PBG lattice were defined by two parameters: the rod radii and spacing. These two parameters were constrained further to tune the cavity frequency. In a quasi-crystal the only requirement is on the frequency, freeing up the positions of many of the rods. Optimizing cavity parameters involves HOM damping, as discussed in Section 3.2.5, as well as the field measures discussed here with regard to pulsed heating. Future experimental directions will dictate what cavity parameters are desired for subsequent testing. Once the parameters for a future PBG structure are decided, the large number of free parameters can be optimized to determine an exact solution of geometry and PBG lattice deformations.

Chapter 6

Experimental Results of X-Band PBG Structure Testing

6.1 Introduction

As part of the United States high gradient research collaboration, single cell breakdown testing of an MIT designed PBG structure was proposed at SLAC. Design of the structure was described in Chapter 5. Fabrication of the structure was completed by engineering teams at SLAC, with cold testing done collaboratively, high power testing by SLAC staff, data analysis done at MIT, post high power cold testing collaboratively, and final surface imaging done at SLAC.

The design presented in Chapter 5 was provided to SLAC, and translated into engineering drawings. The PBG cell was machined from a single block of OFHC copper including one of the cell iris plates, the other iris was included in the facing cell piece, into which the PBG lattice rods were brazed. The structure, after passing machining quality control, prior to brazing is shown in Figure 6-1. The structure was then brazed into a single copper unit, and the stainless steel flanges were welded into place.

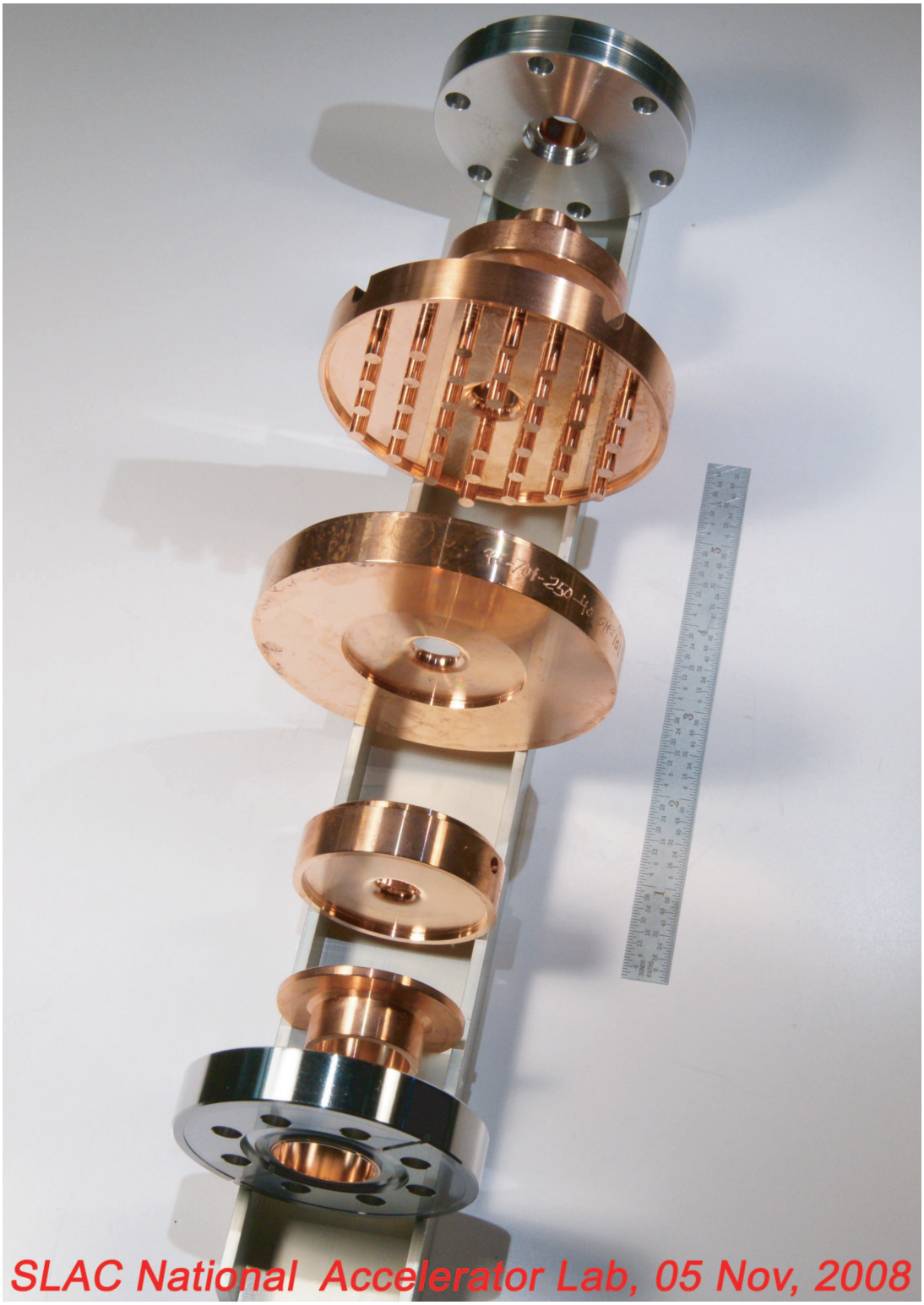

Figure 6-1: Machined PBG structure parts prior to brazing. Courtesy of SLAC.

6.2 Cold Test and Bead Pull

Cold testing of the PBG structure was done to confirm manufacturing, and enable tuning. The parameters measurable in cold test are the mode frequencies, mode Qs, and mode identification via bead pull.

6.2.1 Setup

The single cell standing wave PBG structure, identified by SLAC code as 1C-SW-A5.65-T4.6-Cu-PBG-SLAC#1, was matched with a TM_{01} mode launcher, T52219-1, for all cold testing, and the same launcher remained connected for high power testing, and final cold testing. The author is shown in Figure 6-2 with the PBG structure mounted for cold test. An HP 8510C vector network analyzer (VNA) was used with X-band adapters and full calibration kit. A full two port calibration was done for each measurement, to insure accuracy across the frequency range of interest, and to most effectively utilize the 800 frequency points per measurement. A dry nitrogen flow was provided through a straight length of WR-90 waveguide to preserve structure cleanliness, and limit measurement fluctuations due to humidity. Temperature fluctuations were monitored by a sensor for the room, and an additional sensor lead attached to the body of the PBG structure.

Measuring the field profile of the cavity modes is accomplished by introducing a small perturbation to the cavity and measuring the response. For two port devices this is done in a resonant way, in which the electric field strength at the bead position is proportional to the frequency shift of the resonance [61]. For a one port device, a non-resonant technique must be adopted [62]. The practical technique for both methods involves the suspension of a small dielectric perturbation, or "bead", on a thin dielectric wire. This suspension is accomplished using the mounting attached to the PBG structure shown in Figure 6-2, and in more detail in Figure 6-3.

The mounting allows the smooth draw of the bead through the structure precisely on axis. The mounting is attached with three bolts, threaded through springs, so that they can be adjusted to exactly center the bead. The wire used was Ashaway

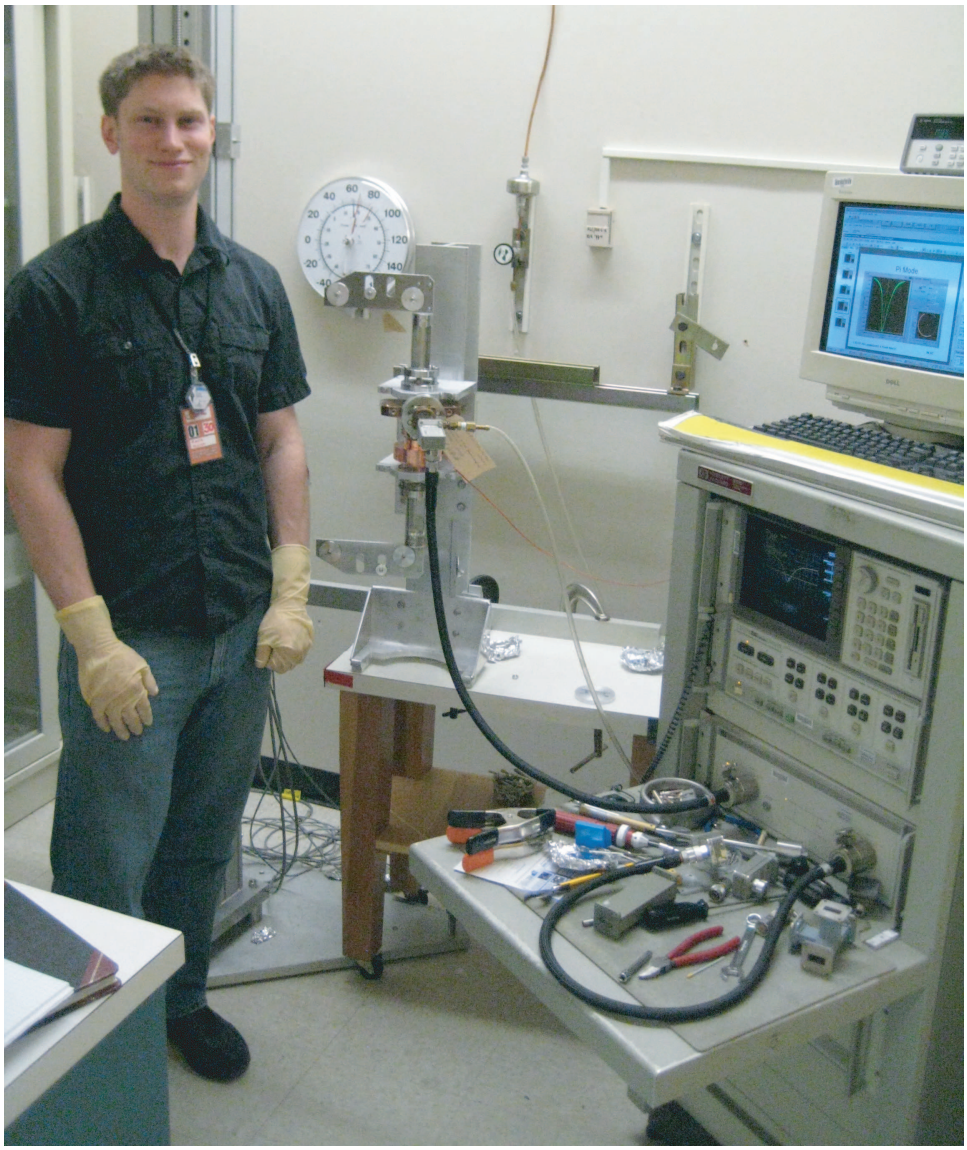

Figure 6-2: Author and cold test laboratory.

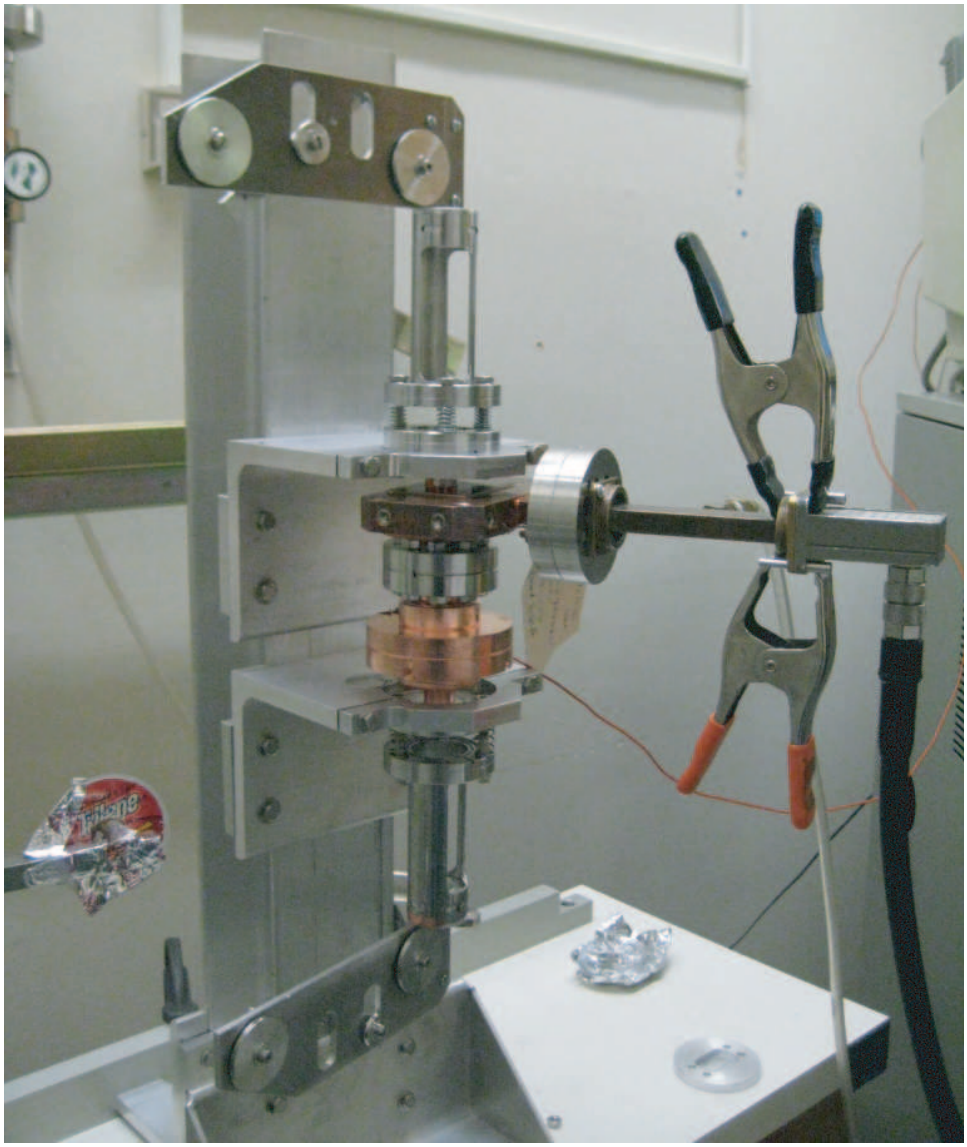

Figure 6-3: Mounting for bead pull measurement.

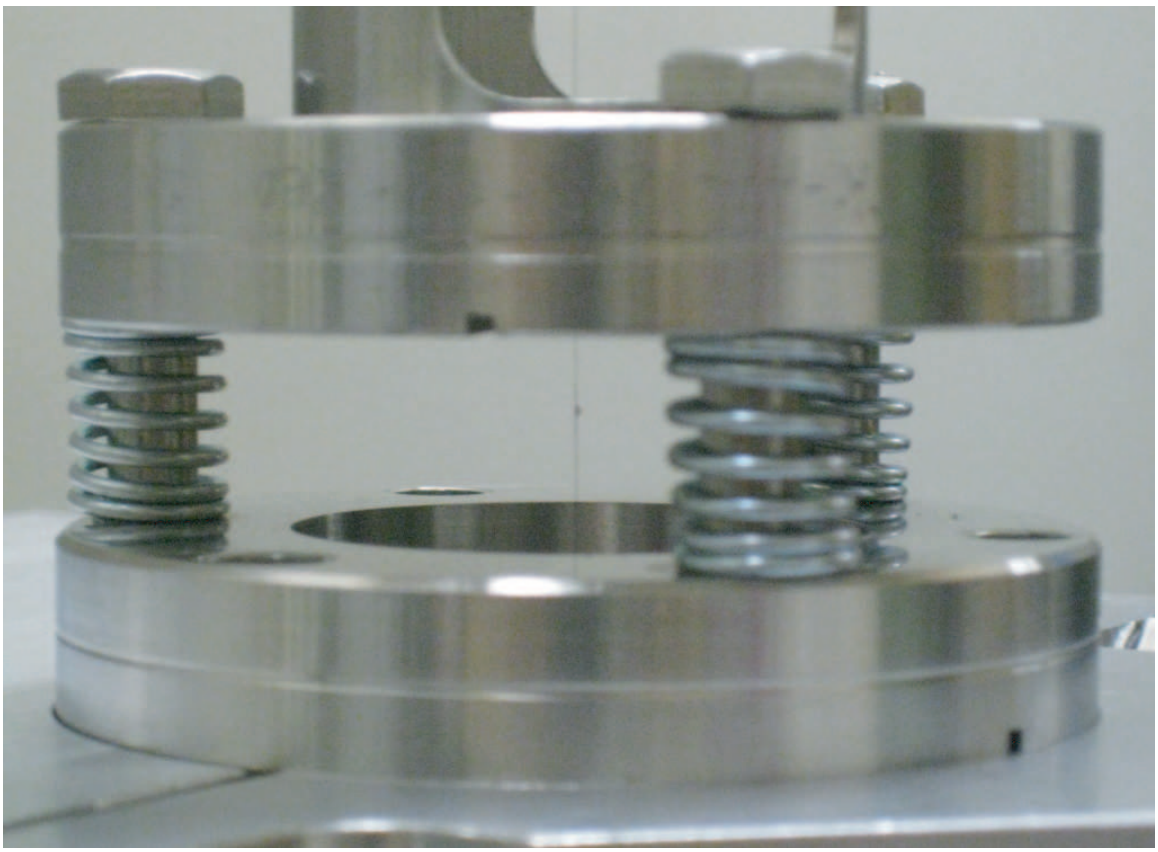

Figure 6-4: Detail of bead on wire and adjustable bead pull mounting.

10/0 black monofilament 2 lb Trilene; the bead is made of a small drop of superglue. The bead pull mounting and bead can be seen in Figure 6-4.

6.2.2 Bead Pull Measurements

Cold test enables measurement of the cavity mode structure, frequency, and Q. The mode field profile is calculated by identifying a resonance in S_{11} on the VNA and performing a calibration over a frequency range that fully encloses the resonance (id est, a full Q-circle when viewing the Smith chart). The real and imaginary phase is then measured on resonance (or slightly off resonance) as a function of bead position. This method is non-resonant because no shift in resonant frequency is measured, as with [61], but the field is probed directly as a phase shift [62].

To get a quantitative measure of the electric field strength, the phase data must first be centered. The arbitrary path length between the VNA and the cavity functions

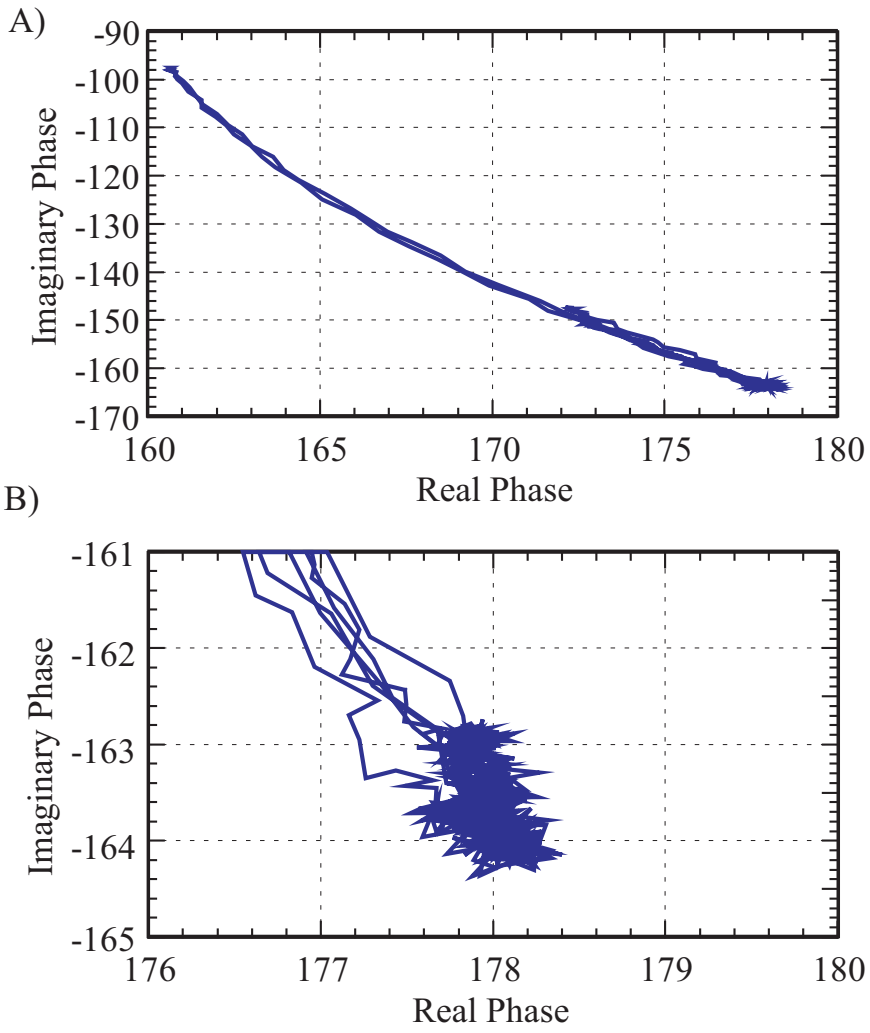

Figure 6-5: Recentering of real and imaginary phase measurements.

to offset the cavity resonance in both real and imaginary phase. The raw data for a bead pull measurement is shown in Figure 6-5 A; data is shown for advancing bead position at 11.4323 GHz. The collection of small random phase change, shown in detail in Figure 6-5 B, is not the resonance, and the data is shifted by 178° and –163.5° in real and imaginary phase, respectively so that the phase measurement is centered on zero.

Once the data has been centered, the field strength squared is proportional to the total phase shift, as expressed in Equation 6.1, allowing the normalized electric field

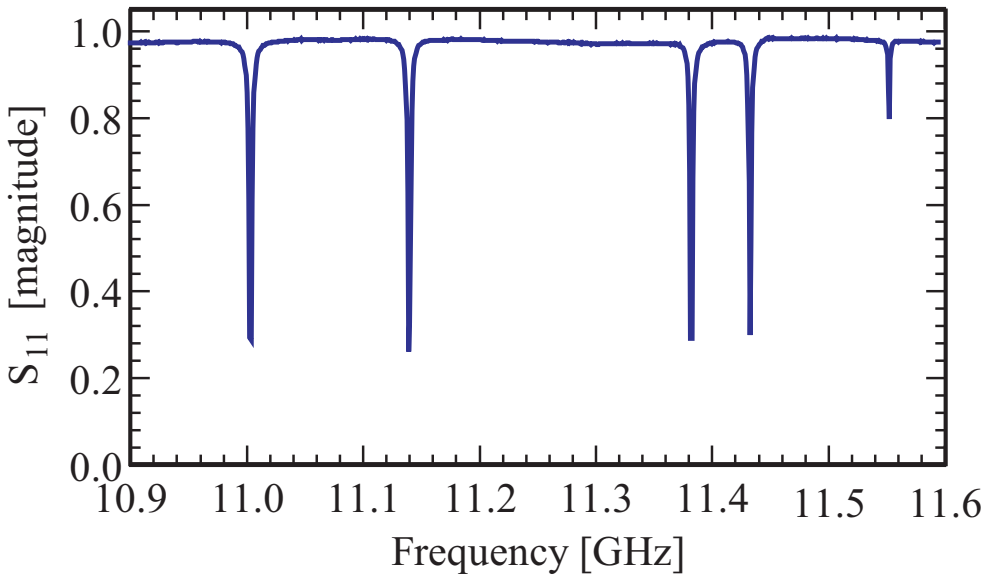

Figure 6-6: Broad S_{11} measurement showing all observed resonances of the PBG structure and mode launcher.

magnitude to be expressed as in Equation 6.2.

$$E^2 \propto \sqrt{\phi_{real}^2 + \phi_{imaginary}^2} \tag{6.1}$$

$$|E| \propto \left(\phi_{real}^2 + \phi_{imaginary}^2\right)^{1/4} \tag{6.2}$$

Equation 6.2 and the recentering of the bead pull data shown in Figure 6-5 allow field profiles to be created for all resonances seen in the broad S_{11} measurement shown in Figure 6-6. Field profiles, shown in Figures 6-7, 6-8, and 6-9 identify the modes.

Three modes are expected in the PBG structure itself: the 0-mode, $\pi/2$-mode, and π-mode, which correspond to the field shape in the structure cells. Two coupler modes are also observed, formed by multiple peaks in the oversized waveguide connecting the TM_{01} launcher and the PBG structure. This accounts for all the peaks observed in Figure 6-6. Primary interest is in the matching of the π-mode to its design prediction, which is shown in Figure 6-10. Slightly less field strength is seen in the last pillbox cell, but the overall agreement is quite good.

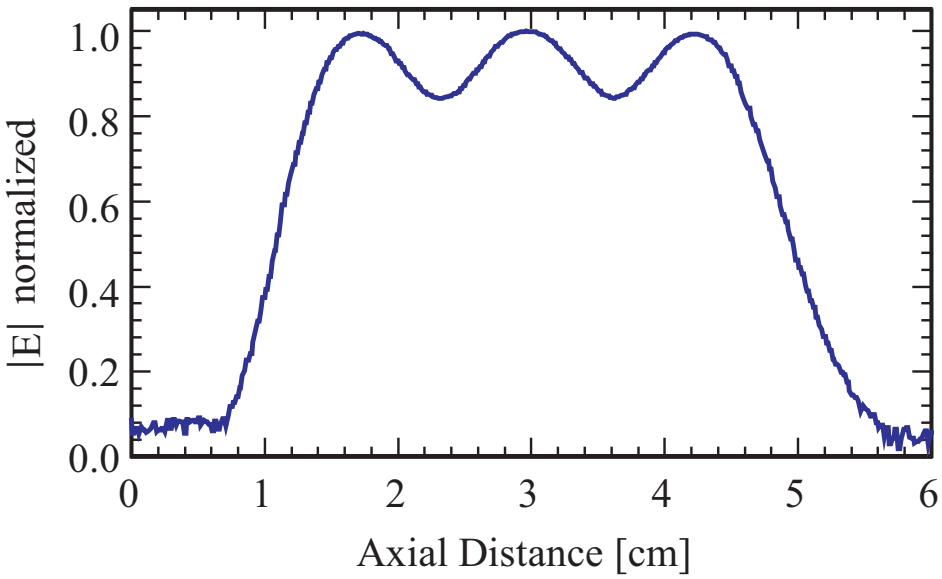

Figure 6-7: Bead pull result for "0-mode".

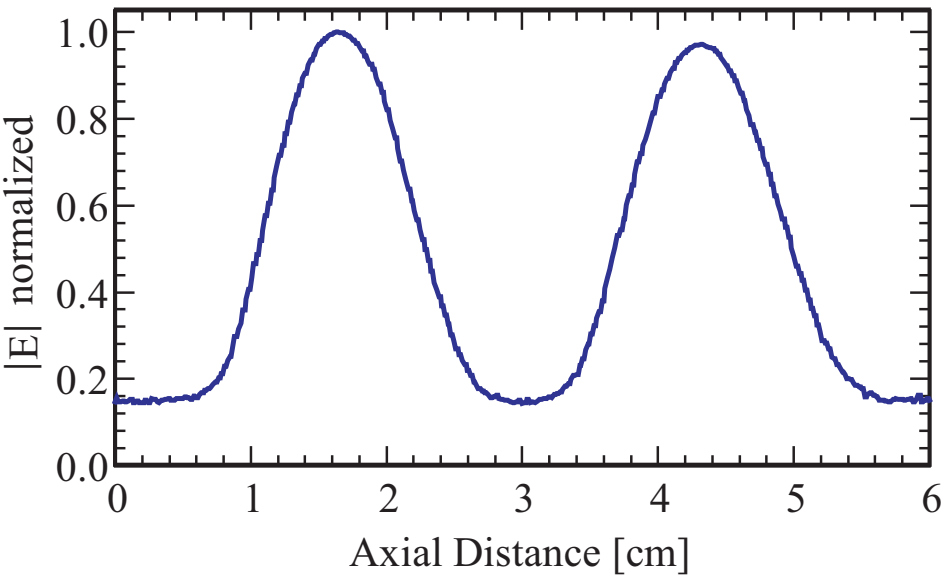

Figure 6-8: Bead pull result for "$\pi/2$-mode".

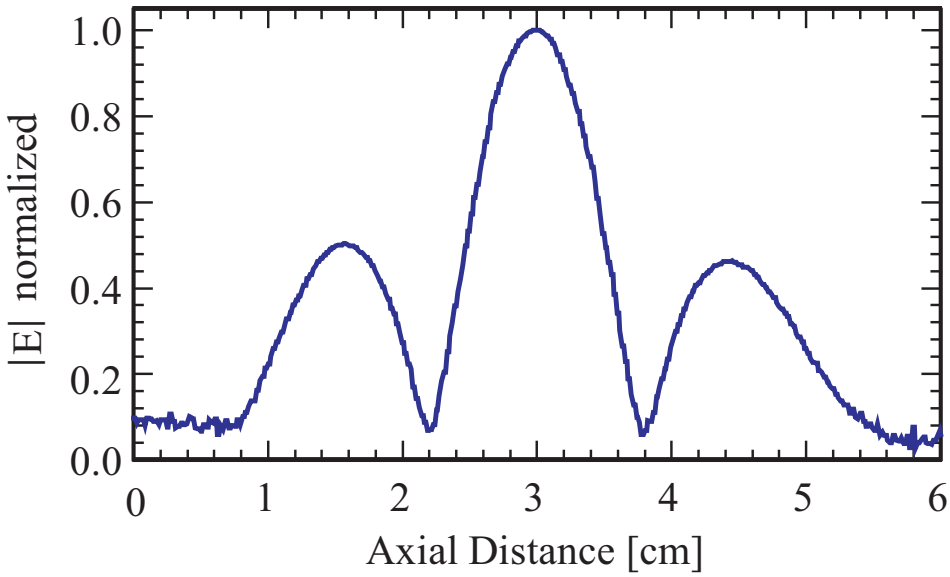

Figure 6-9: Bead pull result for "π-mode".

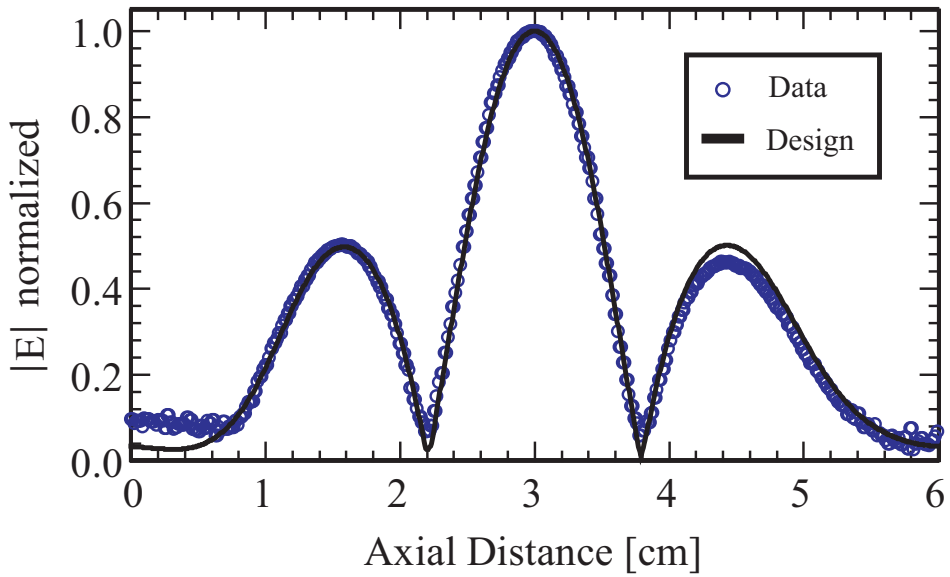

Figure 6-10: Bead pull results for PBG standing wave structure. Good agreement is seen between before cold test bead pull measurements and design simulation.

Mode	Frequency [GHz]	Q		
		Q_0	Q_L	Q_{ext}
0	11.0036	8347	3390	5708
$\pi/2$	11.1397	9044	3796	6541
Coupler	11.3819	8299	4304	8941
π	11.4323	7401	4695	12844
Coupler	11.5517	12746	11224	9395

Table 6.1: Table of measured Q values for PBG structure modes.

6.2.3 Coupling

Once the modes have been identified, their coupling can be measured without the presence of the bead. S_{11} measurements allow the mode frequency and coupling to be directly measured, as well as the mode Q, by measuring the area within the Q-circle formed on a Smith chart [63]. Table 6.1 summarizes the mode Qs: the unloaded Q, Q_0; the loaded Q, Q_L; and the external Q, Q_{ext}. The measured π-mode Q is 7400, the design simulation value was 7600; this close agreement, and the close field profile agreement observed in Figure 6-10 means the structure was well fabricated.

6.3 SLAC Klystron Test Stand Facility

The PBG breakdown structure was installed at SLAC on klystron test station #4. Structure installation requires the removal of lead shielding from the enclosure bunker, and the timely removal of the previous breakdown test structure and installation of the next structure under as clean conditions as possible. Swift and clean structure change insures that the vacuum system recovers quickly, and that no contamination of the structure surfaces occurs, both prior to and after high power testing. Installation of the PBG structure into the bunker under HEPA filtration is shown in Figure 6-11. The interior of the test bunker is shown in Figure 6-12, after the vacuum connections have been made, but prior to water cooling connections and bunker shielding.

Figure 6-11: Photograph of PBG structure being installed in lead enclosure for breakdown testing.

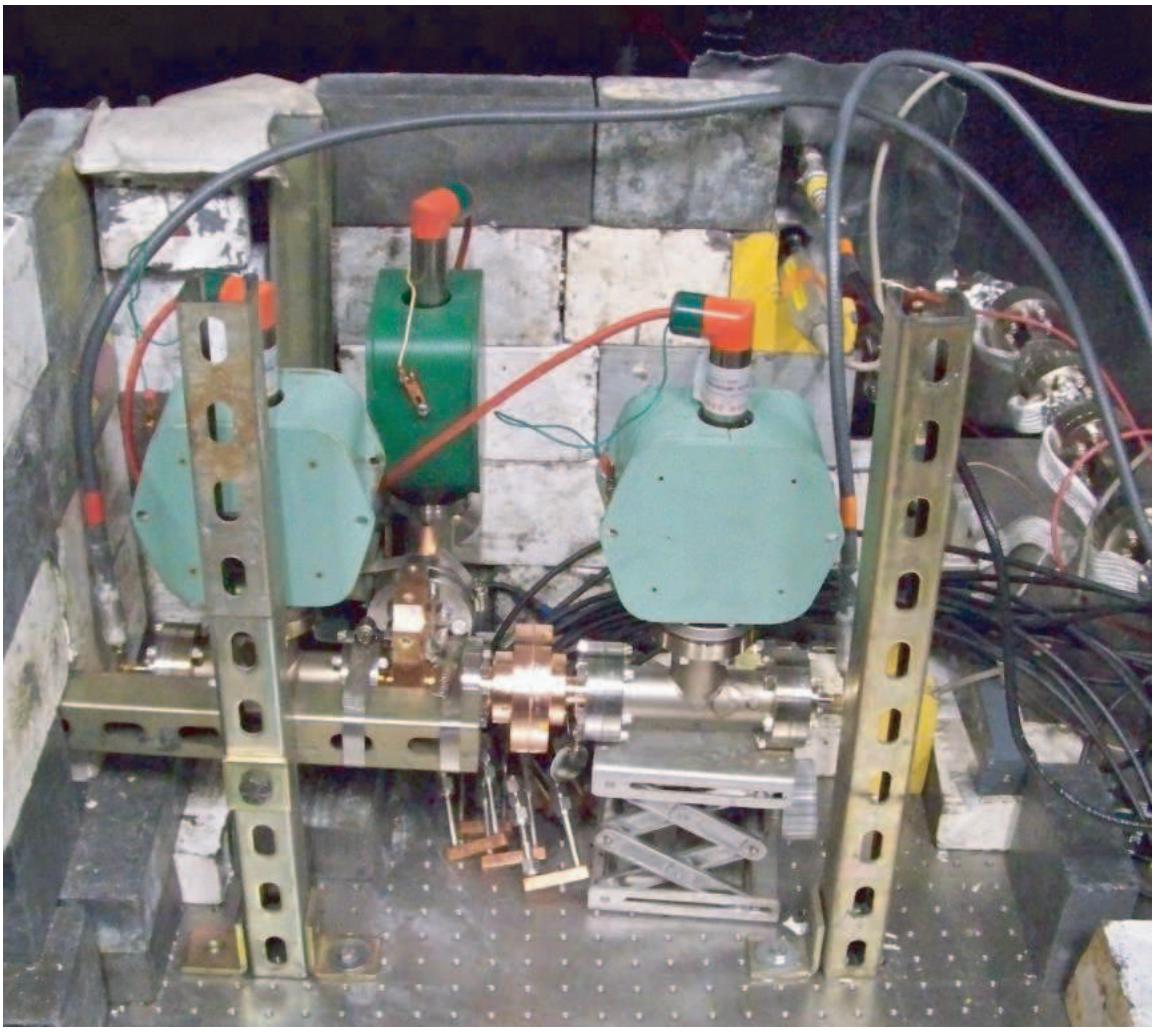

Figure 6-12: Photograph of PBG structure installed in lead enclosure for breakdown testing.

6.3.1 Operation

Klystron test station #4 operates the X-band klystron XL4–6B and related microwave diagnostics. The tube is driven and controlled by computer, allowing pulse shaping and frequency tuning on a shot to shot basis. Filling of the standing wave structures is accomplished in a shaped manner; a high power level initially fills the structure, and then the power is lowered to maintain a constant level over the nominal power pulse length, as discussed further in Section 6.3.2. Power level goals are set for the nominal power level, and the computer changes the klystron drive properties to correct for drift in the klystron operating parameters. The drive frequency is similarly tuned to maximally couple power into the structure by minimizing the reflected power; frequency tuning is necessary as the structure detunes with temperature, videlicet 190 kHz/K. A log is kept for the test station, which provides information regarding operating conditions and the goals set for each operational run.

6.3.2 Diagnostics

Computer connection to microwave diagnostics is necessary to facilitate the algorithm driven control of the klystron. Two primary sets of traces are read and analyzed: the peak power meter, and scope traces. Two HP8990A peak power meters measure the fully calibrated klystron power, and the power being fed into the breakdown structure under test: the forward and reverse power. A typical peak power meter trace is shown in Figure 6-13. The peak power meter is a continuous readout that relies on time averaged sampling. Changes in power level appear discontinuous, and require time to average back to an accurate baseline. The klystron output is much higher than that necessary for testing single cell structures; most of the klystron power is terminated in a high power load. The structure forward and reverse power are the peak power monitor channels that read the power from directional couplers on the structure power arm of the klystron output, after the load. The klystron power is not uniform, but is shaped in order to more rapidly fill the structure.

The forward and reverse structure power can be used to calculate the fields in

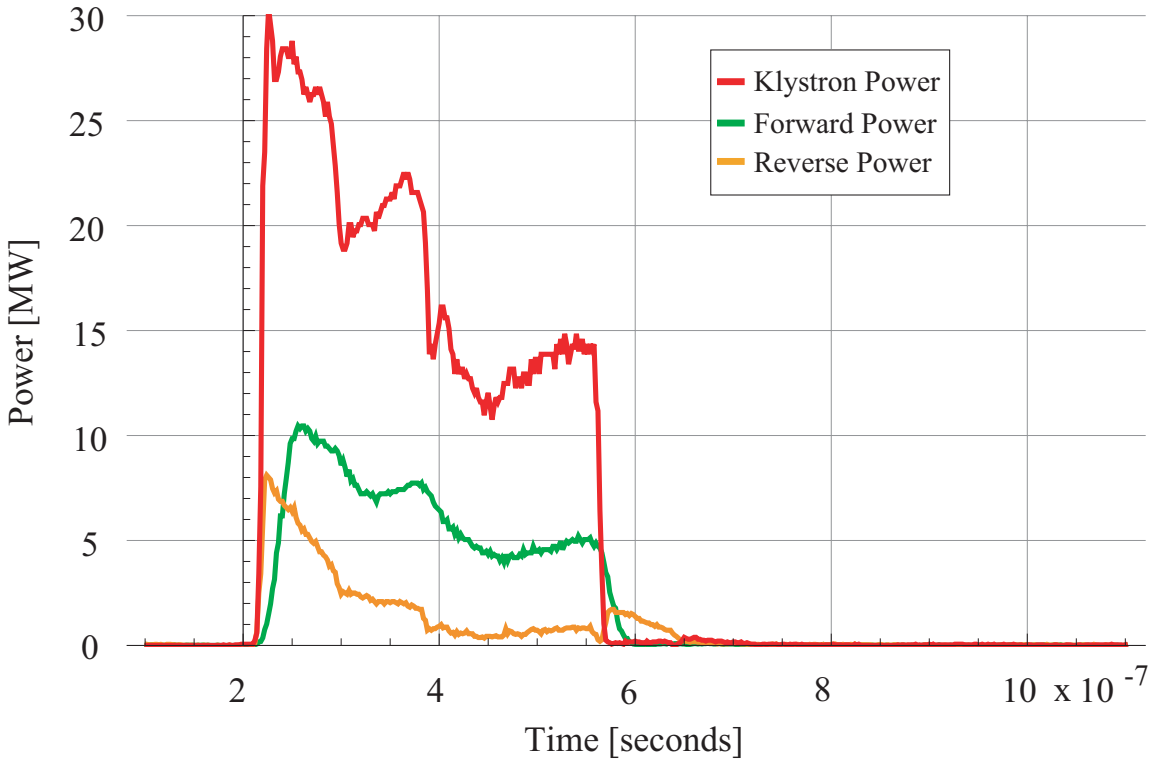

Figure 6-13: Peak power meter trace for klystron signals: klystron output power, structure forward and reverse power traces.

the structure. Precise calibration of this using *HFSS* simulations was discussed in Section 5.3.6. The fields in the structure are a function of the power being fed into the structure, and the Q of the structure and external coupling, or the loaded Q, Q_L [16, 9]. The time constant for power coupling into the structure is then: $\tau = \frac{2Q_L}{\omega}$ [16]. A shaped filling pulse is used to provide a flat field profile in the structure. A flat input pulse is shown in Figure 6-14 with the corresponding cavity accelerating gradient. A shaped pulse is shown in Figure 6-15 with the corresponding cavity accelerating gradient, showing a flat region of the pulse as a result of the pulse shaping. This is why the peak power meter pulse in Figure 6-13 has its non-uniform shape. The approximate input power pulse, and the corresponding cavity accelerating gradient are shown in Figure 6-16, for the input power shown in Figure 6-13.

Scope traces are uncalibrated measurements obtained within the structure bunker enclosure. These include microwave measurements of structure forward and reverse power using diode detectors, and dark current measurement from both forward and reverse Faraday cups (FCs). The scope traces are used as shot to shot diagnostics, and to monitor breakdown events. A typical scope trace is shown in Figure 6-17, a typical scope trace during a breakdown shot is shown in Figure 6-18; for both of these shots, the forward power into the structure (from the peak power meter) was 5.0 MW. The Faraday cup measurements were usually very low for the PBG structure, $\lesssim$ 2–3 mA. During breakdown shots, however, Faraday cup measurements of $>$ 45 mA were observed.

6.3.3 Data

Computer control and diagnostic monitoring provides a wealth of data. Filtering useful shots for analysis is important for both the analysis process itself, and data storage. The peak power meter logs data continuously every day; shots are stored every two seconds while running, and every 15 minutes while not running. The scope traces have a much higher volume, as they are taken continuously, every shot, while operating at a repetition rate of 60 Hz. Scope traces are stored for every breakdown event, as well as the shot immediately preceding each breakdown event.

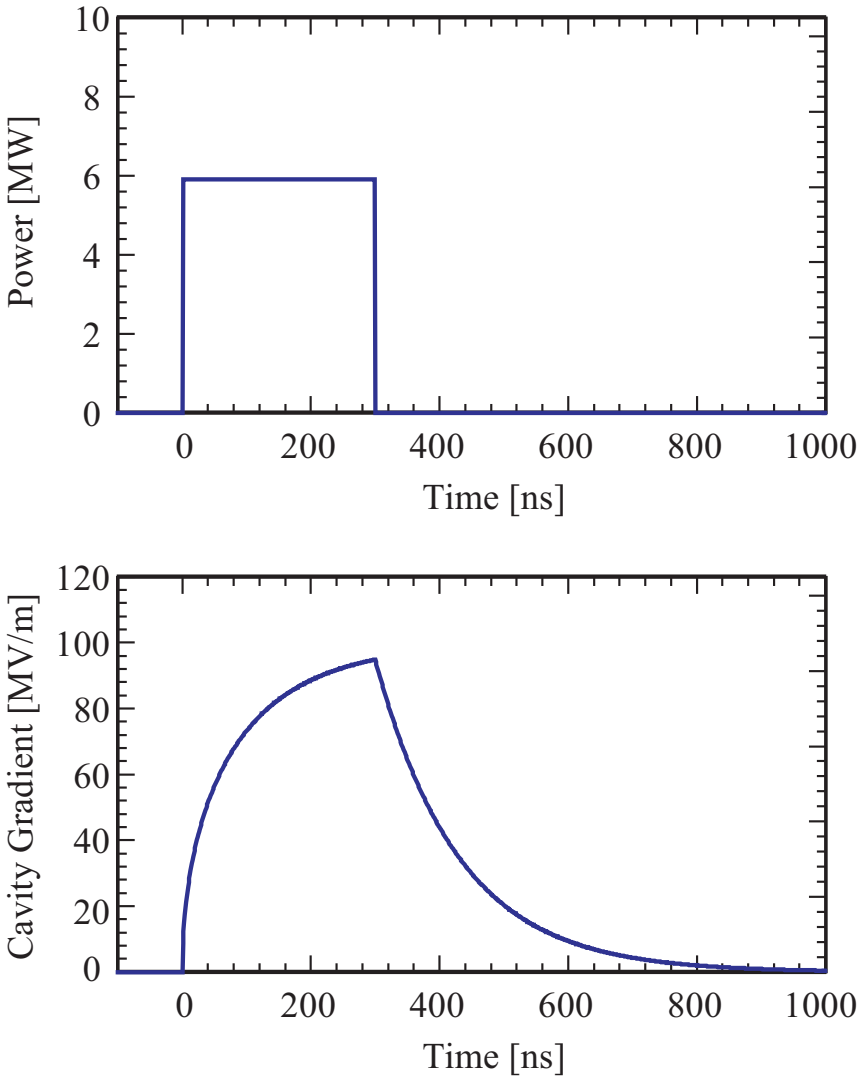

Figure 6-14: Flat input power pulse, and cavity accelerating gradient as functions of time.

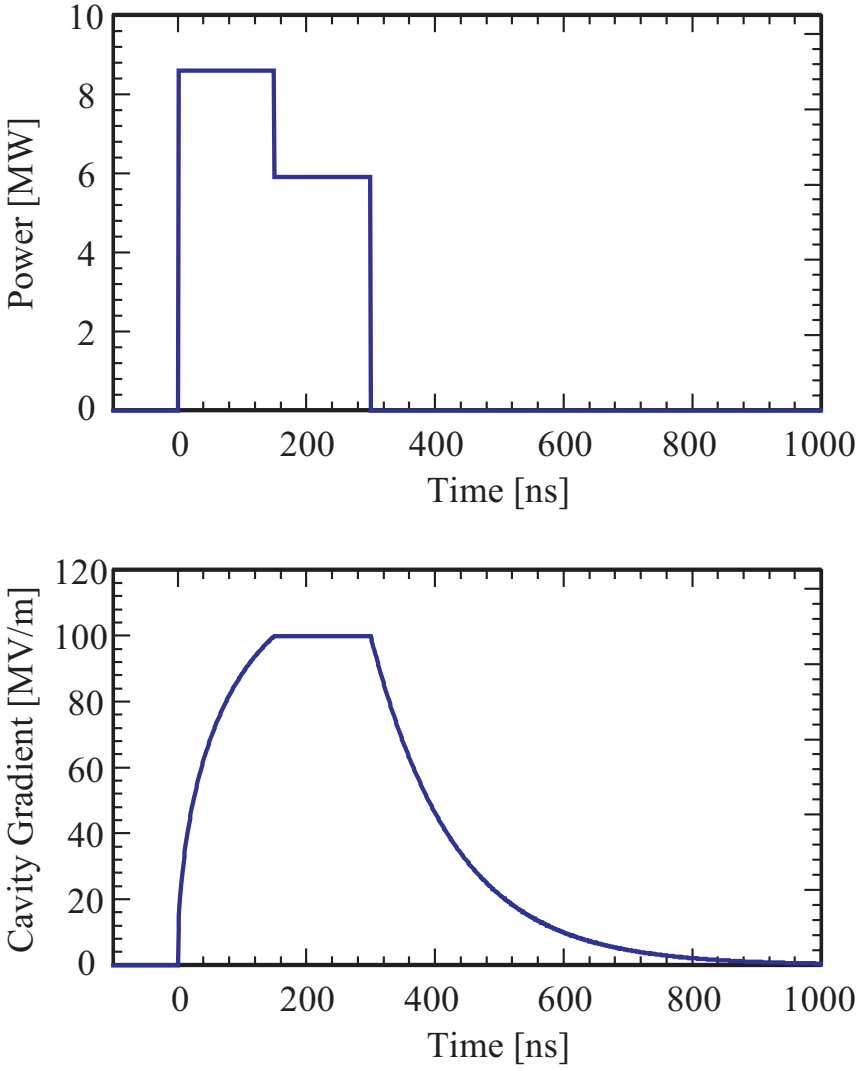

Figure 6-15: Shaped input power pulse, and cavity accelerating gradient as functions of time.

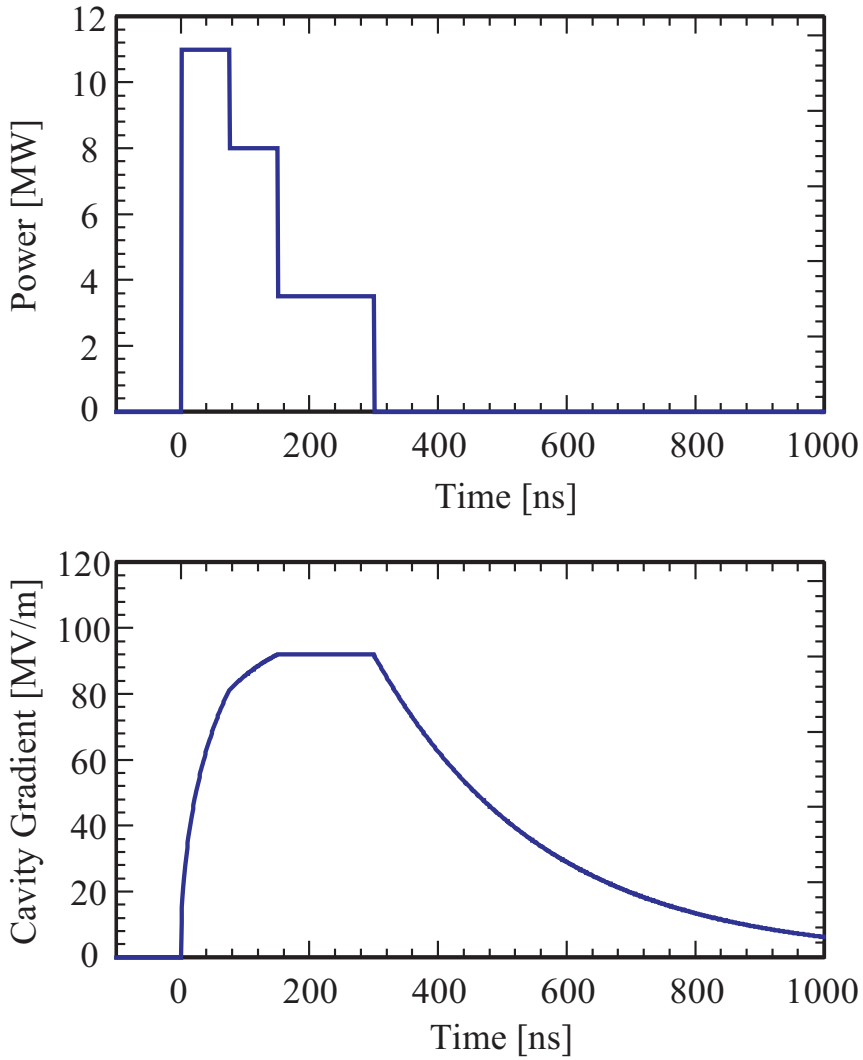

Figure 6-16: Input power pulse, and cavity accelerating gradient as functions of time for the approximate input power of Figure 6-13.

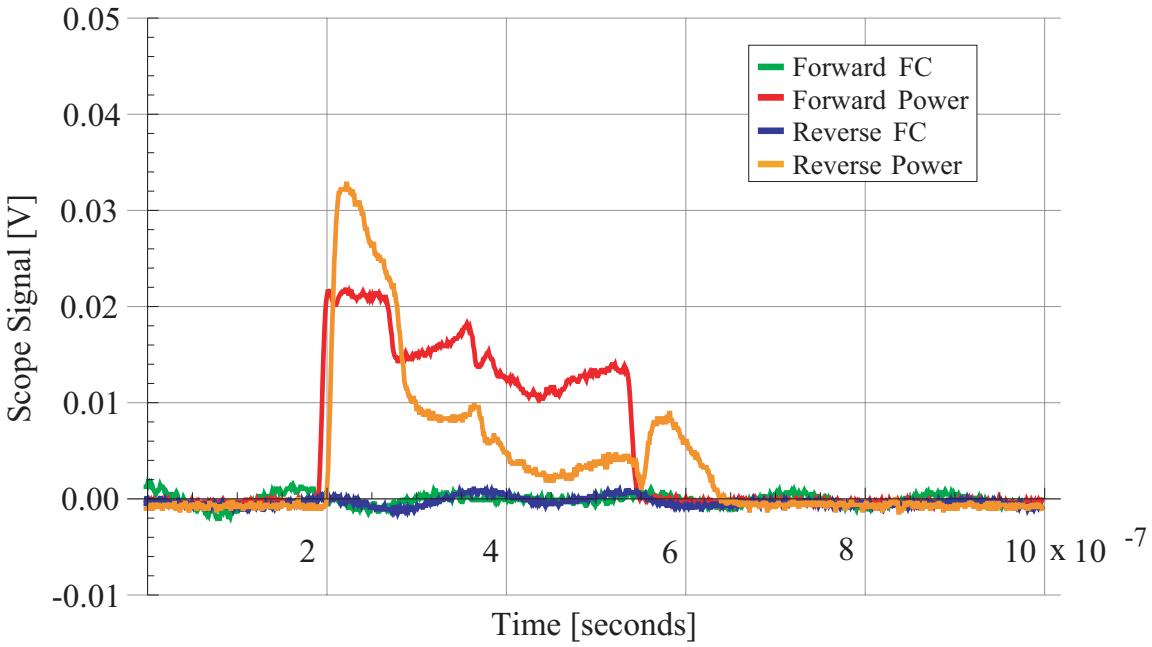

Figure 6-17: Breakdown structure scope traces (uncalibrated) for non-breakdown event. Forward and reverse power in structure, forward and reverse Faraday cup signals. The forward power into the structure (from the peak power meter) was 5.0 MW for this shot.

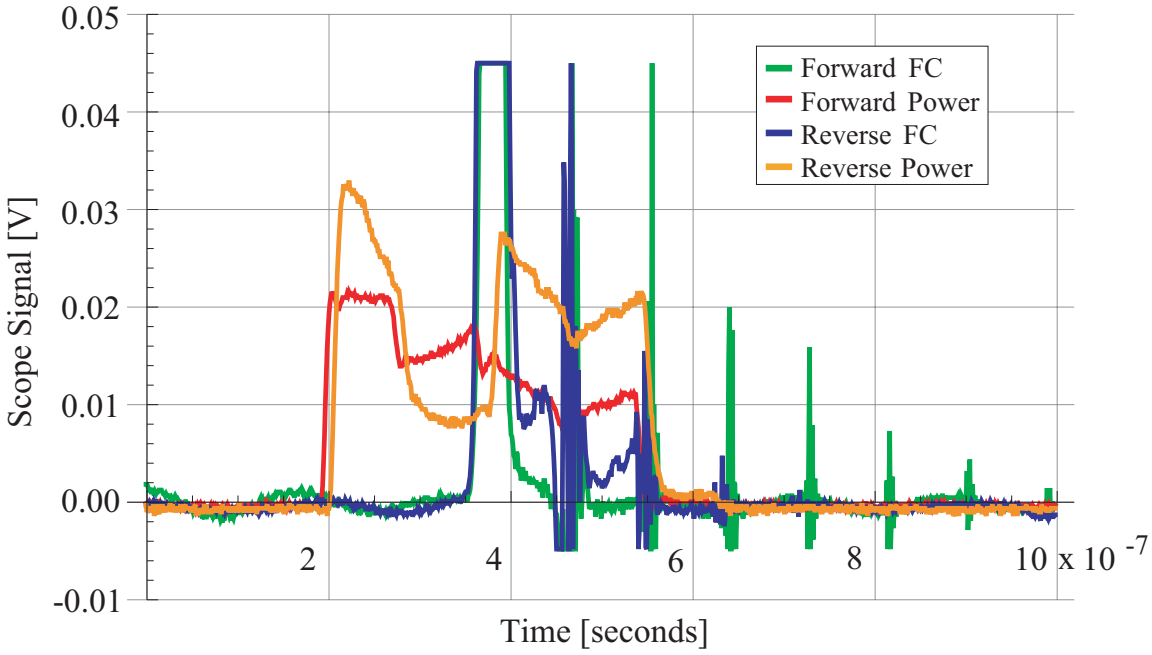

Figure 6-18: Breakdown structure scope traces (uncalibrated) for breakdown event. Forward and reverse power in structure, forward and reverse Faraday cup signals. The forward power into the structure (from the peak power meter) was 5.0 MW for this shot.

6.4 Data Analysis

The peak power meter and scope traces provide the bulk of information concerning the structure performance, but must be processed to provide useful structure information. Breakdown data sets are derived from the scope traces. Power levels and pulse length information is derived from peak power meter data with overlapping temporal coverage of each breakdown data set. These measured power levels are then scaled into structure field information by cross-calibration with *HFSS* simulations. The accuracy of the calibrating simulations is confirmed by their close agreement with structure cold test data. *Mathematica* was used to handle the binary data sets, and individual programs were written to handle the individual tasks associated with the analysis [64]. Care was taken in these programs to efficiently use computational resources, which could easily be overwhelmed repeatedly searching through $\gtrsim 100$ MB files.

The *Mathematica* programs were each structured as modules, so that variable names could be meaningful and reused, without interfering with each other. Three programs functioned to read peak power meter traces, and scope trace headers and traces. These programs kept track of data headers and separators, and each binary data point, so that the data could be separated into data sets. The sets were handled by programs which functioned as loops that ran through each large binary file for shots, or processed information of interest. The following Sections describe the operation of these programs in detail.

6.4.1 Data Processing

Binary data sets are produced for both peak power meter and scope traces. Peak power meter data accumulates in dated data sets, which become quite large: $\gtrsim 100$ MB. Each peak power meter trace set is prefaced with a header, which must be read accurately prior to reading out the bits that represent the trace itself. The header contains time indexing information both in regard to when the data was stored, and the various scope settings and offsets that must be applied to calibrate the trace axes.

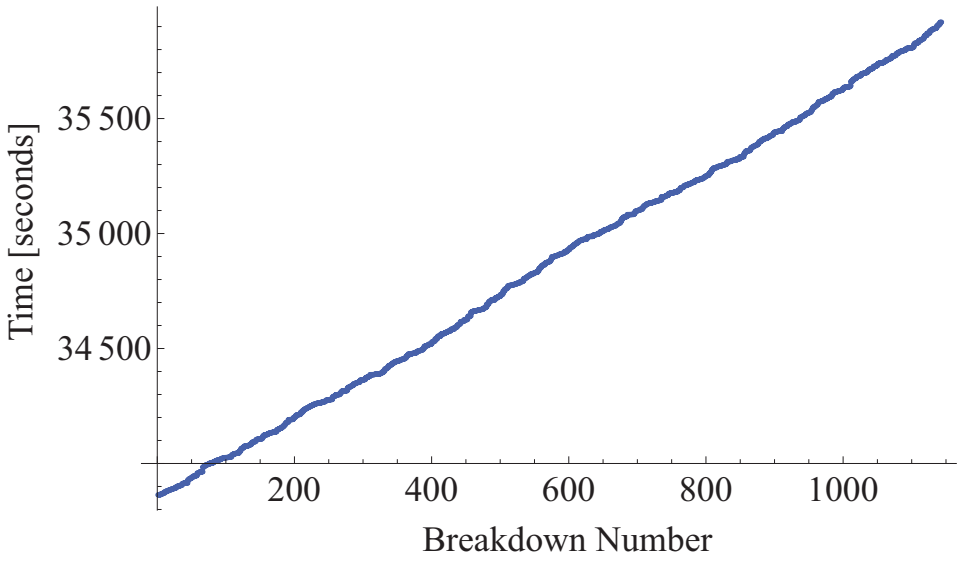

Figure 6-19: Time history of breakdowns for an individual breakdown scope trace data set.

Scope traces are saved in smaller data sets between parameter changes by the test station operator. Scope traces contain both breakdown pulses, exempla gratia, Figure 6-18, and the pulses immediately prior, exempla gratia, Figure 6-17. Breakdown pulses are characterized by an increased power reflection prior to the termination of the forward power, and a dramatic increase in the dark current measured by the Faraday cups. For processing purposes, an off-scale Faraday cup measurement of the dark current was used and verified as indicative of breakdown events. The scope traces contain separate header files, which are indexed with scope settings and temporal calibrations. The timing of the individual shots is stored to millisecond accuracy (sufficient for 60 Hz operation) in the traces themselves. The scope traces provide breakdown data sets with regard to time. The time history of breakdown can then be viewed, as shown in Figure 6-19. The total number of breakdowns in a given time span provides a breakdown rate, quoted after [56] as number per hour at 60 Hz.

Further information is encoded in the breakdown data time series. The time between breakdowns can be calculated directly from the data shown in Figure 6-19, as shown in Figure 6-20. The distribution of these points is shown in the histogram of Figure 6-21. A large number of breakdown events are followed immediately by a subsequent breakdown; a phenomenon that has been observed, but not quantified

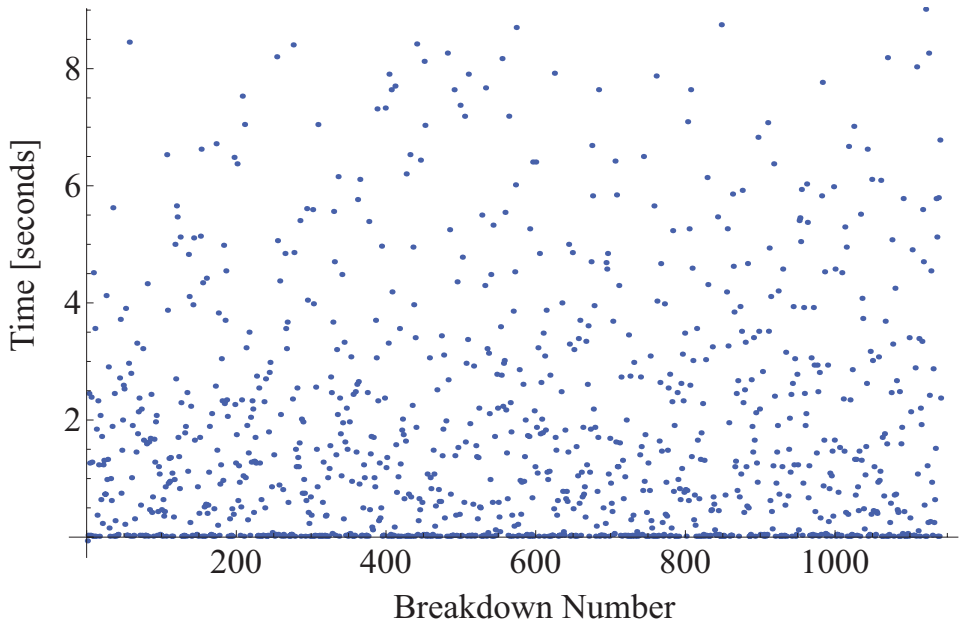

Figure 6-20: Time spacing between breakdowns for an individual breakdown scope trace data set.

as is possible with the large collection of data resulting from this testing process. The percentage of immediate breakdown events ranges from $\sim$ 25–65%. Excluding the singularity for immediate breakdown, the shape of the distribution is roughly exponential, and can be fit as shown in Figure 6-21.

Once breakdown data sets have been generated and a breakdown rate for the data set has been calculated, a power level needs to be attached as well. The time indexing of the breakdown events gives a time span over which the relevant data was taken. The peak power meter data for this time span is then sampled and a pulse length and nominal power level is calculated.

6.5 Structure Performance Comparison

6.5.1 Pillbox Data Analysis

The PBG breakdown structure was designed to be directly compared with a series of SLAC structures, 1C-SW-A5.65-T4.6-Cu, designed by B. Spataro of INFN, Frascati [58, 59]. This is the SLAC baseline pillbox structure shown in Figure 5-2 and

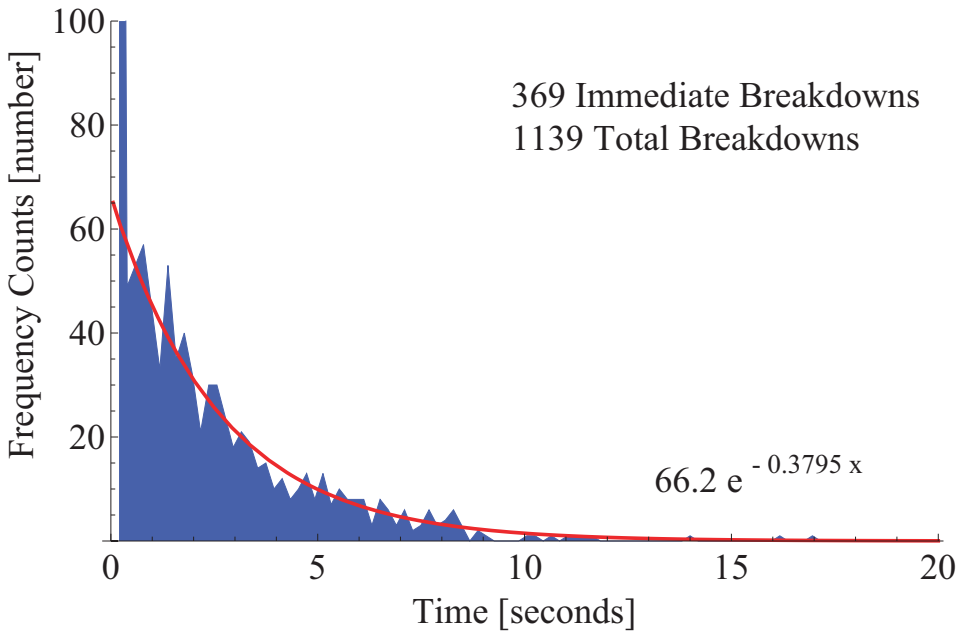

Figure 6-21: Histogram of data plotted in Figure 6-20. Data is truncated to show detail; first bin height is actually 369. Exponential fit to data is made excluding the first bin.

Figure 5-3. The iris geometry for both structures is identical, as required by the shared fixed design parameters in Table 5.2. Analysis of the data for SLAC indexed structure 1C-SW-A5.65-T4.6-Cu-Frascati-#2 provides pillbox comparison data for analysis of the PBG structure results. Full analysis of the pillbox data was performed to limit systematic error arising from differences in analysis techniques.

The steps discussed in Section 6.4.1 and Section 5.3.6 were repeated for the data supplied by SLAC for the pillbox structure. The same *Mathematica* programs were run for the additional data set to produce breakdown rates and power levels. *HFSS* simulations were run to produce the calibration figures shown previously in Table 5.6.

6.5.2 Breakdown Data

Breakdown rates are an exponential process for which there is always a probability of an accelerator structure breaking down, but that probability is higher as the operating gradient of the structure is increased. There is no threshold for breakdown, there is the two dimensional expression of breakdown rates for field levels. The behavior of

breakdown changes as a function of pulse length as well; at a longer pulse length a lower gradient can be maintained at a given breakdown rate, or for the same gradient a higher breakdown rate will be observed.

For the PBG structure, breakdown rates were observed for 150, 170, 300, 360, and 600 nanosecond pulse lengths. Complete data is shown in Tables 6.4, 6.2, 6.6, 6.3, and 6.5. Comparison with pillbox structure data was possible for 170 and 600 nanosecond pulse lengths, with complete data shown in Tables 6.7 and 6.8. As discussed in Section 6.4.1, all data was actually taken with respect to input power, which is rescaled to field information. It is the field properties, gradient, and maximum surface electric field, which are believed to be critical for breakdown. The maximum surface magnetic field is associated with pulsed heating, as described in Section 2.2.4. Equation 2.7 allows an additional rescaling of field data to pulsed temperature rise. This temperature rise is calculated for the flat portion of the pulse; the total temperature rise is higher, and is discussed in more detail in Section 6.5.3. The data was taken in the order indicated over approximately two weeks of operating time. The variation in pulse length and power level can be traced for each structure. The total number of shots in each data set is also shown.

The testing history is generally from shorter to longer pulse lengths, and higher to lower power. These shots are not the only shots the structure experiences, they are only data sets at relatively constant breakdown rate. To investigate the total time history of the structures, the peak power meter traces can be examined to look at the total field, or pulsed heating experienced by the structure as a function of time, as is discussed in Section 6.5.3.

6.5.3 Time History of Testing

A full understanding of the time history of the testing process requires a calculation of pulsed heating, including the contribution from the shaped portion of the rf pulse, and shots that were not included in breakdown data sets. Pulsed heating temperature rise was previously calculated using Equation 2.7 and the numerical values in Table 2.3.

Equation 2.8 is calculated numerically for all peak power meter data, which rep-

Order [#]	Gradient [MV/m]	Electric [MV/m]	Magnetic [kA/m]	BD/hour [#]	Heating [K]	Shots [#]
1	101	210	894	995.20	141	1.4×10^5
17	92	192	816	169.36	117	7.3×10^4
18	82	171	730	115.14	94	6.3×10^5
19	78	162	692	57.04	84	1.7×10^5
20	77	160	682	41.36	82	1.2×10^6
21	74	153	653	14.81	75	1.3×10^6
22	68	141	599	4.13	63	6.3×10^5
23	65	135	577	1.94	59	1.2×10^6

Table 6.2: PBG structure analysis result for 170 nanosecond pulse length.

Order [#]	Gradient [MV/m]	Electric [MV/m]	Magnetic [kA/m]	BD/hour [#]	Heating [K]	Shots [#]
2	101	210	894	8042.55	205	5.6×10^3
3	116	242	1032	7266.93	273	1.1×10^4
4	105	218	930	2303.15	222	1.3×10^4
5	103	215	916	741.73	215	7.0×10^3
6	96	199	848	1030.88	184	6.0×10^4
7	93	193	824	441.26	174	2.8×10^5
8	87	182	774	119.64	154	3.6×10^5
9	77	160	682	42.61	119	1.1×10^6

Table 6.3: PBG structure analysis result for 360 nanosecond pulse length.

Order [#]	Gradient [MV/m]	Electric [MV/m]	Magnetic [kA/m]	BD/hour [#]	Heating [K]	Shots [#]
10	112	233	992	3676.23	163	9.3×10^3
11	116	241	1025	3122.50	174	6.4×10^4
12	114	238	1012	1995.91	170	1.2×10^5
13	113	235	999	1852.34	165	5.4×10^4
14	105	218	930	424.31	143	5.0×10^4
15	100	208	886	248.29	130	2.8×10^5
16	92	192	816	67.41	110	1.5×10^5
32	91	190	808	248.79	108	5.1×10^5
33	87	182	774	179.02	99	1.2×10^5
34	78	162	692	74.93	79	5.9×10^5
35	75	156	663	7.55	73	1.0×10^6
36	71	148	632	6.02	66	1.8×10^6
37	66	138	588	6.85	57	8.2×10^5
38	64	133	565	4.65	53	2.0×10^6

Table 6.4: PBG structure analysis result for 150 nanosecond pulse length.

Order [#]	Gradient [MV/m]	Electric [MV/m]	Magnetic [kA/m]	BD/hour [#]	Heating [K]	Shots [#]
24	82	171	730	253.26	176	4.3×10^5
25	76	158	673	102.09	150	3.6×10^5
26	77	160	682	206.15	154	4.0×10^5
27	68	142	605	113.78	121	5.3×10^5
28	64	133	565	75.33	106	5.8×10^5
29	62	130	553	13.75	101	3.0×10^5
30	61	127	541	42.16	97	2.7×10^5
31	58	121	516	14.28	88	8.9×10^5

Table 6.5: PBG structure analysis result for 600 nanosecond pulse length.

Order [#]	Gradient [MV/m]	Electric [MV/m]	Magnetic [kA/m]	BD/hour [#]	Heating [K]	Shots [#]
39	72	151	642	37.88	97	4.4×10^5
40	65	135	577	14.73	78	1.1×10^6
41	58	121	516	9.09	62	9.7×10^5
42	52	108	461	0.96	50	2.7×10^6

Table 6.6: PBG structure analysis result for 300 nanosecond pulse length.

Order [#]	Gradient [MV/m]	Electric [MV/m]	Magnetic [kA/m]	BD/hour [#]	Heating [K]	Shots [#]
1	108	228	479	77.84	40	9.7×10^4
2	104	219	461	11.81	37	4.2×10^5
3	102	215	452	11.22	36	3.9×10^4
4	101	213	447	17.06	35	6.3×10^4
5	104	219	461	30.08	37	1.8×10^5
6	99	210	442	13.11	34	2.1×10^6
7	96	203	428	8.30	32	2.6×10^6
8	94	198	417	3.12	31	2.7×10^6
26	120	254	534	110.39	50	2.7×10^5
27	90	191	402	0.65	28	1.3×10^6

Table 6.7: Pillbox structure analysis result for 170 nanosecond pulse length.

Order [#]	Gradient [MV/m]	Electric [MV/m]	Magnetic [kA/m]	BD/hour [#]	Heating [K]	Shots [#]
9	102	215	452	1747.54	68	2.0×10^4
10	95	201	423	1224.74	59	8.6×10^3
11	90	191	402	12.15	53	4.3×10^5
12	97	206	432	230.05	62	1.0×10^4
13	97	206	432	169.12	62	4.6×10^5
14	97	206	432	99.19	62	4.4×10^5
15	97	206	432	143.89	62	4.6×10^5
16	95	201	423	40.55	59	6.8×10^5
17	87	183	386	12.11	49	4.3×10^5
18	86	181	380	46.21	48	2.7×10^5
19	84	178	375	7.30	46	4.4×10^5
20	84	178	375	17.99	46	4.9×10^5
21	84	178	375	12.11	46	8.9×10^5
22	80	170	357	3.55	42	7.9×10^5
23	80	170	357	4.90	42	1.9×10^6
24	76	161	339	0.71	38	9.1×10^5
25	78	164	345	2.36	39	1.5×10^6

Table 6.8: Pillbox structure analysis result for 600 nanosecond pulse length.

resents a uniform sampling of all high power structure shots. The result is plotted as a function of shot number for both the PBG and pillbox structures, in Figure 6-22 and Figure 6-23, respectively. The shot numbers correspond to two second sampling: a total of 120 shots occur for each peak power meter calculation.

The PBG structure was tested in the order shown in Tables 6.4, 6.2, 6.6, 6.3, and 6.5, as well as in Figure 6-22, for several reasons. At high breakdown rates, data can be gathered quickly, because many breakdown events are occurring. At low breakdown rates, many shots, and eventually many hours of operation are necessary to gather data. High breakdown rate data is gathered while an operator is present, and can change the experimental parameters in real time; low breakdown rate data is gathered later in the day, when the test stand can be left running unattended. As can be seen in Figure 6-23, pillbox structures have less pulsed heating, when compared with PBG structures. Previous experience with pillbox structures, may have led SLAC operators to damage the PBG structure unintentionally in their pursuit of high gradient results. The PBG structure is the first of its kind to be tested, motivating

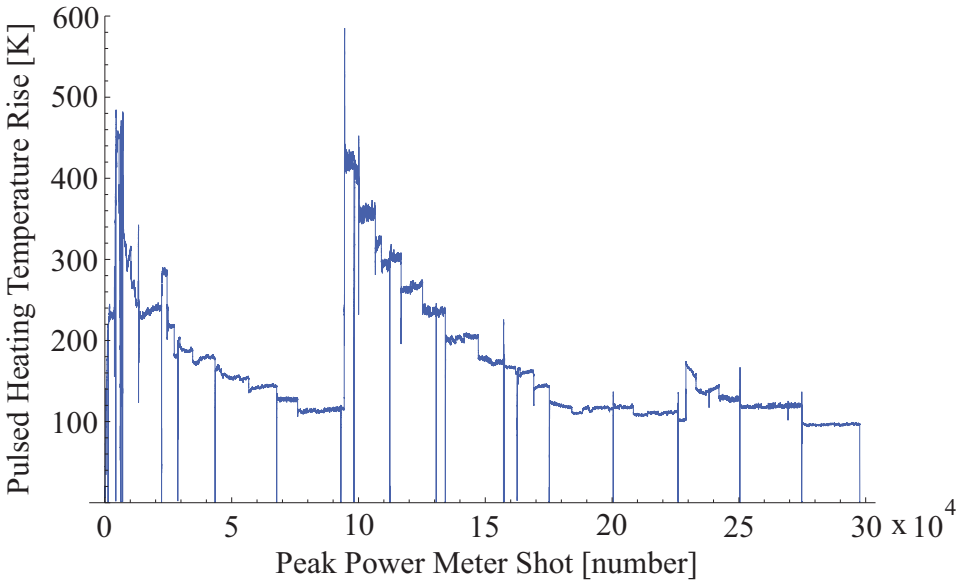

Figure 6-22: Pulsed heating temperature rise calculated for entire rf pulse using Equation 2.8 for all peak power meter shots for the PBG structure.

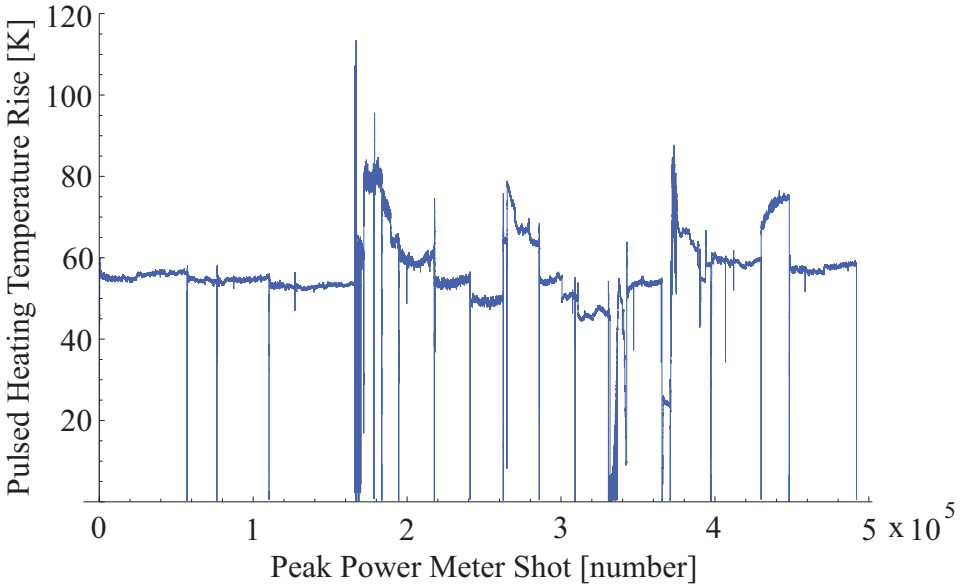

Figure 6-23: Pulsed heating temperature rise calculated for entire rf pulse using Equation 2.8 for all peak power meter shots for the pillbox structure.

the pursuit for as large a dataset as possible. A larger variation in gradient and pulse length was explored in the PBG structure, with comparison to the pillbox structure. This also impacts the large variation in pulsed heating, as the pulse length is varied from 150–600 nanoseconds.

The PBG structure had two large excursions to quite high pulsed heating temperature rises, with a maximum of 585 K, and an average pulsed heating temperature rise of 168 K for 35×10^6 shots. The pillbox structure on the other hand experienced quite mild pulsed heating temperature rise, with a maximum of 114 K, and an average of 56 K for 59×10^6 shots. It is possible that the large excursions to very high temperature rise damaged the PBG structure. It is also possible that the first excursion to high temperature rise, which occurred early in the testing process, damaged the structure, and unduly influenced all subsequent breakdown testing results.

Gradient and Electric Field

Comparison of PBG and pillbox breakdown rates are shown as functions of gradient, and peak surface electric field in Figure 6-24 and Figure 6-25 for 170 nanosecond pulse length, and Figure 6-26 and Figure 6-27 for 600 nanosecond pulse length, respectively. For both pulse lengths the gradient achievable in the PBG structure is less than that reached in the pillbox structure. This can be alternatively phrased that for a given gradient or peak surface electric field, the breakdown rate in the PBG structure was higher than that in the pillbox structure.

Breakdown phenomena are generally understood in terms of maximum surface field, as discussed in Section 2.2. This is not what is seen in Figures 6-25 and 6-27. The performance of the two structures is not identical when compared in terms of peak surface electric field. The PBG structure has a surface field of 208 MV/m for a 100 MV/m accelerating gradient, compared to 211 MV/m peak surface field for the pillbox structure. These nearly identical values would predict that only minor fabrication differences would significantly impact the breakdown performance of the structures. This is not what is seen in Figures 6-24 and 6-26.

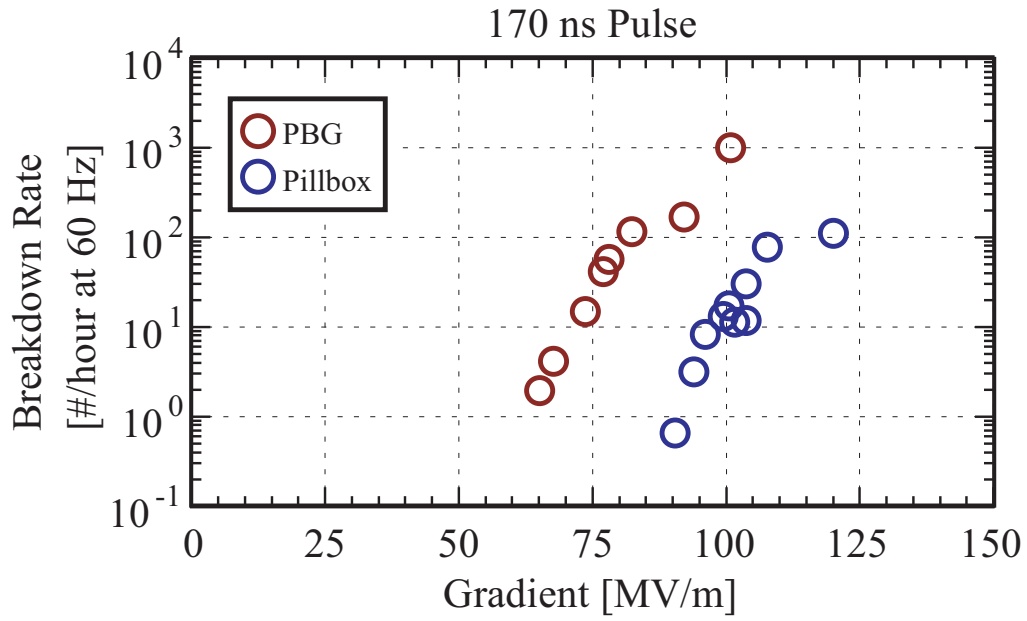

Figure 6-24: Breakdown rate versus accelerating gradient for PBG and Pillbox structures, in red and blue circles respectively. 170 nanosecond pulse length.

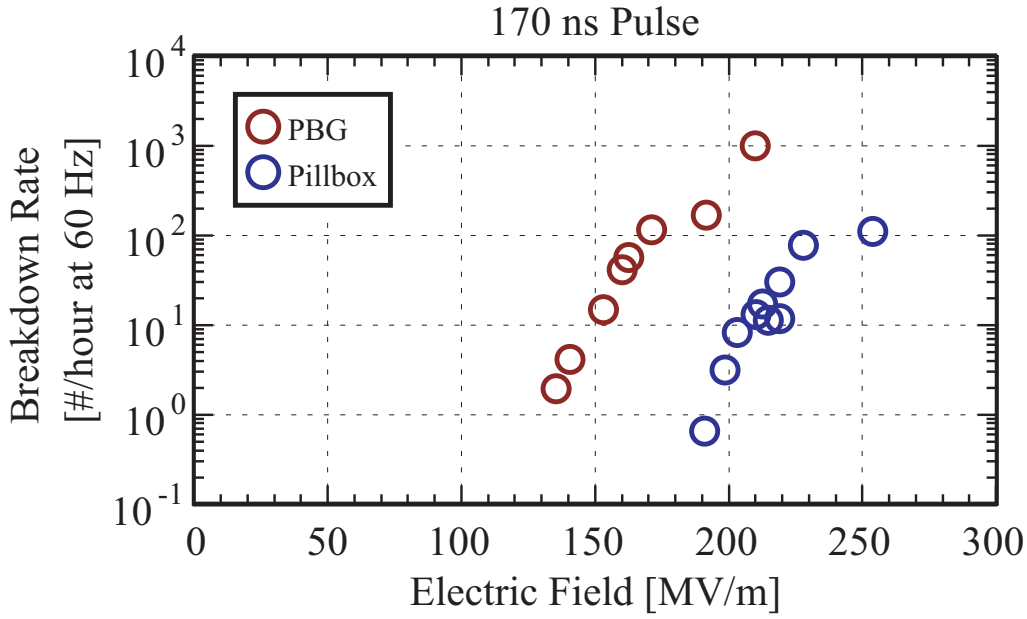

Figure 6-25: Breakdown rate versus peak surface electric field for PBG and Pillbox structures, in red and blue circles respectively. 170 nanosecond pulse length.

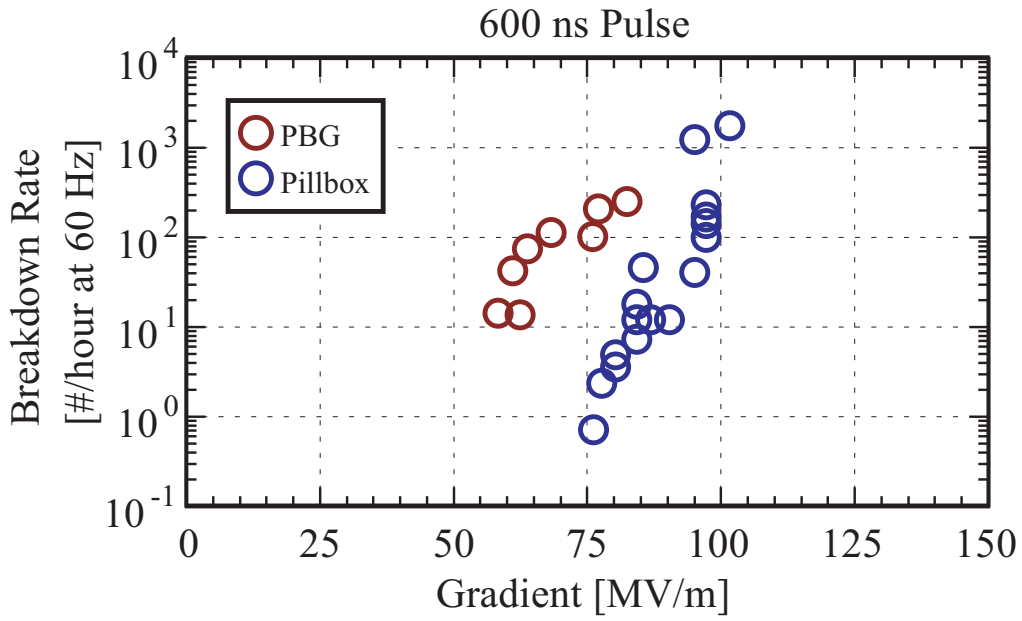

Figure 6-26: Breakdown rate versus accelerating gradient for PBG and Pillbox structures, in red and blue circles respectively. 600 nanosecond pulse length.

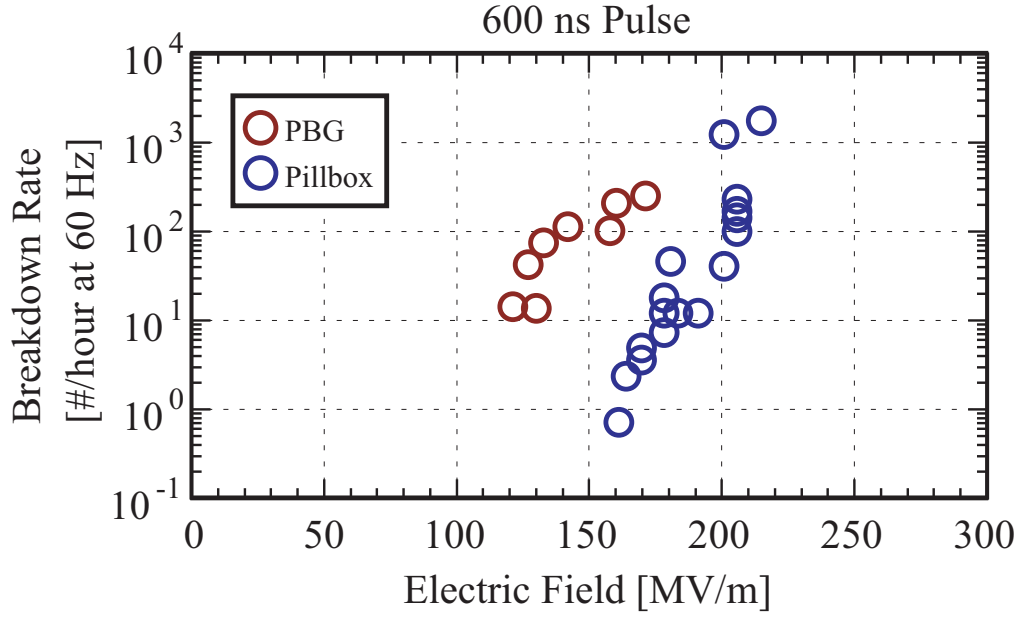

Figure 6-27: Breakdown rate versus peak surface electric field for PBG and Pillbox structures, in red and blue circles respectively. 600 nanosecond pulse length.

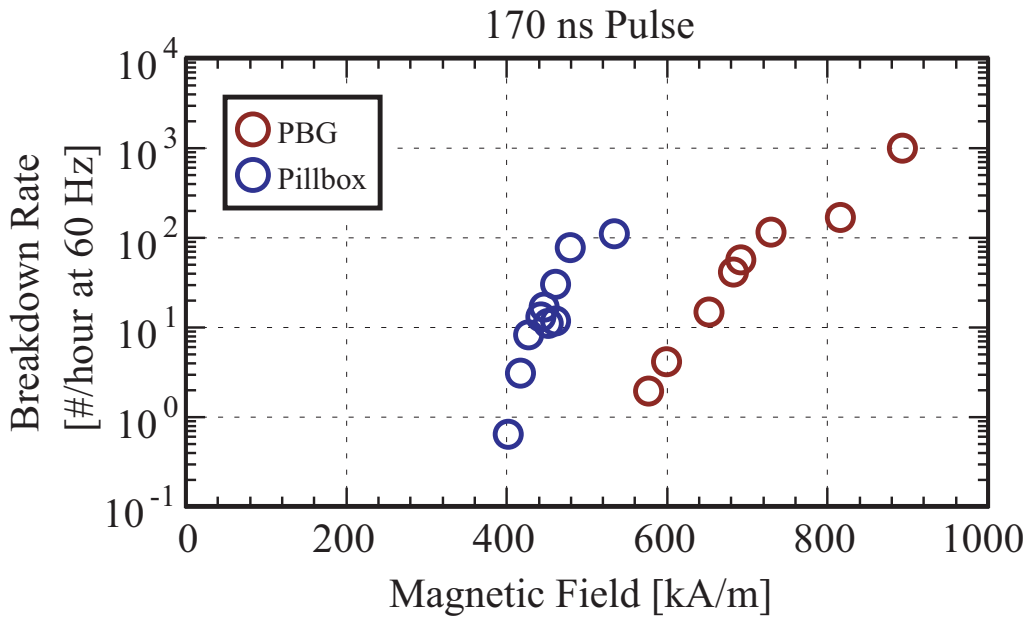

Figure 6-28: Breakdown rate versus peak surface magnetic field for PBG and Pillbox structures, in red and blue circles respectively. 170 nanosecond pulse length.

Magnetic Field and Pulsed Heating

Comparison of PBG and pillbox breakdown rates are shown as functions of peak surface magnetic field in Figure 6-28 and Figure 6-29 for 170 and 600 nanosecond pulse length, respectively. The peak magnetic field is much higher in the PBG structure. This large variation in magnetic field performance is of great interest because all single cell standing wave breakdown tests prior have been done with structures of nearly identical magnetic field performance.

Large variations have been observed in gradient, or electric field performance when the structure iris geometry or aperture is changed, as shown in Figure 6-30. When plotted versus peak magnetic field, the data for various pillbox structures collapses, as shown in Figure 6-31 appearing consistent with being from the same structure.

The high magnetic field in the PBG structure tests will result in high pulsed heating, according to Equation 2.7. Figure 6-32 and Figure 6-33 show the breakdown rate as a function of temperature rise, for pulse lengths of 170 and 600 nanoseconds. A pulsed heating temperature rise of 50 K is deemed safe for long term structure operation. For realistic application, PBG structures must be redesigned or restricted

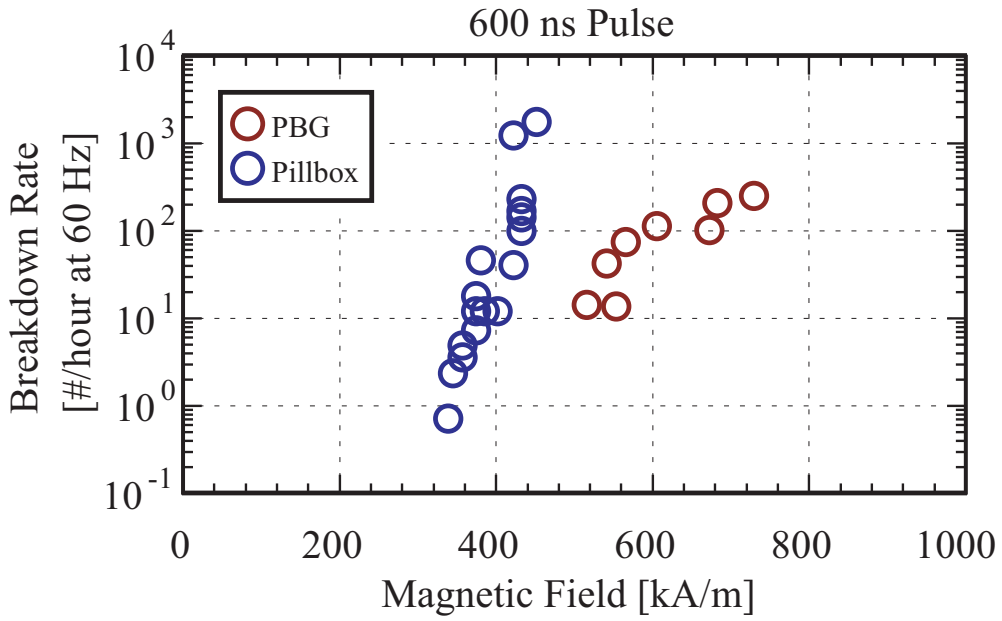

Figure 6-29: Breakdown rate versus peak surface magnetic field for PBG and Pillbox structures, in red and blue circles respectively. 600 nanosecond pulse length.

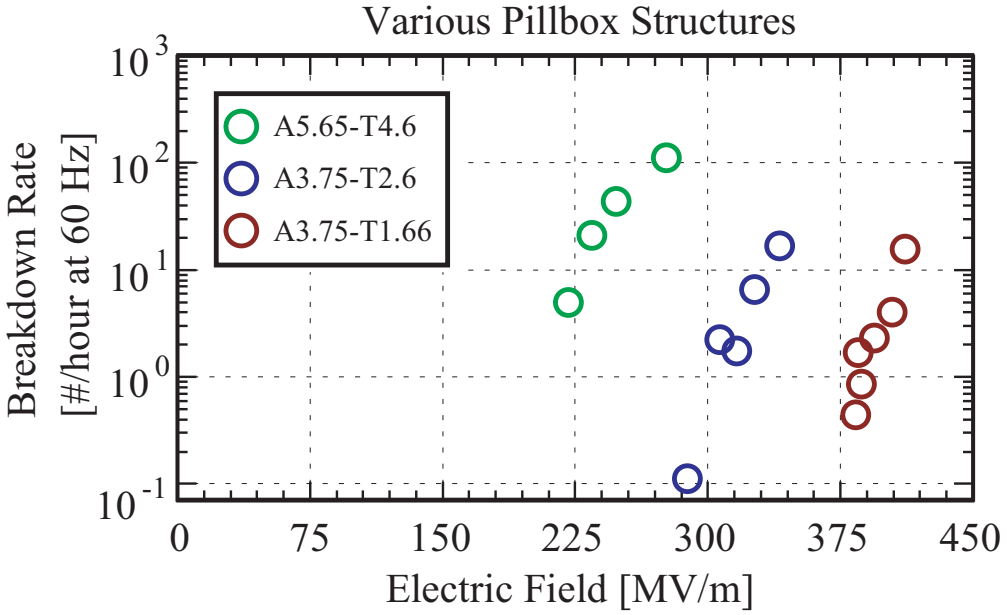

Figure 6-30: Breakdown rate versus peak surface electric field for various pillbox structures [65].

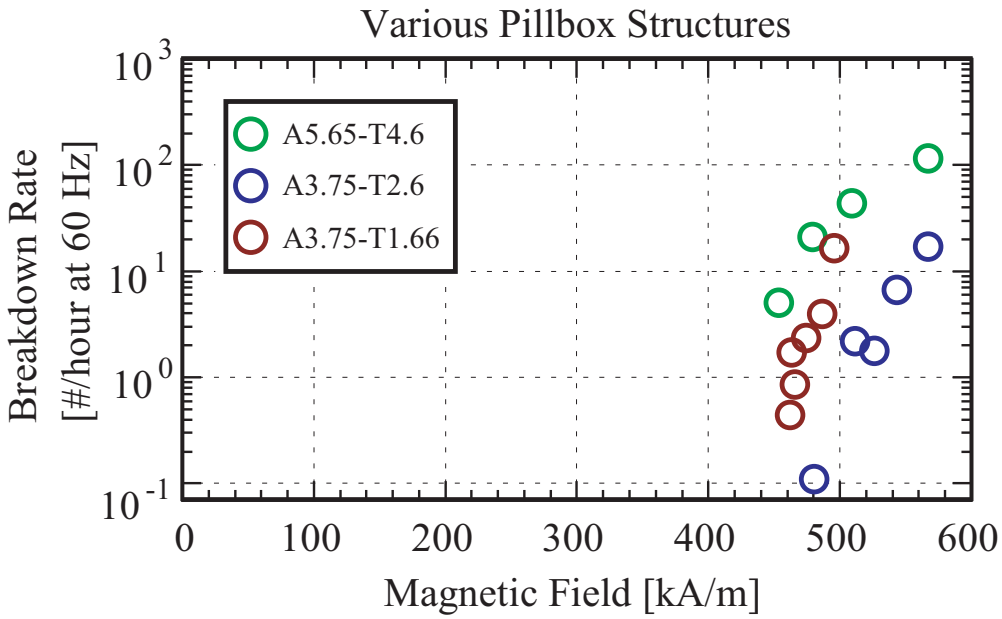

Figure 6-31: Breakdown rate versus peak surface magnetic field for various pillbox structures [65].

to perform at lower gradient levels to maintain allowable temperature rise on the rods.

6.6 PBG Structure Autopsy

Once high power testing of the PBG structure is complete, it is removed in the same semi-clean conditions it was installed under. Cold test of the structure is repeated to confirm structure parameters after testing, and quantify damage prior to destructive surface imaging. Borescope images provide a view of the structure surface prior to cutting it for scanning electron microscope (SEM) imaging.

6.6.1 Cold Test

Structure bead pull measurements are identical to those made prior to high power testing, as shown in Figure 6-34. Mode parameters have changed slightly from those of Table 6.1 to the values shown in Table 6.9. Damage in the central PBG cell has lowered the unloaded Q of the π-mode from 4695 to 4220. The mode frequency has

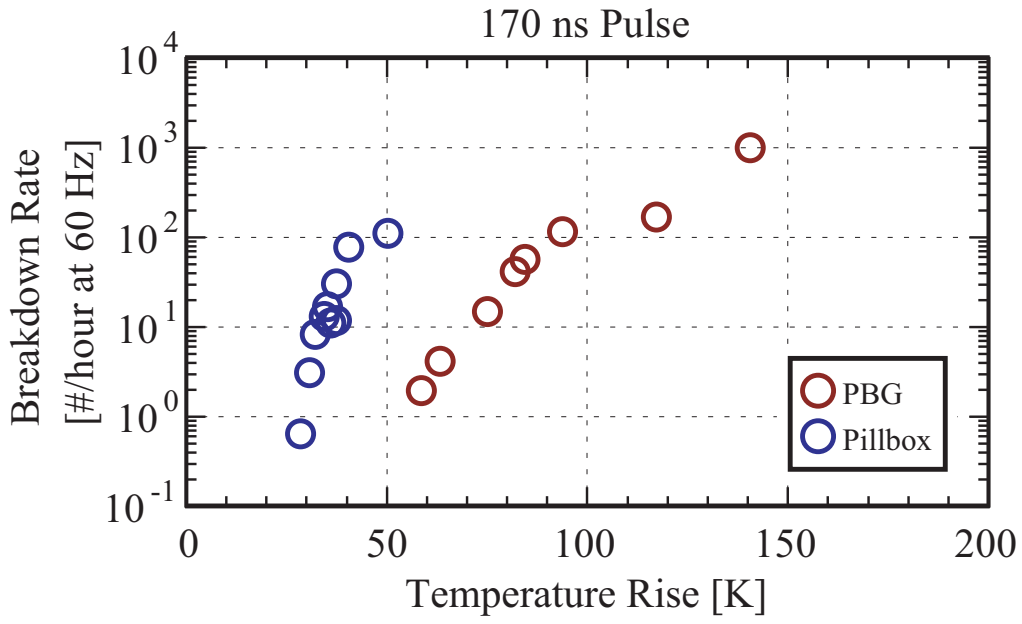

Figure 6-32: Breakdown rate versus pulsed temperature rise for PBG and Pillbox structures, in red and blue circles respectively. 170 ns pulse length.

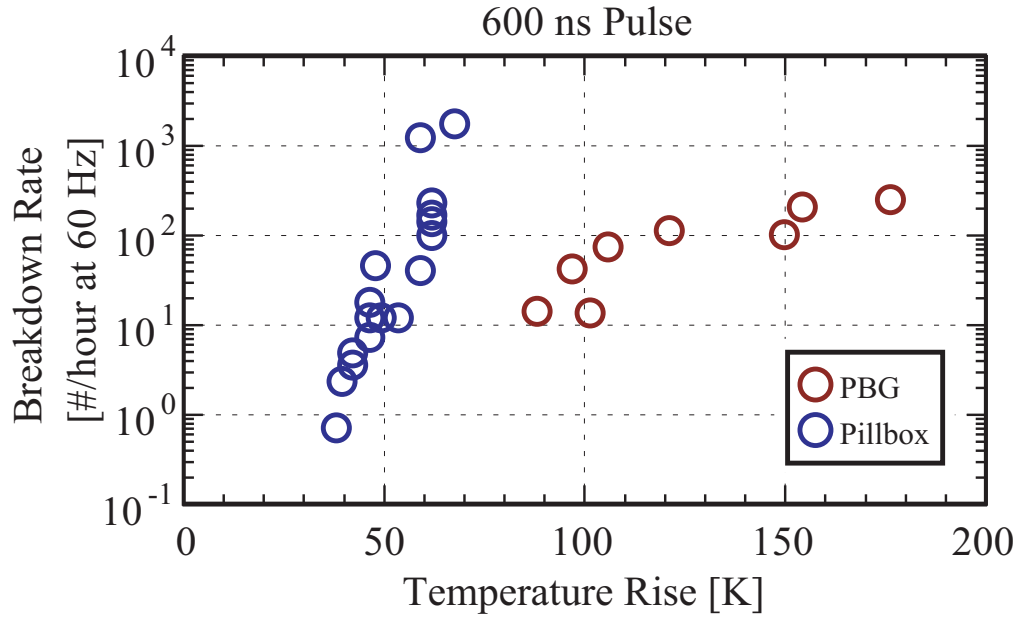

Figure 6-33: Breakdown rate versus pulsed temperature rise for PBG and Pillbox structures, in red and blue circles respectively. 600 ns pulse length.

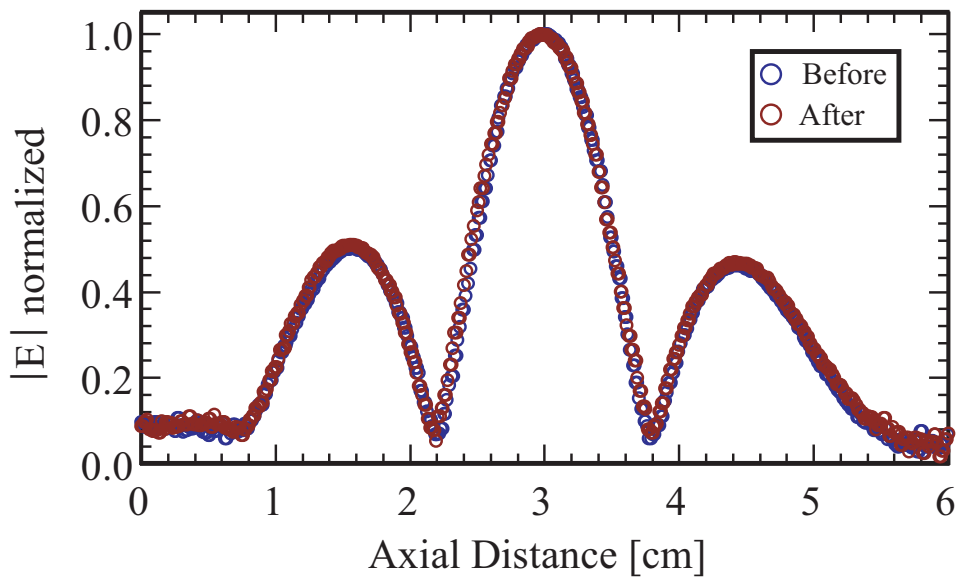

Figure 6-34: Bead pull result for "π-mode" before and after high power testing.

not shifted, implying that the cell geometry has not been altered; the rods themselves and the irises are intact. The change in Q means that the PBG cell is more lossy subsequent to testing.

6.6.2 Borescope

Borescope images provide a baseline for surface appearance, prior to the machining process of cutting the structure in half for SEM imaging. The high polish of the copper surface makes visual images less informative than SEM micrographs because of reflections. Figure 6-35 shows the PBG structure iris, which appears undamaged. Figure 6-36 shows the inner surface of one of the inner row of rods; pulsed heating damage is clear in the observable grain boundaries and surface roughness, similar to [15]. Figure 6-37 shows the brazed joint between an inner cylindrical rod and the flat iris end plate. The brazed joint formed between the cylindrical rods and the facing iris plate appears to be less than ideal. An overhang seems to be visible, and roughness is observed in the annular area of the braze. Borescope images are typically only taken after high power testing. Borescoping before high power testing would clearly indicate what surface features are a product of machining and which

Mode	Frequency [GHz]	Q		
		Q_0	Q_L	Q_{ext}
Before High Power Testing				
0	11.0036	8347	3390	5708
$\pi/2$	11.1397	9044	3796	6541
Coupler	11.3819	8299	4304	8941
π	11.4323	7401	4695	12844
Coupler	11.5517	12746	11224	9395
After High Power Testing				
0	11.0041	7695	3303	5789
$\pi/2$	11.1399	8998	3719	6341
Coupler	11.3820	6756	3874	9084
π	11.4334	6267	4220	12928
Coupler	11.5520	12867	11424	101862

Table 6.9: Table of measured Q values for PBG structure modes, before and after high power testing.

are the results of high power; a procedural change which has been suggested.

6.6.3 Scanning Electron Microscope

The PBG structure is cut in half and SEM micrographs are captured according to the key shown in Figure 6-38 [66]. The three irises are labeled A, B and C. The rods visible to direct SEM probing are labeled outward from 1–7. Rods 1, 2, and 3 are inner rods which saw large peak surface magnetic field, and the associated high currents and pulsed heating. Rods 4, 6, and 7 are outer rods, which provide a baseline for fabricated rod appearance, as very little field strength was experienced by these rods. The cutting was done such that no inner rods were intersected; rod 5 was cut roughly in half.

The structure irises are shown in Figure 6-39: A, B, and C correspond to the irises as labeled in Figure 6-38. In each case the bottom arc of the iris is shown, with the cut through the elliptically contoured iris visible at the bottom of the figure. Irises B and C saw high peak surface field, Iris A did not. No difference is observed in comparing the high field with the low field surfaces. No damage is observed. The surface roughness corresponds to that of the machining process; Figure 6-40 shows a detailed SEM micrograph of the iris surface.

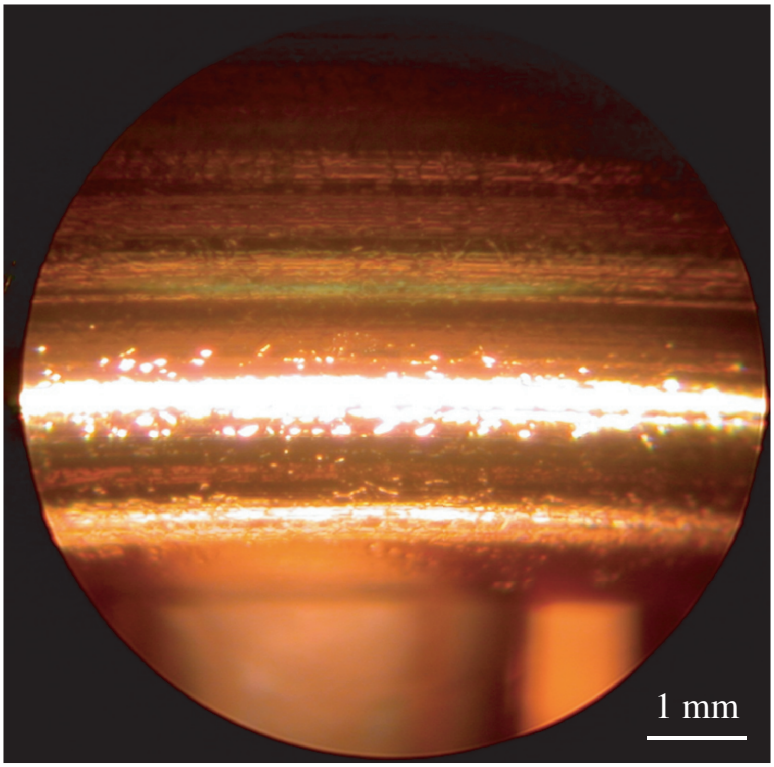

Figure 6-35: Borescope image of PBG structure iris.

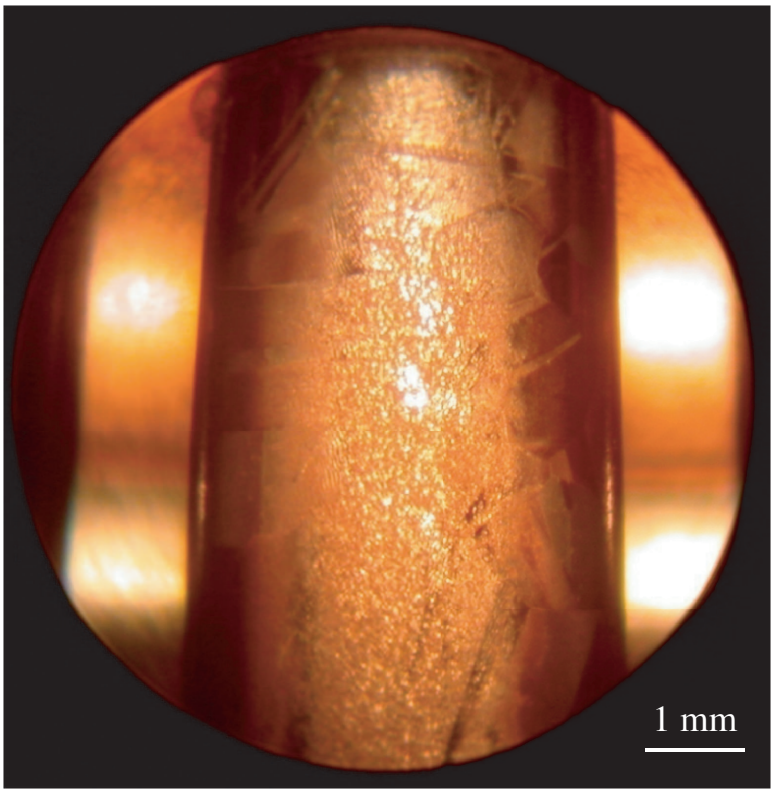

Figure 6-36: Borescope image of PBG structure inner rod.

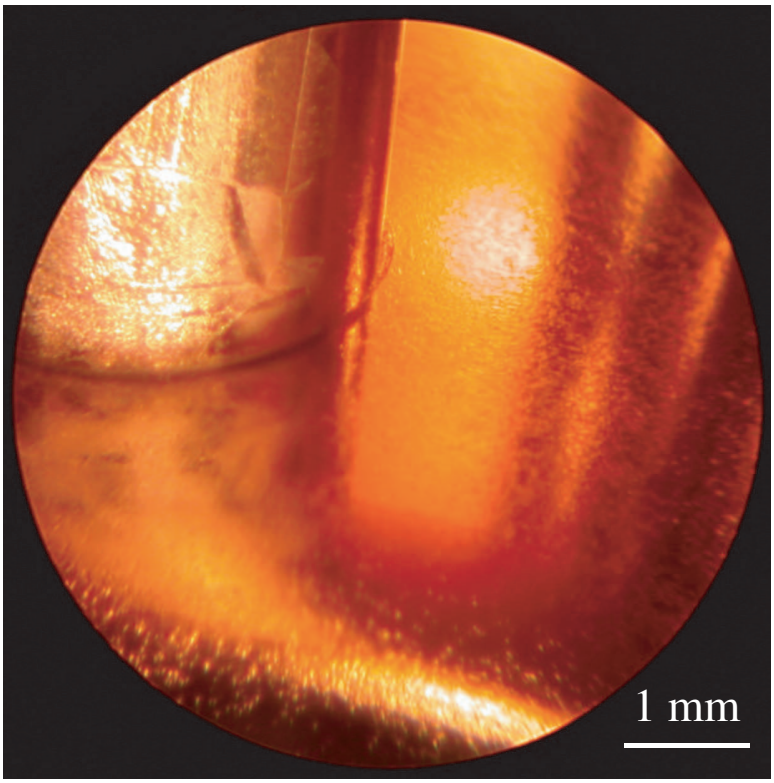

Figure 6-37: Borescope image of PBG structure rod braze joint.

The rods of the structure are shown in full in Figure 6-41; rod 5 is omitted. Grain growth on the high field facing surfaces of rods 1, 2, and 3 is clear. Rods 4, 6, and 7 serve as a control reference, as the field strength on these rods was very low.

Pulsed heating damage is observable on the inner edge of rods 1, 2, and 3. Progressively more detailed SEM micrographs are shown in Figure 6-42. Figure 6-42 B shows the growth of the grain boundaries, as detailed in Figure 6-42 C. Figure 6-42 D shows the growing surface roughness, as detailed in Figure 6-42 E.

The brazed and machined bases of rod 1 are shown in Figure 6-43 A and Figure 6-43 B, respectively. Grain growth and surface roughness are both observed. The damage on the brazed and machined bases is shown in detail in Figure 6-43 C and Figure 6-43 D, respectively. Very different damage patterns are observed on the brazed and machined ends. The machined end is damaged much as the rest of the rod: clear grains and surface roughness, especially along the grain boundaries. The brazed end of the rod is discontinuously damaged: the rod has an increased surface

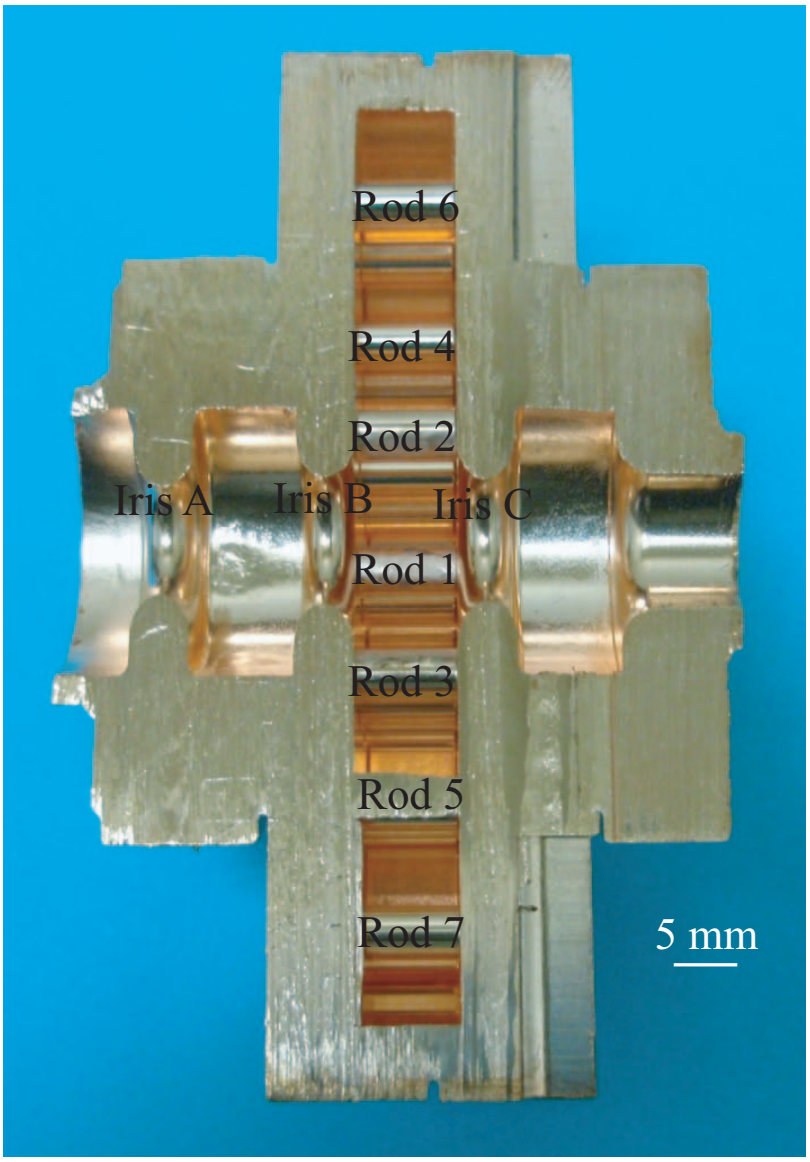

Figure 6-38: Key to Scanning Electron Microscope micrographs of PBG structure surface [66]. Irises are labeled A, B, and C: Iris A is the input coupler aperture, Irises B and C are the high electric field surfaces of the PBG test cell. Rods are numbered outwards 1–7: Rods 1, 2, and 3 are inner rods, which experienced high field strength; Rods 5, 6, and 7 are outer rods, which did not. The PBG structure was cut so that no inner rod was damaged, as a result Rod 5 was bisected.

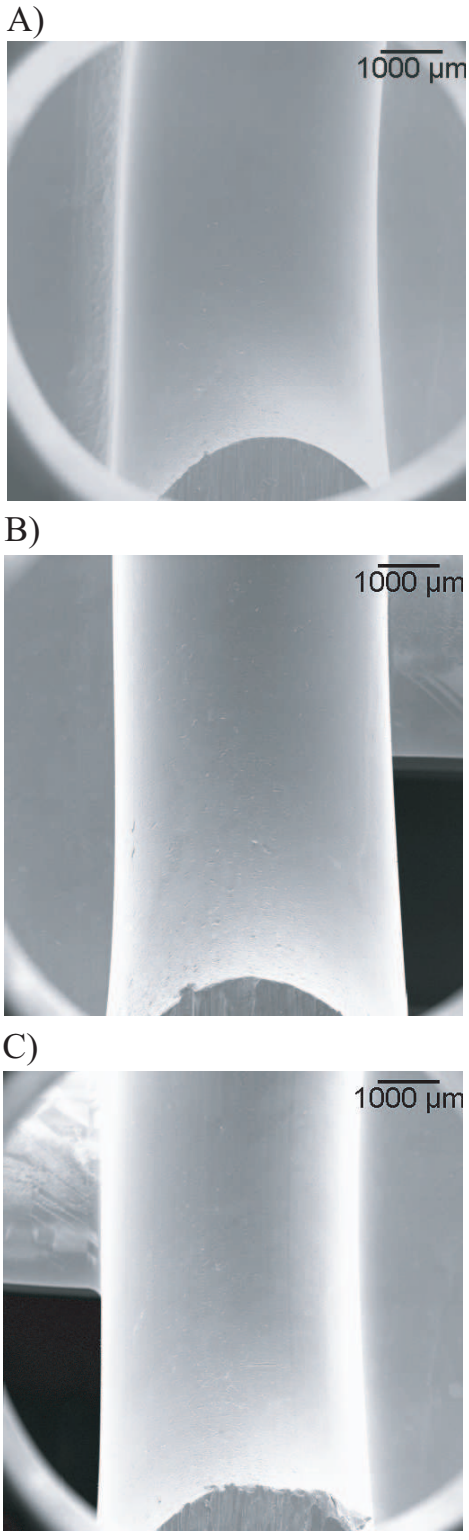

Figure 6-39: SEM micrographs of PBG structure irises [66]. Irises are labeled A), B), and C): A) is the input coupler aperture, B) and C) are the high electric field surfaces of the PBG test cell irises. No breakdown damage is observed.

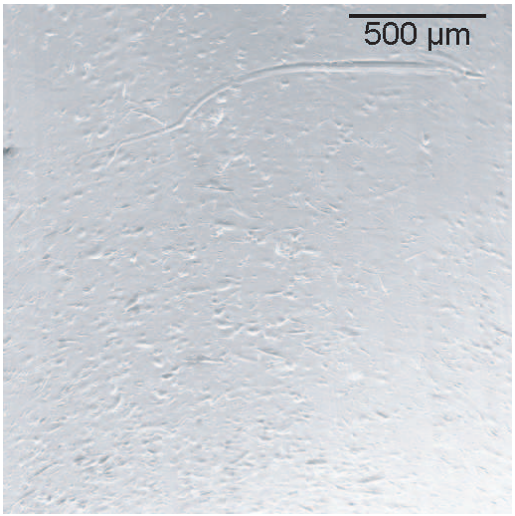

Figure 6-40: Detailed SEM micrograph of PBG structure iris [66]. Tool marks are visible, but no breakdown damage is observed under magnification.

roughness, but at the joint itself, very large accumulations of damage are observed. This pattern of damage is observed on rods 2 and 3 as well, as shown in Figure 6-45 and Figure 6-44.

Observation of the braze joint can be made on one of the outer rods, which saw little field, and no damage. Figure 6-46 A and Figure 6-46 B shows the brazed and machined ends of the rod, respectively. Figure 6-46 C shows the detail of the brazed joint. Braze material has collected annularly around the rod, and the joint itself is convex. Damage on both ends of rods 1, 2, and 3 shows no striking asymmetry. The discontinuity itself is not causing significantly more damage, but the additional material combined with the discontinuity are the source of the larger damaged spots seen in Figures 6-43, 6-45, and 6-44.

6.7 Hypothesis for the Explanation of Results

The breakdown testing results for the PBG structure are quite unexpected. Despite adopting the same iris geometry as the SLAC baseline pillbox structure, the breakdown performance of the PBG structure was lower by $\sim 40\%$ with respect to accelerating gradient. The maximum surface electric field is on the iris, as shown in

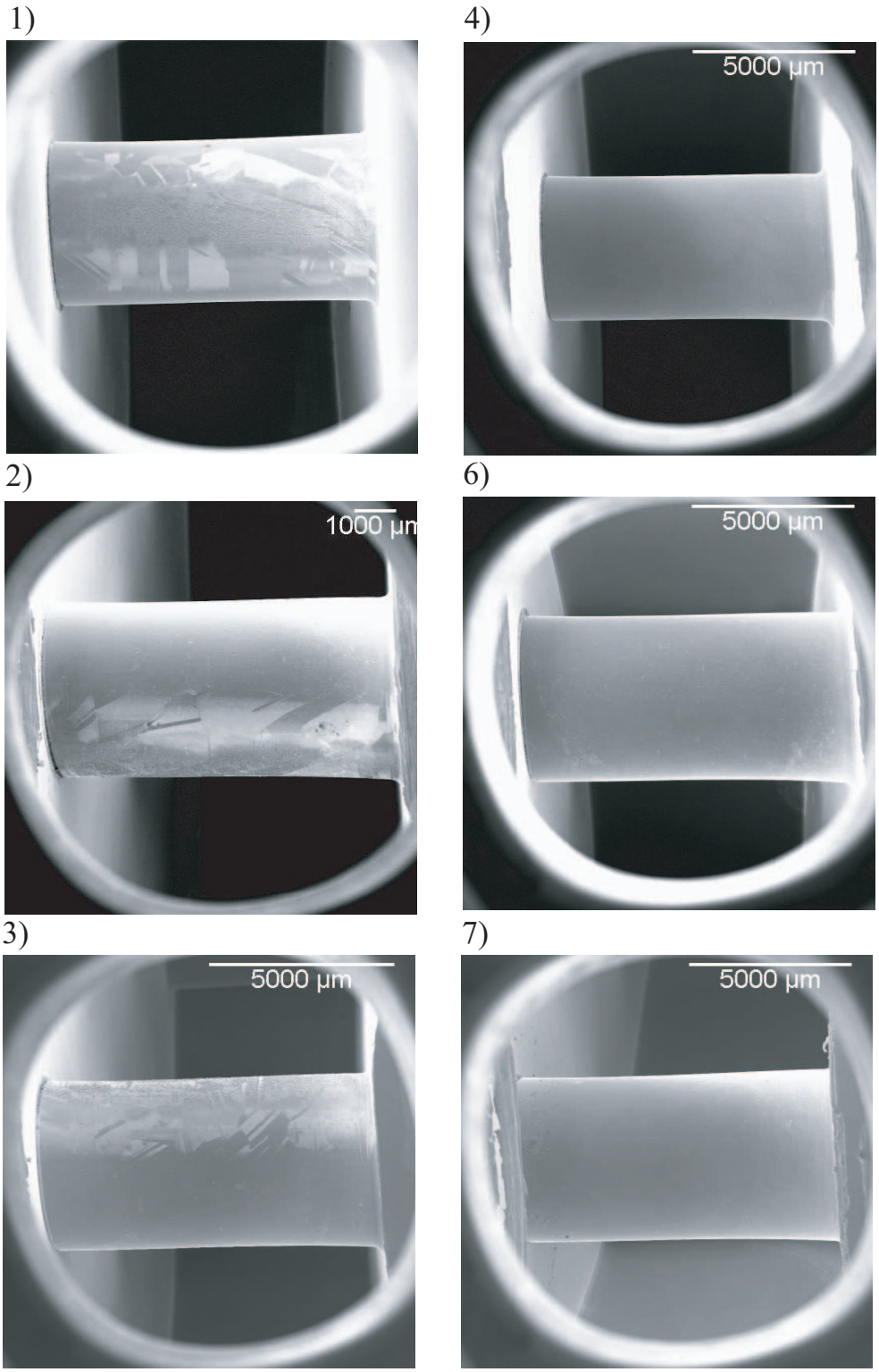

Figure 6-41: SEM micrographs of PBG structure rods as numbered in Figure 6-38 [66]. Rods are numbered outwards, 1–7: 1), 2), and 3) are inner rods, which experienced high field strength; rods 4), 6), and 7) are outer rods, which did not. Damage is visible on the inner surfaces of the rods in 1), 2), and 3).

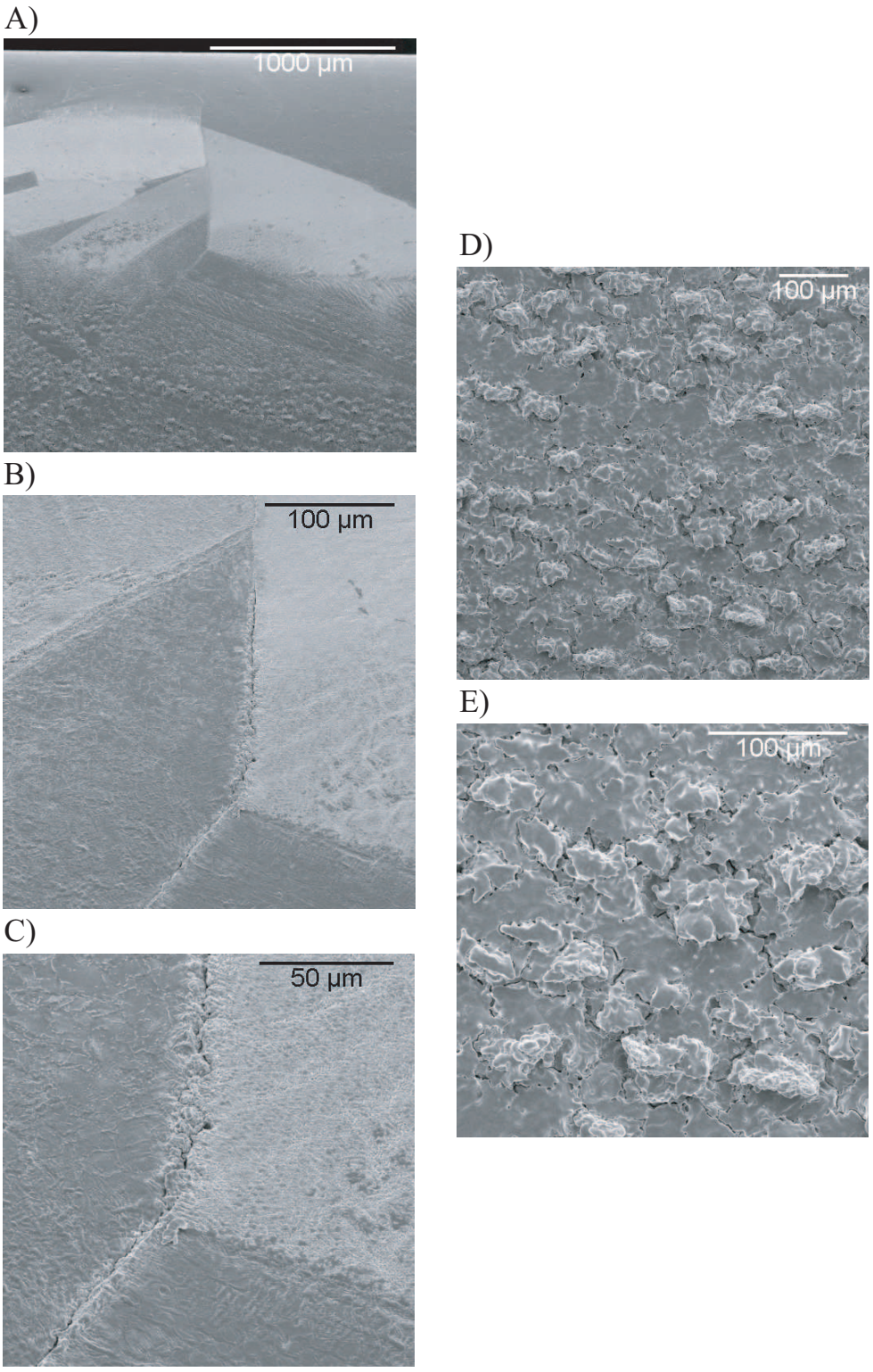

Figure 6-42: Detailed SEM micrographs of the PBG structure rod in Figure 6-41 1, showing pulsed heating damage [66]. Grain growth is clear in A), and shown in increasing detail in B) and C). Increased surface roughness is shown in increasing detail in D) and E).

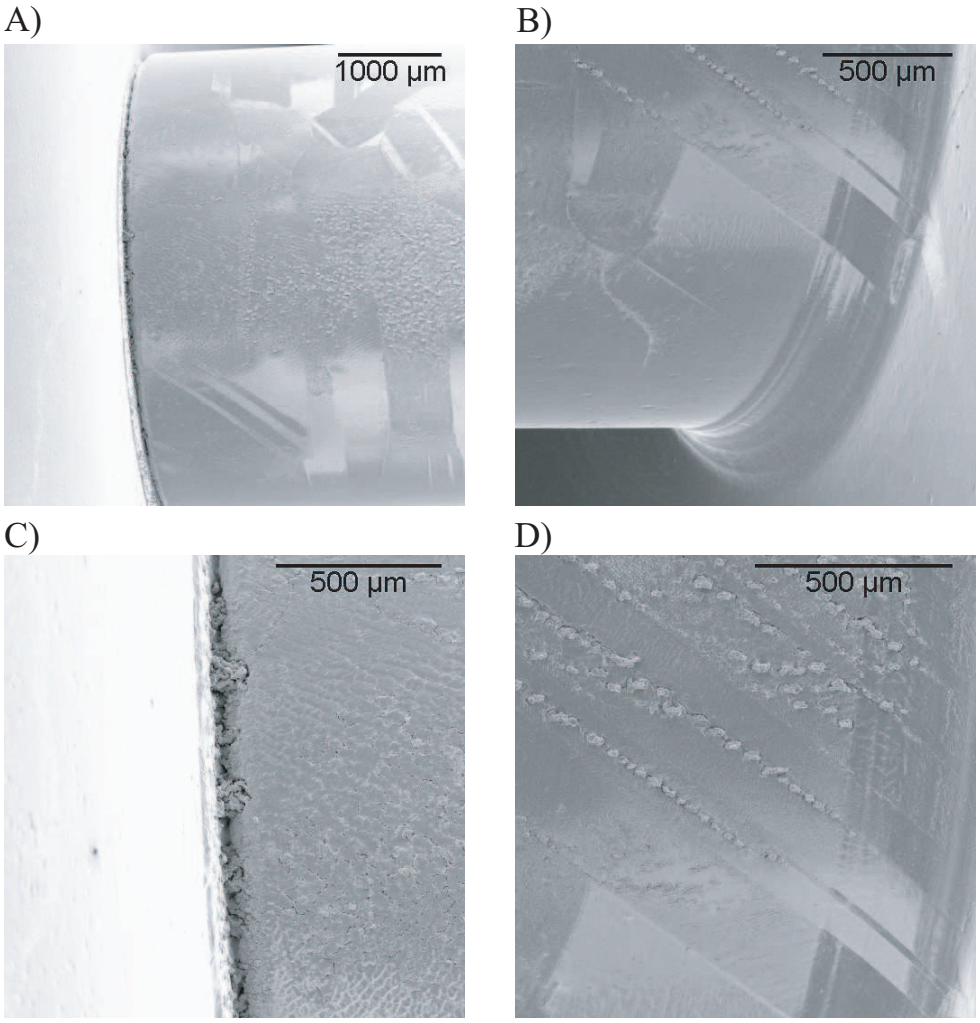

Figure 6-43: SEM micrographs of PBG structure rod 1 [66]. A) and B) show pulsed heating surface damage on the brazed and machined ends of rod 1, respectively, which is shown in greater detail in C) and D), respectively. Grain boundaries are visible, as is increased surface roughness along the grains boundary edges and central portion of the rod.

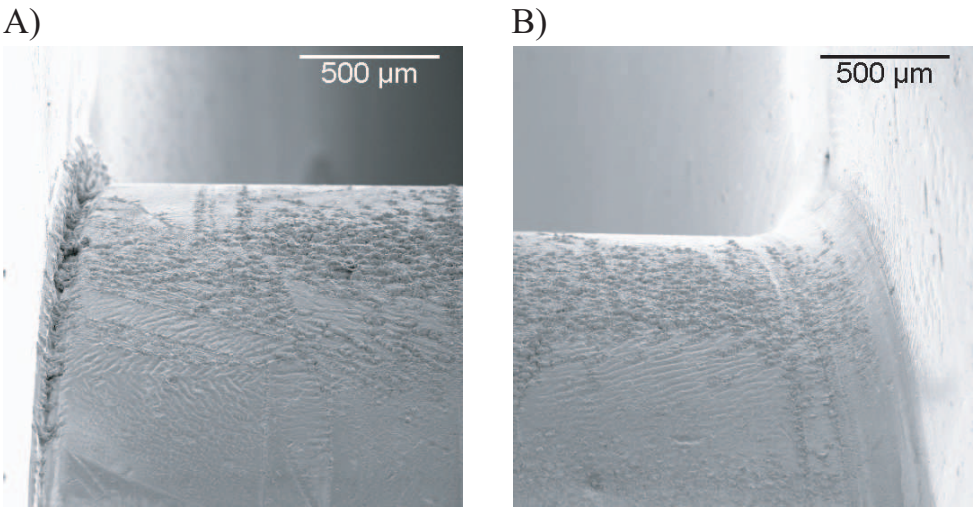

Figure 6-44: SEM micrographs of PBG structure rod 3 [66]. A) and B) show pulsed heating surface damage on the brazed and machined ends of rod 3, respectively.

the calibration simulation results of Figure 5-15. Extensive cratering is expected on the iris surface, in accordance with the phenomenology of Figure 2-3. Instead, the iris surface of the PBG structure appeared undamaged under SEM imaging, as shown in Figure 6-40 and Figure 6-39.

The maximum magnetic field is observed on the inner rod surfaces, as shown in the calibration simulation results of Figure 5-16. Extensive damage was seen on these surfaces as a result of pulsed heating temperature rise induced fatigue, as shown in Figure 6-41, and in detail in Figure 6-42. Though the magnetic field is very large on these surfaces, there is a small electric field, which was shown in Figure 5-17. This low level electric field will be enhanced by local surface defects produced by pulsed heating damage. A low level β enhancement of these fields, with $\beta \sim 20$, will result in the same electric field on the rods as is present on the iris surface.

Evidence of surface roughness is clear in the SEM micrographs of the rod surfaces, and β of order 10–20 can be estimated by looking at the SEM micrographs for rods 2 and 3, which are viewed at an angle with respect to the surface normal. The surface of rod 2 is shown in Figure 2-2 A, with detail in Figure 2-2 B; the surface of rod 3 is shown in Figure 2-2 C, with detail in Figure 2-2 D. The field enhancement β can be estimated from these images, and the scaling shown in Figure 2-2.

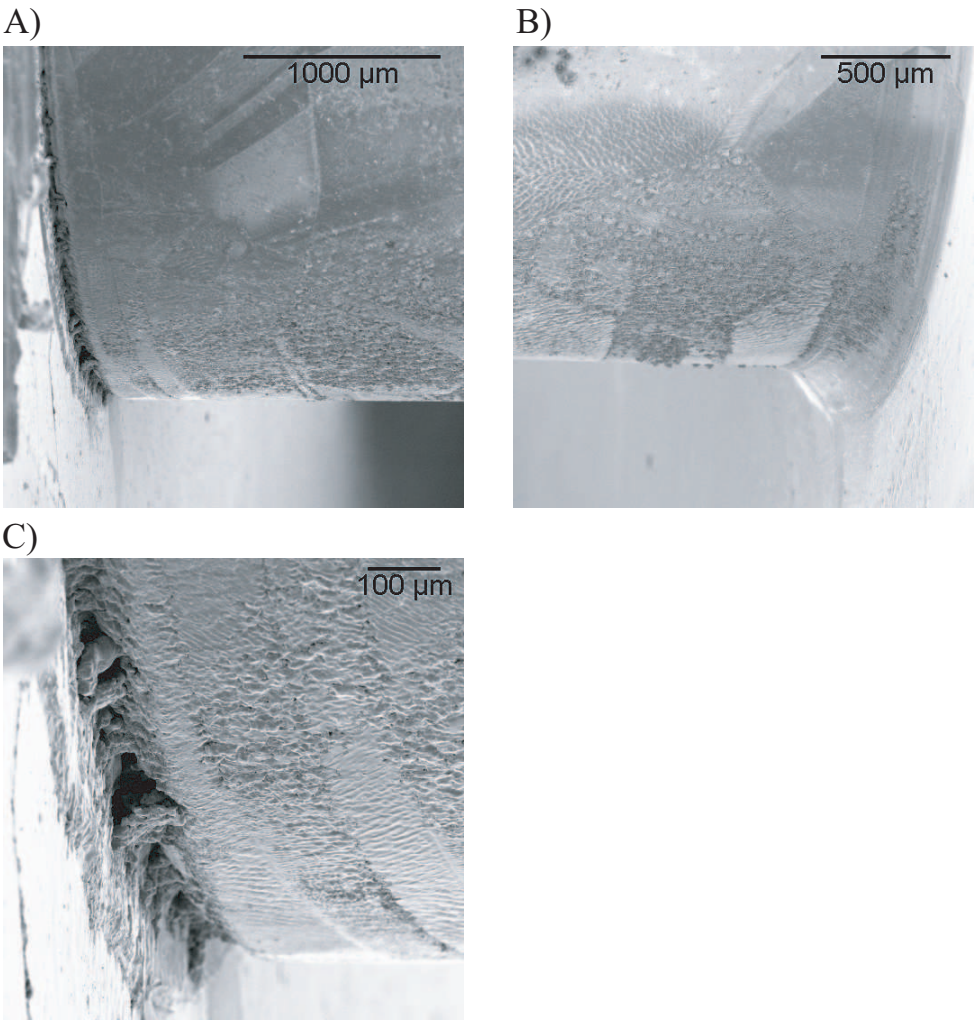

Figure 6-45: SEM micrographs of PBG structure rod 2 [66]. A) and B) show pulsed heating surface damage on the brazed and machined ends of rod 2, respectively. The increased surface damage on the braze joint is shown in detail in C).

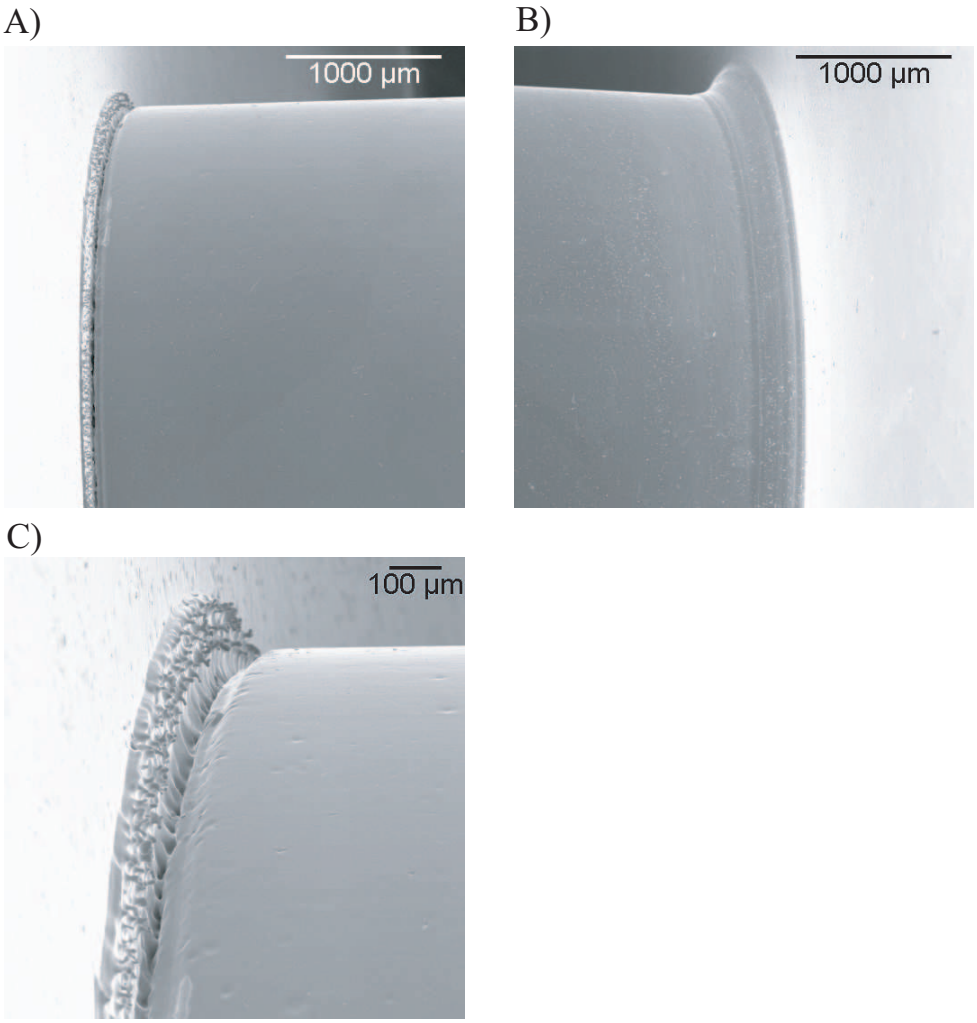

Figure 6-46: SEM micrographs of PBG structure rod 4 [66]. A) and B) show the undamaged surface of the brazed and machined ends of rod 4, respectively. The brazed joint is shown in detail in C); Braze material has collected annularly around the rod, and the joint itself is slightly convex.

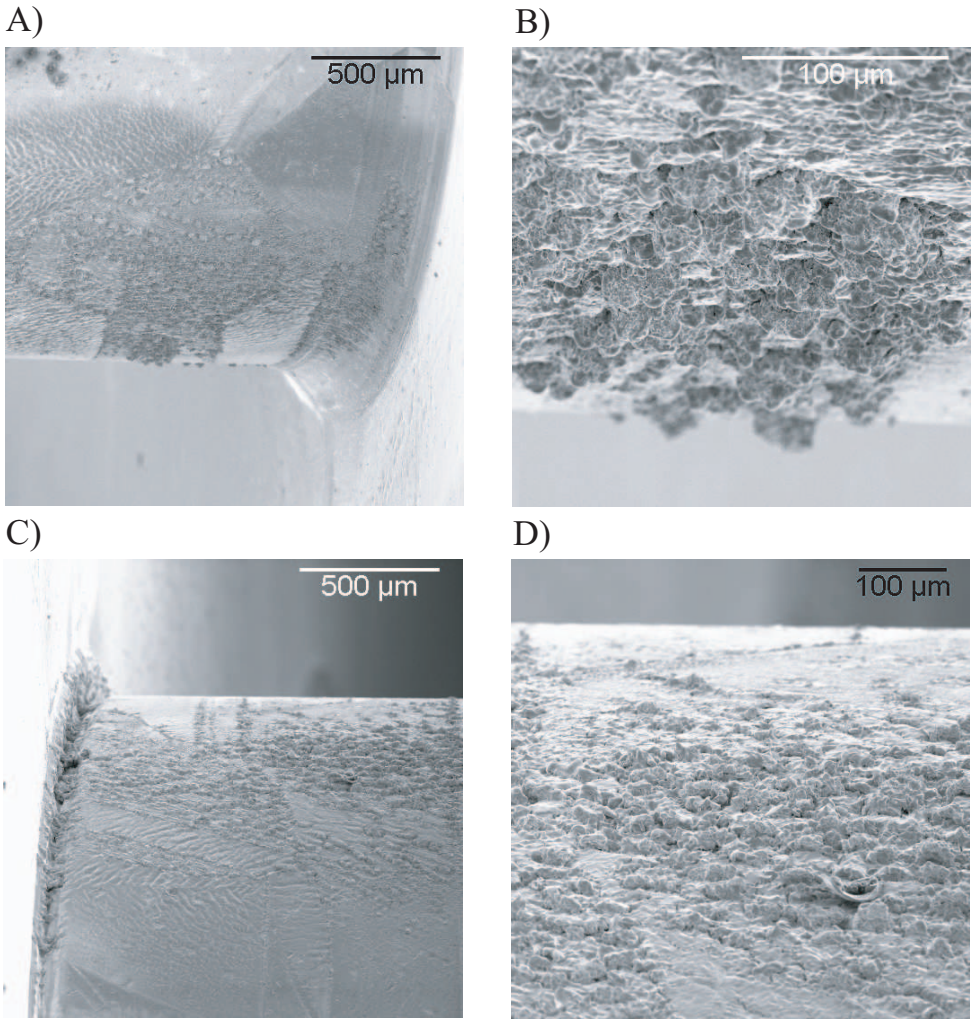

Figure 6-47: SEM micrographs of PBG structure rods 2 and 3 [66]. A) and C) show pulsed heating surface damage on rods 2 and 3, respectively, which is shown in greater detail in B) and C), respectively. β can be estimated using these oblique angle views of increased surface roughness.

Breakdown in the PBG structure can be understood as a two step process: the magnetic field induces pulsed heating damage on the surface, the surface damage results in increased β regions, which instigates electric field breakdown by the process of Figure 2-3. The damage due to pulsed heating is uniform over the rod surface, as demonstrated in SEM micrographs, and predicted by the field plot of maximal magnetic field in Figure 5-16. The damage due to electric field breakdown on the rods will be non-uniform, peaking on the two maxima observed in the rod surface electric field plot in Figure 5-17. This asymmetry is not observed in SEM imaging of the rods surface, but can be explained by the convolved uniformity of pulsed heating damage.

6.8 Comparison with Other Breakdown Phenomena

6.8.1 Traveling Wave Structures

The present results may be compared with breakdown observed on the input couplers of traveling wave structures, where there is high magnetic field, and low electric field. These coupler irises experienced high magnetic fields and large pulsed heating temperature rises. Damage was observed on the coupler irises, and they were redesigned for lower temperature rise [55]. A pulsed heating temperature rise of 270 K produced sufficient damage that the 13 MV/m electric field on the iris surface was increased to the point that breakdown occurred [67]. This is the same explanation put forward to explain the PBG structure breakdown results. The difference between breakdown phenomena in standing wave and traveling wave accelerators is an active area of research, and results are generally not deemed to be applicable across these domains.

6.8.2 Outgassing

Breakdown at low gas pressure can occur at fields much lower than those in vacuum. F. Paschen discovered a relation for the DC breakdown limit as a function of gas pressure [68]. The effect of gas on rf breakdown is less understood in the current era of high quality vacuum systems. During rf conditioning, adsorbed surface gas is emitted, and the structure performance improves [69]. High pulsed heating in the PBG structure could have produced copper gas in the vicinity of the inner row of rods, where the surface magnetic field is maximum. This surface outgassing could itself breakdown, or lower the breakdown threshold for the structure as a whole. The gas could also remain in the structure between shots, and due to the 60 Hz operation, lower the breakdown threshold for subsequent shots.

6.8.3 High Magnetic Field

Breakdown has also been observed in low frequency cavities, at 200 and 800 MHz, with large DC magnetic fields, up to 5 T [70]. Recent theory work has focused on the motion of electrons emitted from the surfaces, and their complicated motion in these high fields. A model of breakdown has been put forward by R. B. Palmer, et alia, in which electrons are accelerated by the electric field, and sufficiently focused by the magnetic fields to induce damage on the cavity surfaces and instigate breakdown. This model is not applicable to the PBG structure, but particle tracking simulations would be necessary to understand the motion of emitted particles in the complicated field patterns of PBG structures. Back bombardment of emitted electrons is possible in the high magnetic field region near the rod, and may cause additional damage of the surface. However, the surface damage observed on the rods in the PBG structure is consistent with high pulsed heating damage observed in previous experiments [15].

6.9 Conclusions

The cold test, borescope images, and SEM imaging provide a large amount of information on the surface of the PBG structure after high power testing. Cold testing confirmed that the coupling cell modes were unchanged, but the operating π-mode of the structure Q has degraded by 10%. Q degradation was attributed to surface roughness, which was observed on the inner row of rods in both borescope and SEM micrographs. Borescope and SEM micrographs reveal undamaged irises, with only tool marking roughness. SEM micrographs followed up on what appeared to be deficient brazing of the rods to one of the irised end plates. Damage was observed on both ends of the rods, and the mode Q in original cold test was quite close to its design value; the braze was sufficient for testing even if it created material and a defect for enhanced growth of pulsed heating damage. Extensive grain growth was seen on the inner rods. The grain boundaries show the cracking and enhanced surface roughness typical of high temperature pulsed heating [15].

The breakdown performance of the PBG structure was limited by the damage produced by high pulsed heating on the inner row of rods. The structure should perform more closely to the reported results for the SLAC baseline pillbox structure, if the pulsed heating temperature rise is limited to < 50 K. Another PBG structure could be built and tested at SLAC using the old design to verify this prediction. A full redesign of the PBG structure to lower the peak magnetic field on the inner row of rods was reported in Section 5.4. This next generation structure could be built and tested at SLAC, and will perform better than the first PBG structure.

Several major recommendations for future testing have arisen as a result of this testing. Surface condition should be verified by borescope imaging prior to high power testing, so that the surface condition can be gauged prior to high power rf conditioning. Structure processing and high power testing should be restricted in power and pulse length so that the structure experiences less than 50 K pulsed heating temperature rise. A real time integration of the structure power could be implemented into the computer control system to provide immediate feedback on the structure

heating. More extensive experimental diagnostics would provide information on the structure properties during high power testing. The pressure record for the structure, and other pertinent testing parameters should be stored and indexed to structure testing so that uniformity or deviation can be ascertained across structure testing runs.

Chapter 7

Discussion and Conclusion

7.1 Summary of Results

Major advances in the theoretical understanding of higher order modes in PBG structures have been made. HOMs are seen to be low Q modes, present primarily in the lattice of the PBG structure. The quality factors of the modes are seen as the quantitative measure of HOM damping in PBG structures. PBG HOMs have been observed in cold test of the 17 GHz six cell PBG structure previously demonstrated at MIT. HOMs were observed at dipole mode frequencies, and had Q factors on the order of 100, as predicted by *HFSS* simulations. PBG wakefields were directly excited and measured in the six cell structure. The 17 GHz PBG structure was unpowered by rf, and the electron beam excited wakefields that were experimentally observed. Excellent agreement was seen at 17 GHz with comparison to an analytic traveling wave excitation theory, and numerical wakefield simulations.

As part of the US high gradient research collaboration, an 11.424 GHz PBG structure was designed for breakdown testing at SLAC. This structure is the first PBG structure to be tested for breakdown phenomena and limits. Design of the structure predicted very high pulsed heating on the inner row of rods, and extensive design work has been done on structure improvements. A next generation PBG structure design was completed with an elliptically contoured inner row of rods.

The single cell breakdown PBG structure was fabricated by collaborators at SLAC.

Cold testing bead pull measurements revealed the modes predicted, in very good agreement with design parameters. The mode frequencies, coupling, and quality factors were also close to design. The structure was installed at SLAC, and testing was completed. Cold test and bead pull measurements were repeated after high power testing, showing a decrease in the operating mode Q, indicating damage. The mode frequency and field profile showed little change indicating the damage was an increase in surface roughness, or wall losses. This was confirmed by borescope imaging of the surface and subsequent SEM imaging.

The breakdown data for the PBG structure was analyzed to produce breakdown rate plots with respect to the field quantities in the structure. Exponential trends were seen across the field strengths and pulse lengths tested. The SLAC baseline pillbox structure data was analyzed and compared with PBG structure results. The PBG structure performance was $\sim 40\%$ worse with respect to accelerating gradient or electric field performance. The surface magnetic field in the PBG structure was much higher than that seen in any other structure testing. This resulted in the pulsed heating surface damage, but also indicates exciting new physics involved in the interplay of electric and magnetic field effects in the breakdown performance of accelerator structures.

7.2 Discussion of Relevance

Theory work on PBG HOMs represent a major advance. PBG wakefields are understood as modes that can be excited by the accelerated beam. Quantitative measure of mode damping, via the mode Qs allows PBG design damping to be compared directly against other damping solutions, or PBG structure variations.

The results of the PBG structure breakdown testing are very exciting. A pillbox structure is not a viable future linear collider concept. The PBG structure red points stand alone, on the breakdown plots in Figure 6-24, and Figure 6-26. If lower accelerating gradients are achievable in damped structures when compared with pillbox structure performance, it is an important issue that must be dealt with in both col-

lider and structure design and development. The performance of damped structures must be understood, and the testing of this first PBG structure is an important step.

The importance of magnetic field effects in breakdown performance has been highlighted in this work as a vital area of investigation. Pulsed heating damage of structures with high peak magnetic fields has been observed, and the structures have been redesigned to reduce the peak field in the high field regions. Breakdown on the input couplers of devices has been a limiting factor in testing the breakdown performance of some structures [55]. This has not been understood as the observation of magnetic field induced breakdown, but as the limiting of input power for testing the entirety of the accelerator structure. Differentiation of breakdown phenomena according to source, or damage potential has been an important establishment of vocabulary in normal conducting accelerator research. Magnetically induced breakdown, or the interplay of magnetic field effects on breakdown has not been a part of previous models of breakdown, and the results we have seen were not anticipated.

Breakdown data for various geometry pillbox structures shows variation in the maximum surface electric field, or accelerating gradient with breakdown rate; little variation is seen with respect to surface magnetic field. The PBG breakdown data provides an unique insight on this unexplored territory. PBG data is very disparate from pillbox magnetic field data, and shows significant disagreement with the magnetic field breakdown rate correlation implied by pillbox data. The PBG structure provides an unique interplay of electric and magnetic fields. This interplay results in the two theoretical models put forward to explain the breakdown results.

The breakdown results for the PBG structure are understood as the result of a low electric field on the PBG lattice rods being enhanced by pulsed heating damage. The expected asymmetry in electric field induced damage is obscured by the uniformity of pulsed heating damage. Alternative hypotheses involve the role of copper ions and electrons expelled by the high pulsed heating on the rod surface, and either their direct interaction with the electric and magnetic fields, or the subsequent complex motion of these particles in the electric and magnetic fields present in the structure.

7.3 Future Directions

7.3.1 Experiments at 17 GHz

The 17 GHz accelerator laboratory at MIT is well suited to single cell breakdown testing of structures. The TM_{01} mode launchers can be scaled to 17 GHz so that testing identical to that done at SLAC can be accomplished at MIT. To protect the klystron tube from high power reflections, isolators or a circulator must be built or purchased. PBG structures provide an excellent opportunity for diagnostics. Faraday cups, x-ray monitors, acoustic sensors, and dark current spectroscopy can all be done. In addition, the open nature of the structure enables real time observation of the material surfaces under high power conditions, as well as easily implemented real time diagnostics of the cavity environment.

7.3.2 Breakdown and Pulsed Heating

The link between rf breakdown and pulsed heating has been raised by the work in this thesis. This can be further investigated by the fabrication of more single cell PBG structures for breakdown testing. The same PBG structure that has been tested at SLAC can be rebuilt, and tested again under more stringent pulsed heating conditions, so that the structure performance can be insured to be free from early damage. A second structure can be built and tested as described in the design of Section 5.5. A second structure could also explore the parameter space in the other direction, by increasing the pulsed heating on the rods.

7.3.3 New Photonic Bandgap Structures

Breaking the perfect symmetry of the triangular lattice of cylindrical rods, greatly extends the parameter space for PBG structures (often called photonic quasi-crystals when symmetry is lost). Ideas for improving the E/H ratio were presented in Section 5.4, but need not be limited to minor changes to the triangular lattice of cylindrical rods. Ideal PBG structures have only two degrees of freedom: the rod radius

and rod spacing. These two parameters are limited to just one, the a/b ratio, when the other is used to fix the structure frequency. New photonic bandgap structure ideas must make some concession to this high degree of symmetry to improve the accelerator performance of the structure.

7.3.4 Damping

Damping HOMs is the motivation for PBG structures. The first proof of principle experiment at MIT was open, allowing the wakefields to escape the structure. These wakefields have been measured and must be damped by absorbing material. The exact shape of external damping for vacuum application is a valuable future direction for design research.

Bibliography

[1] Alexander Chao et al. 2001 Snowmass Accelerator R&D report. Prepared for APS / DPF / DPB Summer Study on the Future of Particle Physics (Snowmass 2001), Snowmass, Colorado, 30 June–21 July 2001.

[2] M. Stanley Livingston. *Particle accelerators by M. Stanley Livingston and John P. Blewett*. International series in pure and applied physics. McGraw-Hill, New York, second edition, 1962.

[3] Thomas Hambye and Kurt Riesselmann. Matching conditions and Higgs boson mass upper bounds reëxamined. *Phys. Rev. D*, 55(11):7255–7262, June 1997.

[4] M. Grünewald. hep-ex/0511018.

[5] Fumihiko Takasaki. Presentation at International Accelerator School for Linear Colliders. Sokendai, Hayama, Japan, May 20, 2006.

[6] P. Garcia-Abia, W. Lohmann, and A. Raspereza. Prospects for the measurement of the Higgs boson mass with a linear e+ e– collider. *The European Physical Journal C*, 44(4):481–488, December 2005.

[7] K. Saito. Presentation at ILC GDE Meeting at LICWS06, March 12, 2006, Bangalore, India.

[8] J. D. Jackson. *Classical Electrodynamics*. John Wiley & Sons, New York, 2 edition, 1962,1975.

[9] S. Y. Lee. *Accelerator Physics*. World Scientific, Singapore, 1999.

[10] David H. Whittum. Introduction to electrodynamics for microwave linear accelerators. Talk given at Joint CERN-US-Japan Accelerator School: Course on Frontiers of Accelerator Technology: RF Engineering for Particle Accelerators, Tsukuba, Japan, 9–18 September 1996.

[11] W. D. Kilpatrick. Criterion for vacuum sparking designed to include both rf and DC. *Review of Scientific Instruments*, 28(10):824–826, 1957.

[12] G. A. Loew, and J. W. Wang. RF breakdown studies in room temperature electron linac structures. Originally part of an invited presentation to 13th Int. Symp. on Discharges and Electrical Insulation in Vacuum, Paris, France, June 27–30, 1988.

[13] H. H. Braun, S. Döbert, I. Wilson, and W. Wuensch. Frequency and temperature dependence of electrical breakdown at 21, 30, and 39 GHz. *Phys. Rev. Lett.*, 90(22):224801, June 2003.

[14] S. V. Kuzikov and M. E. Plotkin. Model of thermal fatigue of a copper surface under the action of high-power microwaves. *Radiophysics and Quantum Electronics*, 50:885–892, October 2007.

[15] David P. Pritzkau and Robert H. Siemann. Experimental study of rf pulsed heating on oxygen free electronic copper. *Phys. Rev. ST Accel. Beams*, 5(11):112002, November 2002.

[16] Thomas Wangler. *RF Linear Accelerators*. John Wiley & Sons, Inc., New York, 1998.

[17] K. L. F. Bane, P. B. Wilson, and T. Weiland. Wake fields and wake field acceleration. *AIP Conference Proceedings*, 127(1):875–928, 1985.

[18] R. D. Ruth. The Next Linear Collider Test Accelerator: status and results. Proceedings of the 1996 European Particle Accelerator Conference, Barcelona, Spain, (1996), pp. 47–51.

[19] Y. H. Chin, N. Akasaka, Y. Takeuchi, K. Tajima, and C. K. Ng. Design of HOM power absorbers for the KEK B-Factory. Proceedings of the 1996 European Particle Accelerator Conference, Barcelona, Spain, (1996), pp. 2000–2002.

[20] A. Grudiev, and W. Wuensch. A newly designed and optimized CLIC main linac accelerating structure. Proceedings of LINAC 2004, Lubeck, Germany, (2004), pp. 779–781.

[21] B. Aune, R. Bandelmann, D. Bloess, B. Bonin, A. Bosotti, M. Champion, C. Crawford, G. Deppe, B. Dwersteg, D. A. Edwards, H. T. Edwards, M. Ferrario, M. Fouaidy, P.-D. Gall, A. Gamp, A. Gössel, J. Graber, D. Hubert, M. Hüning, M. Juillard, T. Junquera, H. Kaiser, G. Kreps, M. Kuchnir, R. Lange, M. Leenen, and M. Liepe. Superconducting TESLA cavities. *Phys. Rev. ST Accel. Beams*, 3(9):092001, September 2000.

[22] Tsumoru Shintake. The choke mode cavity. *Jpn. J. Appl. Phys.*, 31, Part2(11A):L1567–L1570, 1992.

[23] S. Schultz, D.R. Smith, and N. Kroll. Photonic band gap resonators for high energy accelerators. *Proceedings of the 1993 Particle Accelerator Conference*, pages 2559–2563 vol.4, May 1993.

[24] D. R. Smith, S. Schultz, N. Kroll, M. Sigalas, K. M. Ho, and C. M. Soukoulis. Experimental and theoretical results for a two-dimensional metal photonic bandgap cavity. *Applied Physics Letters*, 65(5):645–647, 1994.

[25] Christophe Caloz and Tatsuo Itoh. *Electromagnetic metamaterials: Transmission line theory and microwave applications*. John Wiley & Sons, New York, 2006.

[26] John D. Joannopoulos, Steven G. Johnson, Joshua N. Winn, and Robert D. Meade. *Photonic Crystals: Molding the flow of light*. Princeton University Press, Princeton, 2 edition, 2008.

[27] E. I. Smirnova. *Novel Photonic Band Gap structures for accelerator applications*. PhD thesis, Massachusetts Institute of Technology, 2005.

[28] Evgenya I. Smirnova, Ivan Mastovsky, Michael A. Shapiro, Richard J. Temkin, Lawrence M. Earley, and Randall L. Edwards. Fabrication and cold test of photonic band gap resonators and accelerator structures. *Phys. Rev. ST Accel. Beams*, 8(9):091302, September 2005.

[29] Evgenya I. Smirnova, Amit S. Kesar, Ivan Mastovsky, Michael A. Shapiro, and Richard J. Temkin. Demonstration of a 17 GHz, high gradient accelerator with a Photonic Band Gap structure. *Physical Review Letters*, 95(7):074801, 2005.

[30] T. J. Boyd, Jr. Kilpatrick's Criterion. Los Alamos Group AT-1 report AT-1:82-28, February 12, 1982.

[31] R B Palmer. Prospects for high energy e+ e– linear colliders. *Annual Review of Nuclear and Particle Science*, 40(1):529–592, 1990.

[32] J. W. Wang and G. A. Loew. Field emission and rf breakdown in high gradient room temperature linac structures. Talk given at Joint CERN-US-Japan Accelerator School: Course on Frontiers of Accelerator Technology: RF Engineering for Particle Accelerators, Tsukuba, Japan, 9–18 September 1996.

[33] W. J. Brown, S. Trotz, K. E. Kreischer, M. Pedrozzi, M. A. Shapiro, and R. J. Temkin. Experimental and theoretical investigations of a 17 GHz rf gun. *Nuclear Instruments and Methods in Physics Research Section A: Accelerators, Spectrometers, Detectors and Associated Equipment*, 425(3):441–459, 1999.

[34] W. J. Brown, S. E. Korbly, K. E. Kreischer, I. Mastovsky, and R. J. Temkin. Low emittance electron beam formation with a 17 GHz rf gun. *Phys. Rev. ST Accel. Beams*, 4(8):083501, August 2001.

[35] R. H. Fowler and L. Nordheim. Electron emission in intense electric fields. *Proc. R. Soc. A*, 119(781):173–181, May 1928.

[36] F. Rohrbach. Sur les mècanismes qui conduisent à la formation de l'étincelle électrique à très haute tension et sous ultra-vide par la mesure des temps de retard à la disruption. CERN 71-28, October 1971.

[37] G.A. Mesyats. Explosive processes on the cathode in a vacuum discharge. *Electrical Insulation, IEEE Transactions on*, EI–18(3):218–225, June 1983.

[38] M. Chodorow, E. L. Ginzton, W. W. Hansen, R. L. Kyhl, R. B. Neal, W. K. H. Panofsky, and the Staff. Stanford high-energy linear electron accelerator (Mark III). *Review of Scientific Instruments*, 26(2):134–204, 1955.

[39] Karl L. F. Bane, Valery A. Dolgashev, Tor Raubenheimer, Gennady V. Stupakov, and Juhao Wu. Dark currents and their effect on the primary beam in an X-band linac. *Phys. Rev. ST Accel. Beams*, 8(6):064401, June 2005.

[40] Perry B. Wilson. Scaling linear colliders to 5-TeV and above. *AIP Conf. Proc.*, 397:191–202, 1997.

[41] J. E. Leiss. Beam loading and transient behavior in traveling wave electron accelerators. In Pierre M. Lapostolle and Albert L. Septier, editors, *Linear Accelerators*, section Electron Linacs: Theory. B.1.3, pages 147–172. North-Holland Publishing Company, Amsterdam, 1969.

[42] Bruno W. Zotter and Semyon A. Kheifets. *Impedances and Wakes in high-energy particle accelerators*. World Scientific, Singapore, 1998.

[43] W. K. H. Panofsky and W. A. Wenzel. Some considerations concerning the transverse deflection of charged particles in radio-frequency fields. *Review of Scientific Instruments*, 27(11):967–967, 1956.

[44] High Frequency Structure Simulator, Ansoft Corporation, www.hfss.com.

[45] M. Luong, I. Wilson, and W. Wuensch. RF loads for the CLIC multibunch structure. *Proceedings of the 1999 Particle Accelerator Conference*, 2:821–823 vol.2, 1999.

[46] N. Kroll, S. Schultz, D.R. Smith, and D.C. Vier. Photonic band gap accelerator cavity design at 90 GHz. *Proceedings of the 1999 Particle Accelerator Conference*, 2:830–832 vol.2, 1999.

[47] J. Haimson, B. Mecklenburg, G. Stowell, K. E. Kreischer, and I. Mastovsky. Preliminary performance of the MKII 17 GHz traveling wave relativistic klystron. volume 474, pages 137–137. AIP, 1999.

[48] W.J. Mulligan, S.C. Chen, G. Bekefi, B.G. Danly, and R.J. Temkin. A high-voltage modulator for high-power rf source research. *IEEE Transactions on Electron Devices*, 38(4):817–821, April 1991.

[49] J. Haimson and B. Mecklenburg. HV injection phase orbit characteristics for sub-picosecond bunch operation with a high gradient 17 GHz linac. *Proceedings of the 1995 Particle Accelerator Conference*, 2:755–757 vol.2, May 1995.

[50] J. Haimson, B. Mecklenburg, G. Stowell, and B. Ishii. A circularly polarized beam deflector for direct measurement of ultra short electron bunches. volume 647, pages 810–820. AIP, 2002.

[51] J. Haimson. Longitudinal phase space measurements of short electron bunches using a 17 GHz circularly polarized beam deflector. volume 737, pages 95–108. AIP, 2004.

[52] I. Gonin, N. Solyak, J. DeFord, B. Held, in Proceedings of the 2007 Particle Accelerator Conference, (IEEE, Piscataway, NJ, 2007), pp. 2248–2250.

[53] J. DeFord, B. Held, J. J. Petillo, in Proceedings of the 2007 Particle Accelerator Conference, (IEEE, Piscataway, NJ, 2007), pp. 3600–3602. .

[54] S. Kuhlman et al. Physics and technology of the Next Linear Collider: A Report submitted to Snowmass ' 96. 1996.

[55] Christopher Nantista, Sami Tantawi, and Valery Dolgashev. Low-field accelerator structure couplers and design techniques. *Phys. Rev. ST Accel. Beams*, 7(7):072001, July 2004.

[56] V.A. Dolgashev, S.G. Tantawi, C.D. Nantista, Y. Higashi, and T. Higo. RF breakdown in normal conducting single-cell structures. *Proceedings of the 2005 Particle Accelerator Conference*, pages 595–599, May 2005.

[57] E. Smirnova, Private communication.

[58] B. Spataro, Private communication. SLAC baseline pillbox structure.

[59] V. A. Dolgashev, Private communication. SLAC baseline pillbox structure.

[60] Carl A. Bauer, Gregory R. Werner, and John R. Cary. Truncated photonic crystal cavities with optimized mode confinement. *Journal of Applied Physics*, 104(5):053107, 2008.

[61] Jr. L. C. Maier and J. C. Slater. Field strength measurements in resonant cavities. *Journal of Applied Physics*, 23(1):68–77, 1952.

[62] C.W. Steele. A nonresonant perturbation theory. *Microwave Theory and Techniques, IEEE Transactions on*, 14(2):70–74, February 1966.

[63] David M.Pozar. *Microwave Engineering*. John Wiley & Sons, Inc., New York, 3 edition, 2005.

[64] Mathematica 7, Wolfram Research, www.wolfram.com.

[65] V.A. Dolgashev, S.G. Tantawi, Y. Higashi, and T. Higo. Status of high power tests of normal conducting single-cell structures. In *Proceedings of The 2008 European Particle Accelerator Conference, Genoa, Italy*, pages 742–744. June 23–27 2008.

[66] L. Laurent, Private communication. 1C-SW-A5.65-T4.6-Cu-PBG-SLAC#1 scanning electron microscope micrographs.

[67] Valery A. Dolgashev and Sami G. Tantawi. Effect of rf parameters on breakdown limits in high-vacuum X-Band structures. volume 691, pages 151–165. AIP, 2003.

[68] Friedrich Paschen. Ueber die zum Funkenübergang in Luft, Wasserstoff und Kohlensäure bei verschiedenen Drucken erforderliche Potentialdifferenz. *Annalen der Physik*, 273(5):69–96, 1889.

[69] J. Haimson and B. Mecklenburg. Design features and initial rf performance of a gradient hardened 17 GHz TW linac structure. volume 1086, pages 464–469. AIP, 2009.

[70] R. B. Palmer, R. C. Fernow, Juan C. Gallardo, Diktys Stratakis, and Derun Li. RF breakdown with external magnetic fields in 201 and 805 MHz cavities. *Phys. Rev. ST Accel. Beams*, 12(3):031002, March 2009.